TAMPEREEN TEKNILLINEN YLIOPISTO
TAMPERE UNIVERSITY OF TECHNOLOGY

Elli Käpylä

Direct Laser Writing of Polymer-Ceramic and Hydrogel Microstructures by Two-Photon Polymerization

Julkaisu 1243 • Publication 1243

Tampere 2014

Tampereen teknillinen yliopisto. Julkaisu 1243
Tampere University of Technology. Publication 1243

Elli Käpylä

Direct Laser Writing of Polymer-Ceramic and Hydrogel Microstructures by Two-Photon Polymerization

Thesis for the degree of Doctor of Science in Technology to be presented with due permission for public examination and criticism in Tietotalo Building, Auditorium TB109, at Tampere University of Technology, on the 10th of October 2014, at 12 noon.

Tampereen teknillinen yliopisto - Tampere University of Technology
Tampere 2014

ISBN 978-952-15-3361-7 (printed)
ISBN 978-952-15-3383-9 (PDF)
ISSN 1459-2045

Abstract

Additive manufacturing techniques enable the fabrication of sophisticated micro- and nanostructures through computer controlled deposition of either energy, material or both. By combining these techniques with biomaterials, microstructures suitable for cell culturing and other biomedical applications can be created. Among these approaches, direct laser writing by two-photon polymerization (2PP-DLW) is a highly accurate and flexible technique that can be used for the processing of various synthetic and natural materials. 2PP-DLW is based on nonlinear two-photon absorption, which enables selective photopolymerization and realization complex three-dimensional (3D) microstructures in a single processing step.

This thesis focuses on the microfabrication of polymer-ceramic and hydrogel materials by custom built 2PP-DLW laser systems. The main objective was to determine how 2PP-DLW processing parameters affect the quality of microstructures aimed at cell culturing applications. The optimal processing conditions for a commercial polymer-ceramic material Ormocomp® were studied with the Irgacure® 127 photoinitiator and a picosecond laser system. It was found that the achievable Ormocomp® feature size could be reduced from microscale to nanoscale by careful tuning of laser power and exposure time. Within the determined fabrication window, the Ormocomp® microstructure dimensions could be tuned in a wide range by the choice of focusing optics and processing parameters. With help of these findings, Ormocomp® scaffold structures with a variable and defined degree of porosity and interconnectivity were successfully fabricated. The 85% porous scaffolds supported the attachment, viability and growth of human adipose stem cells in a six day culture.

Aimed at creating biomimetic microstructures, the 2PP-DLW processing of custom-synthetized poly(amino acid) hydrogels (poly(AA)s) was studied and compared to commercial poly(ethylene glycol) diacrylates (PEGdas). The acryloylated and methacryloylated poly(AA)s combined with the Irgacure® 2959 photoinitiator were found applicable to 2PP-DLW over a relatively wide range of processing parameters. Due to the wider fabrication window, the dimensions of poly(AA) microstructures could be tuned more than PEGda microstructures. Stable poly(AA) microstructures could be fabricated with 80% water content and with improved 3D fabrication performance with increasing acryloylation.

In the future, this work could be expanded to the fabrication of custom scaffolds for different cell types and stem cell lineages. These types of structures could combine areas of different chemical composition and porosity within a single scaffold. The poly(AA) hydrogels could also be combined with cells to fabricate cell-laden 3D microstructures.

Acknowledgements

The work presented in this thesis was done during 2010-2014 at Tampere University of Technology, Department of Electronics and Communications Engineering (formerly Department of Biomedical Engineering).

I wish to express my gratitude to my supervisor Prof. Minna Kellomäki for her support and guidance throughout this work. I also wish to thank the official pre-examiners, Prof. Jürgen Stampfl from TU Wien and Prof. Douglas B. Chrisey from Tulane University, for the careful evaluation of this thesis.

I would like to thank all my co-authors, Sanna Turunen, Jouko Viitanen, Jani Pelto, Sanni Virjula, Sari Vanhatupa, Susanna Miettinen, Jari Hyttinen, Tomáš Sedlačík and František Rypáček, for their contributions and the rewarding collaboration. I am very grateful to Jouko for sharing his lab and expertise with me and for helping me with the laser processing. I am most grateful to Sanna for all her help, support and friendship throughout this work. I would also like to thank my colleagues and the staff at the University for the pleasant work atmosphere and the interesting discussions. I have enjoyed working with you all. I especially want to thank Anne-Marie Haaparanta for sharing with me both the challenges and the humorous aspects of work.

I am extremely grateful for the financial support of the Finnish Cultural Foundation, Emil Aaltonen Foundation, Tekniikan edistämissäätiö (TES) and the Doctoral Program of Tampere University of Technology's President. I especially wish to express my gratitude to the Ulla and Eino Karosuon rahasto of the Finnish Cultural Foundation for the support given to me in 2010-2012, which made all of this work possible.

I want to thank all my dear friends and family who continue to enrich my life beyond measure. I am deeply grateful to my sisters Hanna and Kaisa and their families for their support with not only my work but with all other aspects of life. I want to express my deepest gratitude to my parents, Pirjo and Markku Käpylä, for their constant love and support throughout my life and this thesis project. Thank you for always being there for me and for encouraging me to be the best I can be.

Finally, I dedicate this work to Baran. Thank you for being you, my rock, my inspiration, my everything.

Tampere, September 2014

Elli Käpylä

Table of Contents

List of original publications

This thesis is based on the following original publications that are referred to as Publications I-IV in the text. The publications are reprinted with permissions from the publishers.

I. E. Käpylä, S. Turunen, M. Kellomäki. Two-Photon Polymerization of a Polymer-Ceramic Hybrid Material with a Low-Cost Nd:YAG Laser: Preliminary Resolution Study and 3D Fabrication. Micro and Nanosystems 2(2010)2, pp. 87-99.

II. E. Käpylä, S. Turunen, J. Pelto, J. Viitanen, M. Kellomäki. Investigation of the optimal processing parameters for picosecond laser-induced microfabrication of a polymer-ceramic hybrid material. Journal of Micromechanics and Microengineering 21(2011)6, p. 065033

III. E. Käpylä, D. B. Aydogan, S. Virjula, S. Vanhatupa, S. Miettinen, J. Hyttinen, M. Kellomäki. Direct laser writing and geometrical analysis of scaffolds with designed pore architecture for three-dimensional cell culturing. Journal of Micromechanics and Microengineering 22(2012)11, p. 115016.

IV. E. Käpylä, T. Sedlačík, D. B. Aydogan, J. Viitanen, F. Rypáček, M. Kellomäki. Direct laser writing of synthetic poly(amino acid) hydrogels and poly(ethylene glycol) diacrylates by two-photon polymerization. Materials Science and Engineering C: Materials for Biological Applications 43(2014), pp. 280-289.

Author's contribution

I. The author designed and performed the 2PP-DLW experiments in collaboration with the second author, who also co-wrote the Experimental section. The author analyzed the data and wrote the manuscript as the first author.

II. The author designed and performed the 2PP-DLW experiments with assistance from the second author, who also co-wrote the Materials and methods section. The author analyzed and interpreted the data and wrote the manuscript as the first author.

III. The author designed and performed all the 2PP-DLW experiments and co-designed the cell culture experiments. The author analyzed and interpreted all the data and wrote the manuscript as the first author.

IV. The author designed and performed all the experiments. The second author synthesized the poly(amino acid) macromolecules. The author analyzed and interpreted all the data and wrote the manuscript as the first author.

Abbreviations

1PA	Single photon absorption
2D	Two-dimensional
2PA	Two-photon absorption
2PP	Two-photon polymerization
2PP-DLW	Direct laser writing by two-photon polymerization
3D	Three-dimensional
A	Electron acceptor
AAAP	Alkylaminoacetophenone
AFM	Atomic force microscopy
AM	Additive manufacturing
BM	Basal medium (BM)
BSA	Bovine serum albumin
CAD	Computer assisted drawing
CCD	Charge-Coupled Device
ECM	Extra cellular matrix
D	Electron donor
DAPI	4',6-diamidino-2-phenylindole
DLW	Direct laser writing
FAD	Flavin adenine dinucleotide
FGF	Fibroblast growth factor
FITC	Fluorescein isothiocyanate
FMN	Flavin mononucleotide (FMN)
fs	Femtosecond
FWHM	Full-width-at-half-maximum
HA	Hyaluronan
HAGM	Hyaluronan-glycidyl methacrylate conjugate
HAP	Hydroxyacetophenones
hASC	Human adipose stem cell
HEMA	2-hydroxyethyl methacrylate
hESC	Human embryonic stem cell
I127	Irgacure® 127
I2959	Irgacure® 2959

IR	Infrared
ISC	Inter-system crossing
LAP	Lithium phenyl-2,4,6-trimethylbenzoylphosphinate
LIFT	Laser induced forward transfer
M	Monomer
MAPLE DW	Matrix-assisted pulsed laser evaporation direct writing
MAPTMS	3-(trimethoxysilyl) propyl methacrylate
MPA	Multiphoton absorption
NA	Numerical aperture
NDM	Neural differentiation medium
Nd:YAG	Neodymium-doped yttrium aluminum garnet
Ormocer®	Organically modified ceramic
PI	Photoinitiator
P_D	Damage threshold
ps	Picosecond
P_{th}	Polymerization threshold
P_w	Polymerization window
PBS	Phosphate buffered saline
PDMS	Polydimethylsiloxane
PEG	Poly(ethylene glycol)
PEGda	Poly(ethylene glycol) diacrylate
PEGda-10000	Poly(ethylene glycol) diacrylate with molecular weight of 10000
PEGda-575	Poly(ethylene glycol) diacrylate with molecular weight of 575
PEGda-575-20	20% of PEGda-575 in water
PEO	Poly(ethylene oxide)
PETA	Pentaerythritol triacrylate
PGMEA	Propylene glycol monomethyl ether acetate
PHEG	Poly[N^5-(2-hydroxyethyl) L-glutamine]
PHEG-A9	9% acryloylated poly[N^5-(2-hydroxyethyl) L-glutamine]
PHEG-A13	13% acryloylated poly[N^5-(2-hydroxyethyl) L-glutamine]
PHEGMA11	11% methacryloylated poly[N^5-(2-hydroxyethyl) L-glutamine]
PHEG-MA21	21% methacryloylated poly[N^5-(2-hydroxyethyl) L-glutamine]
Poly(AA)	Poly(amino acid)
PROVE	Proportional velocity

PSF	Point spread function
RAPID	Resolution augmentation through photo-induced deactivation
RGDS	Arginine-glycine-aspartic acid-serine
RP	Rapid prototyping
SEC	Size exclusion chromatography
SEM	Scanning electron microscopy
$Si(OR)_4$	Silicon alkoxide
SLA	Stereolithography
μSLA	Microstereolithography
SLS	Selective laser sintering
SSF	Solid freeform fabrication
STED-DLW	Stimulated emission depletion two-photon direct-laser-writing
TE	Tissue engineering
UV	Ultraviolet
v/v	volume to volume
w/w	weight to weight

Symbols

a	Unit cell size
a_0	Unit cell width in the x-direction from 0° tilt
a_{90}	Unit cell width in the x-direction from 90° tilt
b_0	Unit cell width in the y-direction from 0° tilt
b_{90}	Unit cell width in the z-direction from 90° tilt
c	Diameter of circular opening connecting
c_0	Opening width in the x-direction from 0° tilt
c_{90}	Opening width in the x-direction from 90° tilt
c/a	Interconnectivity parameter
d_0	Opening width in the y-direction from 0° tilt
d_{90}	Opening width in the z-direction from 90° tilt
d_{xy}	Lateral resolution limit
Đ	Dispersity
E	Energy
GM	10^{-50} cm^4s $photons^{-1}molecule^{-1}$
h	Planck's constant
ħ	Reduced Planck's constant
I	Intensity (power per unit area)
M_n	Number average molecular weight
M_w	Mass average molecular weight
mol %	Mole percent
N	Number of ground state photoinitiator molecules per unit volume
n	Refractive index
N_0	Photon flux on the optical axis
n_p	Number of laser pulses
P	Laser power
r	Radius
r_0	Radial distance from the optical axis at the $1/e^2$ level
t	Exposure time
T	Transmittance
x	Power factor (0.10, 0.25, 0.50, 0.75 or 0.90)
x_2	Scaffold width at the top

x_1	Scaffold width at the bottom
z	Scaffolds height
z_R	Rayleigh length
λ	Wavelength
ν	Frequency
ρ_0	Initial photoinitiator concentration
ρ_{th}	Threshold photoinitiator concentration
σ	Two-photon absorption cross-section
σ_2	Effective two-photon cross-section of the photoinitiator
τ	Laser pulse duration
ϕ	Photon flux (number of photons per unit area)
ω	Angular frequency of light

1 Introduction

Cells sense and respond to their environment on the micro- and nanoscale and ideal cell culture platforms should thus be constructed with features down to this level [1]. The traditional two-dimensional (2D) culture conditions are often drastically different from the native, 3D extracellular matrix (ECM) environment, which can lead to abnormal cell behavior [2]. Computer controlled microfabrication techniques, often referred to as rapid prototyping or additive manufacturing, enable the realization of cell culture scaffolds with intricate 3D features that can mimic ECM microarchitecture [3]. With these techniques, scaffold structures with predefined properties can be fabricated within a few hours instead of days required by conventional fabrication approaches [4].

Among additive manufacturing techniques, 2PP-DLW offers 3D microfabrication capability with superior accuracy compared to other methods, such as UV laser stereolithography and 3D printing [5]. 2PP-DLW is based on the nonlinear optical phenomenon of two-photon absorption (2PA), which enables feature size of less than 100 nm [6] together with length scales ranging to millimeter [7].

Different cell types require different type of materials as culture substrates. 2PP-DLW can be used for the processing of a variety of materials ranging from synthetic photopolymers to biopolymers, such as proteins [8]. This thesis presents the 2PP-DLW processing of polymer-ceramic and hydrogel materials with custom-built laser systems. The first part of the thesis is a literature review covering the principles and applications of 2PP-DLW with an emphasis on biomedicine. The second, experimental part presents the work based on four original publications. The experimental results are divided into three major themes: processing of a commercial polymer-ceramic material Ormocomp®, fabrication of Ormocomp® scaffolds for adipose stem cell culturing and the processing of custom-synthetized poly(amino acid) hydrogels. The main results present the combined effect of different 2PP-DLW processing parameters on microstructure quality, the response of adipose stem cells to highly porous and interconnected Ormocomp® scaffolds and the comparison of the 2PP-DLW performance of custom and commercial hydrogels.

2 Literature review

2.1 Additive manufacturing

Combining cells and biomaterials with advanced microfabrication approaches is a growing area in tissue engineering (TE) that holds great potential for recreating complex tissue architectures. [4] These advanced techniques are referred to as rapid prototyping (RP), solid freeform fabrication (SFF) or most recently additive manufacturing (AM) [3]. AM techniques are characterized by the production of objects through sequential deposition of energy, material or both [5]. The selective adding of materials layer-by-layer is specified by cross-sections of a CAD (computer assisted drawing) model. This additive nature distinguishes these techniques from conventional, subtractive machining and minimizes material waste [3, 9]. AM techniques enable reproducible fabrication of microstructures with well-defined size, shape and physical and chemical properties including pore size, porosity, pore interconnectivity, mechanical strength and diffusion characteristics [3, 10]. TE constructs can be fabricated within a few hours instead of days often required by conventional fabrication approaches, such as porogen leaching and gas foaming [4].

AM techniques can be classified into thermal, mechanical or optical methods. Techniques often also combine different types of processing approaches. [3] Based on the type of processing system, AM techniques can also be divided into nozzle-, printer- and laser-based approaches [5]. Nozzle- and printer-based techniques use thermal and mechanical methods to directly deposit cells and materials, whereas laser-based techniques deposit light energy in order to achieve the desired effect. [3, 5] Nozzle-based techniques, such as fused deposition modelling (FDM), are often based on melt extrusion [11]. The printer-based approaches of inkjet printing [12] and 3D printing [13] have successfully modified commercial printing systems for the deposition of cells and biomaterials.

Compared to dispensing techniques, laser-based AM techniques are generally more accurate [3]. A laser (Light Amplification by Stimulated Emission of Radiation) is a quantum device that produces a strong beam of coherent photons by stimulated emission [14, 15] The light exposure by lasers can be used to manipulate cells, to remove material by ablation or to crosslink photosensitive materials [3]. For cell printing, techniques such as laser induced forward transfer (LIFT) and matrix-assisted pulsed laser evaporation direct writing (MAPLE DW) are mostly used [16]. Selective removal of material by laser ablation can be used either to directly create microstructures from bulk material [17] or as a complementary technique to achieve more refined geometries [18] and improved fabrication accuracy [19]. Finally, methods such as

selective laser sintering (SLS), stereolithography (SLA), microstereolithography (μSLA) and 2PP-DLW are used to create solid 3D microstructures from different starting materials. SLS is a thermal method, in which a focused laser beam is used to selectively heat and sinter a material in powder form [10]. SLA, μSLA and 2PP-DLW are all optical methods based on photopolymerization. They share the same basic principle of selectively curing photosensitive materials according to 2D slices of a 3D CAD model. What is fundamentally different between SLA and 2PP-DLW is the curing method and flexibility. In SLA, the material is cured layer-by-layer and a new coat of the liquid material needs to be deposited after each layer. In 2PP-DLW, 3D patterns of essentially arbitrary complexity can be written directly inside the material volume. [5] The principles of 2PP-DLW will be covered in detail in Sections 2.3 and 2.4.

2.2 Photopolymerization

Photopolymerization in the broad sense refers to the conversion of liquid starting materials to solid macromolecules through light-induced reactions [20]. Photopolymerization is induced by light in the UV, visible or IR part of the spectrum [21]. More specifically, the solidification of materials by light exposure can occur with two different mechanisms: photopolymerization and photocrosslinking [20]. Photopolymerization refers to the formation of macromolecules from monomers or oligomers through polymerization chain reactions [22]. Photocrosslinking, on the other hand, describes the formation of a 3D network through crosslinks between unsaturated moieties of macromolecular chains [20]. In the case of multifunctional monomers, photopolymerization and photocrosslinking may also occur simultaneously [22]. Photopolymerization and photocrosslinking differ significantly in their quantum yield, which is the number of polymerized monomers to the number of incident photons. Photocrosslinking requires the absorption of a photon in each propagation step and thus has quantum yield of less than 1. Photopolymerization, in contrast, is caused by a chain reaction in which the absorption of one photon can give rise to a quantum yield of several thousands. [21]

Selective photopolymerization of liquid starting materials is employed by the laser-based AM techniques of SLA and 2PP-DLW, for example. The photosensitive starting materials are composed of monomers and oligomers and are often referred to as photoresists or photoresins. [21] Most of the commonly used monomers and oligomers do not possess photosensitive groups with sufficient quantum yield. Consequently, low-molecular-weight organic compounds called photoinitiators (PI) are utilized to initiate the photopolymerization chain reaction. [22] A PI is chromophore-containing compound that is excited to a higher energy state by the absorption of light. This is generally followed by cleavage that creates reactive initiating species, such as

radicals or ions. [20] Based on the type of initiation, photopolymerization can be divided into radical photopolymerization and cationic photopolymerization. Examples of these include the double bond addition of acrylates and the ring-opening polymerization of epoxides, respectively. [22] In addition to a PI, a photosensitizer is sometimes used to enhance the excitation process [20]. In this case, the sensitizer molecule first absorbs the incident light and then efficiently transfers the excitation energy to the PI [23].

In the most common case of radical photopolymerization, the light exposure excites the PI molecules to a higher energy state, which results in cleavage of the molecules and the formation of free PI radicals. This first step is called initiation. [20, 24] In the next step of propagation, a PI radical attacks the double bond of a monomer and transfers a high energy radical electron to the end of the monomer. This creates a highly reactive monomer, which reacts with another monomer to create an activated dimer, which again reacts with a monomer. The chain reaction continues to build the polymer until the final step of termination, in which the active centers of two growing chains meet and combine by forming a covalent bond. Alternatively to combination, termination can also through disproportionation, which involves the transfer of a hydrogen atom from one chain to another to form two separate terminated polymers. [25] The typical steps of radical photopolymerization also given by Equation (1)-(3)

Initiation: $$PI \xrightarrow{h\nu} PI^{*} \longrightarrow PI^{\bullet} \quad (1)$$

Propagation: $$PI^{\bullet} + M \longrightarrow PIM^{\bullet} \xrightarrow{M} PIMM^{\bullet} \dashrightarrow PIM_{n}^{\bullet} \quad (2)$$

Termination: $$PIM_{n}^{\bullet} + PIM_{m}^{\bullet} \longrightarrow PIM_{n+m}PI \quad (3)$$

in which PI is the photoinitiator molecule, PI^{*} is the photoinitator in the excited state, $PI^{\bullet}$ is the photoinitiator radical, M is the monomer and $M^{\bullet}$ the monomer radical [20, 24]. In addition to the reactions described above, other processes such as chain transfer and chain inhibition can occur and complicate the mechanism of radical polymerization [26].

2.3 Direct laser writing by two-photon polymerization (2PP-DLW)

2PP-DLW is an additive manufacturing technique, in which laser-induced photopolymerization enables the fabrication of 2D and 3D microstructures. The technique is based on the nonlinear optical phenomenon of simultaneous two- or multiphoton absorption (2PA or MPA). [27] 2PP-

DLW was first demonstrated by Maruo et al. in 1997 [28]. 2PP-DLW is typically realized by tightly focusing a pulsed laser beam into a photosensitive material deposited on a glass substrate. Inside the material, PI molecules are excited by 2PA or other nonlinearities to form radicals, which initiate the polymerization chain reaction within the focal volume of the laser beam. [29, 30] This results in the polymerization of so-called voxels (volume elements), which are the basic building blocks of 2PP-DLW microstructures [31]. By scanning the laser focus relative to the sample or vice versa, microstructures are formed by overlapping voxels according to CAD-models. Unlike traditional photolithography and soft lithography techniques, microfabrication by 2PP-DLW requires no masks, molds or stamps and three-dimensional microstructures of virtually arbitrary complexity can be fabricated in a single processing step [30, 32]. After the selective illumination, samples are developed by washing off the non-irradiated material with the appropriate organic solvents [8].

Lasers are used in 2PP-DLW in order to achieve high enough intensities needed for two-photon excitation [33]. Mode-locked lasers that emit photons intermittently in high intensity bursts instead of a continuous beam are generally used [34, 35]. The most widely used laser type in 2PP-DLW is the Titanium:Sapphire femtosecond (fs) laser operating at infrared wavelengths, typically 780 nm, with a repetition rate of 80 MHz and pulse duration of a few tens to a few hundreds of femtoseconds [8] It has been recently shown, however, that also continuous-wave [36] and picosecond (ps) lasers [37-42] are applicable to 2PP-DLW.

In 2PP-DLW, the polymerization is restricted to the close vicinity of the laser beam focal spot, where the required threshold intensity is exceeded [43]. Due to this highly confined nature of the 2PA phenomenon, 2PP-DLW is an inherently 3D fabrication method that can reach feature sizes below 100 nm [6]. The smallest features are many times smaller than the wavelengths of the commonly used laser beams [44]. Compared to competing AM techniques, the unique combination of sub-micron accuracy and intrinsic 3D fabrication capability makes 2PP-DLW the most universally applicable microfabrication tool to date. The widely used techniques of UV laser stereolithography [45, 46], 3D printing [47, 48] and laser sintering [49, 50] also enable 3D fabrication but with minimum feature sizes limited to a few microns or half a micron at best [51]. Furthermore, although lithographic techniques such as electron beam or atomic force lithography offer superior accuracy, they can only produce 2D structures. [52] Compared to short wavelength radiation or charged particles, visible light is also less energetic and easier to generate and work with [44, 53].

Due to the nonlinear nature of 2PA, threshold behavior is typical to 2PP-DLW [24, 43]. Two types of material specific processing thresholds can be determined, namely the

polymerization threshold (P_{th}) and the damage threshold (P_D) [54]. In practice, the P_D is simply defined as the power at which bubbles and microexplosions start to appear. The occurrence of this optically induced damage can be observed using a video camera and an online monitoring system [54, 55]. The P_{th}, however, has been defined in the literature as either the minimum power at which a feature becomes visible during the polymerization process [56, 57] or the smallest power with which the fabricated structures, such as polymerized lines, can survive the development process [30, 54, 55, 58]. A lower P_{th} is linked to a better two-photon photosensitivity [59]. However, it should be noted that both of these methods inherently overestimate P_{th} to some degree because features fabricated very close to the threshold power are not necessarily visible under a microscope, let alone able to survive the development rinses. The actual polymerization thresholds can thus be lower than the values measured by these approaches. [56] The power range between the polymerization and damage thresholds is the fabrication window, which can be characterized by the relative dynamic power range (P_D/P_{th}). [54, 55, 60] A larger dynamic power range is generally considered beneficial for 2PP-DLW as it enables more substantial tuning of feature size [41, 61].

Perhaps the main drawback of 2PP-DLW is the low fabrication throughput that stems from the high precision and the serial voxel-by-voxel nature of single beam scanning. To address this issue, several different strategies have been introduced. Voxel size and thus scanning speed can be increased by the choice of laser power and the numerical aperture (NA) of the objective lens [52]. Processing time can also be reduced by optimal 3D design strategies that minimize scanning steps [62]. The so-called contour scanning technique, in which only the outer shell of the microstructure is formed by 2PP-DLW, also makes the process considerably more efficient. After contour scanning, structures can be reinforced by solidifying the inner part by UV light exposure, for example [22, 63, 64]. Contour scanning can also be extended to multipath scanning, which enables the fabrication of microstructures that are more resistant to deformation [65]. Even higher throughput has been demonstrated by parallel scanning with multiple focal spots [66-72] and by combining 2PP-DLW with micromolding [73-78].

As a highly accurate 3D microfabrication technique, 2PP-DLW has found numerous applications in fields such as optics, microelectronics and biomedicine. In the field of optics, 2PP-DLW has been used to create photonic crystals [79-82], wave guides [83-85] and microlenses [64, 86], whereas conductive wires [87] and mechanical oscillators [88] have been fabricated for micro-electromechanical systems (MEMS). The use of 2PP-DLW in biomedical applications, such as microneedles [89], cell growth guidance patterns [90], tissue engineering

scaffolds [91] and even macroscale implants [92], has been rapidly increasing in recent years. These applications will be discussed in detail in Section 2.7.

2.3.1 Two-photon absorption

Two-photon absorption is a third-order nonlinear optical phenomenon in which an atom or a molecule is excited from ground state to a higher quantum state by the simultaneous absorption of two photons [33, 93]. The absorption can also occur with more than two photons, in which case the phenomenon is referred to as multiphoton absorption [8]. 2PA was first theoretically described in 1931 by Maria Göppert-Mayer [94] and experimentally confirmed by Kaiser and Garrett [34] in 1961 after the emergence of lasers. 2PA has found applications in analysis methods such as laser spectroscopy and two-photon fluorescence microscopy as well as in data storage and microfabrication in the form of 2PP-DLW [8, 33].

The process of 2PA can be described by the attenuation of a beam of light incident on a 2PA material [95, 96] as

$$\frac{\partial \phi}{\partial z} = -\sigma N \phi^2 \tag{4}$$

where ϕ is the photon flux (number of photons per unit area), z is the distance into the medium, N is the number of ground state PI molecules per unit volume and σ is the 2PA cross-section. The photon flux is related to beam intensity I (power per unit area) and photon energy E by

$$\phi = \frac{I}{E} \tag{5}$$

where E = ħω is given by the reduced Planck's constant ħ and the angular frequency of the incident light ω. Substituting Equation (5) in (4) gives

$$\frac{\partial I}{\partial z} = -\frac{\sigma}{\hbar \omega} N I^2 \tag{6}$$

The incidence of 2PA is thus proportional to the square of the light intensity, which makes it a nonlinear process. The 2PA cross-section σ describes the strength of the 2PA process. In contrast to the linear single photon absorption (1PA) cross-section which is a constant, 2PA cross-section increases linearly with laser intensity. [97] The unit of σ is called Göppert-Mayer and 1 GM =

10^{-50} cm^4s photons^{-1}molecule^{-1} [95]. The 2PA cross-section is proportional to the imaginary part of the third-order susceptibility $\chi^{(3)}$, which describes third-order nonlinear polarization of a material under an electric field [96, 97].

In ordinary 1PA, the number of excited molecules is constant in any transverse plane of a laser beam and absorption occurs everywhere along the light path [8]. AM techniques based on 1PA, such as stereolithography, are thus essentially planar processes and 3D structures have to be fabricated 2.5 dimensionally by solidifying one layer at a time [33]. Due to the quadratic intensity dependence, 2PA is confined to the immediate vicinity of the focal spot of the laser beam, an area with the greatest photon intensity [8, 35]. This confinement of the 2PA excitation enables true 3D processing, as depicted by Figure 1.

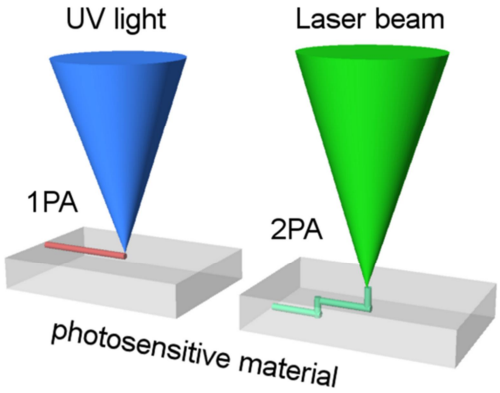

Figure 1. The principles of single-photon (1PA) and two-photon absorption (2PA) based laser processing.

Two-photon excitation can occur via two different mechanisms: sequential or simultaneous 2PA. In sequential 2PA, the absorption of the first photon excites the photoinitator to a real intermediate state with a typical lifetime of 10^{-4} to a 10^{-9} s. From this state, the molecule is then excited to a higher energy level by the absorption of another photon. [21, 24] The existence of a real intermediate state signifies that the material absorbs the wavelength of the incident photons [26]. Sequential 2PA does not require the use of coherent light and can be regarded as two sequential single photon absorptions [21]. In the second mechanism of simultaneous 2PA, there is no real intermediate state and the material is transparent to the wavelength of the laser beam [26]. Instead, the absorption of the first photon creates a virtual intermediate state and only if the second photon arrives within the short lifetime of this virtual state, usually in the order of 10^{-15} s, can the molecule be excited to a higher energy state. [24] Under normal conditions, the rate of simultaneous 2PA is extremely low as it depends on both

the spatial and temporal overlap of the two-photons at the virtual intermediate state. [24, 98] However, with high intensities of light, such as the ones provided by focused laser beams, simultaneous 2PA can be induced [24]. From here on, simultaneous 2PA is referred simply as 2PA.

In 2PA, each photon has half of the energy ($h\nu/2$) of the gap between the two energy levels, which is given by $h\nu = E_2 - E_1$, where h Planck's constant, ν the frequency of light and E_2 and E_1 are the energies of the upper and lower energy levels. [24, 26, 93] This type of 2PA is referred to as degenerate 2PA, distinguishing it from non-degenerate 2PA, in which the two absorbed photons have different energies and frequencies. Most 2PA applications, including 2PP-DLW, are based on the degenerate process. [23]

2.3.2 Mechanisms of 2PP-DLW

As described in Section 2.2, the standard view of 2PP-DLW is that the photoinitiator molecules are excited by nonlinear 2PA or MPA and then dissociate to form radicals that initiate the polymerization and selective solidification of the photopolymer [22, 99]. Although this description forms a basis for many of the experimental findings, the underlying mechanisms of the initiation and polymerization processes are not known. [55, 99] To date, the term two-photon polymerization (2PP or TPP) has been widely used to describe this laser processing technique in addition to various other terms, such as two-photon and nonlinear lithography. Due to possible contributions of other mechanisms in addition to 2PA, the more general term of direct laser writing (DLW) has recently been introduced to the 2PP literature [32, 36, 100]. However, the term direct laser writing alone is somewhat ambiguous as it can also refer to other laser-based techniques, such as LIFT or MAPLE DW [16]. For this reason, the term 2PP-DLW is used in this work to distinguish the fabrication technique from other laser-based direct write approaches and to highlight the nonlinear nature of the process. Similar terms such as direct laser writing via photopolymerization or two-photon induced photopolymerization can also be found in the literature [32, 100].

The specific mechanisms of 2PP-DLW have recently been under intensive study. Several studies have proposed that thermal effects due to local heat accumulation contribute significantly to the polymerization process with materials such as epoxy-based SU-8 [101], hybrid polymer-ceramic material SZ2080 with the PIs Irgacure® 369 and Michler's ketone [41, 102] and pentaerythritol triacrylate (PETA) with Irgacure® 369 [103]. However, another study with PETA and Irgacure® 369 found no evidence of a heat accumulation effect on polymerization [55]. Also, recent *in situ* measurements with PETA and the PI Irgacure® 819 by the same group revealed no

significant temperature increase under typical writing conditions [99]. Instead, notable temperature increase was observed together with microexplosions and local heat accumulation was thus proposed as a damage mechanism for acrylate-based photopolymers. The damage process was considered to be highly nonlinear and could be explained by either direct vaporization of the monomer or by avalanche photoionization and subsequent plasma formation. [55, 99] Based on the most recent reports, heat induced polymerization does not seem to be significant in the 2PP-DLW of acrylate-based materials with common photoinitiators. However, in the absence of more comparative studies, the effect of heat accumulation on the polymerization of other types of materials cannot be excluded.

In addition to heat accumulation, linear avalanche ionization has been recently proposed as the mechanism dominating over of the nonlinear multiphoton excitation of photoinitiator molecules [41, 102]. In this process, nonlinear 2PA and multiphoton ionization act as seeding mechanisms and produce the initial density of energetic free electrons for the subsequent avalanche ionization [102, 104] Juodkazis et al. observed this type of behavior for the polymer-ceramic material SZ2080 in combination with the Irgacure® 369 and Michler's ketone photoinitators and with both picosecond and femtosecond lasers. [41, 102] They concluded that avalanche ionization dominates over 2PA in most conditions at tight focusing of 30–300 fs laser pulses [102] and at high repetition rates (> 500 kHz) with ps laser pulses [41]. Recently, the same group also demonstrated PI-free processing of SZ2080, PEGda and polydimethylsiloxane (PDMS) using controlled avalanche [105].

The theory of multiphoton ionization was recently studied further by Fischer et al. [55] by modeling of a photoresist system composed of PETA with and without PIs (Irgacure® 369, Irgacure® 819). According to their work, the polymerization of pure PETA was consistent with a highly nonlinear, multiphoton ionization dominated process. However, in combination with the common Irgacure® photoinitiators, the classical 2PA process was found to dominate at laser frequencies above 100 kHz. Higher nonlinearities, such as multiphoton ionization, became dominant only at low frequencies below 10 kHz.

In the light of recent studies, it is clear that the process of 2PP-DLW is much more complex than has been previously thought. It seems likely that multiple competing mechanisms can contribute to the polymerization process depending on the materials and the processing conditions used. Formulation of a comprehensive theory requires more comparative studies with different types of materials, e.g. polymer-ceramic and acrylate photopolymers, and laser processing parameters to be performed.

2.4 Fabrication accuracy of 2PP-DLW

The resolution of 2PP-DLW can be associated with the basic concepts of optics and microscopy. For a conventional diffraction-limited optical system, the classic Abbe and Rayleigh criteria apply. The Abbe diffraction limit states that the maximum lateral (xy) resolution is given by

$$d_{xy} = \frac{\lambda}{2NA} \tag{7}$$

in which λ is the wavelength of the incident light and NA is the numerical aperture of the imaging lens [106]. This means that two objects can be resolved if they are separated by distance equal to or larger than the Abbe limit of the imaging system [107]. The Rayleigh criterion can be derived from the response of an imaging system to a point source or an object, which is called the point spread function (PSF) [108]. Due to the finite size of the optics, a point source of light produces not a point but an intensity distribution in the focal plane, which is the PSF. The PSF of a lens is affected by diffraction and aberration. The so-called full-width-at-half-maximum (FWHM) of a PSF is the diameter at one-half of the maximum intensity and is a measure of the imaging systems sharpness. [107] In the common case of a planar wavefront incident on a circular aperture, the resulting distribution is a so-called Airy diffraction pattern with alternating circular bright (maxima) and dark zones (minima) [109]. The bright central core inside the first minimum of the Airy pattern is called the Airy disk, radius r of which is given by [109, 110]

$$r = 0.61\frac{\lambda}{NA} \tag{8}$$

The radius of an Airy disk is also the resolution limit according to Rayleigh. The Rayleigh criterion states that minimum distance between the intensity maxima of two resolved point sources is the radius of an Airy disk. [111] This means that the central intensity peak of one source coincides with the first minimum of the other, resulting in central a minimum between the two intensity distributions [107]. In contrast to the Rayleigh criterion, the Sparrow criterion states that the resolution limit is reached when the minimum is just about to appear [112]. The Sparrow limit is closer to the Abbe value and is approximately two-thirds of the Rayleigh limit [112]. All the above mentioned resolution criteria deal with the lateral xy-direction. In the z-direction, the resolution limit in a diffraction-limited system is given by [113]

$$z = \frac{2\lambda n}{NA^2} \tag{9}$$

where n is the refractive index of the microscope objective medium, which is most commonly immersion oil.

Based on the Abbe diffraction limit, Fischer and et al. have recently redefined the terms of resolution and feature size in 2PP-DLW. In accordance with the Abbe condition, they define the resolution of 2PP-DLW as the minimum center-to-center distance between two adjacent yet separated features, whereas feature size is the dimension of a single, isolated structure, such as a voxel, for example. [29, 114] These definitions are also used in this work. Prior to the work of Fischer et al., the concepts of resolution and feature size had not been clearly defined in 2PP-DLW and were in most cases used interchangeably [115-117]. In fact, most reports of the resolution of 2PP-DLW have actually studied feature size instead and will be covered accordingly in this work.

As discussed in Subsection 2.3.1, 2PA is a nonlinear process proportional to the square of the light intensity. The quadratic intensity distribution of 2PA is narrower than the PSF of one-photon exposure, which results in a more confined light-matter interaction volume. [32, 114] This effect is also referred to as optical nonlinearity [8, 32]. In addition to the narrower PSF, 2PA benefits from negligible absorption beyond the focal point, which further decreases the achievable feature size [8]. In addition to optical nonlinearity, the so-called chemical nonlinearity and material linearity also contribute to the fabrication accuracy of 2PP-DLW. Chemical nonlinearity is also referred to as the threshold effect. It causes polymerization to occur only within the region of focal volume with highest intensity and sufficient radical concentration. [8, 32] The threshold effect is caused by the presence of radical quenchers, such as dissolved oxygen molecules [8, 32, 43]. The third factor reducing feature size is material nonlinearity, which means that polymerized features can further shrink in size during the development phase due to the removal of weakly crosslinked portions of the polymer network [32].

The combined effect of optical, chemical and material nonlinearities during 2PP-DLW has enabled the fabrication of voxels and lines with dimensions well below the Abbe diffraction limit. [32] In fact, in a threshold material system, feature size is not fundamentally diffraction-limited and diffraction is simply a measure of focal spot size [43, 114]. Infinitely small features could in theory be produced by tuning the exposure dose close to the polymerization threshold. [43, 114] Resolution, however, is fundamentally limited by diffraction in a so-called “non-forgetting” photoresist. This means that despite the existence of a threshold, exposure with below threshold intensity can still contribute to the polymerization once the threshold is exceeded by

broadening the effective interaction volume. In a perfectly “forgetting” photoresist, resolution and feature size would indeed be interchangeable terms and the distance between to features could be arbitrarily small. However, commonly used materials are “non-forgetting”, which limits the achievable resolution. [114]

2.4.1 Effect of processing parameters

The size and shape of voxels are influenced by both the properties of photopolymerizable material and the laser processing parameters. Material properties include PI concentration, radical quantum yield, viscosity and photosensitivity of the photoresist and the concentration of radical quenchers. [8, 118] Takada et al. showed with the commercial urethane acrylate resin SCR500 that feature size can be reduced by increasing the concentration of radical quenchers [119]. For (meth)acrylate resins, it has been shown that the addition of a PI and an increasing PI concentration notably lower the polymerization threshold [56, 58, 120]. The damage threshold, however, has been found to remain largely unaffected by the increase in PI concentration. According to Fischer et al., damage threshold thus seems to be governed by the properties of the monomer instead of the PI. [55] On the other hand, decreasing the PI concentration has been shown to decrease voxel size and thus improve fabrication accuracy [119]. The optimum PI concentration therefore depends on the intended application and whether minimum feature size or greater fabrication window is desired.

The effect of photoresist sensitivity on feature size is not yet fully understood. Xing et al. demonstrated smaller voxels with a highly sensitive photoinitiator due to a decreased polymerization threshold [120]. It should be noted, however, that they did not compare the performance of the sensitized resin to an unsensitized resin. Recent studies have found that smallest feature size is achieved with unsensitized resins [55, 102], possibly due to higher order nonlinearities [55]. However, using unsensitized resins is often not practical due to much higher polymerization thresholds and limited dynamic power range [55].

Processing parameters including laser wavelength, pulse width, repetition rate, power, exposure time and NA of the objective lens all affect the achievable feature size and resolution. A shorter laser wavelength reduces the diffraction limit of a focal spot in accordance with the Abbe and Rayleigh limits. Multiple studies have also shown that using shorter laser wavelengths can be beneficial due to lower polymerization thresholds and thus increased fabrication windows [41, 102, 121]. The effect of pulse width is less clear. Tan et al. recently studied the 2PP-DLW of a commercial polymer-ceramic material Ormocomp® and found that increasing laser pulse width from approximately 200 fs to 700 fs linearly increased the polymerization threshold and voxel

size [122]. However, Malinauskas et al. showed with a ps laser system and SZ2080 that increasing the pulse width from 8 ps to 25 ps slightly lowered the polymerization threshold. They also found that increasing the pulse width notably lowered the damage threshold and thus reduced the available fabrication window. [41] More comparative studies are thus needed to determine effect of pulse width on 2PP-DLW.

The effect of laser repetition rate has recently been under intensive study. Malinauskas et al. studied this by using a picosecond laser system with the repetition rate ranging from 200 kHz to 1 MHz. For SZ2080, they found that the best fabrication accuracy was achieved with the highest repetition rate combined with short pulses. Increasing the repetition rate was also found to linearly increase the fabrication window. [41] Emons et al. have also reported reduced voxel size for another polymer-ceramic resist with the repetition rate of 80 MHz compared to 1 MHz. However, the direct comparison in this study was somewhat questionable since two different laser systems and different writing conditions were used. [123] Contrary to these results, Fischer et al. have recently showed that increasing the repetition rate from low (4 kHz) to high (80 MHz) does not change the feature size scaling in a sensitized acrylate resist system. The resolution, however, was found to be significantly higher at the low repetition rate due to effects of higher order nonlinearity compared to high repetition rates. It was also demonstrated that at higher repetition rates the pulse energies needed for polymerization are lower due to accumulation of the exposure dose over many pulses. [55] These studies highlight the complex nature of 2PP-DLW processing as parameters scale differently depending on the laser and material systems used.

Perhaps the most dominant processing parameter in 2PP-DLW is the laser dose, which is a product of average laser power (P) and exposure time (t). Exposure time is reciprocal of scanning speed. Voxel size can be decreased either by lowering the laser power or by shortening the exposure time [103]. The only exception to this has been reported by Stocker et al. for a class of photoinitiators including malachite green carbinol hydrochloride, which have a proportional velocity (PROVE) dependence [53] According to linear exposure theory, voxel size is often assumed to be proportional to $P^N t$ for N-photon absorption process (N = 1 for 1PA and N = 2 for 2PA, etc.) when other processing parameters are not varied [36, 124]. However, deviations from this theory have been observed. Sun et al. studied the urethane acrylate resin SCR500 and found that voxel aspect ratio, that is the ratio of height to width, is more sensitive to an increase in power than in exposure time. They proposed a model, in which voxels form by two different mechanisms. The initial “focal spot duplication” is defined by threshold power relative to the laser beam PSF. At long exposure times, this is followed by radical diffusion-dominated “voxel

growth", which is analogous to dark polymerization. [125] DeVoe et al. have observed similar behavior with SU-8 and an acrylate resin [126]. These findings demonstrate that the dependence of voxel shape on laser dose is more complex than the simple P^2t model.

The NA of the objective lens also significantly affects the achievable feature size of 2PP-DLW. Tighter focusing with higher NA produces a narrower PSF, which lowers the polymerization threshold and decreases voxel size. At low laser powers, high NA focusing produces smaller voxels in both the lateral and longitudinal directions. [60] However, when the power is at intermediate to high level, a low NA has been shown to produce laterally smaller voxels. This is because low NA focusing (NA < 1) distributes the laser power to larger focal volume with the threshold intensity level closer to the peak of the PSF than with high NA focusing (NA = 1.4, for example). This makes the active polymerization area vertically expanded and laterally very narrow, leading to the formation of elongated and slim voxels. [58, 60] Low NA focusing can thus be used to fabricate high aspect ratio structures with a single scan [127, 128]. Low NA focusing is also useful in the fabrication of large-scale 3D structures as the increased voxel size enables the use of higher scanning speeds and reduces the overall fabrication time [129].

2.4.2 Feature size and resolution

The feature size of 2PP-DLW is usually determined by studying either voxels or lines, which are essentially joined voxels. Voxels are generally ellipsoidal in shape [130]. However, as the laser power, irradiation time or both are increased, the side peaks of the laser beam's Airy pattern can begin to contribute to the polymerization process. In this case, the voxels are no longer ellipsoidal but can have a more irregular, multi-part structure instead. [131] In the literature, a variety of different terms have been used to describe voxel shape. In this work, the term height is used for the vertical voxel dimension and width for the horizontal dimension, that is, the voxel diameter. For accurate feature size measurements, the so-called truncation effect has to be taken into account. This refers to the variation of voxel height depending on the extent of focal spot submersion in the substrate. Complete voxels can be produced by the so-called ascending scan technique first reported by Sun et al. [130] It involves performing a point by point exposure of a material while the laser beam focus position relative to substrate surface is raised and translated. In this manner, a critical height can be found at which complete yet surface bound voxels are generated. However in practice, the smallest voxels are sometimes mechanically too weak to survive the development process [32]. Lines fabricated on the substrate surface [55] or

suspended lines fabricated between support structures [126] are thus often studied instead of voxels.

The minimum feature size achieved by 2PP-DLW has improved steadily over the last decade and dimensions as small as λ/30 have been reported. Kawata et al. were the first to report a voxel width of 120 nm and a 3D fabrication accuracy of 150 nm for SCR-500 in 2001 [115]. In following studies, they achieved voxel widths of 100 nm by introducing a radical quencher into the polymer resin [119] and line widths of 80 nm by using a highly efficient anthracene-based PI [120]. Dong et al. have since reported even smaller line widths of 50 nm for SCR500 [117]. In another study, Haske et al. fabricated woodpile structures of an acrylate resin with a minimum line width of 65 nm [6]. Most recently, line widths of approximately 40 nm have been reported by Emons et al. for a polymer-ceramic material combined with an additional crosslinker [123] and by Gan et al. for an optimized acrylate resin [132].

In addition to the work listed above, some studies have reported even smaller line widths by polymerizing nanofibers between closely spaced supports. Because the region between the supports has already been exposed, an immediate second scan is sufficient to polymerize thin lines. [44] Using this technique, Juodkazis et al. were the first to demonstrate fibers as small as 30 nm fabricated from SU-8 [116]. Park et al. [133] and Tan et al. [134] have since reported similar fiber widths for SCR-500. The realization of nanofibers in this manner is due to the "non-forgetting" nature of the photoresists and is thus fundamentally different than the fabrication of individual voxels and lines. [44, 114]

Whereas features sizes below 100 nm have been repeatedly demonstrated, the achievable resolution of conventional 2PP-DLW seems to be limited to a few hundreds of nanometers. As the concept of resolution as minimum separation was not formulated until recently, only a handful of publications have demonstrated line gratings so far. The earliest results of approximately 100 nm wide lines separated by 300 nm were published by Park et al. for SCR500 [135]. Haske et al. were able to fabricate woodpiles using an acrylate resin with an inter-line spacing of 500 nm [6]. Most recently, Wegener et al. have reported a resolution of 300 nm for the commercial IP-L photoresist [36] and for an acrylate resin with or without an additional photoinitiator [55].

To further improve resolution, a new type of 2PP-DLW approach called resolution augmentation through photo-induced deactivation (RAPID) lithography [136] or stimulated emission depletion two-photon direct-laser-writing (STED-DLW) [27] has recently been introduced. In this technique, two lasers beams are used: one to activate and another to simultaneously deactivate polymerization. This approach reduces the effective polymerization

volume and thus enables improved resolution. [29] Different types of depletion-DLW approaches with respect to materials and depletion modes have been reported. Li et al. were the first to report a voxel height of 40 nm (λ/20) [136]. Since then, feature size has been reduced even more, with the current record of 9 nm (λ/42) reported by Gan et al. together with a 52 nm (λ/7) resolution [132]. Due to the significant improvement in both feature size and resolution, STED-DLW enables new and exciting applications, such as nano-anchors [137] and invisibility cloaks [138].

2.4.3 Shrinkage and deformation

One of the practical issues impairing the fabrication accuracy of 2PP-DLW is the shrinkage and deformation of microstructures following development. The deformation is dominated by a capillary force induced by the surface tension of an evaporating developer [139]. When fabricated features, such as suspended lines, are close enough, the surface tension of an evaporating solvent pulls the structures towards each other causing permanent adhesion [140]. The deforming force is directly proportional to surface tension and inversely proportional to contact angle [141]. The degree of deformation is also influenced by microstructure dimensions [142]. Park et al. have shown that increasing height increases the deformation of hollow rectangular columns of identical cross sections [143].

In practice, freestanding structures shrink uniformly and structures that are bound to a substrate shrink nonuniformly [144]. The shrinkage of the bottom layers is restricted due to attachment to the substrate surface and subsequent layers shrink increasingly until a saturation height is reached [145]. Shrinkage thus increases with microstructure height until the layers can shrink freely, which results in a typical trapezoidal shape for cubic structures [146]. Nonuniform shrinkage is one the most commonly faced issues in 2PP-DLW as completely freestanding structures are challenging to construct.

Several methods have been proposed to reduce shrinkage and deformation. Highly crosslinked structures are more resistant to deformation, which can thus be decreased by increasing laser power [147] or by optimizing resin composition [148]. When the degree of shrinkage is known, CAD models can also be numerically compensated [149]. Structures can also be made more shrinkage resistant by reinforcing of the walls by multipath scanning [143] or by stabilizing the structures with support frames [79, 149]. Another approach is to fabricate freestanding structures using shrinkage guiders that minimize deformation [150]. Deformation can also be reduced by minimizing the capillary force by supercritical CO_2 drying [151] or by the use of a hydrophilic solvent on a hydrophobic surface [142].

2.5 Photoinitiators for 2PP-DLW

An ideal PI for 2PP-DLW should have a large 2PA cross-section, high radical quantum yield, high initiation velocity, good thermal and dark stability and high solubility in the polymerization medium [8, 26]. In addition to a large 2PA cross-section, the PI should have a low fluorescence quantum yield in order to achieve efficient radical generation [152]. An ideal PI should also be optically transparent at the laser wavelength in order to exclude 1PA and have an absorption maximum close to half the laser wavelength [24]. The two main classes of 2PP-DLW PIs are radical and cationic PIs, of which radical PIs are the most widely used [52]. Assuming a similar mechanism to 1PA, radical PIs in 2PA are first excited from the ground state S_0 to an electronically and vibrationally excited level S_1^* by the simultaneous absorption of two photons. The excitation is followed by rapid non-radiative relaxation to an intermediate state S_1, which normally has a very short lifetime. From the intermediate state, the molecules can undergo inter-system crossing (ISC) to the triplet state T_1, from which radicals initiating the polymerization chain reaction are formed. [27, 29] It is also possible that the formation of radicals after 2PA follows a different energetic route than 1PA, such as successive absorption and non-radiative excited state decay [103].

Radical PIs can be divided into type I and type II initiators depending on the mechanism of radical formation. In a type I scission process, the energy of the incident light is sufficient to cleave the PI molecule and produce two free radicals. In a type II abstraction process, the absorbed energy excites the PI to a triplet state but is insufficient for bond cleavage. The excited PI then needs to react with a suitable hydrogen donor, such as a tertiary amine, ether, ester or thiol, which results in the formation of an inactive ketyl radical and highly reactive donor radical that initiates the polymerization. [153]

Most 2PP-DLW studies so far have been conducted with commercial radical PIs originally designed for 1PA photopolymerization in the UV-visible range. These PIs can be excited by 2PA if the light intensity is high enough [21]. The commercial PIs include the widely used Irgacure® series, which are mostly type I PIs. The most commonly used commercial PI has been Irgacure® 369, which belongs to the group of alkylaminoacetophenones (AAAPs) absorbing in the mid UV range around 280–350 nm. Irgacure® 369 is the most reactive of commercial AAAP PIs [153] and has been extensively used for the 2PP-DLW processing of polymer-ceramic materials [89, 129], for example. Other two Irgacure®s which have been used in 2PP-DLW, Irgacure® 2959 and Irgacure® 127, are type I hydroxyacetophenones (HAPs) that absorb mainly around 250 nm. HAPs are much less reactive than AAAPs. [153] However, Irgacure® 2959 has the advantage of being slightly water soluble due to its p-hydroxyethoxy

group [153], which has enabled its use in the 2PP-DLW processing of water-based hydrogels [154]. In addition to Irgacure®s, other PIs such as Lucirin® TPO-L and Michler's ketone have also been used. Lucirin® TPO-L belongs to phosphine oxides, which absorb in the long wave UV of around 350–420 nm. Because Lucirin® TPO-L is a liquid, it has good miscibility with resins. [153] In 2PP-DLW, Lucirin® TPO-L benefits from a high quantum yield that compensates for a relatively low 2PA cross-section [155]. The benzophenone derivative Michler's ketone [156] and thioxanthen-9-one [157] are examples of type II PIs that have been used in 2PP-DLW. However, Michler's ketone is known to be carcinogenic and its use is thus controversial, especially in biomedical applications [153].

With the exception of Irgacure® 2959, most commercial PIs are not water soluble. Instead, commercial dyes have been used as photosensitizers for the 2PP-DLW processing of water-based material formulations, such as proteins. These photosensitizers include xanthene dyes, such as Rose Bengal [158] and eosin Y [159], and methylene blue [160] that promote crosslinking mainly via type II singlet oxygen mechanisms. Due to the possible cytotoxic effects of Rose Bengal and methylene blue, the more cytocompatible alternatives flavin adenine dinucleotide (FAD) [160] and flavin mononucleotide (FMN) [161] have also been tested for 2PP-DLW.

Although conventional 1PA PIs have been successfully applied to 2PP-DLW, these PIs often suffer from small 2PA cross-sections limited to a few tens of GM units at best [162]. These PIs require high powers and long exposure times, which can result in optical damage [162]. In order to increase the efficiency 2PP-DLW processing, the synthesis of novel electron-rich PIs with large 2PA cross-sections has been increasingly studied [61]. As 2PA is strongly correlated with intramolecular charge-transfer processes, efficient PIs comprise a strong π-electron donor (D) separated from a strong π-electron acceptor (A) by a polarizable π-bridge. Based on the combination and number of the D and A group in the system, PI molecules can be divided into the general classes of dipolar (A-π-D), quadrupolar (A-π-A, D-π-D, A-π-D-π-A and D-π-A-π-D) and octupolar (three-branched, A_3-(D-core) and D_3-(A-core)) PIs. The 2PA cross-section is affected by conjugation length and planarity with maximum values achieved with long π-conjugated chains with enforced coplanarity. [95, 163] These types of molecules have extended σ values to the order of 10^4 GM. Watanabe et al. reported D-π-A-π-D type PIs with σ values of 2000 GM in chloroform [164, 165]. Following this, Zhao et al. reported multi-branched ketocoumarin derivatives with σ values of 1117 GM in chloroform [166]. Gu et al. also reported carbazole-based PIs with σ values as large as 1740 GM in methanol [167]. Recently, D-π-A-π-D type PIs based on aromatic ketones have been reported by Liska et al. with σ values of 466 GM

in dichloromethane [168-170] and D-π-D type heteroaromatic PIs have been reported by Hao et al. with σ values as large as 10000 GM in dimethylformamide [171]. Although large σ values are generally desired, the achievable processing window is not correlated only with a large σ. Liska et al. showed that a PI with a smaller σ value can enable more efficient 2PP-DLW processing. [170] It should also be noted that the 2PA cross-section is sensitive to solvent polarity and can be greatly reduced in water, for example [163, 172, 173]. The solvent affects should thus be taken into account when comparing σ values reported in different studies.

In addition to engineering PIs with larger σ values, there are also increasing efforts to synthesize new water-soluble PIs, which would be better suitable for the biomedical applications of 2PP-DLW. Efficient PIs have been synthesized by introducing water-soluble groups, such as quaternary ammonium cations or carboxylic sodium salts, in the structure of molecules with known large σ values [174]. Using this strategy, Wan et al. [175] and Liska et al. [174] have recently synthesized water-soluble, benzylidene ketone-based PIs by the addition of hydrophilic sodium carboxylate groups. Zhang et al. have also recently reported 2PP-DLW using the water-soluble PI lithium phenyl-2,4,6-trimethylbenzoylphosphinate (LAP) [176].

When 2PP-DLW is applied in biomedicine, one of the key aspects is possible the cytotoxicity of the PIs and their residues. Recently, Ovsianikov et al. evaluated the cytotoxicity of Michler's ketone, Irgacure® 369 and Irgacure® 2959 in combination with PEGda. It was found that the higher PI concentrations of 2 wt % and above resulted in higher levels of cytotoxicity in mouse fibroblasts. Additionally, freshly prepared samples were found to be significantly more cytotoxic than aged samples even with low PI concentrations of 0.5 wt %. Irgacure® 2959 was found to be the least cytotoxic out of the three PIs, and the aged Irgacure® 2959 samples were considered non-cytotoxic. [177] However, it should be noted that PEGda is resistant to protein and cell adhesion, which could have affected the cell viability results of this study. Other studies have also shown that Irgacure® 2959 is well tolerated by many mammalian cell types [178], especially with concentrations of 0.05 wt% and lower [179]. Higher PI concentrations generally lead to higher toxicity due to increased number of free PI radicals [180, 181]. The recently reported PI LAP has been demonstrated to perform as well as Irgacure® 2959 with human fibroblasts [182].

2.6 Photosensitive materials for 2PP-DLW

The most important properties of a photopolymerizable material in 2PP-DLW are suitable viscosity, fast and efficient polymerization and low shrinkage after polymerization [21]. The suitable materials can be divided into negative-tone and positive-tone materials, which are

combined with the appropriate PIs. In negative-tone materials, laser exposure renders the exposed area insoluble in the development solvent by the crosslinking of polymer chains, for example, and forms a solid structure. In positive-tone materials, on the contrary, the laser exposure renders the material soluble through chain scission and a reverse structure is written inside the material. [26]

Negative-tone materials are most commonly used in 2PP-DLW. They can be divided into liquid and solid materials, which are referred to as photoresins and photoresists respectively [100]. In liquid resins, the laser exposure results in an almost instantaneous liquid to solid transition and generally the only post-processing procedure needed is the removal of the non-irradiated liquid with a suitable solvent [100]. Lower viscosity facilitates the removal of the unsolidified material during development but can also cause undesired motion of the microstructures during fabrication [8]. Resins also commonly shrink significantly during the liquid-to-solid transition, which can cause additional deformation and deviation from the original design [26, 100]. Compared to liquid resins, the sample preparation and processing of solids and gels is more laborious, as it generally requires both pre- and postbaking. However, the higher viscosity helps to stabilize microstructures before development and facilitates the fabrication of complex structures, such as freely moving components. [8] All in all, as low viscosity liquids require a containment cell during processing, viscous liquids, gels and amorphous solids are generally preferred in 2PP-DLW due to easier sample handling [8, 148].

The most widely used commercial photoresist in 2PP-DLW has been the epoxy-based SU-8 [116, 183]. The photomodification of SU-8 is based on cationic polymerization and occurs latently during a postbaking step [100]. The most common photoresins in 2PP-DLW are acrylate monomers. Acrylates benefit from are wide availability and simple sample preparation by drop casting or spin coating. The rapid free radical polymerization of acrylates results in highly crosslinked structures that are optically transparent and resistant to deformation during the development phase. [8] Combining different acrylate monomers in a photoresin enables the tuning of microstructure properties, such as mechanical strength and surface properties [137]. The most popular commercial acrylate-based photoresins include SCR500 (JSR, Japan) [117, 125], Nopcocure800 (San Nopco, Japan) [184, 185], the SR series (Sartomer, France) [6, 137] and PETA [29, 55]. Recently, Nanoscribe GmbH in Germany has also developed an acrylic-based liquid photoresin IP-L especially for 2PP-DLW [36, 186].

In addition to epoxy photoresists and acrylic photoresins, photosensitive biodegradable polymers, hybrid polymer-ceramic materials and hydrogels have been applied in 2PP-DLW. The 2PP-DLW of biodegradable poly(ε-caprolactone)-based [187] and polylactide-based

photopolymers [156] has been demonstrated by Claeyssens et al. The 2PP-DLW of another poly(ε-caprolactone)-based oligomer has been studied by Koskela et al. [188]. The 2PP-DLW of polymer-ceramic materials and hydrogels is discussed in detail in Subsections 2.6.1 and 2.6.2 respectively.

2.6.1 Polymer-ceramic materials

Hybrid polymer-ceramic materials are molecular level composites of inorganic ceramics and organics polymers [189]. As the simple mixing of these materials is not possible due to temperature restraints, polymer-ceramic hybrids are produced by sequential sol-gel synthesis of inorganic and organic networks [190]. This results in strong covalent bonds connecting the different structural elements instead of weak interactions typical in conventional composites [191]. Typical precursors for polymer-ceramic materials are silicon alkoxides ($Si(OR)_4$) with possible heteroelements, such as Zr, Ti or Al and organofunctional alkoxysilanes with epoxy, vinyl or methacrylate groups, for example. [190-192]. The Si-C bonds in these molecules are stable under the mild conditions of sol-gel synthesis. The inorganic network is formed by the classical sol-gel reactions of hydrolysis and condensation:

Hydrolysis:
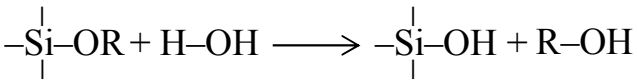
(10)

Polycondensation:
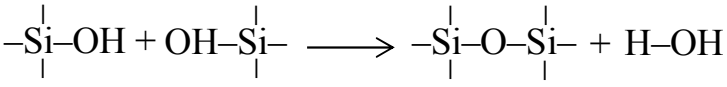
(11)

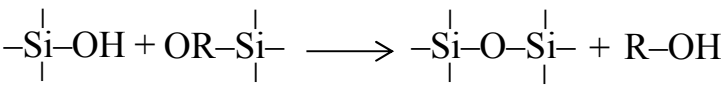

Polycondensation occurs simultaneously with hydrolysis as soon as the first molecules have been hydrolysed and is affected by processing conditions, such as pH, solvent, temperature and water concentration. [189] Condensation is achieved by heating the sol at a temperature of 100°C, which eliminates solvent such as water or alcohol from the material forming a gel of reduced volume [193]. In the final step, thermally or photochemically induced polymerization of the organic functional groups forms the organic network between the inorganic nanoclusters or –particles [192].

The concept of hybrid polymer-ceramic materials is to combine the beneficial properties of organic polymers, such as toughness, functionalization and low processing temperatures with the characteristics of glass-like materials such as hardness, chemical and thermal stability and transparency. [190] The high optical transparency stems from the non-crystalline structure of polymer-ceramic hybrids. The materials are also highly crosslinked thermosets, which makes

them resistant to chemicals and solvents. The properties of the materials, such as Young's modulus, refractive index, electrical resistivity and permeability can be adjusted in a wide range by varying the amount and nature of the inorganic and organic networks. [191] The thermal, optical and mechanical properties are dominated by the inorganic elements whereas the organic network contributes to the flexibility and processability [192].

Polymer-ceramic materials can be processed by 2PP-DLW either directly as viscous liquids without any pre-treatments or as condensated soft glass matrices formed by prebaking. The advantage of the latter approach is minimal shrinkage during photopolymerization. [193] The most commonly used polymer-ceramic hybrids in 2PP-DLW have been so-called Ormocer®s (organically modified ceramics). These materials were originally developed by Fraunhofer-Institut für Silicatforschung in Germany and are commercially available through Micro resist technology GmbH. [190] An Ormocer® US-S4 by the trade name of Ormocomp® has been one of the most widely studied Ormocer®s in 2PP-DLW [39, 89, 151, 194]. According to the supplier, Ormocomp® contains a polysiloxane based inorganic network and the organic crosslinker trimethylolpropane triacrylate but the detailed chemical composition is proprietary. Ormocomp® has been shown to bind proteins [195] and to be cytocompatible with various cell types [196]. Due to these favorable properties, Ormocomp® has been recently used to fabricate microstructures for various biomedical applications, which are discussed in detail in Section 2.7. Recently, other non-commerical polymer-ceramic materials have also been developed, such as the zirconium-silicon sol-gel SZ2080 [148, 197], titanium-silicon sol-gel [198] and tantalum-based sol-gel [199]. Nanoscribe GmbH has also developed a polymer-ceramic IP-G photoresist [200].

2.6.2 Hydrogels

Hydrogels are 3D hydrophilic polymer networks that can absorb up to thousands of times their dry weight in water without dissolving [201-203]. Hydrogels are formed by chains of homopolymers, copolymers or macromers that are of natural or synthetic origin or a combination of these. The chains are crosslinked physically or chemically to form insoluble matrices. [204] Physical crosslinks, such as molecular entanglements or hydrogen bonding, are reversible whereas chemical crosslinks are covalent and permanent [201, 202]. The water absorption of hydrogels is due to hydrophilic functional groups in the polymer backbone and the crosslinks between the polymer chains prevent dissolution. The gel state is therefore between a liquid and a solid. [203]

Hydrogels are biomimetic, that is, they are more similar to living tissues that any other type of synthetic materials [201]. This is due to their biocompatibility, high water content and tunable mechanical and physicochemical properties that can mimic those of the natural extracellular matrix (ECM) [204]. Hydrogels are typically soft, elastic and highly permeable to oxygen, nutrients and waste products [204, 205]. Due to their favorable properties, hydrogels have been increasingly combined with AM techniques for recreating ECM microarchitectures [4].

Recently, 2PP-DLW of a variety of natural and synthetic hydrogels has been reported. The 2PP-DLW of protein hydrogels was first demonstrated more than a decade ago by Campagnola et al. with bovine serum albumin (BSA), fibrinogen and type I collagen [206, 207]. Since then, the group has also reported the processing of fibronectin [208, 209], BSA-laminin combination [210] and even cytoplasmic proteins inside live cells [211]. Another pioneering group in the field of protein 2PP-DLW led by Shear has concentrated on the processing of BSA and avidin and the utilization of avidin-biotin chemistry to create functionalized microstructures [38, 160, 212-214].

Natural hydrogels benefit from biodegradability and cytocompatibility but often suffer from batch-to-batch variation and relatively poor mechanical properties [215]. Better mechanical properties and photoreactivity for 2PP-DLW can be achieved by chemically modifying natural hydrogels. This type of work has been recently demonstrated using methacrylamide-modified gelatin [42, 91, 216, 217], vinyl ester-modified gelatin [216] and methacrylate-modified dextran and hyaluronan (HA) [218]. The 2PP-DLW of HA-glycidyl methacrylate conjugates (HAGM) has been reported by Kufelt et al., who also showed that further improved mechanical properties could be achieved by combining HAGM with PEGda [219]. In addition to chemical modification and blending, the mechanical stability of protein microstructures can also be improved by fabricating hybrid structures in which the protein part is supported by a synthetic polymer support frame [42, 220].

Compared to natural hydrogels, synthetic hydrogels benefit from adjustable properties and customizable chemistry [215]. Among synthetic hydrogels, PEGda is one of the most widely studied materials. PEGda is the acrylated form of poly(ethylene glycol) (PEG), which is one of the most hydrophilic polymers and has been approved by FDA for several medical applications due to its low toxicity and biocompatilibity. [4, 221] A drawback of PEGda is that it is not inherently biodegradable but modification by degradable groups is feasible [215]. The 2PP-DLW of pure PEGda has been studied by several groups. [62, 177, 188, 222-224]. Jhaveri et al. have demonstrated the 2PP-DLW of a co-polymer of PEGda and 2-hydroxyethyl methacrylate

(HEMA) [57]. Zhang et al. also recently reported fabrication of sophisticated web-like microstructures using 2PP-DLW and PEGda combined with acrylate-PEG RGDS (arginine-glycine-aspartic acid-serine) peptide [176].

2.7 Biomedical applications of 2PP-DLW

Due to the high accuracy and intrinsic 3D fabrication capability, 2PP-DLW is currently used increasingly for the processing of biomaterials for various biomedical applications. The main types of applications are microneedles, surface patterns for 2D cell growth guidance and scaffolds for 3D cell culturing. Microneedles are among the first biomedical applications of 2PP-DLW. Needles with micron dimensions that penetrate the outer most stratum corneum skin layer are a painless and effective method for transdermal drug delivery [225]. The fabrication of microneedles by 2PP-DLW has been mainly studied by Narayan et al. In their first studies, they fabricated hollow Ormocomp® microneedles of various designs that were shown to penetrate porcine skin without fracturing [89, 226]. More recently, they have demonstrated more efficient microneedle fabrication using 2PP-DLW and combined with micromolding and demonstrated the ability of these microneedles to penetrate human skin [75]. They have also shown that microneedles fabricated by 2PP-DLW can be used for quantum dot delivery [227].

Culturing mammalian cells in vitro is a powerful tool to study cell and tissue physiology and pathophysiology [2]. Traditionally, single cell populations have been cultured on 2D substrates, such as tissue culture polystyrene. Cells, however, sense and respond to their environment on the scale of one micron or less and features in this range can be used guide cell behavior. [1] 2PP-DLW has been mainly used for the fabrication of surface patterns to study cell adhesion and migration. The patterns are most commonly line or grid arrays fabricated on substrate surfaces by scanning a single layer in the z-direction. Both proteins and synthetic materials have been used for this purpose. Kaehr et al. were the first to report the growth guidance of neuronal cells using BSA and avidin lines [38, 212]. Synthetic Ormocomp® microstructures in the form of lines [228] and cages [229] have also been shown suitable for neuronal cell growth guidance. Fibroblast growth guidance has been studied by Campagnola et al. using collagen [230], BSA, fibrinogen and fibronectin lines [208, 209]. Fibroblast orientation has also been demonstrated using synthetic Ormocomp® lines [90, 127]. Using gelatin methacrylamide lines, Engelhardt et al. have demonstrated the orientation of porcine chondrocytes [42].

Although remarkable progress in biology has been made using 2D cell cultures, these conditions are often drastically different from the native 3D environment [2]. The native ECM is

a complex, dynamic structure formed by: 1) structural fibrous proteins collagen and elastin, 2) amorphous matrix composed mainly of proteoglycans, solutes and water, 3) adhesive proteins including laminin and fibronectin and 4) specialized proteins such as growth factors. The exact composition of the ECM varies from tissue to tissue. As a whole, the ECM is analogous to a fiber-reinforced composite, in which the fibrous proteins are embedded in and linked to a glycoprotein-water hydrogel. [231] It has been shown that cells can behave abnormally and exhibit different morphologies when confined to 2D monolayer instead of a 3D environment. [2] Ideal cell culture scaffolds should thus mimic the complex 3D microarchitecture of the natural ECM [1].

Creating carefully designed porous microstructures for 3D cell culturing is currently one of the key application areas of 2PP-DLW. The work in this area is summarized in Table 1. Studies in which scaffold fabrication was reported without any cell culture data have been omitted. Thus far, scaffolds have been mostly fabricated using synthetic materials, such as polymer-ceramic hybrids. Custom silicon-zirconium hybrids have been applied to 3D culturing studies of fibroblasts [232] and pre-osteoblastic cells [233, 234]. Fairly simple Ormocomp® structures, such as fibers [235] and cylinder arrays [89, 196, 236] have been cultured with different neuroblast, endothelial, epithelial and fibroblast cell lines. Ormocomp® woodpiles have also been used for the culturing bovine chondrocytes [237]. More sophisticated, web-like Ormocomp® scaffolds have been reported by Bastmeyer et al. for cardiomyocyte cell force measurements [238]. They have also fabricated two-component scaffolds of protein binding Ormocomp® and protein resistant PEGda/PETA mixture for the 3D culturing of fibroblasts [195]. Recently, they also used PETA scaffolds fabricated on porous membranes to study chemically driven cancer cell invasion [239]. Chemotaxis of dendritic cells has also been studied by Tayalia et al. using acrylate scaffolds in a PDMS chamber [240].

In addition to studying the behavior of immortalized cell lines, 3D culturing is becoming vital in studying the proliferation and differentiation of stem cells. Recently, Ovsianikov et al. cultured porcine mesenchymal stem cells and human adipose-derived stem cells in large-scale gelatin scaffolds with promising results [91, 241]. Mesenchymal stem cell niches have also been created by Raimondi et al. using SZ2080 [242] and Su et al. using BSA combined with laminin [210]. 2PP-DLW offers exciting new possibilities also for co-culturing studies [223] and even for in situ microfabrication in the presence of cells [217] and whole organisms [224].

Table 1. Microstructures fabricated by 2PP-DLW for 3D cell culturing.

2PP-DLW system	3D structures	Materials	Photoinitiators	Cells	Culture time	References
800 nm fs laser NA = 0.75	Tunnels, cylinders and woodpiles	Ethoxylated trimethylolpropane triacrylate or 50/50 mixture of fibrinogen and BSA[(a)]	Rose Bengal	L1210 lymphocytes, primary neurons or fibroblasts	4 h	[243]
780 nm 80 fs 94 MHz	Cylinders	Ormocomp®	Irgacure® 369	B35 neuroblast-like cells, GFSHR-17 granulosa cells, CHO cells, GM7373 endothelial cells or SH-SY5Y neuroblastoma cells	48 h or 3–4 days	[89, 196, 236]
523 nm < 500 fs 1 MHz NA= 0.14	Fibers between glass plates	Ormocomp® coated with fibronectin	Not specified	NIH 3T3 mouse fibroblasts or MDCK canine epithelial cells	24 h	[235]
800 nm 100 fs 80 MHz NA = 1.4	Pillars with connective beams	Ormocomp® coated with fibronectin	Not specified	Embryonic chicken cardiomyocytes	1–2 days	[238]
Commercial system by Nanoscribe NA = 1.4	Pillars with connective beams and cubes	Ormocomp® coated with fibronectin and PEGda[(b)] with PETA[(c)]	Irgacure® 396	Primary chicken fibroblasts	2 h	[195]
Not specified	Woodpiles	PETA	Irgacure® 379	A549 human lung carcinoma cells or wildtype mouse embryonic fibroblasts	16 or 24 h	[239]
800 nm 130 fs 80 MHz NA = 0.65	Woodpiles	Triacrylate monomer	Lucirin-TPOL	HT1080 fibrosarcoma cells or primary mouse bone marrow-derived dendritic cells	24 h	[240, 244]
750-800 nm 100-120 fs 80 MHz NA = 1.4, 0.7 or 0.6	Woodpiles and cubic lattices	Ormocomp®, PEGda, UDM[(d)], methacrylated oligolactones, dextran and hyaluronan, polyglycerine UM[(e)], poly(ethylene glycol) UM	Irgacure® 396	Bovine chondrocytes	3 days	[62, 218, 237]
780 nm 120 fs 80 MHz NA = 0.4	Tubular structures comprising hollow cylinders	PEGda	Irgacure® 369	Ovine vascular smooth muscle-like cells and endothelial cells	Not reported	[223]
515 nm 200 fs 1 MHz NA = 0.40	Cubic lattices	Methacrylamide-modified gelatin	Irgacure® 2959	Porcine bone marrow-derived mesenchymal stem cells or primary human adipose-derived stem cells	7–22 days	[91], [241]

Modified stereolithography system Air lens	Cubes lattices	Accura™ SI10 coated with type I collagen	Not specified	Primary rat hepatocytes or HepG2 liver cancer cells	6 days	[245]
Commercial system by Nanoscribe	Porous cylindrical and hexahedral structures	SU-8 coated with Ni, Ti and poly-L-lysine	Not specified	HEK293 human embryonic kidney cells	4 days	[246]
800 nm <20 fs 75 MHz NA = 0.95	Guidewires, woodpiles and sea-shell structures	Custom polylactide-based photopolymer	Michler's ketone	NG108-15 or PC12 neuronal cells	48 h to 7 days	[156]
800 nm <20 fs 75 MHz NA = 0.95	Cubes, woodpiles and cubic lattices	Custom hybrid silicon–zirconium and silicon–titanium materials	Irgacure® 369	NIH 3T3 mouse fibroblasts	7 days	[232]
780 nm NA = 0.75	Solid modules with arches and tunnels	BSA and BSA combined with laminin	Rose Bengal	H9 embryonic stem cell derived human mesenchymal stem cells	1–3 days	[210]
Commercial system by Nanoscribe NA = 1.4	Helices	SU-8 or IP-L coated with Ni and Ti	Not specified	C2C12 mouse myoblasts	3 days	[247]
780 nm 150 fs 100 MHz NA = 1.4	Posts connected by rods	IP-L or IP-G coated with TiO_2	Not specified	SaOs-2 osteosarcoma cells	48 h	[248]
800 nm 40 fs 87 MHz NA = 1.4	Cubic lattices	SZ2080	Michler's ketone	MG63 human osteosarcoma cells and rat mesenchymal stem cells	6 days	[242]
800 nm <20 fs 75 MHz NA = 0.65 or 0.95	Woodpiles	Custom hybrid silicon-zirconium material with amino functionality	Michler's ketone	MC3T3-E1 pre-osteoblastic cells	2–8 days	[233, 234]
800 nm 100 fs 80 MHz	Suspended web structures	PEGda with acrylate-PEG RGDS peptide	LAP[f]	10T1/2 embryonic mesenchymal cells	12 h	[176]

[a]bovine serum albumin, [b]poly(ethylene glycol) diacrylate, [c]pentaerythritol tetraacrylate, [d]urethane dimethacrylate, [e]urethane methacrylate, [f]lithium phenyl-2,4,6-trimethylbenzoylphosphinate

3 Aims of the work

The main objective of this thesis was to determine how 2PP-DLW processing parameters affect microstructure quality and to apply these findings to the microfabrication of biomaterials for cell culturing applications. In order to achieve the main objective, the following specific aims were set:

1. Developing 2PP-DLW processing based on an affordable Nd:YAG picosecond laser of low frequency (Publications I-II).

2. Finding optimal processing parameter combinations for the microfabrication of Ormocomp® with a picosecond laser system (Publications I-III).

3. Designing and fabricating 3D Ormocomp® scaffolds with a varying degree of porosity and interconnectivity (Publication III).

4. Verifying the functionality of the Ormocomp® scaffolds in stem cell culturing (Publication III).

5. Optimizing 2PP-DLW processing of novel poly(amino acid) hydrogels and the systematic comparison of the 2PP-DLW performance of different hydrogels (Publication IV).

4 Materials and methods

4.1 2PP-DLW systems

Three different custom-built 2PP-DLW systems and two different laser types were used in this work. The first generation system was used in Publication I. It was based on a passively Q-switched frequency doubled Nd:YAG picosecond laser (PULSELAS-P-1064-300-FC, Alphalas GmbH, Germany) operating at 532 nm with a pulse duration of 800 ps, maximum repetition rate of 15 kHz and maximum average output power of 100 mW. The system was built over an upright microscope frame (Nikon ECLIPSE ME 600, Nikon, Japan) and a 50× oil immersion objective (NA = 0.90, Meiji Techno, Japan) was used for processing. In order to overfill the back aperture of a microscope objective, the beam was passed through a 10× expander. The measured average transmittance of the 50× objective with this set-up was 56%. The laser exposure was controlled by a mechanical shutter (SH05 Beam Shutter, Thorlabs, Germany) connected to a controller (TSC001 T-Cube Shutter Controller, Thorlabs, Germany) and a stepper motor xyz-stage (SCAN 130x85, Märzhäuser Wetzlar, Germany), which was used to move a sample with respect to a fixed focal point. The shutter and the xyz-stage were controlled by the commercial software WinPos (ITK Dr.Kassen, Germany) and the custom CorvusControl software. The real-time monitoring of the polymerization process was enabled by a Charge-Coupled Device (CCD) camera (CV-M10RS, JAI Corporation, Japan) mounted behind a dichroic mirror and used in combination with a commercially available visualization program (Ulead DVD Movie FactoryTM 4.0, Ulead Systems, Inc., Taipei, Taiwan).

The second generation system was used in Publications II and III. It was also based on the Nd:YAG picosecond laser and the microscope frame with a either the 50× or a 20× oil immersion objective (NA = 0.75, Nikon, Japan). In addition to the 10× expander, a second adjustable 1–3× beam expander was added to the optical path. With this setup, the measured average transmittance of the 50× objective was 30%. The mechanical shutter of the first system was replaced by a fast electronic shutter (Oriel 76992, Newport Corporation, USA). The xyz-stage was only used for initial sample positioning. Instead of sample movement, the displacement of the laser beam in the xy- and z-directions was controlled by a fast steering mirror scanner (FSM-300, Newport Corporation, USA) and a piezo focus positioning unit (Mipos 250 SGEX, Piezosystem Jena GmbH, Germany) respectively. The six motion axes, the shutter and the camera were controlled by the new custom operating software LaserControlSystem. Unlike in the first generation system, the shutter movement and thus the laser exposure time could be accurately controlled.

In both the first and second generation systems, the average power of the expanded laser beam was attenuated by optical absorptive filters. A 25% throughput attenuator was used in Publication I, 25% and 10% attenuators in Publication II and the 10% attenuator in Publication III. The attenuated power was fine-tuned by changing the pump diode current in the range of 1.75 A-2.52 A. Adjusting the diode current also linearly affected the pulse frequency between 5-15 kHz. The power values were measured with a manual power meter (LaserCheck, Coherent Inc., USA) in Publications I-II and with a computer-controlled power meter (Thorlabs PM100 Series with S 310 C sensor, accuracy 200 mW) in Publication III.

The third generation system was used in Publication IV. It was based on a frequency doubled femtosecond fiber laser (FP-532-0.2-FS-01, Fianium Ltd., United Kingdom) operating at 532 nm with a pulse duration of 200 fs, repetition rate of 40 MHz and maximum average output power of 200 mW. The laser power was accurately controlled with a motorized attenuator system (UAB Altechna, Lithuania). The laser powers were measured before the objective with the Thorlabs PM100 power meter. All the other components in the third generation system were the same as in the second generation system. With this setup, the measured average transmittance of the 50× objective was 48%.

4.2 Materials and photoinitiators

Ormocomp® (Micro Resist Technology GmbH, Germany) was used as the photoresin in Publications I-III. Ormocomp® is a viscous liquid that contains 1% of the PI Darocur® TPO. It was used either as received or in combination with 2 wt% of the PI Irgacure® 127 (I127, Ciba Specialty Chemicals, Switzerland). Both forms were tested in Publication I whereas only the I127 version was used in Publications II and III. The UV-visible absorption spectrum of Ormocomp® in propylene glycol monomethyl ether acetate (PGMEA) was measured in Publication I (Unicam UV 540 UV-Vis spectrometer (Thermo Spectronic, England) over the scan range of 190-900 nm with and without I127.

Custom synthesized poly(α-amino acid) hydrogels and commercial PEGdas were tested for 2PP-DLW in Publication IV. The poly(AA)s were based on methacryloylated and acryloylated poly[N^5-(2-hydroxyethyl) L-glutamine]s (PHEGs). The detailed synthesis is reported in Publication IV. The chemical structures of the PHEGs and PEGda are shown in Figure 2.

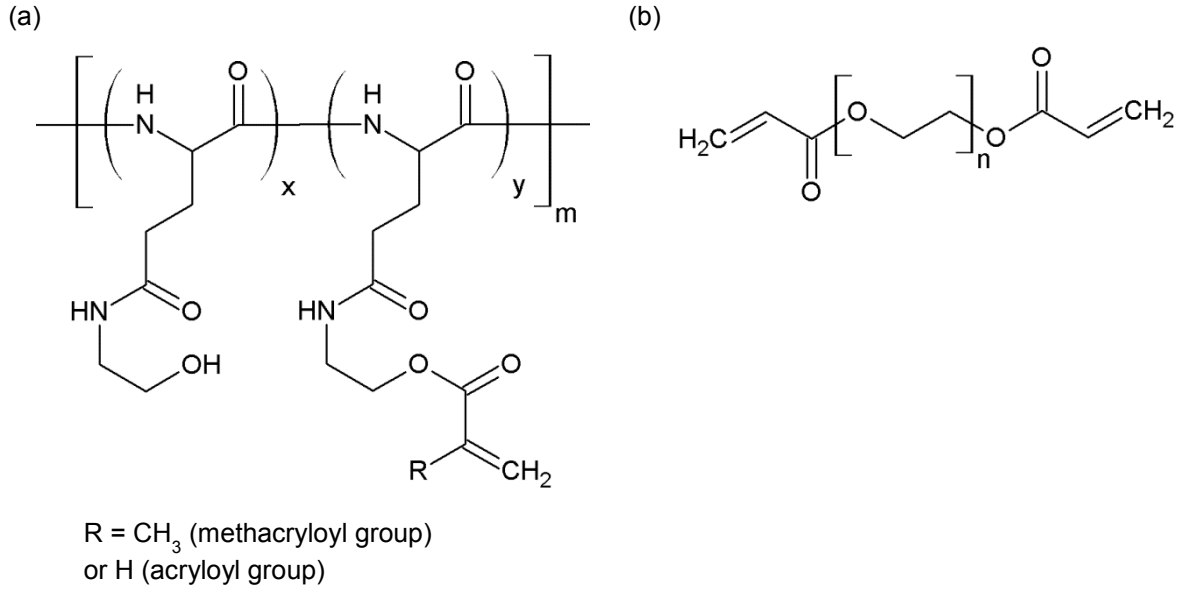

Figure 2. Chemical structures of (a) PHEGs and (b) PEGda.

Two methacryloylated poly(AA)s (PHEG-MA21 and PHEGMA11) and two acryloylated poly(AA)s (PHEG-A13 and PHEG-A9) were tested in addition to PEGdas with two different molecular weights, M_n = 575 g/mol (PEGda-575) or 10000 g/mol (PEGda-10000) (Sigma-Aldrich Finland Oy, Finland). Both the PHEGs and the PEGdas were combined with 0.6 wt% of the PI Irgacure® 2959 (I2959, courtesy of BTC Nordic). The chemical structures of I127 and I2959 are shown in Figure 3.

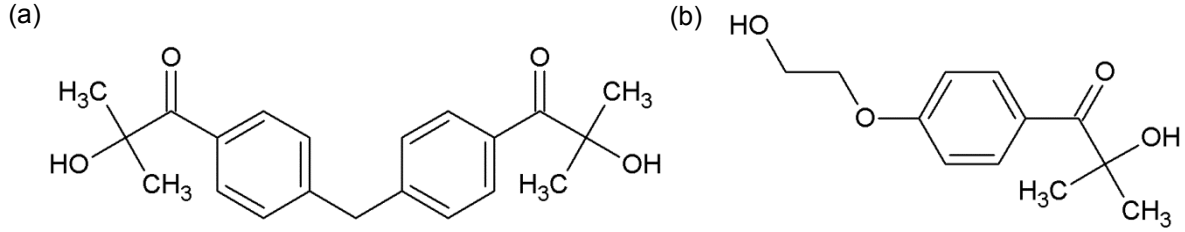

Figure 3. Chemical structures of (a) Irgacure® 127 and (b) Irgacure® 2959.

The molecular weight averages of the methacryloylated and acryloylated PHEGs were determined by size exclusion chromatography (SEC) analysis, details of which are reported in Publication IV. The degrees of PHEG modification were calculated from ^{1}H-NMR spectra in D_2O from the peak area ratio of the methylenes of the side chain acryloyl/methacryloyl groups to the γ-methylenes of the poly(L-glutamine) units: δ(methylenes of methacryloylated PHEGs) = 5.7 and 6.1 ppm, δ(methylenes of acryloylated PHEGs) = 6.0 and 6.4 ppm, δ(γ-methylenes of poly(L-glutamine) unit of polymer) = 2.2–2.5 ppm. The error of these measurements is below 1% of MA units in polymer [249].

4.3 Sample preparation

All the samples for 2PP-DLW were prepared by drop casting without any pre- or post-baking steps. Ormocomp® solution containing 2 wt% (w/w) of I127 was prepared by mixing overnight. Solutions of the solid PHEGs and PEGda-10000 were prepared by dissolving 20 wt% (w/w) of each of the materials in ion-exchanged water containing 0.6 wt% (w/w) of I2959. The liquid PEGda-575 was used either as a 100 wt% solution with 0.6 wt% (w/w) of I2959 (PEGda-575) or as a 20 wt% (w/w) solution in ion-exchanged water containing 0.6 wt% (w/w) of I2959 (PEGda-575-20). A droplet of the Ormocomp®, PHEG or PEGda solutions was sandwiched between a glass slide and coverslip separated by a stainless steel spacer. A 150 μm thick spacer was used in Publications I-II and IV and a 250 μm spacer in Publicationd III. In Publications II and IV, the slides were pretreated with 3-(trimethoxysilyl) propyl methacrylate (MAPTMS, Sigma-Aldrich Finland Oy, Finland) to enhance the adhesion of the microstructures to the glass surface. For MAPTMS treatment, the slides were first cleaned by a strong soap solution, rinsed with water and 99.5% ethanol and allowed to air dry. The slides were then immersed in a MAPTMS solution (1:200 of MAPTMS in 99.5% ethanol with 3:100 of dilute acetic acid (1:10 glacial acetic acid: water)) for approximately 3 min, rinsed with 99.5% ethanol and allowed to air dry. After the polymerization, the non-illuminated Ormocomp® was removed by immersing the samples in the Ormodev® solvent (50:50 mixture of 4-methyl-2-penthanone and 2-propanol, Micro Resist Technology GmbH, Germany) for 15–60 min in Publication I, 2–5 min in Publication II and 5 min in Publication III. Finally, the samples were thoroughly rinsed with 2-propanol (Publications I-II) or by Ormodev® and hexamethyldisilazane (Publication III). The non-illuminated PHEG and PEGda solutions were washed off by immersion in ion-exchanged water for 5–15 min and by rinsing with 99.5% ethanol.

4.4 Microstructure design and fabrication

Voxels, lines and different 3D microstructures were fabricated in this work by 2PP-DLW. The microstructures were designed with either WinPos, Rhinoceros® CAD (Robert McNeel & Associates, USA), Matlab® (The MathWorks, Inc., USA) or custom-designed programs. Voxels were fabricated using the ascending scan method introduced in [130] by increasing the laser focus position relative to the glass surface by 1 μm between each point exposure. All 3D microstructures were fabricated by contour scanning, in which only the profile of a structure is traced and polymerized by the laser beam. Solid 3D structures were first designed with Rhinoceros® or Matlab® and then sliced into contours of the appropriate spacing in the z-direction.

4.4.1 Ormocomp® voxels and lines

Ormocomp® voxels and lines were fabricated in Publications I-II with the 50× objective (NA = 0.90) in order to study the effect of processing parameters on achievable feature size. In Publication I, voxel and line arrays were fabricated using WinPos. Lines having the length of 100 μm were fabricated either with a constant scanning speed of 100 μm/s and varying laser power (1.6–7.6 mW) or with a constant laser power of 2.0 mW and varying scanning speed (50–500 μm/s). In Publication II, voxels were fabricated with a custom program with the constant average laser power of 0.6 mW and exposure times 5–1000 ms. Lines were fabricated similarly to Publication I either with a constant scanning speed of 50 μm/s and varying laser power (0.4–2.7 mW) or with a constant laser power of 1.0 mW or 1.2 mW and varying scanning speed (10–350 μm/s).

In Publication II, lines were also fabricated using the ascending scan method with the constant laser power of 1.4 mW and scanning speed of 50 μm/s. With these parameters, lines were also fabricated on top of supporting walls of different height (5–15 μm) in order to define which laser beam focus position could produce suspended structures.

4.4.2 3D Ormocomp® microstructures

3D Ormocomp® microstructures of were reported in Publications I and III. In Publication I, cones of different designs were fabricated with the 50× objective (NA = 0.90). The cones had the diameter of 50 μm and height of 50 μm or 100 μm. A contour spacing of 3 μm was used in combination with a laser power of 2.0–2.9 mW and scanning speed of 100–200 μm/s. Cones were produced either by simple contour scanning or by multipath scanning originally reported Yang et al. [65]. Multipath scanning involved polymerizing two sets of concentric contours separated by 3 μm.

In Publication III, scaffold structures consisting of repeating unit cells of hollow spheres were designed and fabricated of Ormocomp®. A coded Matlab® routine generated the scaffold models as 3D matrices based on initial design parameters such as unit cell size and interconnectivity. Five different scaffold models (types I-V) were designed, as shown by Figure 4. The design parameters of the different scaffold models are summarized in Table 2.

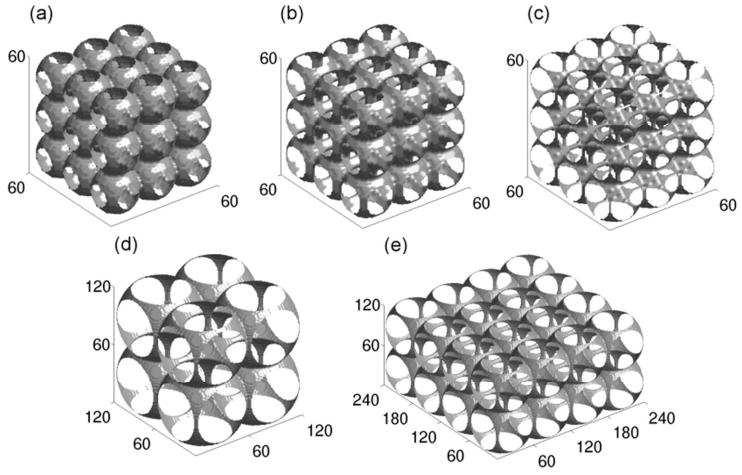

Figure 4. The designed scaffold models: (a) type I, (b) type II, (c) type III, (d) type IV and (e) type V. The dimensions are given in micrometers.

Table 2. Design parameters of the scaffold models.

Scaffold model type	**I**	**II**	**III**	**IV**	**V**
Number of unit cells	3 x 3 x 3	3 x 3 x 3	3 x 3 x 3	2 x 2 x 2	4 x 4 x 2
Overall size (µm × µm × µm)	60 x 60 x 60	60 x 60 x 60	60 x 60 x 60	120 x 120 x 120	240 x 240 x 120
Wall thickness (µm)	1.0	1.0	1.0	1.0	1.0
Porosity (%)	87.8	89.3	93.5	97.8	97.8
Unit cell dimension (a) (µm)	20	20	20	60	60
Opening diameter (c) (µm)	12	14	18	54	54
Interconnectivity parameter (c/a)	0.60	0.70	0.90	0.90	0.90

The scaffold models were designed to have high porosities (88–98%) and varying interconnectivity. The porosities of the scaffold models were calculated using a Matlab® code by calculating: 1) the total volume of each unit cell, 2) the volume of material in each unit cell and 3) the total porosity using the results of the two previous steps. The details of the computation are reported in Publication III. The degree of interconnectivity was assessed by the ratio of the diameter of the circular opening connecting the unit cells to the unit cell size. If *c* represents the diameter of circular opening connecting the unit cells and *a* is the unit cell size, then *c/a* is assigned as the interconnectivity parameter. Based on this, the type I scaffold had the lowest interconnectivity and the type III, IV and V scaffolds had the highest interconnectivity. The scaffold models were exported to Rhinoceros® in .stl file format and sliced to contours of 0.5 µm

spacing. The type I, II and III scaffolds were fabricated using the 50× objective (NA = 0.90), average laser power of 1.1 mW and scanning speed of 120 μm/s. The type IV scaffold model was used to optimize processing parameters and minimize fabrication times for the larger type V scaffolds. With an average laser power of approximately 1 mW, scanning speeds of 80, 100 and 120 μm/s were tested with the 50× objective and scanning speeds of 150, 200, 240 and 300 μm/s with the 20× (NA = 0.75) objective. Type V scaffolds were fabricated with the 20× objective, scanning speed of 200 μm/s and an average laser power of 1.2–1.7 mW.

4.4.3 Determination of polymerization and damage thresholds

In Publication I, the polymerization threshold of Ormocomp® was estimated by writing line patterns with the scanning speed of 100 μm/s. The laser power was tuned so that the line became barely visible and the corresponding value was measured with a manual power meter (LaserCheck, Coherent Inc., USA).

In Publication IV, the 2PP-DLW performance of the PHEGs and PEGdas was compared by determining the P_{th} and P_D values with respect to laser power and scanning speed. Lines were polymerized on the glass surface with scanning speeds of 1–175 μm/s. With each scanning speed, the laser power was tuned to a point where the polymerized line just became visible and to a point where the solution started to bubble. The threshold values were determined from three separate samples for all the materials. From the average threshold values, the dynamic power range, defined as P_D/P_{th}, and the polymerization window (P_w) were calculated for each material. P_w was defined as the power range between the polymerization and the damage thresholds. The power values corresponding to approximately 10–90% of the polymerization window were used for 2PP-DLW processing of each material. The power values were calculated according to the formula $P = P_w*x + P_{th}$, where x = 0.10, 0.25, 0.50, 0.75 or 0.90 is the power factor. These values are denoted as 10%, 25%, 50%, 75% and 90% powers for the different PHEGs and PEGdas and are given as the transmitted values after the objective.

4.4.4 Hydrogel microstructures

In Publication IV, voxels, grids and wall structures were fabricated of the different PHEGs and PEGdas. Voxel arrays were fabricated using a custom program. Exposure times 5–1000 ms were tested with 10% (8%–11%), 50% (41%–52%) and 90% (74%–94%) laser powers for each material and three identical arrays were fabricated with each laser power. 3D rectangular grids and walls were designed with Rhinoceros®. The grids were used for line width measurements and comprised lines written on rectangular support structures. The lines were written with the

scanning speeds of 1–125 μm/s and approximately 25% (25%–26%), 50% (50%–51%), 75% (72%–76%) and 90% (84%–91%) powers corresponding to each scanning speeds for each material. Rectangular walls of different dimensions were fabricated to study post-development swelling and deformation. The walls were fabricated with a constant scanning speed of 100 μm/s and approximately 90% power for each material (PHEG-A13 96%, PHEG-A9 89%, PHEG-MA21 92%, PHEG-MA11 82% and PEGda-575 90%). The walls were produced using the multipath scanning method with a combination of four different wall thicknesses (1, 4, 6 or 8 contours separated by 1 μm) and three different heights (5, 8 or 11 contours separated by 1.5 μm).

4.4.5 Analytical 2PP-DLW model

In Publication IV, the measured width and height of PHEG and PEGda voxels were compared with estimates calculated using an analytical model developed by Serbin et al. [250]. In this model, the voxel width (d) and the voxel height (l) are given by

$$d(N_0, t) = r_0 \sqrt{\ln\left(\frac{\sigma_2 N_0^2 n_p \tau}{C}\right)} \tag{12}$$

$$l(N_0, t) = 2z_R \sqrt{\sqrt{\frac{\sigma_2 N_0^2 n_p \tau}{C}} - 1} \tag{13}$$

$$C = \ln\left(\frac{\rho_0}{\rho_0 - \rho_{th}}\right) \tag{14}$$

$$N_0 = \frac{2}{\pi r_0^2 \tau} \frac{PT}{\upsilon \hbar \omega} \tag{15}$$

where r_0 is the radial distance from the optical axis at the $1/e^2$ level, N_0 is the photon flux on the optical axis, $n_p = \nu t$ is the number of pulses, in which ν is the laser repetition rate and t is the exposure time, τ is the laser pulse duration, σ_2 is the effective 2PA cross-section of the photoinitiator, which is a product of 2PA cross-section and quantum efficiency, z_R is the Rayleigh length, ρ_0 is the initial photoinitiator concentration (0.6 in this study), ρ_{th} is the threshold photoinitiator concentration, P is the average laser power measured before the objective and T is the transmittance of the objective. The unknown model parameters, ρ_{th}, σ_2, r_0 and z_R were estimated using a custom-written Matlab® code by solving the optimization problem that minimized the sum of mean square error between the measurements and the model fit.

4.5 Analysis of microstructures

The fabricated microstructures were analyzed by scanning electron microscopy (SEM), atomic force microscopy (AFM) and confocal microscopy. In Publication I, the Ormocomp® structures were sputter coated with gold in an argon atmosphere (SCD 050 Sputter Coater, BAL-TEC AG, Liechtenstein) and analyzed by SEM (JEOL JSM-6360 LV, JEOL Ltd., Japan). The average sputtering time was 160 s resulting in a gold layer of approximately 60 nm. The dimensions of voxels and lines were measured from SEM images with the free image processing software GIMP 2.6 (http://www.gimp.org/). Line widths were measured from top view (0° tilt) images and line height, voxel width and voxel height from side view (45° tilt) images. The produced Ormocomp® lines had an upward curvature at both ends due to the acceleration and deceleration of the xyz-stage. The widths and heights were thus measured around the center of the lines considered to best represent the true dimensions. Five measurements were made per line. From the fabricated voxel arrays, the voxels with the maximum width were identified, which were considered to represent halves of complete voxels. The widths and heights of these voxels were measured and multiplied by two to obtain the values for complete voxels.

In Publication II, the Ormocomp® samples were analyzed by SEM (JEOL JSM-6360 LV, JEOL Ltd, Japan or Philips XL-30, Philips Electron Optics, The Netherlands) and AFM (XE-100, Park Systems Inc., USA). For SEM imaging, the samples were sputter coated with gold in argon atmosphere (SCD 050 Sputter Coater, BAL-TEC AG, Liechtenstein or S 150 Sputter Coater, Edwards Ltd, UK) for 120 s or 190 s to nominal thickness of 75 nm or 80 nm, respectively. Ormocomp® voxels and lines were studied by noncontact mode AFM using silicon probes (ACTa-905M, Applied NanoStructures Inc., USA) with a nominal resonance frequency of 300 kHz, spring constant of 4 Nm^{-1}, a pyramidal-shaped tip (radius <10 nm) and an aluminum reflective coating. Images were acquired with a scan speed of 0.14, 0.15 or 0.20 Hz. After AFM imaging, the same samples were analyzed by SEM in order to compare the accuracy of measuring microstructure dimensions with these two methods. The microstructure dimensions were measured from AFM images with the XEI image processing software (Park Systems Inc., USA) and from SEM images with GIMP 2.6. Voxel widths and heights as well as line widths were measured from top view (0° tilt) SEM images. The heights of upright lines were measured from side view images (45° tilt) and the heights of fallen lines top view images.

In Publication III, the dimensions of the fabricated Ormocomp® scaffolds were measured from SEM images (Philips XL-30, Philips Electron Optics, the Netherlands) with GIMP 2.6. For the imaging, samples were sputter coated with gold in an argon atmosphere (S 150 Sputter

Coater, Edwards Ltd, UK) for 180 s to a nominal thickness of 113 nm. The dimensions of type I, II, III and V scaffolds were measured from SEM images as demonstrated by Figure 5.

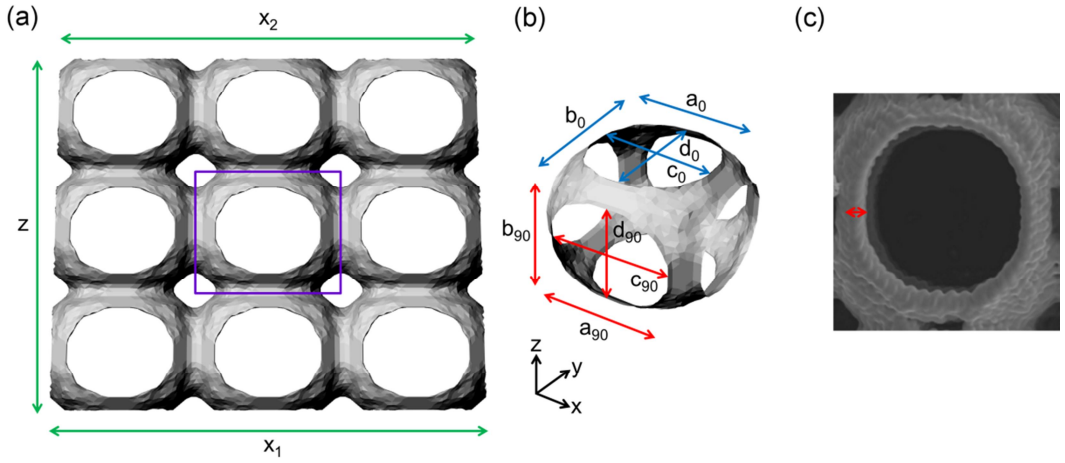

Figure 5. Schematic diagrams of the microstructure dimensions used to evaluate the 2PP-DLW fabrication accuracy: (a) Scaffold dimensions, (b) unit cell dimensions (magnification of the area indicated by the purple box) and (c) wall thickness.

As shown by Figure 5(a), the lateral x-shrinkage was calculated by comparing the width at the top of the scaffold (x_2) to the width at the bottom of the scaffold (x_1). The vertical z-shrinkage was evaluated by comparing the height of the fabricated scaffolds (z) to the height of the models. Unit cell and opening dimensions were measured according to Figure 5(b) from top view (0° tilt) and side view (90° tilt) SEM images. Scaffold wall thickness was estimated by measuring layer thickness as demonstrated in Figure 5(c). Based on the measurements, the porosities of the fabricated scaffolds were calculated using the same three-step method as for the scaffold models.

In Publication IV, the PHEG and PEGda microstructures were studied by SEM (Philips XL-30, Philips Electron Optics, the Netherlands or Zeiss ULTRAplus, Carl Zeiss Microimaging GmbH, Germany) and confocal microscopy (LSM 700, Carl Zeiss Microimaging GmbH, Germany). Prior to SEM imaging, the samples were vacuum dried for a minimum of 20 h and then sputter coated with gold in an argon atmosphere to a nominal thickness of 75 nm (150 Sputter Coater, Edwards Ltd, UK). Structure dimensions were measured from top view (0° tilt) and side view (90° tilt) SEM images with GIMP 2.6. The dimensions of rectangular wall structures were measured both in the swollen and dry state. For the swollen state measurements, the samples were imaged with the confocal microscope with a 20× air objective (NA = 0.55). Prior to imaging, the samples were first soaked in ion-exchanged water for approximately 20 h and then treated with a fluorescein isothiocyanate (FITC, Sigma-Aldrich Finland Oy, Finland) solution (1 mg/ml FITC in dimethyl sulfoxide), which was washed off by ion-exchanged water. The samples were imaged inside a droplet of ion-exchanged water with the xy-resolution of 100

nm–1.19 mm and a z-resolution of 1 mm. The width, height, thickness and volume the swollen walls were measured from thresholded confocal image stacks with the free image analysis software FIJI (http://fiji.sc/Fiji). The dry volumes were calculated from top view and side view SEM images based on the overall wall area, opening area and wall height measured with GIMP 2.6. Volumetric swelling ratios were assumed to be independent of the wall dimensions and were calculated as

$$Volumetric\ swelling\ ratio = \frac{swollen\ volume}{dry\ volume} \tag{16}$$

The widths of the walls in the dry state were measured from side view SEM images and the dimensional change caused by the swollen-to-dry transition, referred to as xy-deformation %, was calculated as

$$xy - deformation\ \% = \frac{width_{swollen} - width_{dry}}{width_{swollen}} \times 100 \tag{17}$$

4.6 Statistical analysis

Majority of the data are presented as mean ± standard deviation. In Publication IV, the dynamic power range data and the volumetric swelling ratio data were analyzed with the Kruskal-Wallis test followed by post-hoc comparison by the Wilcoxon rank-sum test with Bonferroni correction. A p-value of less than 0.05 was considered significant.

4.7 Cell tests

4.7.1 Human embryonic stem cell (hESC) derived neuronal cells

In Publication I, the effect of Ormocomp® and I127 on cell viability and migration was studied by culturing of human embryonic stem cell (hESC) derived neuronal cells on UV-polymerized Ormocomp® thin films. 150 µm thin films of Ormocomp® with 2 wt% of 127 were polymerized on glass slides by 10 s exposure to UV light (300-450 nm, ~3000 mW/cm^2, BlueWave® 50 UV curing spot lamp, DYMAX Corporation, USA). Following polymerization, the films were immersed in Ormodev® for 20 min, thoroughly rinsed with 2-propanol and die cut into 6 mm in diameter discs. The discs were disinfected by immersion in 70% ethanol (v/v) for 15 and 30 min and by immersion in sterile Na-PBS buffer solution for three times 30 min. Four disinfected Ormocomp® samples and four control samples of polystyrene coated with laminin (10 µg/ml)

were cultured with hESC derived neuronal cells. The hESCs had been differentiated towards neuronal cells for 8 weeks in neural differentiation medium (NDM) in the presence of fibroblast growth factor (FGF) as described in [251]. The small cell aggregates consisting of more than 90% of young neurons, some astrocytes and non-neural, epithelial-like flat cells [251] were cultured on the samples in NDM for 7 days and the medium was changed three times a week. After the culturing, the viability of the cells was assessed by live/dead staining (Live-Dead® Viability/Cytotoxicity Kit for mammalian cells, Sigma-Aldrich Finland Oy, Finland) with calcein acetoxymethyl ester and ethidium homodimer-1. The viable cells (green fluorescence) and necrotic cells (red/yellow fluorescence) were analyzed by fluorescence imaging (Olympus IX51, Olympus, Japan).

4.7.2 Human adipose stem cells (hASCs)

In Publication III, Ormocomp® scaffolds were cultured with human adipose stem cells (hASCs). Round glass coverslips (diameter 9 mm) each containing two type V scaffolds were disinfected by immersion in 70% (v/v) and 99.5% (v/v) ethanol for 15 min each. The ethanol was allowed to fully evaporate before the samples were placed in sterile 24-well plates. The study was conducted in accordance with the Ethics Committee of the Pirkanmaa Hospital District (Tampere, Finland, R03058). The hASCs were isolated from an adipose tissue sample collected from one female donor (age 42 yrs) undergoing elective plastic surgery at Tampere University Hospital (Tampere, Finland). The isolation was carried out using mechanical and enzymatic isolation procedures that have been described previously in [252, 253]. The details of the hASC isolation, primary culture and characterization by flow cytometric surface marker expression analysis are reported in Publication III. Thawed hASCs were expanded in basal medium (BM) and seeded at passages 2–5 onto pre-incubated type V scaffolds in a 24-well plate. The scaffolds in each well were first embedded in 500 µl of BM and then seeded with 2×10^4 hASCs in approximately 200 µl of BM. No additional protein coating was used to enhance cell adhesion. A total of four samples were cultured per time point (4 h, 2 d and 6 d). The culture medium was changed twice a week.

The attachment and viability of hASCs in type V scaffolds were studied using live/dead staining of duplicate samples at each time point. Briefly, the samples were incubated for 35 min at room temperature with a mixture of 0.8 µm ethidium homodimer-1 and 1.0 µm calcein acetoxymethyl ester (Molecular Probes/Invitrogen, USA). The viable cells (green fluorescence) and necrotic cells (red fluorescence) were analyzed by fluorescence imaging (Olympus IX51, Olympus, Japan). The live/dead stained samples were also analyzed by SEM (Philips XL-30, Philips Electron Optics, the Netherlands). The samples were first fixed with 5% glutaraldehyde

(Sigma-Aldrich) in phosphate buffer (pH 7.4) at room temperature for at least 48 h and then dehydrated by a graded ethanol series. The samples were immersed in ion-exchanged water for 15 min and in 10%, 20%, 40%, 60%, 80% (all v/v) ethanol solutions for 10 min each. Lastly, the samples were immersed in 99.5% (v/v) ethanol for 15 min and allowed to fully air dry before storing under vacuum. Prior to SEM imaging, the samples were sputter coated with gold for 120 s in an argon atmosphere (S 150 Sputter Coater, Edwards Ltd, UK) to a nominal coating thickness of 75 nm.

The migration and proliferation of hASCs were studied by a light microscope (Nikon Eclipse TE2000-S, Nikon, Japan) in bright field mode with a 10× air objective at each time point. The 2D and 3D cell orientations were studied at each time point from duplicate samples with a confocal microscope (LSM 700, Carl Zeiss Microimaging GmbH, Germany) with a 20× air objective. For the confocal imaging, the actin cytoskeleton and the cell nucleus were stained. In brief, the cells were first fixed and permeabilized with 4% paraformaldehyde containing 0.2% Triton x-100 (Sigma-Aldrich) for 10 min at room temperature and then blocked with 1% bovine serum albumin (Sigma-Aldrich) for 40 min at 4 °C. The primary antibody (goat anti-human vimentin, Millipore Chemicon) was diluted 1:100 with the blocking solution and then incubated with the cells overnight at 4 °C. The next day, Alexa Fluor® 488 conjugated antigoat secondary antibody (1:500, Invitrogen) together with DAPI (1:1000, Molecular Probes) was diluted in the blocking solution and incubated with the cells for 35 min at room temperature. During the imaging, the samples were immersed in a droplet of distilled water without any additional mounting medium.

5 Results

The laser power values of Publications I-III are given before the objective. The power values of Publication IV are given as transmitted values after the objective.

5.1 Ormocomp® studies

In this work, Ormocomp® was combined with the additional PI I127 to enhance the sensitivity of the resin around the spectral region of 266 nm, which was the theoretical 2PA wavelength of the 532 nm 2PP-DLW system. Figure 6 shows the normalized UV-visible absorption spectrum of Ormocomp® resin in PGMEA measured with and without I127.

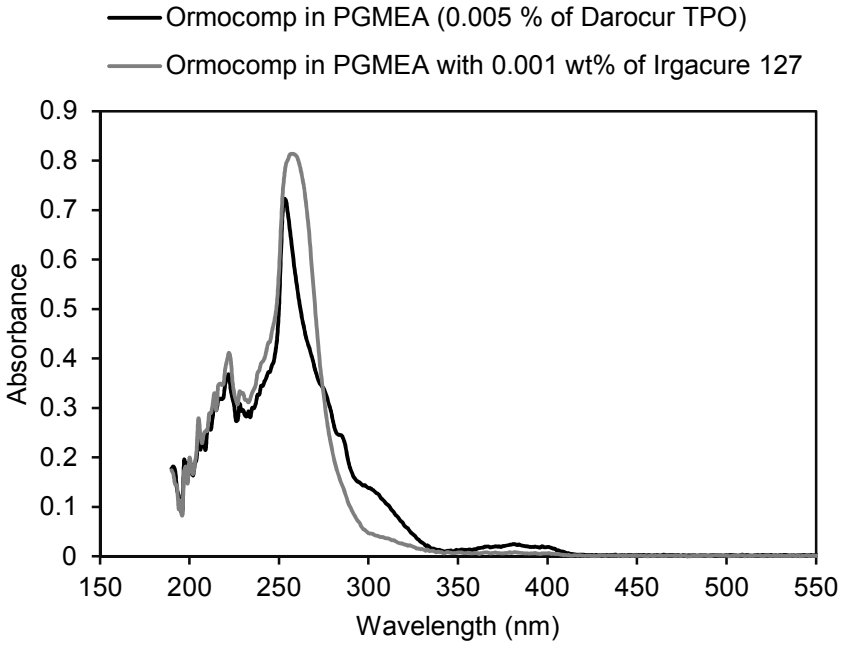

Figure 6. The normalized UV-visible absorption spectrum of Ormocomp® in propylene glycol monomethyl ether acetate (PGMEA) with and without Irgacure® I127**.**

Without I127, Ormocomp® had an absorption maximum at 253 nm and additional, broader peak at 381 nm due to the Darocur® TPO PI. The addition of I127 broadened and shifted the absorption maximum to a slightly to a higher wavelength of 257 nm. The Ormocomp® resins exhibited no linear absorption beyond 410 nm in the green spectral region. This verified that Ormocomp® was not solidified by 1PA at 532 nm.

5.1.1 Effect of processing parameters

In Publication I, processing of Ormocomp® was studied for the first time with a ps laser 2PP-DLW system. The polymerization threshold of Ormocomp® was estimated as 55 μW for the

scanning speed of 100 μm/s. Voxels were fabricated using the ascending scan method with different laser powers as shown by Figure 7(a). As the performed ascending scan was not sufficient to produce whole voxels, the voxels representing half voxels were identified and measured. The measured voxel dimensions are shown in Figure 7(b).

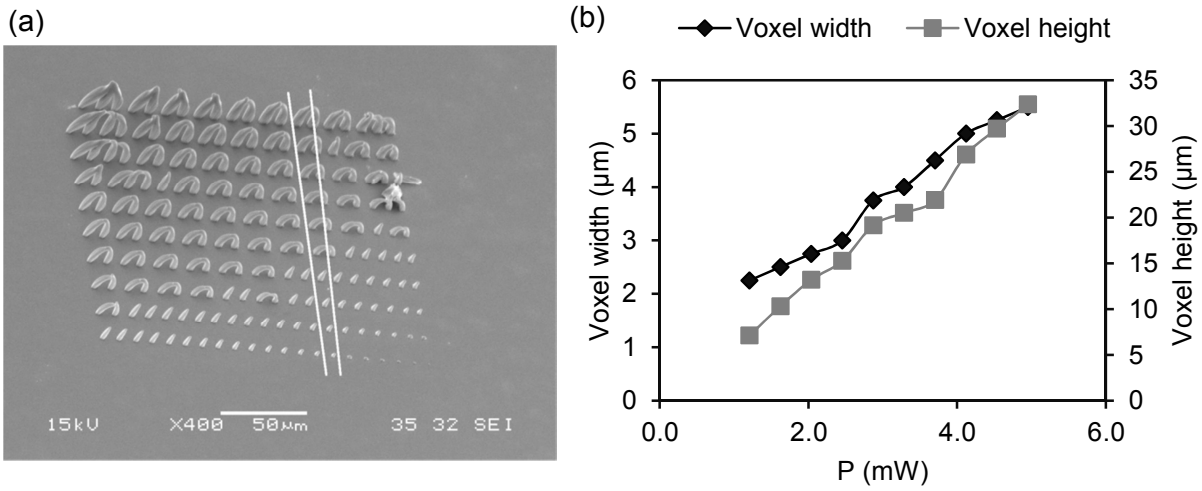

Figure 7. (a) SEM image of Ormocomp® voxels fabricated using the ascending scan method and increasing laser power (1.2 mW–5.0 mW, from bottom to top row, before objective). The voxels indicated by the white lines were identified to represent voxel halves. (b) Ormocomp® voxel dimensions as functions of average laser power (P, before objective). The heights were measured from voxel halves and multiplied by two to obtain the values for complete voxels. Solid lines are guides to the eye.

Both voxel width and height increased approximately linearly with laser power. Voxel heights were more strongly affected and increased more rapidly than voxel widths. The minimum estimated width and height of a whole voxel were 2.3 μm and 7.1 μm (2 × 3.55 μm) respectively.

In addition to voxels, Ormocomp® lines were fabricated with varying laser power and scanning speed, as shown in Figure 8.

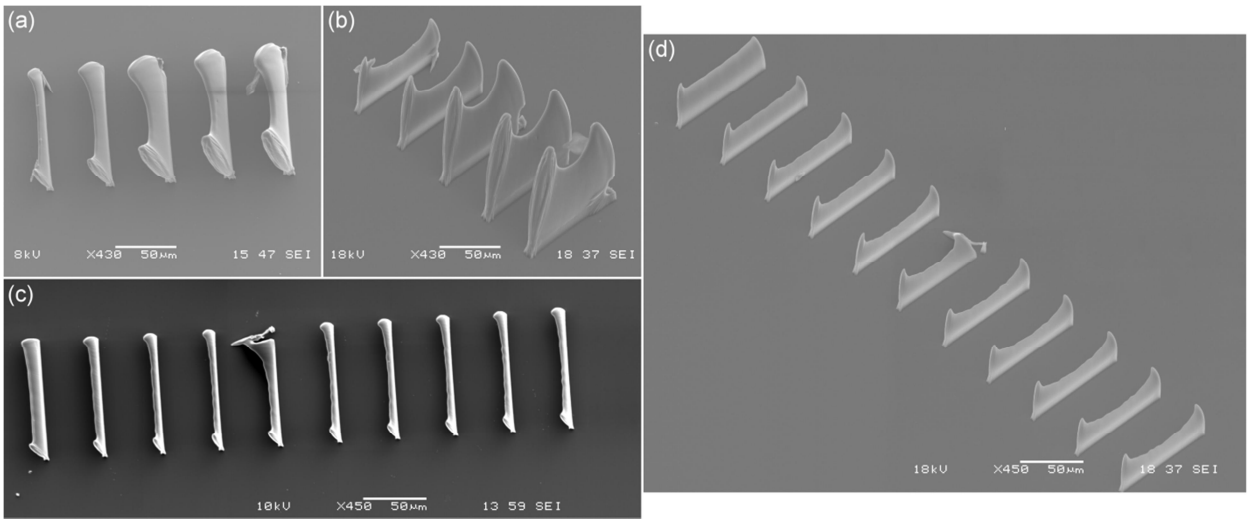

Figure 8. SEM images of Ormocomp® lined fabricated with (a-b) varying laser power (1.6–7.6 mW, before objective) and (c-d) varying scanning speed (50–500 µm/s). Top view images are shown in (a) and (c) and side view (45°) images in (b) and (d).

As shown by the top view SEM images in Figure 8(a, c), all the lines were tilted in some degree due to their high aspect ratio. Also, the line in in the middle of Figure 8(c-d) was distorted by a microbubble during polymerization. The dimensions of the lines as functions of average laser power and scanning speed are presented in Figure 9.

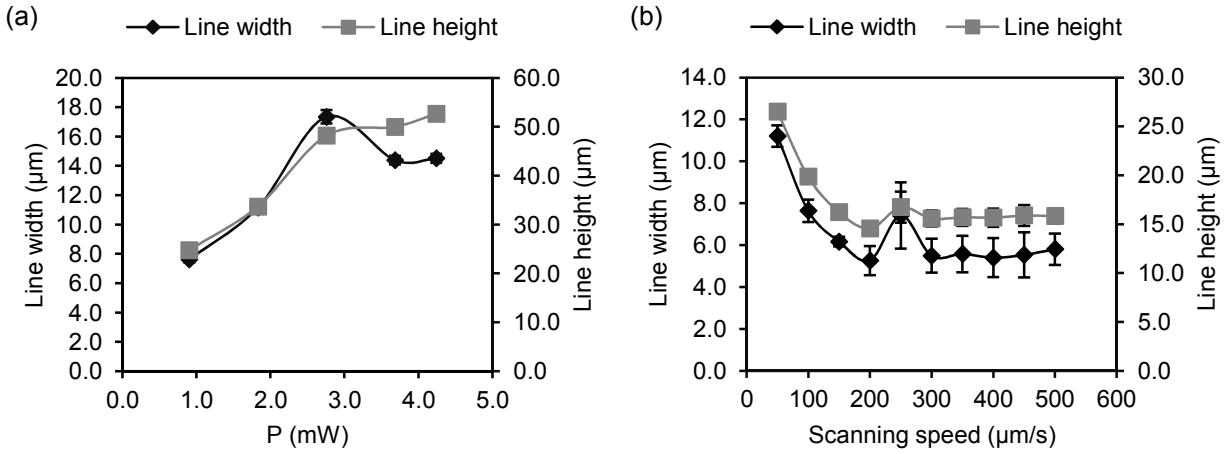

Figure 9. Ormocomp® line dimensions as functions of (a) average laser power (P, before objective) and (b) scanning speed. Data points represent mean ± standard deviation (n = 5). Solid lines are guides to the eye.

Similarly to voxels, both line width and height increased with laser power, as shown by Figure 9(a). However, the observed tilting of the lines likely caused overestimation of the line widths. The pronounced tilting of one of the lines also distorted the graph. By removing this outlier, an

approximately linear relationship between line width and laser power was observed with the limited data. As shown by Figure 9(b), both the line width and height decreased rapidly with scanning speed until the value of 200 µm/s. The dimensions of the line polymerized with 250 µm/s were distorted by a microbubble and were considered outliers. Taking this into account, the line dimensions remained nearly constant with the scanning speeds of 200–500 µm/s.

The processing of Ormocomp® was studied further in Publication II with the second generation ps laser system. The effect of laser power on line dimensions was studied more extensively, as shown by Figure 10.

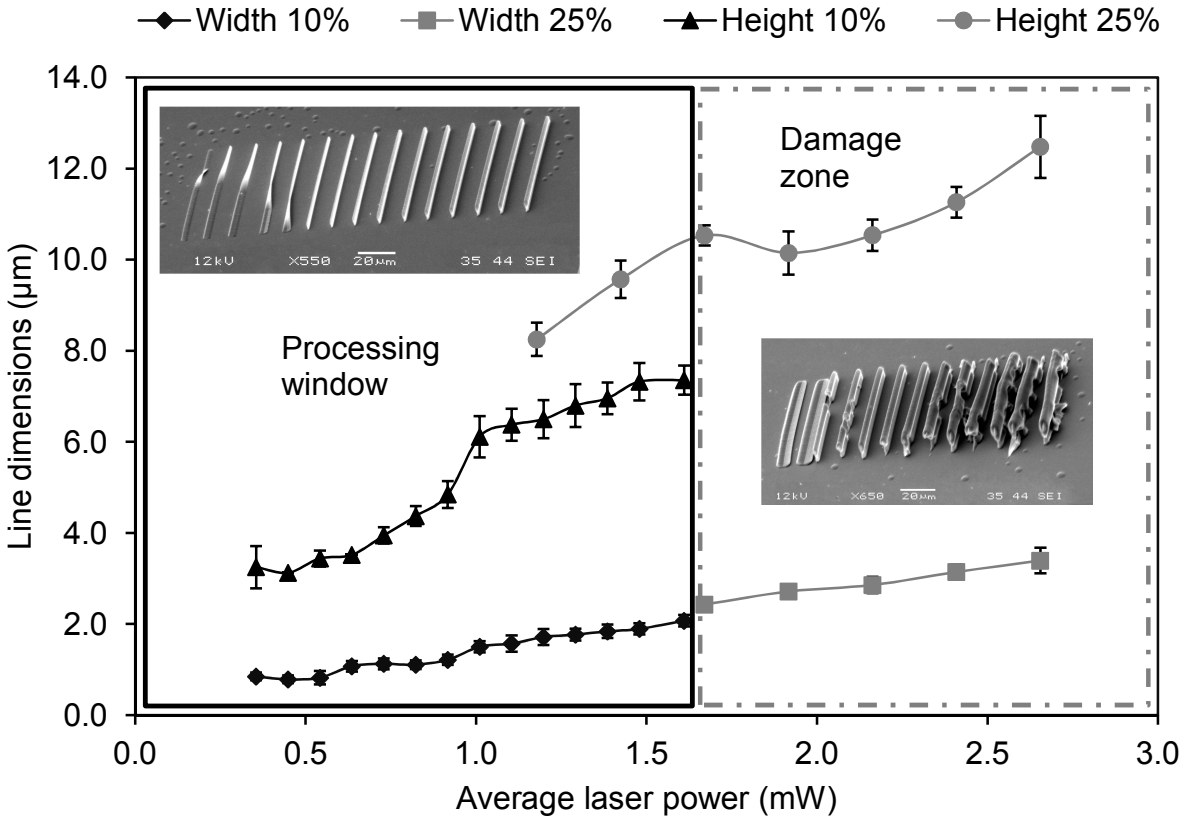

Figure 10. Ormocomp® line dimensions as functions of average laser power (10% and 25% attenuators, measured before objective). SEM images show structure quality inside the processing window (solid line) and the damage zone (dashed line). Data points represent mean ± standard deviation (n = 5). Solid lines are guides to the eye.

It was found that line height increased with laser power more rapidly than line width from 3.3 to 13.6 µm, whereas line widths increased from 850 nm to 3.4 µm. The measured line heights did not form a continuous graph, which most likely due to a slight difference in the initial laser beam focus position between the fabricated line arrays. The line widths increased approximately linearly with laser power. Based on structure quality, the power range could be divided into the

so-called processing window and damage zone. The processing window covered the power range of approximately 0.4–1.6 mW. The onset of the damage zone was observed at the average laser power of 1.7 mW, indicated by microbubble formation and distortion of the Ormocomp® lines.

The influence of scanning speed was also studied with the second generation ps laser system. Figure 11 shows an example of the line arrays fabricated with a constant laser power and a varying scanning speed.

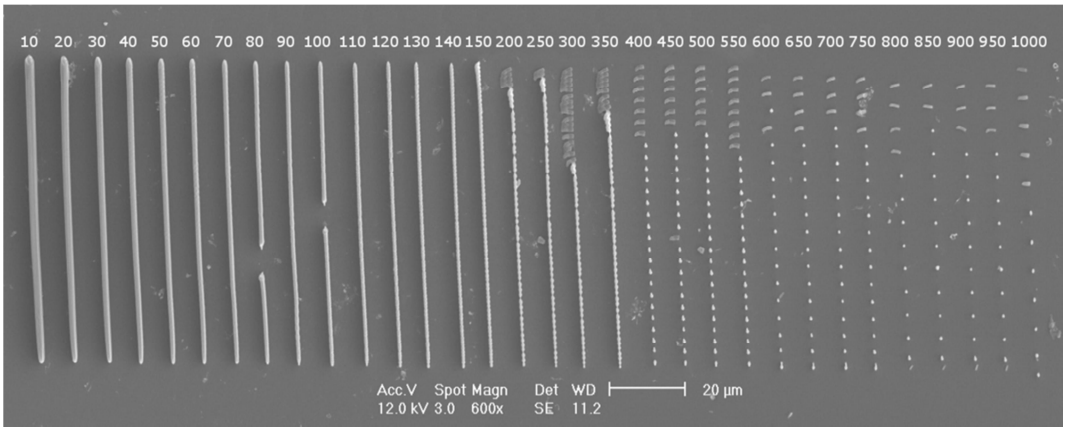

Figure 11. SEM image of Ormocomp® lines polymerized with the constant laser power of 1.0 mW (before objective) and scanning speeds, 10–1000 µm/s (indicated above the lines). The gaps in the lines fabricated with the scanning speeds of 80 µm/s and 100 µm/s were caused by microbubbles.

With the laser power of 1.0 mW, the uniformity of the lines started to decrease after the scanning speed of 150 µm/s. Between the speeds of 200 and 350 µm/s, roughness of the lines increased due to increased voxel separation, which led to the formation discontinuous lines at the scanning speed of 400 µm/s with both the laser powers tested. The inter-voxel distance further increased at the scanning speeds of 600 µm/s and 800 µm/s. In order to explain this phenomenon, the so-called spot overlap was calculated from

$$spot\ overlap\ (\%) = \left(1 - \frac{v}{f \times d}\right) \times 100 \tag{18}$$

where v is the scanning speed, f is the laser frequency and d = 2r is the laser beam spot diameter. The spot diameter was calculated according to Equation (8) and multiplied by the laser beam quality factor (M^2) of 1.2, giving d = 865 nm. For the used laser powers of 1.0 mW and 1.2 mW, the laser pulse frequencies were 6.6 kHz and 3.2 kHz respectively. For 400 µm/s, the spot overlap values were thus 93% and 86%. Rather than affecting the inter-voxel distance, increasing the polymerization power and lowering the pulse frequency resulted in larger voxels and thus reduced the size of the gaps. The inter-voxel distance was approximately 3, 4 and 6 µm for the scanning speeds of 400, 600 and 800 µm/s, respectively, and these values were independent of

the processing parameters used. The number of laser pulses occurring during the measured inter-voxel distances was constant for each array. That is, with 1.0 mW power, 6.6 kHz pulse frequency and 60 GW/cm^2 peak intensity, 49 pulses were needed to produce one voxel, whereas with 1.2 mW and 3.2 kHz and 160 GW/cm^2, only 24 pulses were needed. Peak intensities were calculated as

$$I_{peak} = \frac{2(E_p/t_p)}{\pi w^2} \tag{19}$$

where E_p is the pulse energy, t_p is the pulse duration (800 ps in this case) and w is the laser beam spot radius. The measured line dimensions are shown in Figure 12 as functions of scanning speed.

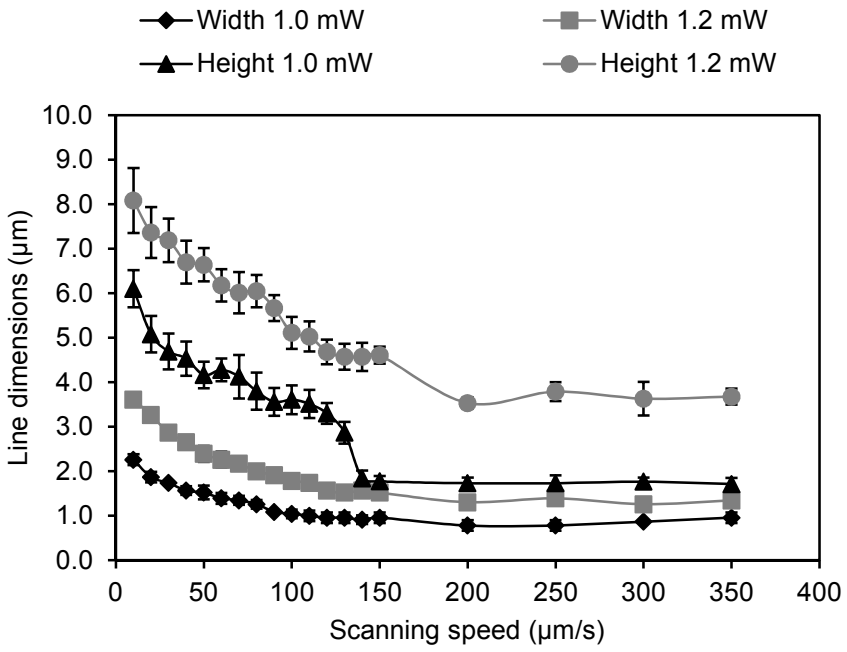

Figure 12. Ormocomp® line dimensions as functions of scanning speed for the laser powers of 1.0 mW and 1.2 mW. Data points represent mean ± standard deviation (n = 5). Solid lines are guides to the eye.

Similarly to Publication I, the line dimensions decreased rapidly with the scanning speed until the value of 200 µm/s and then remained nearly constant at higher speeds.

In Publication II, voxels and lines were produced using the ascending scan method and imaged with both AFM and SEM in order to compare the accuracy of measuring microstructure dimensions with these two methods. The measured dimensions of whole voxels are presented in Figure 13.

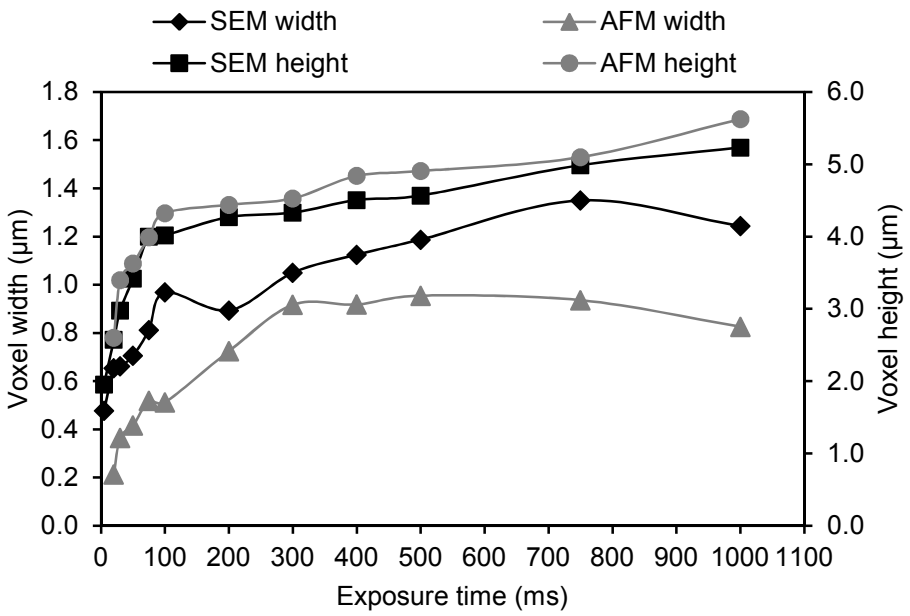

Figure 13. Widths and heights of Ormocomp® voxels measured from SEM and AFM images. Solid lines are guides to the eye.

The minimum measured voxel width and height were 210 nm and 1.95 µm respectively. The average difference between the SEM and AFM measurements was approximately 300 nm for voxel width and only 230 nm for voxel height. Line dimensions were also measured by AFM and SEM and compared, as shown by Figure 14.

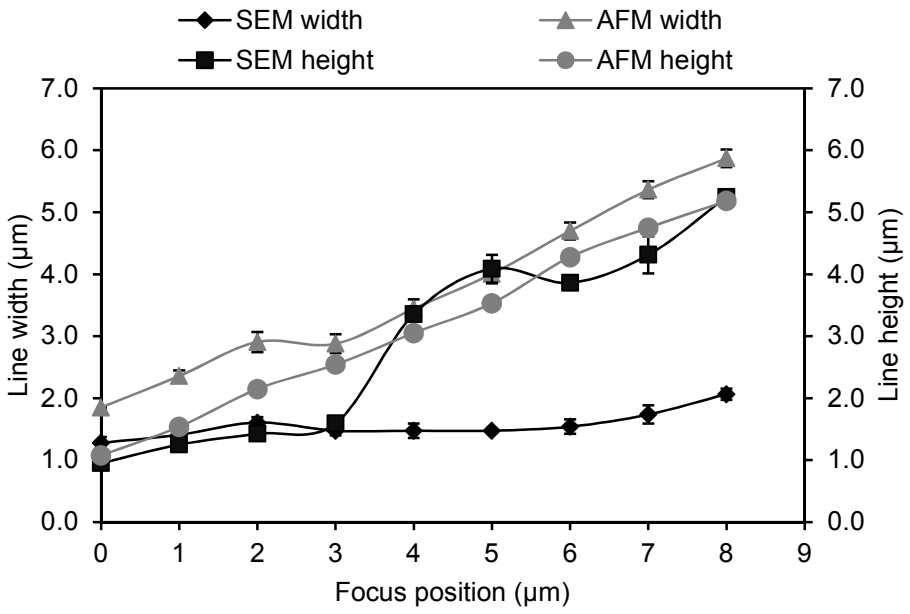

Figure 14. Widths and heights of Ormocomp® lines measured from SEM and AFM images as functions of the laser beam focus position. Data points represent mean ± standard deviation (n = 5). Solid lines are guides to the eye.

Line height could be measured accurately from tilted SEM images, with an average difference of 500 nm compared to the AFM measurements. Line width, however, could not be reliably measured by AFM due to the very steep profile of the lines. This made it impossible for the tip to accurately follow the line profiles, especially with taller lines.

From Ormocomp® lines fabricated using the ascending scan method, it was observed that that only lines with a z-position of ≤ 10 µm remained attached to the surface and survived the development procedure. This implied a minimum laser beam focus position of approximately 9 µm for producing suspended Ormocomp® structures with the tested processing parameters. This hypothesis was tested by the fabrication of suspended lines shown in Figure 15.

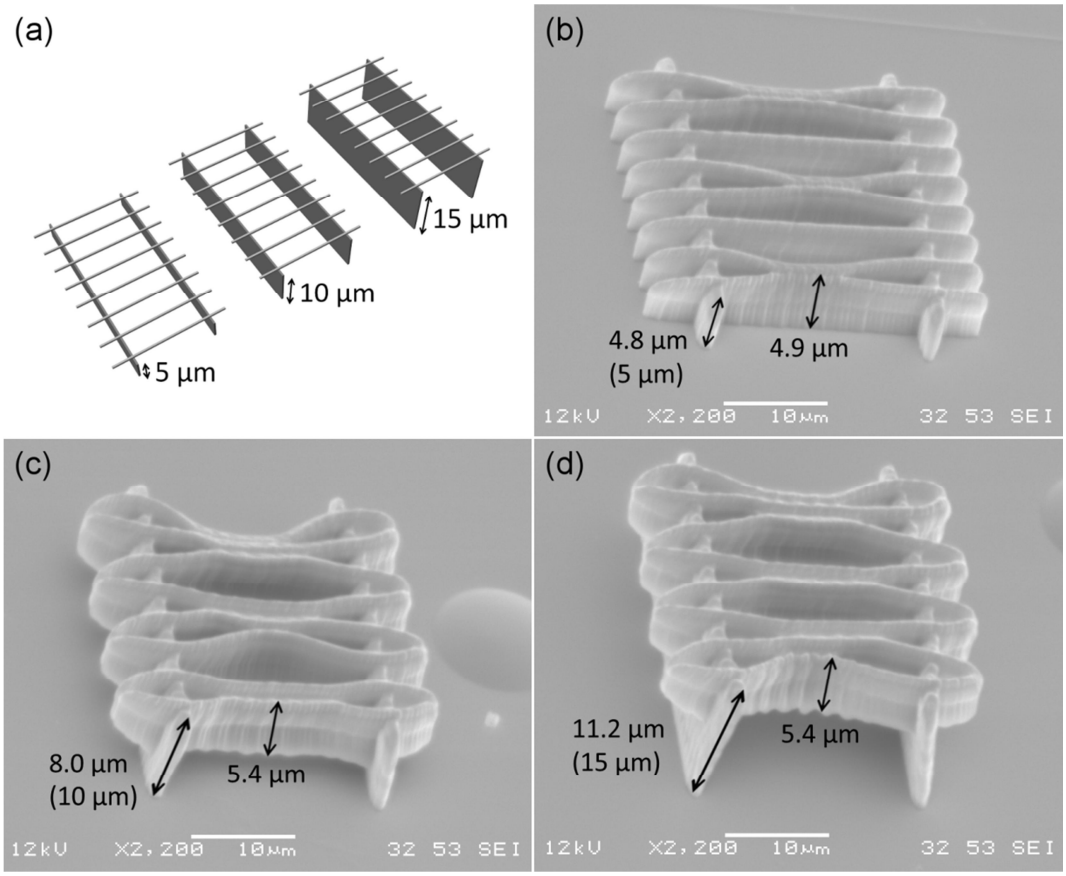

Figure 15. (a) The designs of the suspended structures. The distance between each horizontal line was 5 µm. SEM images of suspended lines polymerized on top of supporting walls of different measured heights: (b) 4.8 µm, (c) 8.0 µm and (d) 11.2 µm. The corresponding model wall heights are in parentheses.

It was confirmed that with the focus position of 10 µm and higher (Figure 15(c-d)), the lines were no longer surface bound and had a height of approximately 5.4 µm. The lines adhered to each other during development due to the capillary force caused the surface tension of the evaporating solvent [140]. The measured heights of the supporting walls differed from the model

dimensions presented in Figure 15(a) as the wall height increased. The measured heights of the taller walls in Figure 15(c-d) were approximately 23% smaller than the model heigths.

5.1.2 Fabrication of cones

In Publication I, Ormocomp® cones of different designs were fabricated with the first generation 2PP-DLW system, as shown by Figure 16.

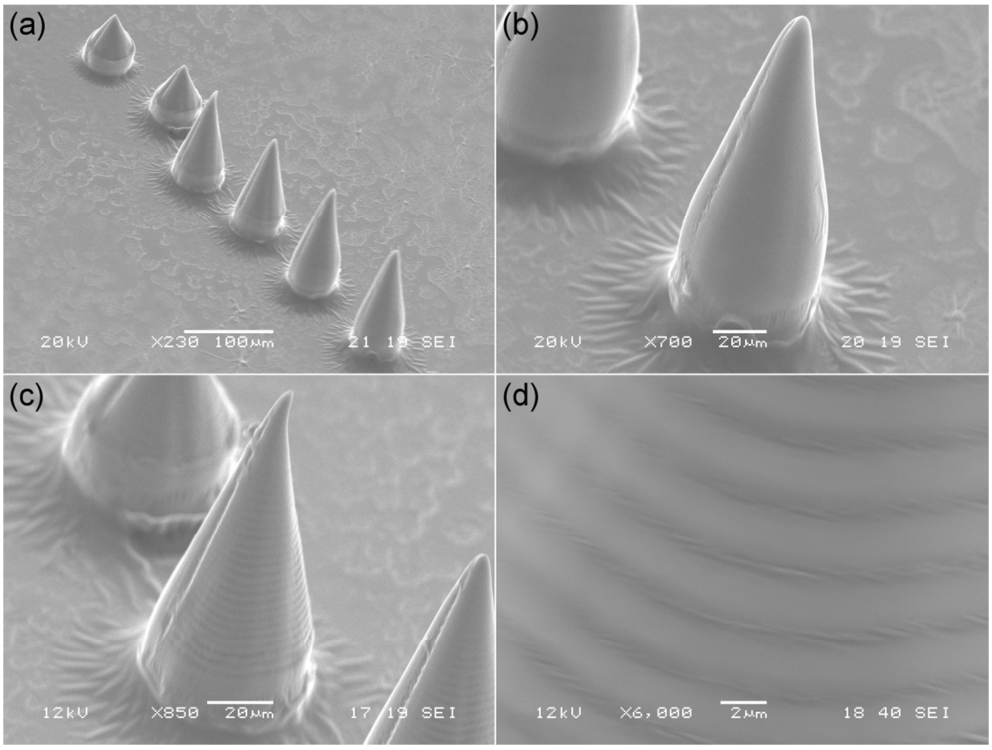

Figure 16. SEM images of Ormocomp® cones of different designs: (a) General view of cones with the designed height of 50 µm and 100 µm, (b) close-up of the last cone in (a) which was fabricated using multipath scanning, (c) close-up of the first of the taller cones in (a) and (d) the layer structure of the cone in (c). All the cones were fabricated with 2.9 mW laser power and 100 µm/s scanning speed.

Based on Figure 16(a), the measured heights of the small and large cones were 69 µm and 117 µm respectively. These values were considerably larger than the designed heights of 50 µm and 100 µm. It should be noted, however, that the height of the first layer was approximately 15 µm. By subtracting this contribution, the heights of the cones differed from the designed values by less than 10%. As shown by Figure 16(b-d), cones with a smooth surface were produced by multipath scanning produced whereas the individual layers were clearly visible from the cones produced by single contour scanning. Based on Figure 16(d), the thickness of these layers was approximately 3 µm and thus corresponded to the contour spacing.

In addition to individual cones, the simultaneous fabrication of 3 × 3 Ormocomp® cone arrays was tested. One of the successfully fabricated cone arrays is shown in Figure 17.

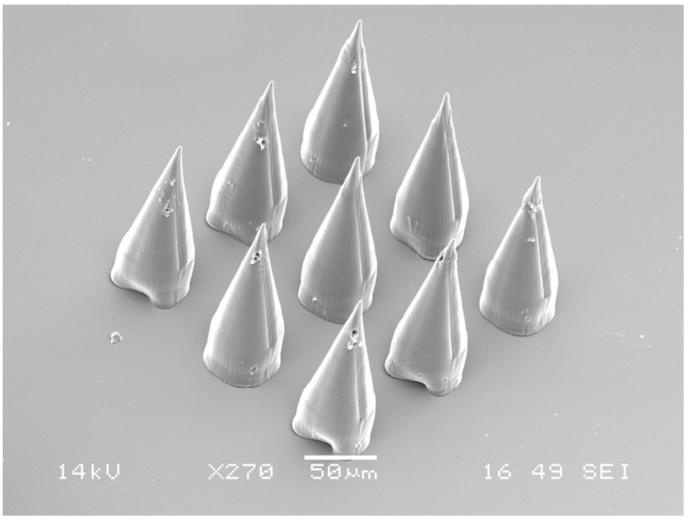

Figure 17. SEM image of a 3 × 3 Ormocomp® cones array fabricated with 2.0 mW laser power and 200 µm/s scanning speed.

The average height of the cones was measured as 113 µm. By again subtracting the height of the first layer, the measured height differed from the designed value of 100 µm by less than 10%. With the scanning speed of 100 µm/s, the polymerization of a single array took approximately 12 minutes. By increasing the scanning speed to 200 µm/s, the polymerization time could be reduced to approximately 7 minutes.

5.1.3 Neuronal cell viability test

hESC derived neuronal cells were cultured on UV-polymerized Ormocomp® discs for 7 days. Fluorescence microscopy images of the live-dead stained cells on Ormocomp® and laminin control surfaces are shown in Figure 18.

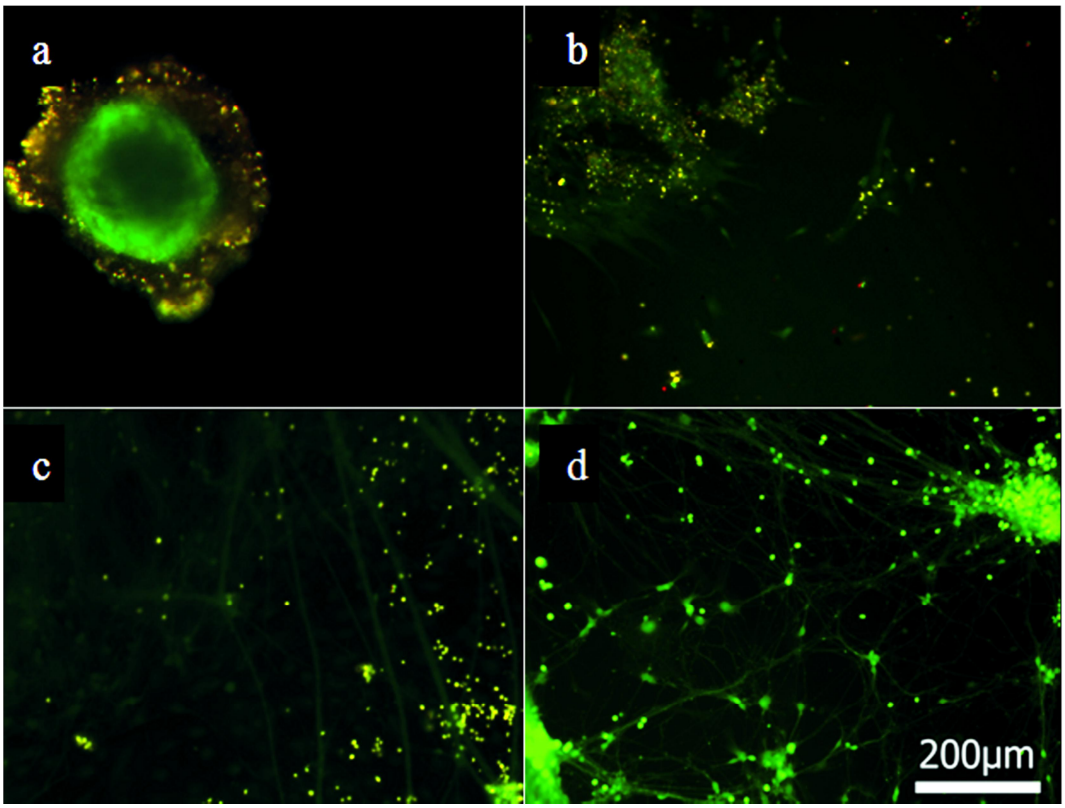

Figure 18. Fluorescence microscopy images of the live-dead stained neuronal cells on (a, b) Ormocomp® and (c, d) laminin coated polystyrene. Live cells are stained green and dead cells red/yellow.

Extensive cell migration was observed on the laminin control surfaces and the morphology of the cells was neural-like. Cell aggregates attached to the Ormocomp® surfaces as well and majority of the cells remained viable during the 7 day culture. Ormocomp® surfaces also promoted cell migration to an extent, but the morphology of the cells was non-neural.

5.1.4 Scaffold fabrication

In Publication III, porous scaffolds models presented in Figure 4 were fabricated of Ormocomp® for the 3D culturing of hASCs. The smaller, type I, II and III scaffolds were successfully fabricated with the 50× objective, as shown by Figure 19.

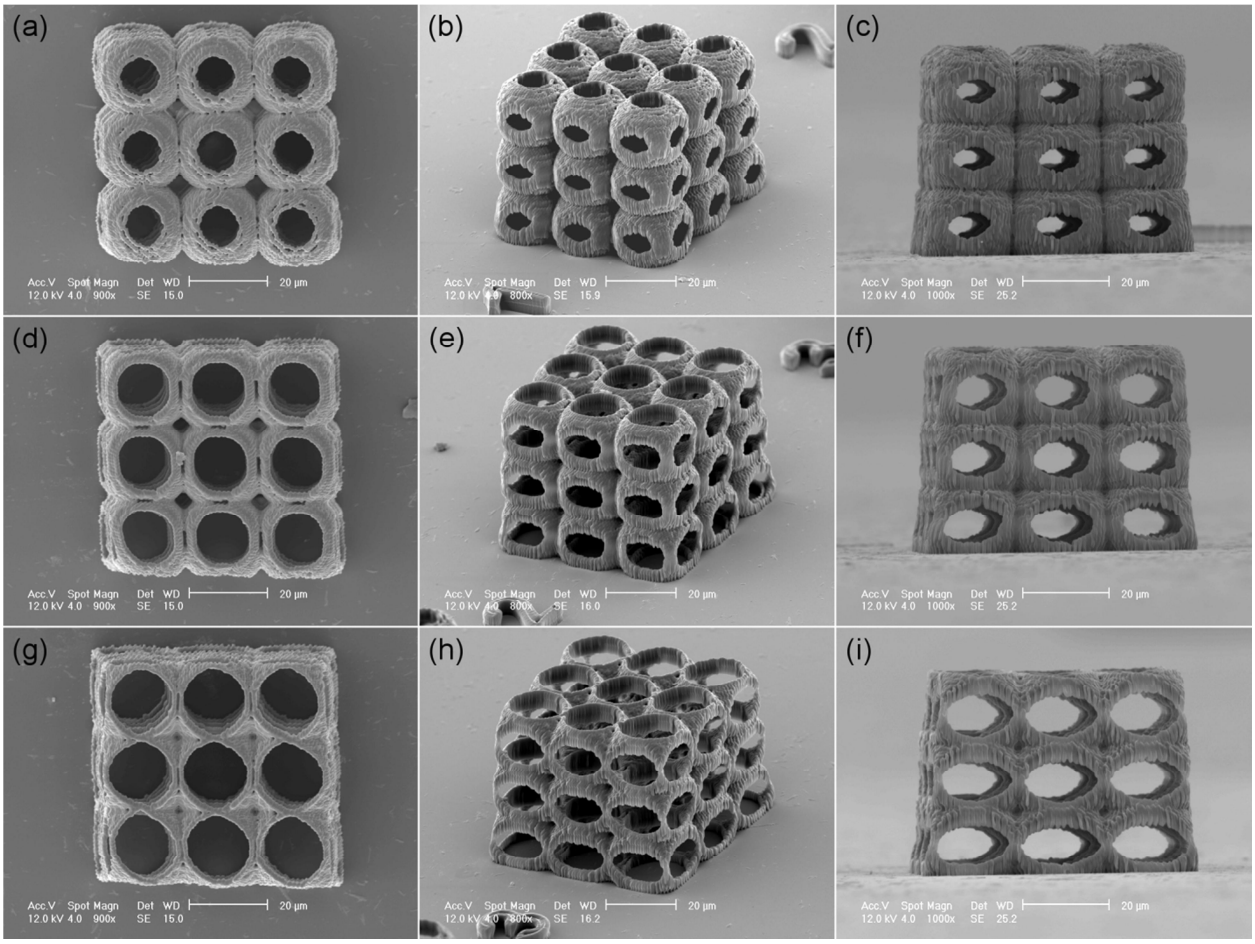

Figure 19. SEM images of Ormocomp® scaffolds fabricated with a 50× objective: (a-c) type I, (d-f) type II and (g-i) type III. The images show the scaffolds from tilt angles of 0° (first column), 60° (second column) and 90° (third column). Scale bars represent 20 µm.

With the scanning speed of 120 µm/s, the polymerization of a type I scaffold took approximately 18 min and type II and III scaffolds approximately 15 min. Type IV scaffolds were fabricated with the 50× and 20× objectives with different scanning speeds. Figure 20 shows SEM images of scaffolds fabricated with the 50× objective.

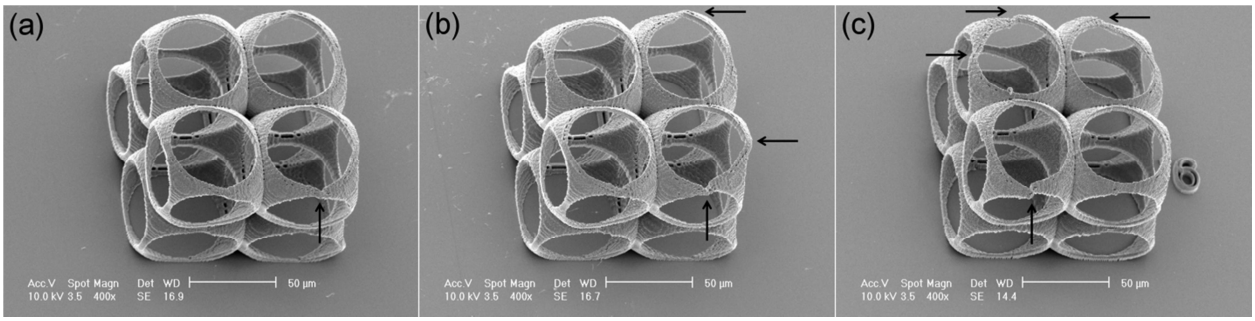

Figure 20. SEM images of type IV Ormocomp® scaffolds fabricated with the 50× objective and scanning speeds of (a) 80 µm/s, (b) 100 µm/s and (c) 120 µm/s. The arrows highlight distortions. All images have been taken from a 30° tilt. Scale bars represent 50 µm.

Increasing the scanning speed from 80 μm/s to 120 μm/s reduced the fabrication time of type IV scaffolds from 60 to 40 min. However, the increase in scanning speed resulted in structural distortion of the scaffolds, as shown by Figure 20(b-c).

The difference in voxel size between the 50× and 20× objectives was evaluated from the interphase of two unit cell layers as demonstrated by Figure 21.

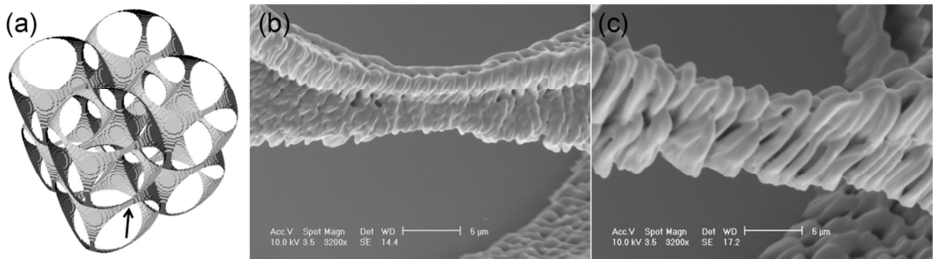

Figure 21. (a) The interphase between two unit cell layers in the type IV scaffold model (indicated by the arrow). SEM images of the interphase polymerized of Ormocomp® with (b) the 50× objective and the scanning speed of 120 μm/s and (c) with the 20× objective and the scanning speed of 300 μm/s. The images were taken from a 30° tilt. Scale bars represent 5 μm.

The scaffold wall height at the interphase increased from approximately 4.1 to 7.9 μm when switching from the 50× objective to the 20× objective. Due to increased voxel size, doubled and tripled scanning speeds could be used for scaffold fabrication with the 20× objective, as shown by Figure 22.

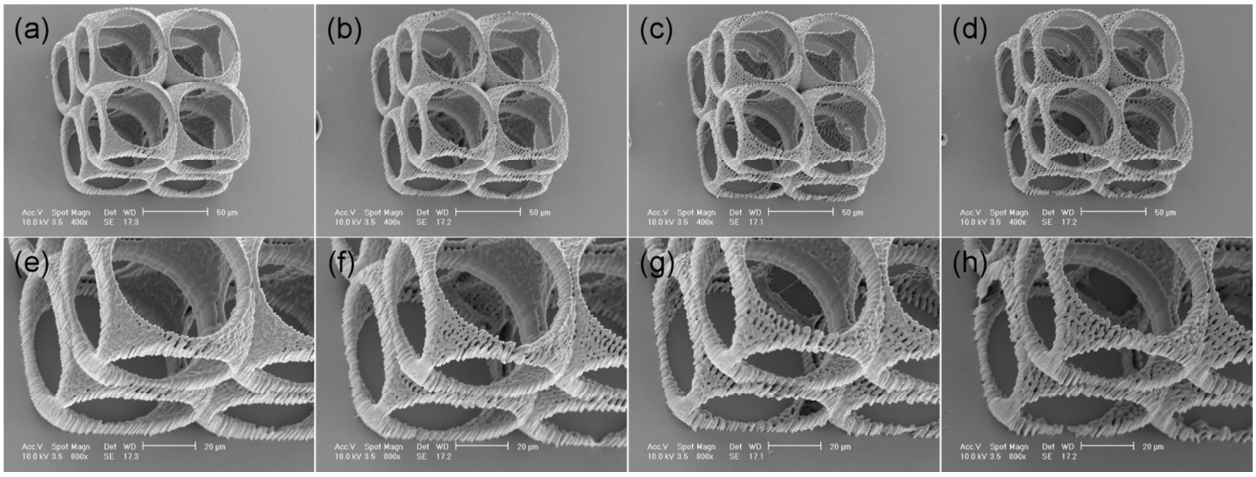

Figure 22. SEM images of type IV Ormocomp® scaffolds fabricated with the 20× objective and scanning speeds of (a, e) 150 μm/s, (b, f) 200 μm/s, (c, g) 240 μm/s and (d, h) 300 μm/s. The images were taken from a 30° tilt. Scale bars represent 50 μm in (a-d) and 20 μm in (e-h).

With the highest tested scanning speed of 300 μm/s, the polymerization time of a type IV scaffold reduced to 14 min. As shown by Figure 22(e-h), surface roughness of the scaffolds increased with scanning speed. Scaffolds fabricated with the highest scanning speeds of 240 and

300 µm/s retained their general shape but suffered from more random distortions than scaffolds fabricated with the scanning speeds of 150 and 200 µm/s. In order to achieve a working compromise between fabrication time and adequate mechanical stability, the 20× objective and scanning speed of 200 µm/s were chosen for type V scaffold fabrication, as shown by Figure 23. The polymerization of one type V scaffold took approximately 78 min.

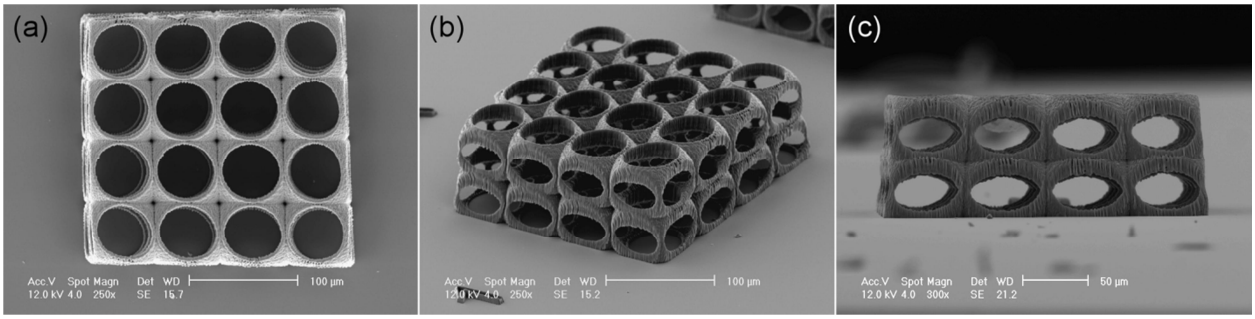

Figure 23. SEM images of a type V Ormocomp® scaffold fabricated with the 20× objective, 1.2 mW laser power and 200 µm/s scanning speed. The images were taken from the tilt angles of (a) 0°, (b) 60° and (c) 90°. Scale bars represent 100 µm in (a) and (b) and 50 µm in (c).

The characteristics of the fabricated type I, II, III and V scaffolds are shown in Table 3.

Table 3. Characteristics of Ormocomp® scaffolds measured from top view (0° tilt) and side view (90° tilt) SEM images. Data represent mean ± standard deviation.

Scaffold type	**I**	**II**	**III**	**V**
a_0 (µm)	19.1 ± 0.2	18.9 ± 0.3	18.7 ± 0.4	58.6 ± 0.9
b_0 (µm)	19.1 ± 0.3	19.0 ± 0.3	19.0 ± 0.6	56.8 ± 0.8
a_{90} (µm)	19.5 ± 0.6	19.3 ± 0.8	19.5 ± 0.7	58.8 ± 2.1
b_{90} (µm)	15.5 ± 0.9	15.4 ± 1.1	15.2 ± 0.6	45.7 ± 1.5
c_0 (µm)	9.9 ± 0.2	12.9 ± 0.2	15.5 ± 0.4	50.3 ± 1.5
d_0 (µm)	10.1 ± 0.2	13.2 ± 0.3	16.0 ± 0.4	47.9 ± 1.3
c_{90} (µm)	9.4 ± 0.5	12.6 ± 0.8	16.5 ± 0.9	49.6 ± 2.0
d_{90} (µm)	5.5 ± 0.2	7.8 ± 0.4	8.9 ± 0.5	27.2 ± 0.5
xy-interconnectivity (c_0/a_0)	0.52 ± 0.01	0.68 ± 0.01	0.83 ± 0.01	0.86 ± 0.02
xz-interconnectivity (d_{90}/b_{90})	0.35 ± 0.02	0.51 ± 0.03	0.59 ± 0.03	0.60 ± 0.02
Wall thickness (µm)	1.0 ± 0.1	1.4 ± 0.1	1.3 ± 0.2	3.1 ± 0.3
x_1 (µm)	61.5	61.0	62.6	243.9
x_2 (µm)	56.8	55.3	55.7	228.5
x-shrinkage (%)	7.6	9.4	11.1	6.3
z (µm)	47.8 ± 0.2	47.1 ± 0.2	46.7 ± 0.1	91.4 ± 0.3
z-shrinkage (%)	20.3 ± 0.3	21.4 ± 0.3	22.1 ± 0.2	23.8 ± 0.3
Porosity (%)	84.7	80.3	81.6	85.0

The accuracy of scaffold fabrication by 2PP-DLW was assessed by comparing the characteristics the fabricated scaffolds to those of the models (Table 2). In the xy-direction, the unit cell and opening sizes of all four scaffold types corresponded well to the models. However, in the xz-direction, the fabricated scaffolds clearly deviated from the original designs. The scaffolds had shrunk by approximately 6–11% in the x-direction and by approximately 20–24% in the z-direction. This decrease in the overall scaffold heights translated to an approximately 45–54% decrease in the vertical opening height (d_{90}) when compared to the original designs. Despite this change in the vertical opening sizes, the interconnectivity ranking of the scaffolds did not change. The fabricated type III and type V scaffolds were still the most interconnected in both xy- and xz-directions. The porosities of the fabricated type I, II, III and V scaffolds were calculated as approximately 85%, 80%, 82% and 85% respectively. The achieved porosities thus differed from the designed values by 4–13%.

5.1.5 Culturing of adipose stem cells

The hASC-seeded type V Ormocomp® scaffolds were studied with light microscopy, fluorescence imaging and SEM imaging in order to qualitatively evaluate cell attachment, viability and orientation. Figure 24 shows bright field microscopy images of a scaffold at different time points.

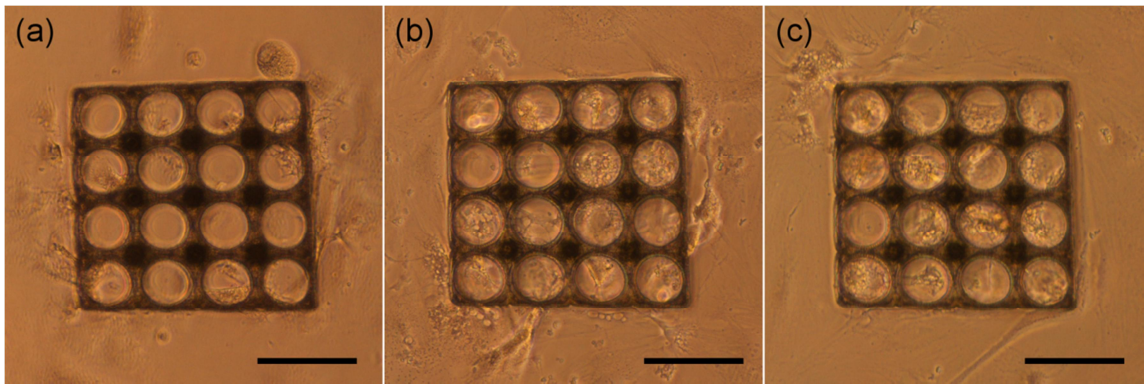

Figure 24. Bright field micrographs of a type V Ormocomp® scaffold after (a) 4 h, (b) 2 d and (c) 6 d of culture with adipose stem cells. Scale bars represent 100 µm.

Most cells were outside the scaffolds right after seeding but tended to migrate inside the scaffolds during the 6 day culture. Due to the migration as well as proliferation, the scaffolds were almost full of cells after day 6. Live/dead stained samples are shown in Figure 25 at different time points.

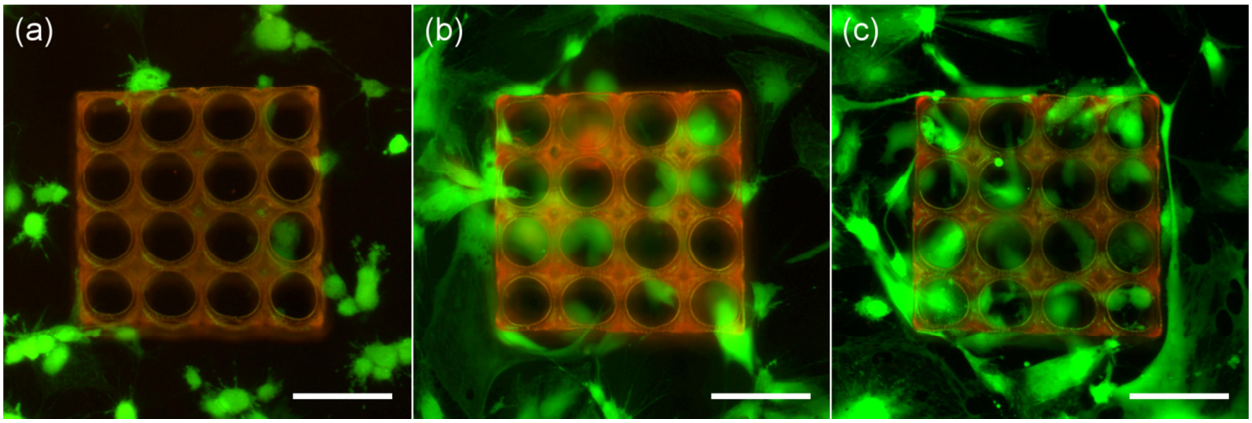

Figure 25. Fluorescence micrographs of type V Ormocomp® scaffolds after (a) 4 h, (b) 2 d and (c) 6 d of culture with adipose stem cells. Live cells are stained green and dead cells red. The scaffold fluorescence is due to nonspecific binding of the red dye. Scale bars represent 100 µm.

The majority of the cells remained viable inside the scaffolds during the culture period. Only a few individual dead cells were seen in samples after 2 days and 6 days of culture and the number of dead cells did not increase between these two time points. As shown in Figure 25(a), the cell morphology was still round after 4 h and the cells had not yet fully attached to the glass surface or the scaffolds. After 2 days (Figure 25(b)), the cells exhibited a spread out morphology and were attached to both the scaffold and the surrounding glass surface. By day 6 (Figure 25(c)), the number of cells inside the scaffolds had increased and the cells had extended processes through the scaffold structure. The live/dead stained samples were also SEM imaged, as shown by Figure 26.

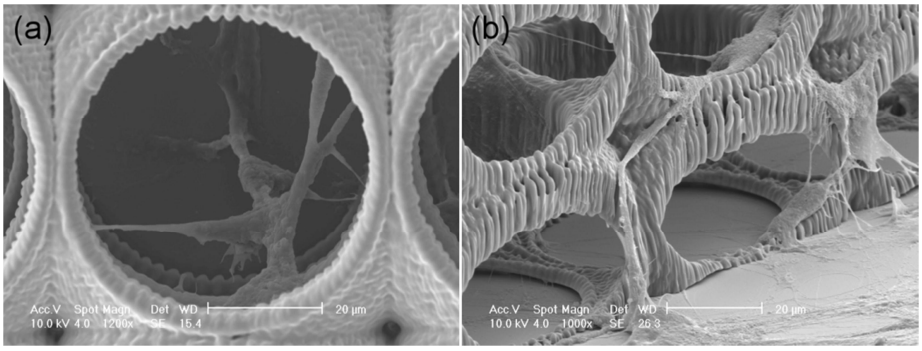

Figure 26. SEM images of type V Ormocomp® scaffolds with adipose stem cells after a 6 day culture. (a) Top view image (0° tilt) of a single cell extending from the glass surface to the upper layers of the scaffold. (b) A side- view image (70° tilt) showing multiple cells attached to the scaffold walls and forming 3D connections through the pores. Scale bars represent 20 µm.

By day 6, the cells were seen to reside three dimensionally inside the scaffolds with connections to both the glass surface and the different scaffold layers (Figure 26(a)). The cells had extended

processes not only along the scaffold walls but also through the open pore space (Figure 26(b)). Processes extending even two to four pores were seen (data not shown).

The 3D orientation of the cells inside the scaffolds was studied further by confocal imaging, as shown in Figure 27.

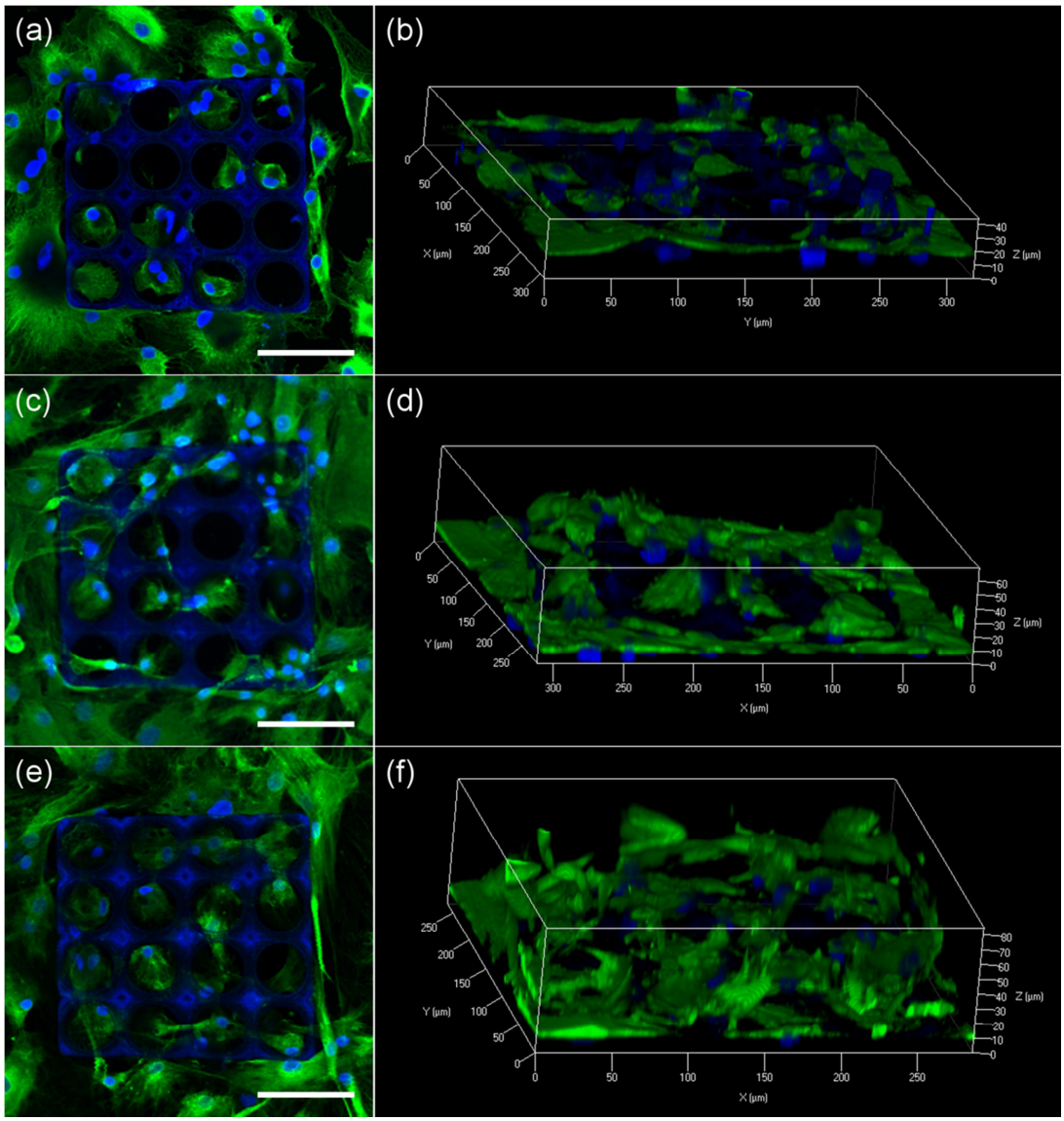

Figure 27. Top views (left column) and 3D reconstructions (right column) of confocal image stacks of type V Ormocomp® scaffolds after (a-b) 4 h, (c-d) 2 d and (e-f) 6 d culture with adipose stem cells. The actin cytoskeleton is stained green and the cell nuclei blue. The scaffolds appear blue in the left column due to autofluorescence. Scale bars represent 100 µm.

The autofluorescence signal of the scaffolds overlapped to some degree with the blue fluorescence signal of the stained cell nuclei, which could, however, be distinguished despite the background fluorescence. The confocal images showed that the cells formed complicated networks through the interconnected pores. Indications of cell divisions were also seen (data not

shown). Based on the 3D reconstructions in Figure 27, the cells were mostly planar after 4 h and were attached to the glass surface or only to the first unit cell layer (z = 40–60 μm). After 2 days, the cells had made connections also to the second unit cell layer (z = 60–90 μm) mainly by growing upward along the outer walls of the scaffolds. Finally, after 6 days, the scaffolds were nearly full of cells extending through the full height of the scaffolds (z = 80–90 μm).

5.2 Hydrogel studies

The measured degrees of modification, molecular weight averages and dispersities of the PHEGs used in this work are summarized in Table 4.

Table 4. Properties of the methacryloylated and acryloylated PHEGs.

Sample Code	Degree of modification (mol %, A – acryloylation, MA – methacryloylation)	Molecular Weight $\overline{M}_w$ [a)]	Dispersity Đ	Total yield to PHEG[b)]	Yield of modification
PHEG-A13	12.9 (A)	92000	7.16	45%	63%
PHEG-A9	9.4 (A)	92000	6.12	45%	73%
PHEG-MA21	20.7 (MA)	20900	1.61	45%	71%
PHEG-MA11	11.2 (MA)	21500	3.00	45%	77%

[a)]Based on poly(ethylene oxide) calibration standards

[b)]Yield from γ-benzyl-L-glutamate to PHEG

The PHEG macromonomers are soluble linear polymers. During 2PP-DLW processing, these linear polymers are covalently crosslinked into a 3D network through radical polymerization of the methacryloyl or acryloyl groups in the side chains. The structure and physical characteristics of the insoluble gel networks are expected to be analogous to that described previously in [249, 254]. The only difference in the gels presented in this work is the use of a PI to enable the 2PP-DLW process.

5.2.1 Polymerization and damage thresholds

Both the P_{th} and the P_D power values of the PHEGs and PEGdas increased with scanning speed, as shown by Figure 28 and 29.

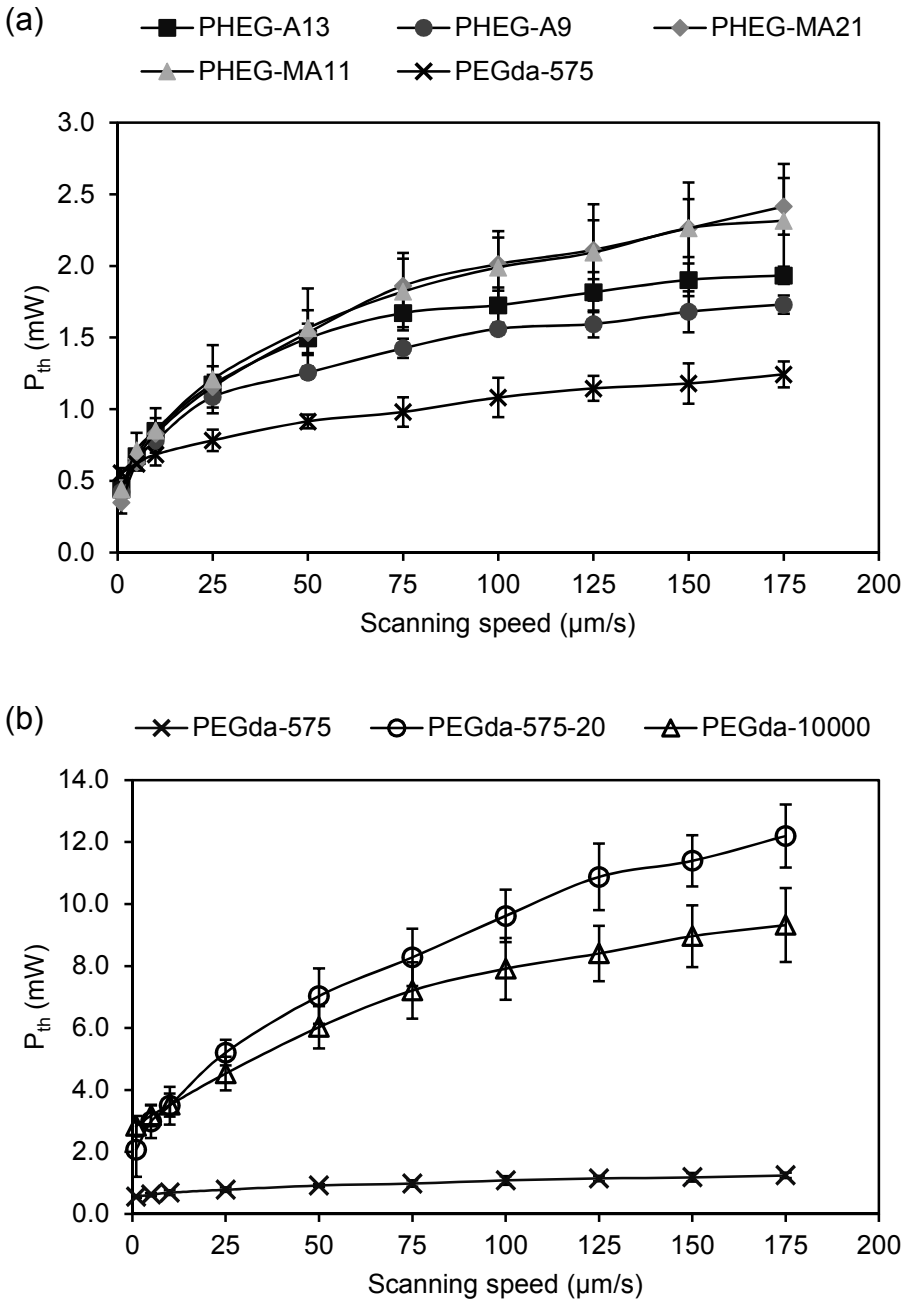

Figure 28. Polymerization threshold powers (P_{th}) of the different (a) PHEGs and (b) PEGdas as functions of scanning speed. The results for PEGda-575 are presented with both the PHEGs and PEGda for easier comparison. The data points represent the mean ± standard deviation (n = 3). Solids lines are guides to the eye.

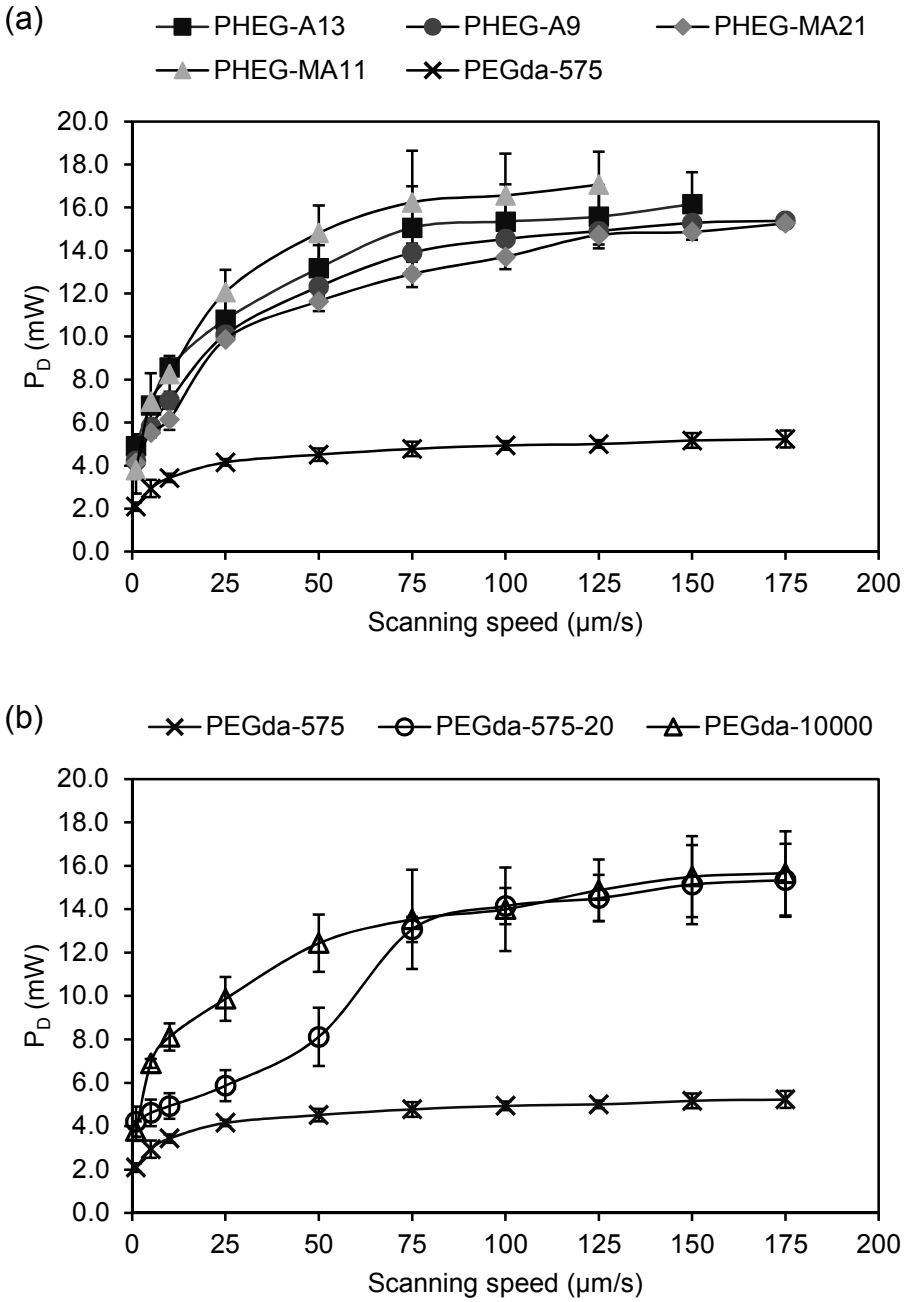

Figure 29. Damage threshold powers (P_D) of the different (a) PHEGs and (b) PEGdas as functions of scanning speed. The results for PEGda-575 are presented with both the PHEGs and PEGda for easier comparison. The data points represent the mean ± standard deviation (n = 3). Solids lines are guides to the eye.

All the PHEGs had very similar thresholds values. The PEGdas, however, had different threshold values depending on the composition of the photopolymer solution. The pure PEGda-575 solution had the lowest P_{th} and P_D that were also the least sensitive to scanning speed. The water-based PEGda-575-20 and PEGda-10000 solutions had approximately 7 times higher P_{th}

values than the pure PEGda-575 and 4–6 times higher P_{th} values than the PHEGs. The P_D values of PEGda-575-20, PEGda-10000 and the PHEGs were similar and approximately three times higher than the values of pure PEGda-575. Compared to pure PEGda-575, the PHEGs had approximately 1.5 times higher P_{th} values, which implies that the PEGda-575-I2959 combination had a slightly better 2PA sensitivity than the PHEG-I2959 combinations.

As shown by Figure 30, all the PHEGs had similar dynamic power range values of 7.8-9.4 with no statistically significant differences ($p > 0.05$).

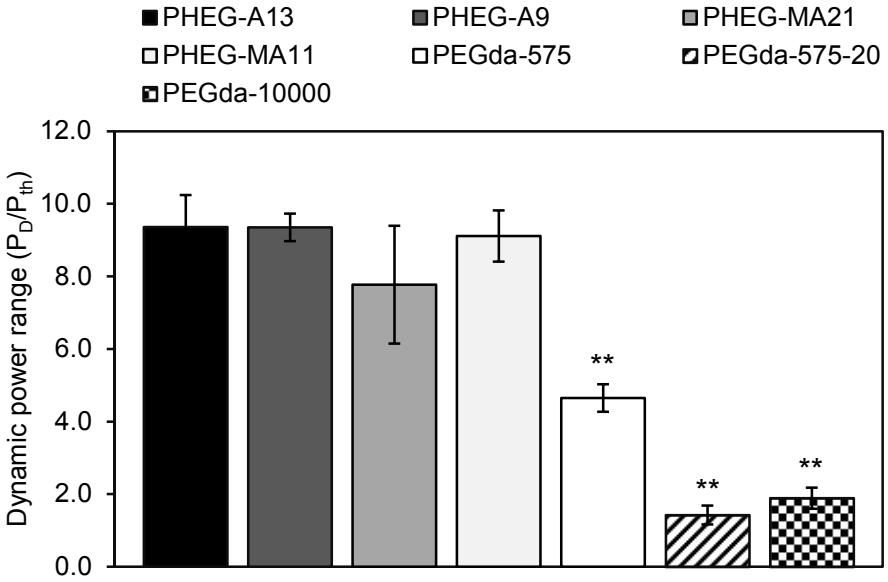

Figure 30. The calculated dynamic power ranges (P_D/P_{th}) of the different PHEGs and PEGdas. The data points represent mean ± standard deviation (n = 8–10).**($p < 0.01$) indicates significance.

The PEGdas, on the other hand, had significantly narrower dynamic power ranges than the PHEGs ($p < 0.01$). Due to the higher P_D, the PHEGs had approximately twice wider dynamic power ranges than pure PEGda-575. Among the PEGdas, PEGda-575 had a significantly wider dynamic power range of 4.6 than the water-based PEGdas ($p < 0.01$). With the very narrow dynamic power ranges of 1.4 and 1.9, the PEGda-575-20 and PEGda-10000 solutions with equal water content to the PHEGs had only limited 2PP-DLW applicability.

5.2.2 Voxel fabrication

Figure 31 shows the measured width and height of whole PHEG and PEGda-575 voxels as functions of exposure time and the curves based on Equation (12)-(15). The values of the estimated model parameters are shown in Table 5.

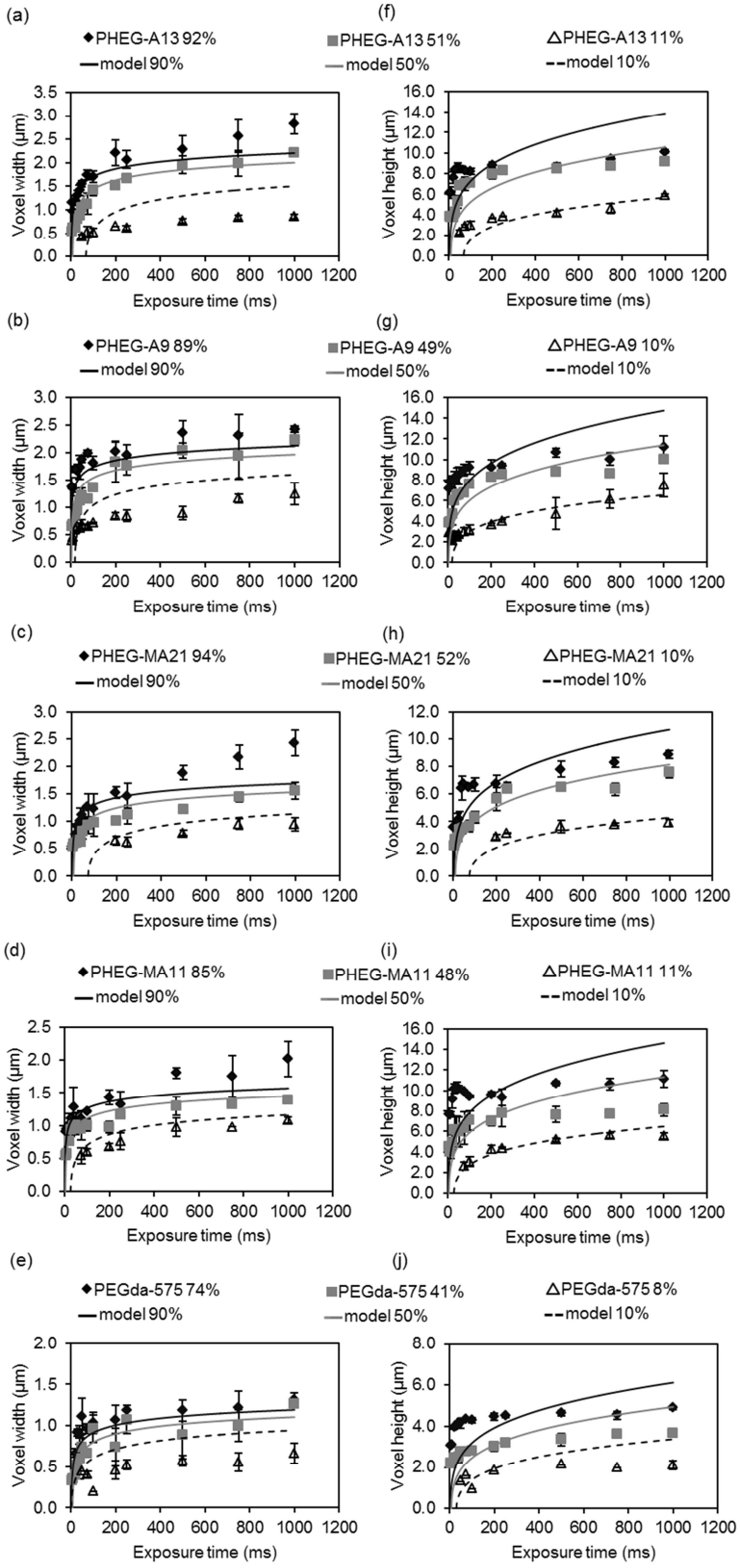

Figure 31. (a-e) Width and (f-j) height of PHEG and PEGda-575 voxels as functions of exposure time for approximately 10%, 50% and 90% laser powers. The data points represent the mean ± standard deviation (n = 3), except for PEGda-575 8%, for which n =1-3. The curves represent the estimated theoretical voxel width and height based on Equation (12)-(15).

Table 5. Estimated values of the parameters ρ_{th}, σ_2, r_0 and z_R according to Equation (12)-(15) for the width and height of PHEG and PEGda-575 voxels.

Estimated parameters	PHEG-A13	PHEG-A9	PHEG-MA21	PHEG-MA11	PEGda-575
ρ_{th}	0.26	0.22	0.22	0.23	0.21
σ_2 (cm^{4}s/photon)	8.8×10^{-52}	2.1×10^{-51}	3.4×10^{-52}	3.7×10^{-52}	3.7×10^{-52}
r_0 (nm)	917	801	704	612	504
z_R (nm)	1684	1298	1305	1435	781

Voxel fabrication with the high water content PEGda-575-20 and PEGda-10000 was also tested but only a few, distorted voxels could be produced, which were not sufficient for further analysis (data not shown). The PHEG and PEGda-575 voxels fabricated with long exposure times and high powers had elongated and occasionally fragmented shapes, which deviated from the ideal ellipsoidal shape of 2PP-DLW voxels described earlier in [130]. These fringed voxel shapes could be explained by the simultaneous recording of zeroth- and higher-order diffraction patterns, as described by Sun et al. [60]. Nevertheless, close to ellipsoidal voxels were achieved with all the materials with short exposure times and 10% laser powers (data not shown).

The minimum achieved voxel sizes (width/height) were 430 nm/2.3 μm for PHEG-A13, 390 nm/2.9 μm for PHEG-A9, 510 nm/2.1 μm for PHEG-MA21, 540 nm/2.6 μm for PHEG-MA11 and 330 nm/2.2 μm for PEGda-575. The minimum voxel sizes for all the materials were approximately 1.4–2.2 times smaller than the diffraction-limited laser spot, which is a strong indication that the polymerization was indeed based on 2PA. The size of the diffraction-limited spot was estimated as 2r = 720 nm and 2z = 4.0 μm based on Equation (8) and (9) respectively.

The measured voxel width and height were in agreement with the analytical model, especially with 10% laser power and short exposure times of 5–250 ms. However, the estimated values for r_0 were approximately 1.7–2.5 times higher for the PHEGs and 1.4 times higher for PEGda-575 than the calculated lateral radius of the diffraction-limited laser spot (r = 360 nm). The estimated values for the effective 2PA cross-section, σ_2, for the PHEGs and PEGda-575 were in the order of 10^{-52}-10^{-51} cm^{4}s/photon. By assuming a quantum efficiency of 0.3 [255], the σ of I2959 is estimated to be in the order of 10^{-53}–10^{-52} cm^{4}s/photon, in other words 0.001–0.01 GM.

5.2.3 Fabrication of grid structures

Stable support structures could not be fabricated using the high water content PEGda-575-20 and PEGda-10000 (data not shown). Figure 32 shows examples of SEM images of PHEG and PEGda lines fabricated on rectangular support structures.

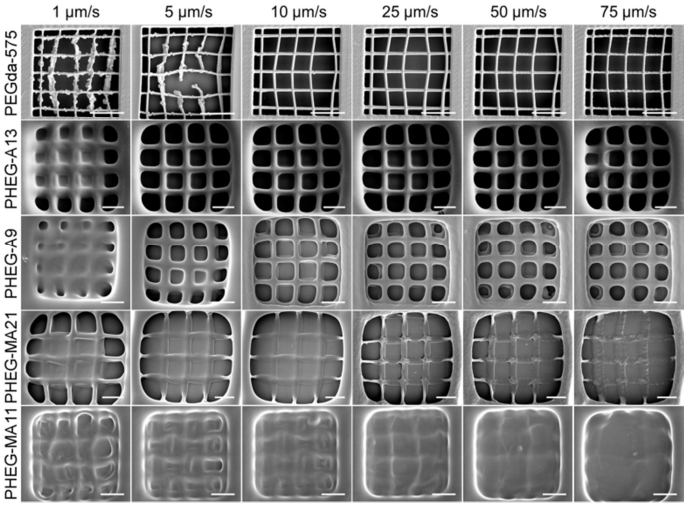

Figure 32. SEM images of PHEGs and PEGda-575 lines fabricated with 75% laser powers and 1–75 µm/s scanning speeds. Scale bars represent 10 µm.

The polymerized PHEG-A lines were substantially thicker and more rigid than the PHEG-MA and PEGda-575 lines. PHEG-MA lines were easily distorted during the development process. The PHEG-MA11 with the lowest degree of methacyloylation performed the worst and the widths of these lines could not be measured due to severe distortion. Although the PEGda-575 lines were mostly stable, with the low scanning speeds of 1–5 µm/s they were severely distorted with all the laser powers tested.

Figure 33 shows the measured widths of the PHEG-A, PHEG-MA21 and PEGda-575 lines.

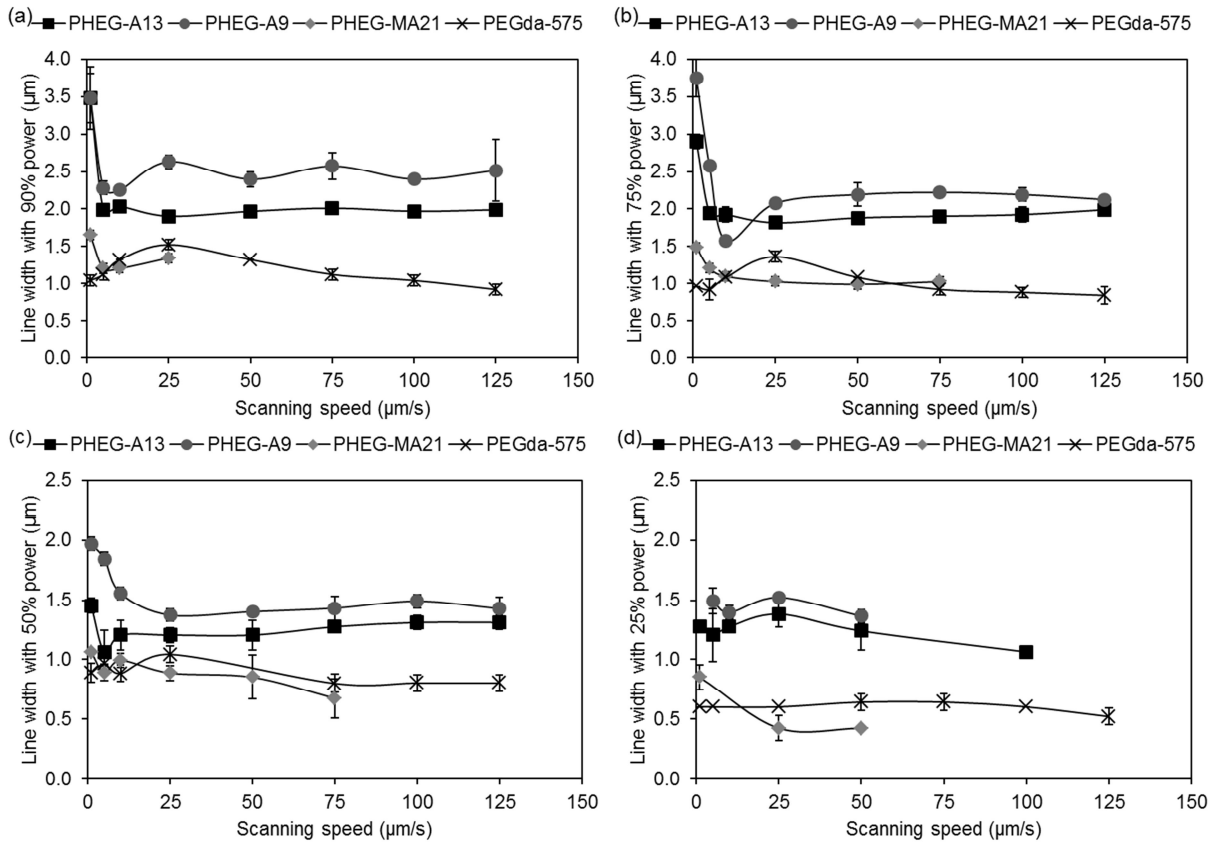

Figure 33. The measured widths of PHEG-As, PHEG-MA21 and PEGda-575 lines as functions of scanning speed for approximately (a) 90%, (b) 75%, (c) 50% and (d) 25% laser powers. The data points represent mean ± standard deviation (n = 3). Solids lines are guides to the eye.

Nearly constant line widths were achieved with the PHEG-As and PEGda-575 with scanning speeds higher than 25 µm/s by simultaneously controlling the laser power and scanning speed. As shown by Figure 33(a-c), the PHEG-As and PEGda-575 polymerized into measurable lines even with the highest tested scanning speed of 125 µm/s. In contrast, only barely measurable lines were produced of PHEG-MA21 with the scanning speed of 75 µm/s.

5.2.4 Swelling and deformation

Figure 34 shows examples of confocal and SEM images of the rectangular walls and the volumetric swelling ratios calculated according to Equation (16).

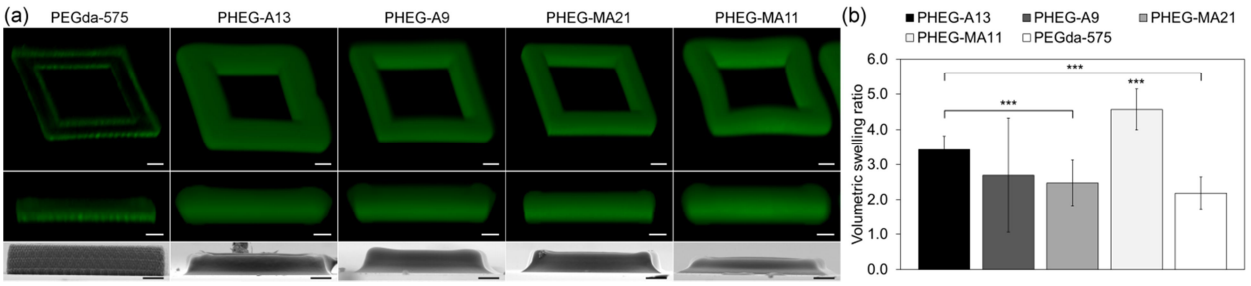

Figure 34. (a) Oblique view (top row) and side view (middle row) 3D reconstructions of confocal image stacks and side view SEM images (bottom row) of rectangular walls. The walls consisted of 8 contours in the xy-direction and 11 contours in the z-direction. Scale bars represent 10 μm. (b) Volumetric swelling ratios. The data points represent mean ± standard deviation (n = 36 for PHEG-A13, n = 35 for PHEG-A9, n = 27 for PHEG-MA21 and PHEG-MA11, n = 30 for PEGda-575). *** ($p < 0.001$) indicates significance.

As shown by the oblique view confocal images in Figure 34(a), the PHEG walls strongly absorbed the FITC dye and were uniformly fluorescent. However with PEGda-575, the dye was bound only to the surface of the microstructures and was not absorbed by the bulk material. As shown by Figure 34(b), PHEG-MA11 had a significantly higher swelling ratio than PHEG-MA21 ($p < 0.001$), PHEG-A13 ($p < 0.001$), PHEG-A9 ($p < 0.05$) and PEGda-575 ($p < 0.001$). Also, PHEG-A13 had a significantly higher swelling ratio than PHEGMA21 and PEGda-575 ($p < 0.001$).

In addition to swelling, the deformation of the hydrogel walls due to the development process was studied. The xy-deformation % of the PHEG and PEGda-575 walls calculated according to Equation (17) are shown in Figure 35 as functions of the average swollen wall width and height.

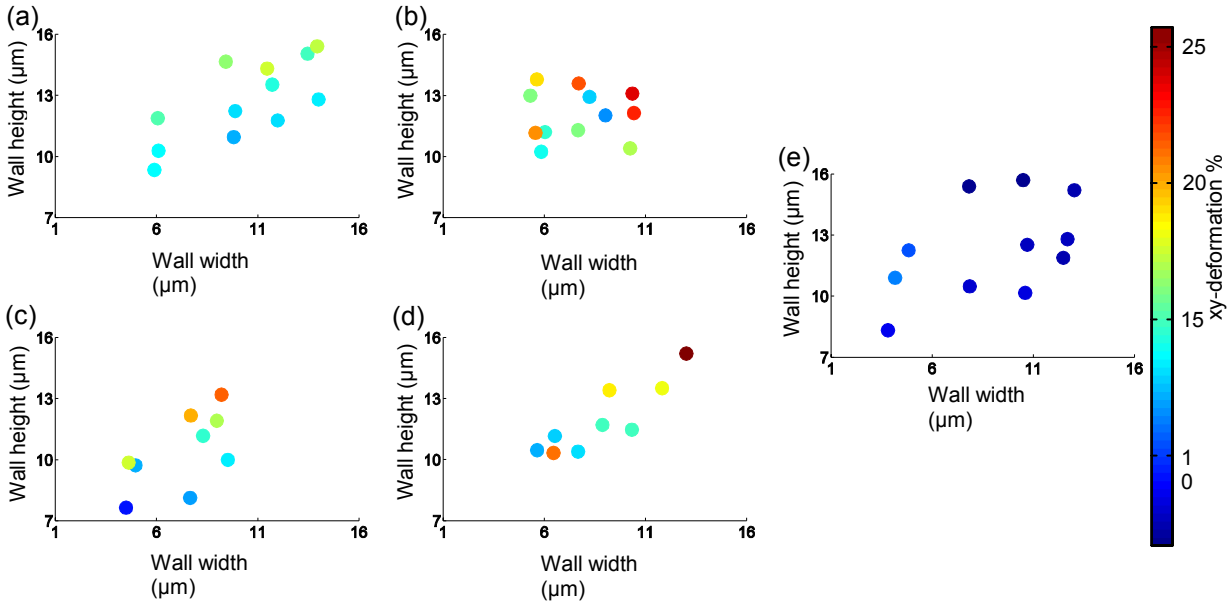

Figure 35. The calculated xy-deformation % (colorbar) of (a) PHEG-A13, (b) PHEG-A9, (c) PHEG-MA21, (d) PHEG-MA11 and (e) PEGda-575 walls as functions of the average swollen wall width and height. The data points represent mean (n = 2–3).

The PEGda-575 walls exhibited the lowest overall deformation of approximately 6–11%. Among the PHEGs, the PHEG-A13 performed the best with the deformation of approximately 12–18%. The deformation of the PHEG microstructures increased notably with both wall width and height, as shown by Figure 35(a-d). Contrary to the PHEGs, the deformation of PEGda-575 walls was seemingly not influenced by the dimensional changes.

The fabrication of the grid and wall structures also enabled evaluation of microstructure adhesion to the glass surface. Adhesion of the PEGda-575 structures was found inferior compared to the PHEGs. Of all the PEGda-575 grid and wall structures, 13% were detached partly or completely during the development process despite the adhesion promoting MAPTMS-treatment on the glass surface. In contrast, none of the PHEG microstructures were detached during fabrication.

6 Discussion

6.1 Processing of Ormocomp®

In 2PP-DLW research so far, the main focus has been to establish the relationships between the various processing parameters and fabrication accuracy. In this work, the effect of different parameters on the size of Ormocomp® voxels and lines was studied Publications I-II with two different 2PP-DLW systems. In Publication I, processing of Ormocomp® using a Nd:YAG ps laser with 532 nm wavelength and kHz repetition rate was demonstrated for the first time. This type of laser is more affordable than the Titanium:Sapphire fs laser that has been typically used for 2PP-DLW. During the time of Publication I, only a handful studies using a 532 nm, low repetition rate (< 20 kHz) Nd:YAG ps laser had been published reporting the processing of acrylate-based photoresins [37, 256] and proteins [38, 257]. The processing of Ormocomp® had been reported by multiple groups, including Chichkov et al. using a MHz repetition rate Titanium:Sapphire fs laser at 780 nm [89, 196, 222] and Fotakis et al. using a MHz repetition rate Yb fs laser at 1028 nm [258-260]. A similar Yb laser system at 515 nm had also been used for Ormocomp® processing by Jariwala et al. [39, 261].

In Publication I, the minimum size (width/height) of a whole Ormocomp® voxel was 2.3 µm/7.1 µm (2 × 3.55 µm). This size was considerably larger than the voxel size of 490 nm/2.3 µm reported by Woggon et al. for a fs laser system [194]. Several factors likely contributed to this outcome. Firstly, a lower NA (0.90 versus 1.4) is known to produce larger, elongated voxels [60]. Secondly, the voxels were fabricated using a laser power of 1.2 mW that was two orders of magnitude higher than the measured polymerization threshold of 55 µW. Thus, it is likely that by tuning of the laser power smaller voxels could have been fabricated.

Based on the results of Publication I, the feature size of Ormocomp® was restricted to the micrometer scale with the first generation Nd:YAG ps laser system. The accuracy of this system was sufficient for the fabrication of simple 3D structures in the form of cones aimed at microneedle applications. Due to the large voxel height, contour spacing of several microns could be used for efficient fabrication of cone arrays with the scanning speed of 200 µm/s. Compared to the sophisticated Ormocomp® microneedles reported by Chichkov et al. [89, 222, 226], the solid cones fabricated in this work represent the simplest possible approach. Nonetheless, with the height of approximately 120 µm, these type of Ormocomp® cones could be sufficient to penetrate the 10-15 µm thick *stratum corneum* layer of the skin [262] and thus be suitable for microneedle applications. The cell test in Publication I also showed the potential of the Ormocomp®-I127 combination as a non-cytotoxic substrate for neuronal cell culturing.

Ormocomp® microstructures fabricated by 2PP-DLW have since been successfully used for the growth guidance of hESc derived neuronal cells [229].

With the second generation ps laser system in Publication II, the minimum achieved size of Ormocomp® voxels was 210 nm/1.95 μm. With the same objective and NA as in Publication I, the considerable reduction in voxel size was most likely due to lower laser power (0.6 mW) and accurate tuning of exposure time. The greater expansion of the laser beam also allowed only the central portion of the beam to pass through the objective, which likely reduced voxel size further. The reduced voxel size also enabled the fabrication of suspended Ormocomp® structures, which was not feasible with the first generation system. The observed 23% decrease in the wall height of the suspended structures was likely due to material shrinkage.

In addition to reduced voxel size, the second generation system with the mirror scanner enabled more accurate fabrication of lines in Publication II compared to the xyz-stage in Publication I. In both studies, a roughly linear relationship was observed between line size and average laser power as well as voxel size and power in Publication I. According to a simple threshold model derived for a Gaussian intensity profile, the relationship between line dimensions and laser power (or intensity) should, in fact, be nonlinear [55, 117]. However, these findings do not necessarily conflict, as it has been shown that larger line widths can deviate from this model with common Irgacure® PIs, possibly due to deviations from the ideal Gaussian intensity profile [55]. As the line widths measured in this work are in the micrometer rather than nanometer scale, it is plausible that the data does not extend to small enough line widths, with which the nonlinear scaling would hold.

In Publication II, the processing window and damage zone were also defined for Ormocomp® for the first time with respect to laser power and scanning speed of 50 μm/s. When smallest achievable feature size is desired, fabrication should be carried out close to the polymerization threshold. In larger-scale 3D fabrication, however, moving to a higher power range within the processing window is beneficial as it allows higher scanning speeds and reduced fabrication times. The damage zone was characterized by microbubble formation with an onset intensity in the order of 0.1 TW/cm^2. By studying the processing of SZ2080, Malinauskas et al. have attributed the damage by micro-explosions to dielectric breakdown, with an intensity threshold in the order of 10 TW/cm^2 [102]. As the value for Ormocomp® in this study was an order of magnitude smaller, it seems unlikely that dielectric breakdown could have contributed to the material damage. The observed micro-explosions could be explained by heat accumulation, as suggested by Fischer et al [55]. However, due to different materials and PIs,

direct comparison cannot be made and an ionization-based damage mechanism cannot be entirely excluded.

With regard to scanning speed, a similar line dimension scaling was found both in Publication I and II. After first decreasing rapidly, the line dimensions remained nearly constant at scanning speeds higher than 200 μm/s. With the first generation system, uniform Ormocomp® were produced even with the scanning speed of 500 μm/s, whereas with the second generation system, line fragmentation occurred at 400 μm/s. However, only relatively low laser powers were tested in Publication II. It is likely that with higher powers, continuous lines could have been produced even with scanning speeds of 500 μm/s and higher. Thus, the maximum power-scanning speed combination applicable for the 2PP-DLW of Ormocomp® with I127 was not defined in this work, but other studies have shown that processing Ormocomp® with mm/s speeds is feasible, at least with fs laser systems [90].

The accuracy of AFM and SEM image-based measurements of microstructure dimensions was compared in Publication II. Despite the manual nature of the SEM-image based approach, it was found more accurate for measuring line widths than AFM imaging. Corroborating findings have recently been reported by Wollhofen et al. [44]. The inaccuracy of the AFM measurements is due to restricted movement of the AFM tip along steep edges. SEM image-based measurements are thus more appropriate for determining the dimensions of 2PP-DLW structures, despite the required conductive coating.

6.2 Ormocomp® scaffolds with adipose stem cells

As shown in Publication II, the fabrication of suspended, open Ormocomp® structures was enabled by the second generation ps laser system. In Publication III, this ability was used for the fabrication porous scaffolds for adipose stem cell culturing. The scaffold design was based on hollow sphere unit cells that enabled the generation of highly porous structures with tunable porosity and interconnectivity values. The quality of the fabricated scaffolds was affected by the choice of the microscope objective, which was in accordance with the previous reports of larger voxels produced by objectives with a smaller NA [60]. The larger voxels produced by the 20× (NA = 0.75) objective enabled the use of a doubled scanning speed compared to the 50× (NA = 0.90) objective without loss of scaffold integrity. Another approach for achieving higher writing speeds and larger scaffold structures in the future could be to use custom synthesized materials and high throughput PIs optimized for 2PP-DLW [169, 170, 263].

The accuracy of scaffold fabrication by 2PP-DLW with respect to design parameters was studied in Publication III for the first time. Porosity values of scaffolds fabricated by 2PP-DLW

have seldom been reported in the literature, although accurately defined scaffold geometry is essential when studying cell response. A porosity value of 90% has been reported by Ovsianikov et al. [223] and values ranging from 40% to 67% by Danilevicius et al. [129, 264]. The methods of obtaining any of these values were not specified. In this work, we could fabricate scaffolds with a maximum porosity of 85%. It was found that both material shrinkage and thicker scaffold walls contributed to deviations from the original scaffold designs. The nonuniform shrinkage of the scaffolds was in accordance with the previously described shrinkage behavior of 2PP-DLW microstructures described in Subsection 2.4.3. The measured lateral shrinkage, approximately 6–11%, was in accordance with the previously reported values of 5–20% for Ormocomp® [145]. The measured vertical shrinkage of 20–24% corresponded to the shrinkage of Ormocomp® observed in Publication II.

From the fabricated small scale scaffolds, the least porous and least interconnected type I scaffold corresponded best to the model. The more porous and open architectures of the type II, III and V scaffolds likely made them more susceptible to shrinkage. As scaffold wall thickness cannot be significantly decreased without compromising structural integrity, the scaffold fabrication process could be improved by compensating for the lateral and vertical shrinkage. Based on the measured shrinkages, this could be realized by introducing a compensation factor to the scaffold models. This method has been previously applied to the fabrication of photonic crystals [145, 149]. By introducing shrinkage correction, it is likely that Ormocomp® scaffolds with over 90% porosity could be fabricated by 2PP-DLW using the spherical unit cell design.

The feasibility of the fabricated Ormocomp® scaffolds as 3D cell culturing platforms was demonstrated by culturing the largest type V scaffolds with hASCs for 6 days. Human ASCs are an attractive and abundant cell source for tissue engineering applications. They can be easily retrieved in high numbers from either liposuction aspirates or subcutaneous adipose tissue fragments and can be readily expanded in vitro. The multipotent cells can undergo at least adipogenic, osteogenic and chondrogenic differentiation in vitro [265]. The culturing of hASCs with 2PP-DLW fabricated scaffolds has previously been reported by Ovsianikov et al. [241]. They showed that methacrylamide-modified gelatin scaffolds with an interconnected, cubic lattice structure supported hASC adhesion, proliferation and differentiation into the adipogenic lineage. However, the porosity and interconnectivity values of these scaffolds were not quantified. Also, the 3D orientation of the cells with respect to scaffold struts and pores was not studied. 2PP-DLW fabricated SZ2080 niches of different pore size have recently been reported by Raimondi et al. for the culturing of porcine mesenchymal stem cells. [242]. They, too, did not specify the achieved accuracy of scaffold fabrication with respect to CAD models. In this work,

hASCs were cultured for the first time with Ormocomp® scaffolds of defined shape, porosity and interconnectivity. Due to the manual static cell seeding, there was some random variation in the initial number of cells in and around the scaffolds in different samples. However, by day 6 all the scaffolds were nearly full of viable cells as a result of both cell migration and proliferation. Due to vertical shrinkage, pore interconnectivity of the type V scaffolds was 30% more restricted from the xz-direction than from the xy-direction. Despite this deviation from the original scaffold design, the cells readily formed connections both along the scaffold walls and through the pore space. This suggests that the three-dimensionally interconnected pore structure promoted hASC attachment and growth.

6.3 Hydrogel processing

In order to realize the full potential of biomimetic microstructures, it is essential to expand the selection of synthetic, degradable hydrogels applicable for 2PP-DLW. In Publication IV, the 2PP-DLW of synthetic poly(AA) hydrogels was studied for the first time. Due to a polypeptide backbone, poly(AA) hydrogels are cleavable in a biological environment by enzyme-catalyzed hydrolysis. The rate and enzyme specificity of the degradation can be controlled through copolymerization. [254, 266, 267] Hydrogels based on synthetic poly(AA)s can be combined with cell adhesion peptides and have been previously shown suitable for culturing porcine mesenchymal stem cells [268]. In this work, the 2PP-DLW performance of poly(AA)s based on methacryloylated and acryloylated PHEGs was compared to commercial PEGda hydrogels.

The PHEGs and PEGdas were first compared in terms of polymerization and damage thresholds, which were defined as the laser powers with which polymerization or bubbling of the materials could be observed. A similar definition for the threshold values has been previously used by Baldacchini et al. [56]. It has been a common practice in 2PP-DLW literature to report threshold values determined for only a few scanning speeds [56, 57, 59, 269, 270] In contrast, the threshold values in this study were determined over a wide range of scanning speeds in order to obtain more reliable results. Moreover, the 10–90% power values of the polymerization window were used for processing for each material instead arbitrary powers. This approach enabled a systematic comparison of the 2PP-DLW performance despite differences in the absolute threshold values. The PHEGs were found to have significantly wider dynamic power ranges than the PEGdas. A larger dynamic power range is beneficial in 3D microfabrication as it enables tuning of microstructure size in a wider range [61].

The measured dimensions of PHEG and PEGda-575 voxels were compared to an analytical model develop by Serbin et al. [250]. The differences between the measurements and

the model could be explained by the simplicity of the model, which does not account for spherical aberration nor the effects of radical diffusion, temperature or polymerization kinetics described in [271]. Spherical aberration is caused by a refractive index mismatch between the immersion oil and the water-based hydrogel materials. It has been shown to affect the size and shape of 2PP-DLW microstructures due to the distortion the laser intensity PSF [272]. In this work, the laser beam was focused through the entire width of the sample (≈ 150 μm), which further increases the effect of spherical aberration [273].

The PI I2959 used in this study is widely used in the 1PA-based photopolymerization of hydrogels [5]. As well as having an absorption peak close to half the laser wavelength used in this work, I2959 is moderately soluble in water and has been reported cytocompatible with many cell types [178]. However, the 2PA cross-section of I2959 has not been reported. The value of 0.001-0.01 GM estimated in this study is in agreement with the low σ values that have been previously reported for other commercial photoresins [185] and photoinitiators [250]. It is likely that the use of a more efficient PI would enable higher scanning speeds than the maximum of 125 μm/s reported in this study with I2959. With highly efficient water-soluble PIs, Li et al. recently reported scanning speeds as high as 100 mm/s [174].

3D fabrication of performance of the PHEGs and PEGdas was studied by fabricating grid and wall structures. Likely due to the very narrow dynamic power ranges, stable 3D structures could not be fabricated of the PEGda-575-20 and PEGda-10000 solutions with equal water content to the PHEGs. Similar results have been recently reported by Torgersen et al. who found that PEGda structures fabricated with 80% water content and a custom PI were prone to deformation due to insufficient crosslinking [224]. The pure PEGda-575 generally performed well but suffered from severe distortions at low scanning speeds. This drawback was likely due to the low viscosity of the PEGda-575 solution and the motion of the liquid disturbing the polymerization process.

Based on the number of parameter combinations that could produce measurable lines, the PHEG-As and PEGda-575 had much wider processing ranges than PHEG-MA21. This indicates a more efficient 2PP-DLW process, which is consistent with previously published findings of higher 2PP-DLW reactivity of acrylated macromers compared to methacrylated analogues [62]. By simultaneously controlling both laser power and scanning speed, nearly constant line widths were achieved with the PHEG-As and PEGda-575. This approach could in the future be used for fabricating microstructures with variable crosslinking density and yet identical dimensions.

The swelling and deformation behavior of the PHEGs and PEGda-575 were studied by fabricating rectangular walls of different dimensions. Volumetric swelling ratio is known to be

directly related to the mesh size of hydrogel networks, which governs diffusive properties and relates to crosslinking density and mechanical strength [201, 274]. The low swelling ratio of the small molecular weight PEGda-575 indicates that highly crosslinked structures are formed by 2PP-DLW. The PEGda-575 walls also did not absorb the FITC dye, which is consistent with highly crosslinked networks of small mesh size. Among the PHEGs, PHEG-MA21 with the highest degree of modification had the lowest swelling ratio and PHEG-MA11 the highest. This is consistent with the observed distortion of PHEG-MA11 microstructures, which was likely caused by limited crosslinking density due to the low degree of methacryloylation. In addition to the degree of modification, the higher swelling ratios of the PHEG-As compared to the PHEG-MA21 could be explained by the over three times higher molecular weights as swelling is known to correlate with molecular weight [275]. It should be noted that the swelling values were based on samples produced with the 90% laser powers and thus represent close to minimal swelling. With lower laser powers, it is likely that swelling ratios would be higher due to a lower degree of crosslinking.

The open geometry of the rectangular walls was designed to mimic porosity, which is an essential requirement for tissue engineering scaffolds. However, porous structures are especially prone to deformation by capillary forces during development [143]. In this study, the water-based PHEG walls deformed more than the pure PEGda-575 walls. The deformation of PHEG walls also increased notably with both wall width and height whereas the deformation of PEGda-575 walls was largely independent of wall dimensions. This difference was most likely due to higher crosslinking, which made the PEGda-575 structures more resistant to deformation. To improve the reliability of the fabrication process, the deformation of PHEG microstructures could be reduced by numerical compensation of the CAD models or by introducing additional crosslinking agents, such as PETA used by Klein et al. [195].

Despite the higher degree of deformation, the high water content of the PHEGs can be beneficial as it facilitates incorporation of cells into the 2PP-DLW process [217]. The pulse energies corresponding to the 90% laser powers used for the fabrication of the PHEG walls were 0.3 nJ, which is well below a reported 1–2 nJ threshold for inducing intracellular ablation [276]. In the future, the PHEGs could be tested for the fabrication of biomimetic, cell-laden microstructures for soft tissue engineering applications.

7 Conclusions and outlook

In the first part of the thesis, the 2PP-DLW processing of Ormocomp® was studied using custom ps laser systems. Based on the findings of Publications I-II, the following are concluded:

- An affordable, low frequency ps laser is suitable for the fabrication of 3D Ormocomp® microstructures by 2PP-DLW.
- Submicron Ormocomp® features are achievable with a ps laser system.
- Suspended Ormocomp® structures can be fabricated by adjusting laser dose for a sufficiently reduced voxel size.
- The Ormocomp®-I127 combination crosslinked by UV light is a suitable substrate for the culturing of hESC derived neuronal cells.

The second part presented the fabrication of Ormocomp® scaffolds and the culturing of hASCs, which were studied in Publication III with the following conclusions:

- Scaffold design based on hollow sphere unit cells enables simple tuning of porosity and interconnectivity values, which can be reproduced by 2PP-DLW with up to 94% accuracy.
- Ormocomp® scaffolds with 85% porosity and interconnectivity can be fabricated by 2PP-DLW using a ps laser system.
- The Ormocomp®-I127 combination processed by 2PP-DLW does not cause cytotoxic effects on hASCs.
- Ormocomp® scaffolds promote hASC attachment and growth in 3D.

The third part focused on the 2PP-DLW of custom and commercial hydrogels. Based on the work presented in Publication IV, the following are concluded:

- Acryloylated and methacryloylated poly(AA)s combined with I2959 are applicable to 2PP-DLW over a wider range of processing parameters than commercial PEGdas.
- 3D poly(AA) microstructures with 80% water content can be fabricated by 2PP-DLW.
- The acryloylated poly(AA)s produce more stable 3D microstructures than the methacryloylated analogs.
- The poly(AA) with the highest degree of acryloylation has the most potential for 3D scaffold applications.

First demonstrated a decade ago, 2PP-DLW is still a relatively new and constantly developing technique. Despite the rapid developments in the past five years, the potential of 2PP-DLW in biomedical applications is still largely unexplored. Two exciting new applications of 2PP-DLW are hydrogel patterning and advanced 3D scaffold fabrication. Creating cell-laden hydrogel constructs and chemical gradients within hydrogels offers new possibilities for studying cell-matrix interactions. By using 2PP-DLW to create scaffolds with defined composition, pore size, porosity and interconnectivity, optimal 3D culture conditions could be determined for different cell types. Gradient scaffolds combining hard and soft materials in zones of optimized geometry could then be used for co-culturing different cell types for applications such as dermal or osteochondral constructs.

References

[1] Lee, J., Cuddihy, M. J., Kotov, N. A. Three-Dimensional Cell Culture Matrices: State of the Art. Tissue Engineering: Part B 14(2008)1, pp. 61-86.

[2] Tibbitt, M. W., Anseth, K. S. Hydrogels as extracellular matrix mimics for 3D cell culture. Biotechnology and Bioengineering 103(2009)4, pp. 655-663.

[3] Melchels, F. P. W., Domingos, M. A. N., Klein, T. J., Malda, J., Bartolo, P. J., Hutmacher, D. W. Additive manufacturing of tissues and organs. Progress in Polymer Science 37(2012)8, pp. 1079-1104.

[4] Zorlutuna, P., Annabi, N., Camci-Unal, G., Nikkhah, M., Cha, J. M., Nichol, J. W., Manbachi, A., Bae, H., Chen, S., Khademhosseini, A. Microfabricated Biomaterials for Engineering 3D Tissues. Advanced Materials 24(2012)14, pp. 1782-1804.

[5] Billiet, T., Vandenhaute, M., Schelfhout, J., Van Vlierberghe, S., Dubruel, P. A review of trends and limitations in hydrogel-rapid prototyping for tissue engineering. Biomaterials 33(2012)26, pp. 6020-6041.

[6] Haske, W., Chen, V. W., Hales, J. M., Dong, W., Barlow, S., Marder, S. R., Perry, J. W. 65 nm feature sizes using visible wavelength 3-D multiphoton lithography. Optics Express 15(2007)6, pp. 3426-3436.

[7] Ovsianikov, A., Mironov, V., Stampfl, J., Liska, R. Engineering 3D cell-culture matrices: multiphoton processing technologies for biological and tissue engineering applications. Expert Review of Medical Devices 9(2012)6, pp. 613-633.

[8] LaFratta, C. N., Fourkas, J. T., Baldacchini, T., Farrer, R. A. Multiphoton Fabrication. Angewandte Chemie International Edition 46(2007)33, pp. 6238-6258.

[9] Derby, B. Printing and Prototyping of Tissues and Scaffolds. Science 338(2012)6109, pp. 921-926.

[10] Hutmacher, D. W. Scaffold-based tissue engineering – design and fabrication of matrices using solid freeform fabrication techniques. In: Gibson, Ian. Advanced Manufacturing Technology for Medical Applications - Reverse Engineering, Software Conversion and Rapid Prototyping. Chichester 2005, John Wiley & Sons. pp. 163-189.

[11] Zein, I., Hutmacher, D. W., Tan, K. C., Teoh, S. H. Fused deposition modeling of novel scaffold architectures for tissue engineering applications. Biomaterials 23(2002)4, pp. 1169-1185.

[12] Wilson, W. C., Boland, T. Cell and organ printing 1: Protein and cell printers. The Anatomical Record Part A: Discoveries in Molecular, Cellular, and Evolutionary Biology 272A(2003)2, pp. 491-496.

[13] Lee, S.-J. J., Sachs, E., Cima, M. Layer position accuracy in powder-based rapid prototyping. Rapid Prototyping Journal 1(1995)4, pp. 24-37.

[14] Sauerbrey, R. Ultraviolet, vacuum-ultraviolet, and X-ray lasers. In: Waynant, R. W. and Ediger, M. N. Electro-Optics Handbook. 2nd Edition. 2000, McGraw-Hill. pp. 3.1-3.45.

[15] Tipler, P. A., Llewellyn, R. A. Molecular structure and spectra. Modern Physics. 4th Edition. USA 2004, W.H. Freeman and Company. pp. 390-432.

[16] Schiele, N. R., Corr, D. T., Huang, Y., Raof, N. A., Xie, Y., Chrisey, D. B. Laser-based direct-write techniques for cell printing. Biofabrication 2(2010)3, pp. 032001.

[17] Masoumi, N., Jean, A., Zugates, J. T., Johnson, K. L., Engelmayr, G. C. Laser microfabricated poly(glycerol sebacate) scaffolds for heart valve tissue engineering. Journal of Biomedical Materials Research Part A 101A(2013)1, pp. 104-114.

[18] Wang, H., Cheng, C., Li, C., Wu, P., Wang, G. Hollow three-dimensional endothelialized microvessel networks based on femtosecond laser ablation. Biomedical Microdevices 15(2013)5, pp. 879-885.

[19] Lim, T., Son, Y., Yang, D., Kong, H., Lee, K. Selective ablation-assisted two-photon stereolithography for effective nano- and microfabrication. Applied Physics A 103(2011)4, pp. 1111-1116.

[20] Suri, S., Singh, A., Schmidt, C. E. Photofunctionalization of materials to promote protein and cell interactions for tissue-engineering applications. In: Puleo, D. A. and Bizios, R. Biological Interactions on Materials Surfaces. 2009, Springer Science + Business Media. pp. 297-318.

[21] Sun, H., Kawata, S. Two-photon photopolymerization and 3D lithographic microfabrication. 2004, Springer Berlin Heidelberg. pp. 169-273.

[22] Sun, H., Kawata, S. Two-Photon Laser Precision Microfabrication and Its Applications to Micro-Nano Devices and Systems. Journal of Lightwave Technology 21(2003)3, pp. 624.

[23] Lee, K., Kim, R. H., Yang, D., Park, S. H. Advances in 3D nano/microfabrication using two-photon initiated polymerization. Progress in Polymer Science, 33(2008)6, pp. 631-681.

[24] Lee, K., Yang, D., Park, S. H., Kim, R. H. Recent developments in the use of two-photon polymerization in precise 2D and 3D microfabrications. Polymers for Advanced Technologies 17(2006)2, pp. 72-82.

[25] Peacock, A. J., Calhoun, A. Polymer chemistry - properties and applications. 2006, Carl Hanser Verlag GmbH & Co. KG. 418 p.

[26] Farsari, M., Vamvakaki, M., Chichkov, B. N. Multiphoton polymerization of hybrid materials. Journal of Optics 12(2010)12, pp. 124001.

[27] Fischer, J., von Freymann, G., Wegener, M. The Materials Challenge in Diffraction-Unlimited Direct-Laser-Writing Optical Lithography. Advanced Materials 22(2010)32, pp. 3578-3582.

[28] Maruo, S., Nakamura, O., Kawata, S. Three-dimensional microfabrication with two-photon absorbed polymerization. Optics Letters 22(1997)2, pp. 132-134.

[29] Fischer, J., Wegener, M. Three-dimensional direct laser writing inspired by stimulated-emission-depletion microscopy. Optical Materials Express 1(2011)4, pp. 614-624.

[30] Fischer, J., Wegener, M. Ultrafast Polymerization Inhibition by Stimulated Emission Depletion for Three-dimensional Nanolithography. Advanced Materials 24(2012)10, pp. OP65-OP69.

[31] Sun, H., Kawakami, T., Xu, Y., Ye, J., Matuso, S., Misawa, H., Miwa, M., Kaneko, R. Real three-dimensional microstructures fabricated by photopolymerization of resins through two-photon absorption. Optics Letters 25(2000)15, pp. 1110-1112.

[32] Zhang, Y., Chen, Q., Xia, H., Sun, H. Designable 3D nanofabrication by femtosecond laser direct writing. Nano Today 5(2010)5, pp. 435-448.

[33] Wu, S., Serbin, J., Gu, M. Two-photon polymerisation for three-dimensional micro-fabrication. Journal of Photochemistry and Photobiology A: Chemistry 181(2006)1, pp. 1-11.

[34] Kaiser, W., Garret, C. G. B. Two-photon excitation in $CaF^2:Eu^{2+}$. Physical Review Letters 7(1961), pp. 229-231.

[35] Oheim, M., Michael, D. J., Geisbauer, M., Madsen, D., Chow, R. H. Principles of two-photon excitation fluorescence microscopy and other nonlinear imaging approaches. Advanced Drug Delivery Reviews 58(2006)7, pp. 788-808.

[36] Thiel, M., Fischer, J., von Freymann, G., Wegener, M. Direct laser writing of three-dimensional submicron structures using a continuous-wave laser at 532 nm. Applied Physics Letters 97(2010)22, pp. 221102-3.

[37] Wang, I., Bouriau, M., Baldeck, P. L., Martineau, C., Andraud, C. Three-dimensional microfabrication by two-photon-initiated polymerization with a low-cost microlaser. Optics Letters 27(2002)15, pp. 1348-1350.

[38] Kaehr, B., Ertas, N., Nielson, R., Allen, R., Hill, R. T., Plenert, M., Shear, J. B. Direct-Write Fabrication of Functional Protein Matrixes Using a Low-Cost Q-Switched Laser. Analytical Chemistry 78(2006)9, pp. 3198-3202.

[39] Jariwala, S., Venkatakrishnan, K., Tan, B. Single step self-enclosed fluidic channels via two photon absorption (TPA) polymerization. Optics Express 18(2010)2, pp. 1630-1636.

[40] Ritschdorff, E. T., Shear, J. B. Multiphoton Lithography Using a High-Repetition Rate Microchip Laser. Analytical Chemistry 82(2010)20, pp. 8733-8737.

[41] Malinauskas, M., Danilevicius, P., Juodkazis, S. Three-dimensional micro-/nano-structuring via direct write polymerization with picosecond laser pulses. Optics Express 19(2011)6, pp. 5602-5610.

[42] Engelhardt, S., Hoch, E., Borchers, K., Meyer, W., Krüger, H., Tovar, G. E. M., Gillner, A. Fabrication of 2D protein microstructures and 3D polymer–protein hybrid microstructures by two-photon polymerization. Biofabrication 3(2011)2, pp. 025003.

[43] Tanaka, T., Sun, H., Kawata, S. Rapid sub-diffraction-limit laser micro/nanoprocessing in a threshold material system. Applied Physics Letters 80(2002)2, pp. 312-314.

[44] Wollhofen, R., Katzmann, J., Hrelescu, C., Jacak, J., Klar, T. A. 120 nm resolution and 55 nm structure size in STED-lithography. Optics Express 21(2013)9, pp. 10831-10840.

[45] Melchels, F. P. W., Feijen, J., Grijpma, D. W. A review on stereolithography and its applications in biomedical engineering. Biomaterials 31(2010)24, pp. 6121-6130.

[46] Skoog, S. A., Goering, P. L., Narayan, R. J. Stereolithography in tissue engineering. Journal of Materials Science: Materials in Medicine (2013), pp. 1-12.

[47] Barry, R. A., Shepherd, R. F., Hanson, J. N., Nuzzo, R. G., Wiltzius, P., Lewis, J. A. Direct-Write Assembly of 3D Hydrogel Scaffolds for Guided Cell Growth. Advanced Materials 21(2009)23, pp. 2407-2410.

[48] Billiet, T., Gevaert, E., De Schryver, T., Cornelissen, M., Dubruel, P. The 3D printing of gelatin methacrylamide cell-laden tissue-engineered constructs with high cell viability. Biomaterials 35(2014)1, pp. 49-62.

[49] Shuai, C., Li, P., Liu, J., Peng, S. Optimization of TCP/HAP ratio for better properties of calcium phosphate scaffold via selective laser sintering. Materials Characterization 77(2013)0, pp. 23-31.

[50] Shahzad, K., Deckers, J., Zhang, Z., Kruth, J., Vleugels, J. Additive manufacturing of zirconia parts by indirect selective laser sintering. Journal of the European Ceramic Society 34(2014)1, pp. 81-89.

[51] Maruo, S., Ikuta, K. Submicron stereolithography for the production of freely movable mechanisms by using single-photon polymerization. Sensors and Actuators A: Physical 100(2002)1, pp. 70-76.

[52] Malinauskas, M., Farsari, M., Piskarskas, A., Juodkazis, S. Ultrafast laser nanostructuring of photopolymers: A decade of advances. Physics Reports 533(2013)1, pp. 1-31.

[53] Stocker, M. P., Li, L., Gattass, R. R., Fourkas, J. T. Multiphoton photoresists giving nanoscale resolution that is inversely dependent on exposure time. Nature Chemistry 3(2011)3, pp. 223-227.

[54] Watanabe, T., Akiyama, M., Totani, K., Kuebler, S. M., Stellacci, F., Wenseleers, W., Braun, K., Marder, S. R., Perry, J. W. Photoresponsive Hydrogel Microstructure Fabricated by Two-Photon Initiated Polymerization. Advanced Functional Materials 12(2002)9, pp. 611-614.

[55] Fischer, J., Mueller, J. B., Kaschke, J., Wolf, T. J. A., Unterreiner, A., Wegener, M. Three-dimensional multi-photon direct laser writing with variable repetition rate. Optics Express 21(2013)22, pp. 26244-26260.

[56] Baldacchini, T., LaFratta, C. N., Farrer, R. A., Teich, M. C., Saleh, B. E. A., Naughton, M. J., Fourkas, J. T. Acrylic-based resin with favorable properties for three-dimensional two-photon polymerization. Journal of Applied Physics 95(2004)11, pp. 6072-6076.

[57] Jhaveri, S. J., McMullen, J. D., Sijbesma, R., Tan, L., Zipfel, W., Ober, C. K. Direct Three-Dimensional Microfabrication of Hycrogels via Two-Photon Lithography in Aqueous Solution. Chemistry of Materials 21(2009)10.

[58] Fitilis, I., Fakis, M., Polyzos, I., Giannetas, V., Persephonis, P. Two-photon polymerization of a diacrylate using fluorene photoinitiators–sensitizers. Journal of Photochemistry and Photobiology A: Chemistry 215(2010)1, pp. 25-30.

[59] Cumpston, B. H., Ananthavel, S. P., Barlow, S., Dyer, D. L., Ehrlich, J. E., Erskine, L. L., Heikal, A. A., Kuebler, S. M., Lee, I. -. S., McCord-Maughon, D., Qin, J., Rockel, H., Rumi, M., Wu, X., Marder, S. R., Perry, J. W. Two-photon polymerization initiators for three-dimensional optical data storage and microfabrication. Nature 398(1999)6722, pp. 51-54.

[60] Sun, H., Maeda, M., Takada, K., Chon, J. W. M., Gu, M., Kawata, S. Experimental investigation of single voxels for laser nanofabrication via two-photon photopolymerization. Applied Physics Letters 83(2003)5, pp. 819-821.

[61] Martineau, C., Anémian, R., Andraud, C., Wang, I., Bouriau, M., Baldeck, P. L. Efficient initiators for two-photon induced polymerization in the visible range. Chemical Physics Letters 362(2002)3-4, pp. 291-295.

[62] Weiß, T., Schade, R., Laube, T., Berg, A., Hildebrand, G., Wyrwa, R., Schnabelrauch, M., Liefeith, K. Two-Photon Polymerization of Biocompatible Photopolymers for Microstructured 3D Biointerfaces. Advanced Engineering Materials 13(2011)9, pp. B264-B273.

[63] Wu, D., Chen, Q., Niu, L., Wang, J., Wang, J., Wang, R., Xia, H., Sun, H. Femtosecond laser rapid prototyping of nanoshells and suspending components towards microfluidic devices. Lab on a Chip 9(2009)16, pp. 2391-2394.

[64] Malinauskas, M., Žukauskas, A., Vytautas, P., Belazaras, K., Momot, A., Paipula, D., Gadonas, R., Piskarskas, A., Gilbergs, H., Gaidukevičiūtė, A., Sakellari, I., Farsari, M., Juodkazis, S. Femtosecond laser polymerization of hybrid/integrated micro-optical elements and their characterization. Journal of Optics 12(2010)12, pp. 124010.

[65] Yang, D., Park, S. H., Lim, T. W., Kong, H., Yi, S. W., Yang, H. K., Lee, K. Ultraprecise microreproduction of a three-dimensional artistic sculpture by multipath scanning method in two-photon photopolymerization. Applied Physics Letters 90(2007)7, pp. 079903-3.

[66] Kato, J., Takeyasu, N., Adachi, Y., Sun, H., Kawata, S. Multiple-spot parallel processing for laser micronanofabrication. Applied Physics Letters 86(2005)4, pp. 044102.

[67] Winfield, R. J., Bhuian, B., O'Brien, S., Crean, G. M. Fabrication of grating structures by simultaneous multi-spot fs laser writing. Applied Surface Science 253(2007)19, pp. 8086-8090.

[68] Bhuian, B., Winfield, R. J., O'Brien, S., Crean, G. M. Pattern generation using axicon lens beam shaping in two-photon polymerisation. Applied Surface Science, 254(2007)4, pp. 841-844.

[69] Dong, X., Zhao, Z., Duan, X. Micronanofabrication of assembled three-dimensional microstructures by designable multiple beams multiphoton processing. Applied Physics Letters 91(2007)12.

[70] Obata, K., Koch, J., Hinze, U., Chichkov, B. N. Multi-focus two-photon polymerization technique based on individually controlled phase modulation. Optics Express 18(2010)16, pp. 17193-17200.

[71] Gittard, S. D., Nguyen, A., Obata, K., Koroleva, A., Narayan, R. J., Chichkov, B. N. Fabrication of microscale medical devices by two-photon polymerization with multiple foci via a spatial light modulator. Biomedical Optics Express 2(2011)11, pp. 3167-3178.

[72] Jesacher, A., Booth, M. J. Parallel direct laser writing in three dimensions with spatially dependentaberration correction. Optics Express 18(2010)20, pp. 21090-21099.

[73] LaFratta, C. N., Baldacchini, T., Farrer, R. A., Fourkas, J. T., Teich, M. C., Saleh, B. E. A., Naughton, M. J. Replication of Two-Photon-Polymerized Structures with Extremely High Aspect Ratios and Large Overhangs. The Journal of Physical Chemistry B 108(2004)31, pp. 11256-11258.

[74] LaFratta, C. N., Li, L., Fourkas, J. T. Soft-lithographic replication of 3D microstructures with closed loops. Proceedings of the National Academy of Sciences of the United States of America 103(2006)23, pp. 8589-8594.

[75] Gittard, S. D., Ovsianikov, A., Monteiro-Riviere, N. A., Lusk, J., Morel, P., Minghetti, P., Lenardi, C., Chichkov, B. N., Narayan, R. J. Fabrication of Polymer Microneedles Using a Two-Photon Polymerization and Micromolding Process. Journal of Diabetes Science and Technology 3(2009)2, pp. 304-311.

[76] Koroleva, A., Schlie, S., Fadeeva, E., Gittard, S. D., Miller, P., Ovsianikov, A., Koch, J., Narayan, R. J., Chichkov, B. N. Microreplication of laser-fabricated surface and three-dimensional structures . Journal of Optics 12(2010)12, pp. 124009.

[77] Koroleva, A., Gittard, S., Schlie, S., Deiwick, A., Jockenhoevel, S., Chichkov, B. Fabrication of fibrin scaffolds with controlled microscale architecture by a two-photon polymerization–micromolding technique. Biofabrication 4(2012)1, pp. 015001.

[78] Koroleva, A., Gill, A. A., Ortega, I., Haycock, J. W., Schlie, S., Gittard, S. D., Chichkov, B. N., Claeyssens, F. Two-photon polymerization-generated and micromolding-replicated 3D scaffolds for peripheral neural tissue engineering applications. Biofabrication 4(2012)2, pp. 025005.

[79] Deubel, M., von Freymann, G., Wegener, M., Pereira, S., Busch, K., Soukoulis, C. M. Direct laser writing of three-dimensional photonic-crystal templates for telecommunications. Nature Materials 3(2004)7, pp. 444-447.

[80] Seet, K. K., Mizeikis, V., Juodkazis, S., Misawa, H. Three-dimensional horizontal circular spiral photonic crystals with stop gaps below 1 μm. Applied Physics Letters 88(2006)22, pp. 221101.

[81] von Freymann, G., Ledermann, A., Thiel, M., Staude, I., Essig, S., Busch, K., Wegener, M. Three-Dimensional Nanostructures for Photonics. Advanced Functional Materials 20(2010)7, pp. 1038-1052.

[82] Vasilantonakis, N., Terzaki, K., Sakellari, I., Purlys, V., Gray, D., Soukoulis, C. M., Vamvakaki, M., Kafesaki, M., Farsari, M. Three-Dimensional Metallic Photonic Crystals with Optical Bandgaps. Advanced Materials 24(2012)8, pp. 1101-1105.

[83] Klein, S., Barsella, A., Taupier, G., Stortz, V., Fort, A., Dorkenoo, K. D. Applied Surface Science 252(2006)13, pp. 4919-4922.

[84] Reinhardt, C., Seidel, A., Evlyukhin, A., Cheng, W., Kiyan, R., Chichkov, B. Direct laser-writing of dielectric-loaded surface plasmon-polariton waveguides for the visible and near infrared. Applied Physics A: Materials Science and Processing 100(2010)2, pp. 347-352.

[85] Lee, C., Pagliara, S., Keyser, U., Baumberg, J. J. Perpendicular coupling to in-plane photonics using arc waveguides fabricated via two-photon polymerization. Applied Physics Letters 100(2012)17.

[86] Wu, D., Wu, S., Niu, L., Chen, Q., Wang, R., Song, J., Fang, H., Sun, H. High numerical aperture microlens arrays of close packing. Applied Physics Letters 97(2010)3, pp. 031109-3.

[87] LaFratta, C. N., Lim, D., O'Malley, K., Baldacchini, T., Fourkas, J. T. Chemistry of Materials 18(2006)8, pp. 2038-2042.

[88] Knoll, A., Dürig, U., Züger, O., Güntherodt, H.-J. Micron-sized mechanical oscillators created by 3D two-photon polymerization: Towards a mechanical logic device. Microelectronic Engineering 83(2006)4-9, pp. 1261-1264.

[89] Doraiswamy, A., Jin, C., Narayan, R. J., Mageswaran, P., Mente, P., Modi, R., Auyeung, R., Chrisey, D. B., Ovsianikov, A., Chichkov, B. Two photon induced polymerization of organic–inorganic hybrid biomaterials for microstructured medical devices. Acta Biomaterialia 2(2006)3, pp. 267-275.

[90] Jeon, H., Hidai, H., Hwang, D. J., Healy, K. E., Grigoropoulos, C. P. The effect of micronscale anisotropic cross patterns on fibroblast migration. Biomaterials 31(2010)15, pp. 4286-4295.

[91] Ovsianikov, A., Deiwick, A., Van Vlierberghe, S., Dubruel, P., Möller, L., Dräger, G., Chichkov, B. Laser Fabrication of Three-Dimensional CAD Scaffolds from Photosensitive Gelatin for Applications in Tissue Engineering. Biomacromolecules 12(2011)4, pp. 851-858.

[92] Ovsianikov, A., Chichkov, B., Adunka, O., Pillsbury, H., Doraiswamy, A., Narayan, R. J. Rapid prototyping of ossicular replacement prostheses. Applied Surface Science, 253(2007)15, pp. 6603-6607.

[93] Park, S.-H., Yang, D.-Y., Lee, K.-S. Two-photon stereolithography for realizing ultraprecise three-dimensional nano/microdevices. Laser & Photonics Review 3(2009)1-2, pp. 1-11.

[94] Göppert-Mayer, M. Elementary processes with two-quantum transitions. Annals of Physics 9(1931), pp. 273-294.

[95] Pawlicki, M., Collins, H. A., Denning, R. G., Anderson, H. L. Two-Photon Absorption and the Design of Two-Photon Dyes. Angewandte Chemie International Edition 48(2009)18, pp. 3244-3266.

[96] Rumi, M., Perry, J. W. Two-photon absorption: an overview of measurements and principles. Advances in Optics and Photonics 2(2010)4, pp. 451-518.

[97] Boyd, R. W. The nonlinear optical susceptibility. Nonlinear Optics (3rd Edition). 2008, Elsevier. pp. 1-67.

[98] Yang, H. K., Kim, M., Kang, S., Kim, K., Lee, K., Park, S. H., Yang, D., Kong, H., Sun, H., Kawata, S., Fleitz, P. Recent Progress of Lithographic Microfabrication by the TPA-Induced Photopolymerization. Journal of Photopolymer Science and Technology 17(2004)3, pp. 385-392.

[99] Mueller, J. B., Fischer, J., Mange, Y. J., Nann, T., Wegener, M. *In-situ* local temperature measurement during three-dimensional direct laser writing. Applied Physics Letters 103(2013)12.

[100] Juodkazis, S., Mizeikis, V., Misawa, H. Three-dimensional microfabrication of materials by femtosecond lasers for photonics applications. Journal of Applied Physics 106(2009)5, pp. 051101.

[101] Seet, K. K., Juodkazis, S., Jarutis, V., Misawa, H. Feature-size reduction of photopolymerized structures by femtosecond optical curing of SU-8. Applied Physics Letters 89(2006)2, pp. 024106-3.

[102] Malinauskas, M., Zukauskas, A., Bickauskaite, G., Gadonas, R., Juodkazis, S. Mechanisms of three-dimensional structuring of photo-polymers by tightly focussed femtosecond laser pulses. Optics Express 18(2010)10, pp. 10209-10221.

[103] Baldacchini, T., Snider, S., Zadoyan, R. Two-photon polymerization with variable repetition rate bursts of femtosecond laser pulses. Optics Express 20(2012)28, pp. 29890-29899.

[104] Gamaly, E., Luther-Davies, B., Rode, A. Laser-matter interaction confined inside the bulk of a transparent solid. In: Misawa, Hiroaki and Juodkazis, Saulius. 3D Laser Microfabrication: Principles and Applications. Weinheim 2006, John Wiley & Sons. pp. 5-36.

[105] Rekštytė,Sima, Linas Jonušauskas, Albertas Žukauskas, Gediminas Gervinskas, Mangirdas Malinauskas and Saulius Juodkazis. Three-dimensional nanostructuring of polymer materials by controlled avalanche using femtosecond laser pulses. Proc. SPIE 8972, Frontiers in Ultrafast Optics: Biomedical, Scientific, and Industrial Applications XIV, San Francisco, California, USA, February 1, 2014. 2014, SPIE. pp. 89721O-89721O-9.

[106] Masters, B. R. Confocal microscopy and multiphoton excitation microscopy: The genesis of live cell imaging. USA 2006, SPIE Press. 230 p.

[107] Cremer, C., Masters, B. R. Resolution enhancement techniques in microscopy. The European Physical Journal H 38(2013)3, pp. 281-344.

[108] Heintzmann, R., Ficz, G. Breaking the resolution limit in light microscopy. Briefings in Functional Genomics & Proteomics 5(2006)4, pp. 289-301.

[109] Breault, R. P., Turner, M. Optical design and stray light concepts and principles. In: Träger, Frank. Handbook of Lasers and Optics. Berlin 2012, Springer Berlin Heidelberg. pp. 427-445.

[110] Lindlein, N., Leuchs, G. Wave optics. In: Träger, Frank. Handbook of Lasers and Optics. Berlin 2012, Springer Berlin Heidelberg. pp. 89-160.

[111] Lindlein, N., Leuchs, G. Geometrical optics. In: Träger, Frank. 2nd. Berlin 2012, Springer Berlin Heidelberg. pp. 35-87.

[112] Sparrow, C. M. On spectroscopic resolving power. Astrophysical Journal 44(1916), pp. 76-86.

[113] Inoué, S. Foundations of confocal scanned imaging in light microscopy. In: Pawley, James B. Handbook of Biological Confocal Microscopy. New York 1995, Springer US. pp. 1-14.

[114] Fischer, J., Wegener, M. Three-dimensional optical laser lithography beyond the diffraction limit. Laser & Photonics Reviews 7(2013)1, pp. 22-44.

[115] Kawata, S., Sun, H.-B., Tanaka, T., Takada, K. Finer features for functional microdevices. Nature 412(2001)16, pp. 697-698.

[116] Juodkazis, S., Mizeikis, V., Seet, K. K., Masafumi, M., Misawa, H. Two-photon lithography of nanorods in SU-8 photoresist. Nanotechnology 16(2005)6, pp. 846.

[117] Dong, X., Zhao, Z., Duan, X. Improving spatial resolution and reducing aspect ratio in multiphoton polymerization nanofabrication. Applied Physics Letters 92(2008)9, pp. 091113.

[118] Maruo, S., Fourkas, J. T. Recent progress in multiphoton microfabrication. Laser & Photonics Review 2(2008)1-2, pp. 100-111.

[119] Takada, K., Sun, H., Kawata, S. Improved spatial resolution and surface roughness in photopolymerization-based laser nanowriting. Applied Physics Letters 86(2005)7, pp. 071122-3.

[120] Xing, J., Dong, X., Chen, W., Duan, X., Takeyasu, N., Tanaka, T., Kawata, S. Improving spatial resolution of two-photon microfabrication by using photoinitiator with high initiating efficiency. Applied Physics Letters 90(2007)13, pp. 131106-3.

[121] Witzgall, G., Vrijen, R., Yablonovitch, E., Doan, V., Schwartz, B. J. Single-shot two-photon exposure of commercial photoresist for the production of three-dimensional structures. Optics Letters 2322, pp. 1745-1747.

[122] Tan, B., Venkatakrishnan, K., Makaronets, A. Effects of pulsewidth on two-photon polymerization. Designed Monomers and Polymers 16(2013)2, pp. 145-150.

[123] Emons, M., Obata, K., Binhammer, T., Ovsianikov, A., Chichkov, B. N., Morgner, U. Two-photon polymerization technique with sub-50 nm resolution by sub-10 fs laser pulses. Optical Materials Express 2(2012)7, pp. 942-947.

[124] Burmeister, F., Steenhusen, S., Houbertz, R., Zeitner, U. D., Nolte, S., Tünnermann, A. Materials and technologies for fabrication of three-dimensional microstructures with sub-100 nm feature sizes by two-photon polymerization. Journal of Laser Applications 24(2012)4.

[125] Sun, H., Takada, K., Kim, M., Lee, K., Kawata, S. Scaling laws of voxels in two-photon photopolymerization nanofabrication. Applied Physics Letters 83(2003)6, pp. 1104-1106.

[126] DeVoe,Robert J., Harvey W. Kalweit, Catherine A. Leatherdale and Todd R. Williams. Voxel shapes in two-photon microfabrication. Proc. SPIE 4797, Multiphoton Absorption and Nonlinear Transmission Processes: Materials, Theory, and Applications, Seattle, WA, USA, July 7, 2002. 2003, SPIE. pp. 310-316.

[127] Jeon, H., Hidai, H., Hwang, D. J., Grigoropoulos, C. P. Fabrication of arbitrary polymer patterns for cell study by two-photon polymerization process. Journal of Biomedical Materials Research Part A 93A(2010)1, pp. 56-66.

[128] Teh, W. H., Dürig, U., Drechsler, U., Smith, C. G., Güntherodt, H. -. Effect of low numerical-aperture femtosecond two-photon absorption on (SU-8) resist for ultrahigh-aspect-ratio microstereolithography. Journal of Applied Physics 97(2005)5, pp. 054907.

[129] Danilevicius, P., Rekstyte, S., Balciunas, E., Kraniauskas, A., Jarasiene, R., Sirmenis, R., Baltriukiene, D., Bukelskiene, V., Gadonas, R., Malinauskas, M. Micro-structured polymer scaffolds fabricated by direct laser writing for tissue engineering. Journal of Biomedical Optics 17(2012)8, pp. 081405-1.

[130] Sun, H., Tanaka, T., Kawata, S. Three-dimensional focal spots related to two-photon excitation. Applied Physics Letters 80(2002)20, pp. 3673-3675.

[131] Serbin, J. Fabrication of Photonic Structures by Two-Photon Polymerization. Dissertation. Göttingen, 2004. Universität Hannover. 94.

[132] Gan, Z., Cao, Y., Evans, R. A., Gu, M. Three-dimensional deep sub-diffraction optical beam lithography with 9 nm feature size. Nature Communications 4(2013).

[133] Park, S. H., Lim, T. W., Yang, D., Cho, N. C., Lee, K. Fabrication of a bunch of sub-30-nm nanofibers inside microchannels using photopolymerization via a long exposure technique. Applied Physics Letters 89(2006)17, pp. 173133-3.

[134] Tan, D., Li, Y., Qi, F., Yang, H., Gong, Q., Dong, X., Duan, X. Reduction in feature size of two-photon polymerization using SCR500. Applied Physics Letters 90(2007)7, pp. 071106-3.

[135] Park, S., Lim, T., Yang, D., Kim, R., Lee, K. Improvement of spatial resolution in nano-stereolithography using radical quencher. Macromolecular Research 14(2006)5, pp. 559-564.

[136] Li, L., Gattass, R. R., Gershgoren, E., Hwang, H., Fourkas, J. T. Achieving λ/20 Resolution by One-Color Initiation and Deactivation of Polymerization. Science 324(2009)5929, pp. 910-913.

[137] Wiesbauer, M., Wollhofen, R., Vasic, B., Schilcher, K., Jacak, J., Klar, T. A. Nano-Anchors with Single Protein Capacity Produced with STED Lithography. Nano Letters 13(2013)11, pp. 5672-5678.

[138] Fischer, J., Ergin, T., Wegener, M. Three-dimensional polarization-independent visible-frequency carpet invisibility cloak. Optics Letters 36(2011)11, pp. 2059-2061.

[139] Sun, Q., Ueno, K., Misawa, H. In situ investigation of the shrinkage of photopolymerized micro/nanostructures: the effect of the drying process. Optics Letters 37(2012)4, pp. 710-712.

[140] Sun, M.-Z., Li, Y., Cui, H.-B., Yang, H., Gong, Q.-H. Minimum spacing between suspended nanorods determined by stiction during two-photon polymerization. Applied Physics A: Materials Science and Processing 100(2010)1, pp. 177-180.

[141] Namatsu, H., Kurihara, K., Nagase, M., Iwadate, K., Murase, K. Dimensional limitations of silicon nanolines resulting from pattern distortion due to surface tension of rinse water. Applied Physics Letters 66(1995)20, pp. 2655-2657.

[142] Kondo, T., Juodkazis, S., Misawa, H. Reduction of capillary force for high-aspect ratio nanofabrication. Applied Physics A: Materials Science and Processing 81(2005)8, pp. 1583-1586.

[143] Park, S., Kim, K. H., Lim, T. W., Yang, D., Lee, K. Investigation of three-dimensional pattern collapse owing to surface tension using an imperfection finite element model. Microelectronic Engineering 85(2008)2, pp. 432-439.

[144] Sun, Q., Juodkazis, S., Murazawa, N., Mizeikis, V., Misawa, H. Freestanding and movable photonic microstructures fabricated by photopolymerization with femtosecond laser pulses. Journal of Micromechanics and Microengineering 20(2010), pp. 035004.

[145] Ovsianikov, A., Passinger, S., Houbertz, R., Chichkov, B. N. Three dimensional material processing with femtosecond lasers. In: Phipps, C. R. Laser Ablation and its Applications. Berlin 2007, Springer. pp. 121-157.

[146] Li, Y., Qi, F., Yang, H., Gong, Q., Dong, X., Duan, X. Nonuniform shrinkage and stretching of polymerized nanostructures fabricated by two-photon photopolymerization. Nanotechnology 19(2008)5, pp. 055303.

[147] Ovsianikov, A., Shizhou, X., Farsari, M., Vamvakaki, M., Costas, F., Chichkov, B. N. Shrinkage of microstructures produced by two-photon polymerization of Zr-based hybrid photosensitive materials. Optics Express 17(2009)4, pp. 2143-2148.

[148] Bhuian, B., Winfield, R. J., O'Brien, S., Crean, G. M. Investigation of the two-photon polymerisation of a Zr-based inorganic–organic hybrid material system. Applied Surface Science, 252(2006)13, pp. 4845-4849.

[149] Sun, H., Suwa, T., Takada, K., Zaccaria, R. P., Kim, M., Lee, K., Kawata, S. Shape precompensation in two-photon laser nanowriting of photonic lattices. Applied Physics Letters 85(2004)17, pp. 3708-3710.

[150] Lim, T. W., Son, Y., Yang, D., Pham, T. A., Kim, D., Yang, B., Lee, K., Park, S. H. Net Shape Manufacturing of Three-Dimensional SiCN Ceramic Microstructures Using an Isotropic Shrinkage Method by Introducing Shrinkage Guiders. International Journal of Applied Ceramic Technology 5(2008)3, pp. 258-264.

[151] Maruo, S., Hasegawa, T., Yoshimura, N. Single-anchor support and supercritical CO2 drying enable high-precision microfabrication of three-dimensional structures. Optics Express 17(2009)23, pp. 20945-20951.

[152] Xing, J., Chen, W., Dong, X., Tanaka, T., Fang, X., Duan, X., Kawata, S. Synthesis, optical and initiating properties of new two-photon polymerization initiators: 2,7-Bis(styryl)anthraquinone derivatives. Journal of Photochemistry and Photobiology A: Chemistry 189(2007)2–3, pp. 398-404.

[153] Green, W. A. Industrial photoinitiators: A technical guide. Boca Raton, USA 2010, CRC Press. 282 p.

[154] Torgersen, J., Qin, X., Li, Z., Ovsianikov, A., Liska, R., Stampfl, J. Hydrogels for Two-Photon Polymerization: A Toolbox for Mimicking the Extracellular Matrix. Advanced Functional Materials 23(2013)36, pp. 4542-4554.

[155] Mendonca, C. R., Correa, D. S., Baldacchini, T., Tayalia, P., Mazur, E. Two-photon absorption spectrum of the photoinitiator Lucirin TPO-L. Applied Physics A 90(2008)4, pp. 633-636.

[156] Melissinaki, V., Gill, A. A., Ortega, I., Vamvakaki, M., Ranella, A., Haycock, J. W., Fotakis, C., Farsari, M., Claeyssens, F. Direct laser writing of 3D scaffolds for neural tissue engineering applications. Biofabrication 3(2011)4, pp. 045005.

[157] Danilevičius, P., Rekštytė, S., Balčiūnas, E., Kraniauskas, A., Širmenis, R., Baltriukienė, D., Bukelskienė, V., Gadonas, R., Sirvydis, V., Piskarskas, A., Malinauskas, M. Laser 3D micro/nanofabrication of polymers for tissue engineering applications. Optics & Laser Technology 45(2013)0, pp. 518-524.

[158] Basu, S., Campagnola, P. J. Enzymatic Activity of Alkaline Phosphatase Inside Protein and Polymer Structures Fabricated via Multiphoton Excitation. Biomacromolecules 5(2004)2, pp. 572-579.

[159] Campagnola, P. J., Delguidice, D. M., Epling, G. A., Hoffacker, K. D., Howell, A. R., Pitts, J. D., Goodman, S. L. 3-Dimensional Submicron Polymerization of Acrylamide by Multiphoton Excitation of Xanthene Dyes. Macromolecules 33(2000)5, pp. 1511-1513.

[160] Allen, R., Nielson, R., Wise, D. D., Shear, J. B. Catalytic Three-Dimensional Protein Architectures. Analytical Chemistry 77(2005)16, pp. 5089-5095.

[161] Turunen, S., Käpylä, E., Terzaki, K., Viitanen, J., Fotakis, C., Kellomäki, M., Farsari, M. Pico- and femtosecond laser-induced crosslinking of protein microstructures: evaluation of processability and bioactivity. Biofabrication 3(2011)4, pp. 045002.

[162] Schafer, K. J., Hales, J. M., Balu, M., Belfield, K. D., Van Stryland, E. W., Hagan, D. J. Two-photon absorption cross-sections of common photoinitiators. Journal of Photochemistry and Photobiology A: Chemistry, 162(2004)2-3, pp. 497-502.

[163] He, G. S., Tan, L., Zheng, Q., Prasad, P. N. Multiphoton Absorbing Materials: Molecular Designs, Characterizations, and Applications. Chemical reviews 108(2008)4, pp. 1245-1330.

[164] Lu, Y., Hasegawa, F., Goto, T., Ohkuma, S., Fukuhara, S., Kawazu, Y., Totani, K., Yamashita, T., Watanabe, T. Highly sensitive two-photon chromophores applied to three-dimensional lithographic microfabrication: design, synthesis and characterization towards two-photon absorption cross section. Journal of Materials Chemistry 14(2004)1, pp. 75-80.

[165] Lu, Y., Hasegawa, F., Ohkuma, S., Goto, T., Fukuhara, S., Kawazu, Y., Totani, K., Yamashita, T., Watanabe, T. Highly efficient two-photon initiated polymerization in solvent by using a novel two-photon chromophore and co-initiators. Journal of Materials Chemistry 14(2004)9, pp. 1391-1395.

[166] Zhao, Y., Li, X., Wu, F., Fang, X. Novel multi-branched two-photon polymerization initiators of ketocoumarin derivatives. Journal of Photochemistry and Photobiology A: Chemistry 177(2006)1, pp. 12-16.

[167] Gu, J., Yulan, W., Chen, W., Dong, X., Duan, X., Kawata, S. Carbazole-based 1D and 2D hemicyanines: synthesis, two-photon absorption properties and application for two-photon photopolymerization 3D lithography. New Journal of Chemistry 31(2007)1, pp. 63-68.

[168] Pucher, N., Rosspeintner, A., Satzinger, V., Schmidt, V., Gescheidt, G., Stampfl, J., Liska, R. Structure-Activity Relationship in D-π-A-π-D-Based Photoinitiators for the Two-Photon-Induced Photopolymerization Process. Macromolecules 42(2009)17, pp. 6519-6528.

[169] Li, Z., Siklos, M., Pucher, N., Cicha, K., Ajami, A., Husinsky, W., Rosspeintner, A., Vauthey, E., Gescheidt, G., Stampfl, J., Liska, R. Synthesis and structure-activity relationship of several aromatic ketone-based two-photon initiators. Journal of Polymer Science Part A: Polymer Chemistry 49(2011)17, pp. 3688-3699.

[170] Li, Z., Pucher, N., Cicha, K., Torgersen, J., Ligon, S. C., Ajami, A., Husinsky, W., Rosspeintner, A., Vauthey, E., Naumov, S., Scherzer, T., Stampfl, J., Liska, R. A Straightforward Synthesis and Structure-Activity Relationship of Highly Efficient Initiators for Two-Photon Polymerization. Macromolecules 46(2013)2, pp. 352-361.

[171] Hao, F., Liu, Z., Zhang, M., Liu, J., Zhang, S., Wu, J., Zhou, H., Tian, Y. Four new two-photon polymerization initiators with varying donor and conjugated bridge: Synthesis and two-photon activity. Spectrochimica Acta Part A: Molecular and Biomolecular Spectroscopy 118(2014)0, pp. 538-542.

[172] Nag, A., Goswami, D. Solvent effect on two-photon absorption and fluorescence of rhodamine dyes. Journal of Photochemistry and Photobiology A: Chemistry 206(2009)2–3, pp. 188-197.

[173] Tan, Y., Zhang, Q., Yu, J., Zhao, X., Tian, Y., Cui, Y., Hao, X., Yang, Y., Qian, G. Solvent effect on two-photon absorption (TPA) of three novel dyes with large TPA cross-section and red emission. Dyes and Pigments 97(2013)1, pp. 58-64.

[174] Li, Z., Torgersen, J., Ajami, A., Muhleder, S., Qin, X., Husinsky, W., Holnthoner, W., Ovsianikov, A., Stampfl, J., Liska, R. Initiation efficiency and cytotoxicity of novel water-soluble two-photon photoinitiators for direct 3D microfabrication of hydrogels. RSC Advances 3(2013)36, pp. 15939-15946.

[175] Wan, X., Zhao, Y., Xue, J., Wu, F., Fang, X. Water-soluble benzylidene cyclopentanone dye for two-photon photopolymerization. Journal of Photochemistry and Photobiology A: Chemistry 202(2009)1, pp. 74-79.

[176] Zhang, W., Soman, P., Meggs, K., Qu, X., Chen, S. Tuning the Poisson's Ratio of Biomaterials for Investigating Cellular Response. Advanced Functional Materials 23(2013)25, pp. 3226-3232.

[177] Ovsianikov, A., Malinauskas, M., Schlie, S., Chichkov, B., Gittard, S., Narayan, R., Löbler, M., Sternberg, K., Schmitz, K.-P., Haverich, A. Three-dimensional laser micro- and nano-structuring of acrylated poly(ethylene glycol) materials and evaluation of their cytoxicity for tissue engineering applications. Acta Biomaterialia 7(2011)3, pp. 967-974.

[178] Williams, C. G., Malik, A. N., Kim, T. K., Manson, P. N., Elisseeff, J. H. Variable cytocompatibility of six cell lines with photoinitiators used for polymerizing hydrogels and cell encapsulation. Biomaterials 26(2005)11, pp. 1211-1218.

[179] Bryant, S. J., Nuttelman, C. R., Anseth, K. S. Cytocompatibility of UV and visible light photoinitiating systems on cultured NIH/3T3 fibroblasts in vitro. Journal of Biomaterials Science, Polymer Edition 11(2000)5, pp. 439-457.

[180] Williams, J. M., Adewunmi, A., Schek, R. M., Flanagan, C. L., Krebsbach, P. H., Feinberg, S. E., Hollister, S. J., Das, S. Bone tissue engineering using polycaprolactone scaffolds fabricated via selective laser sintering. Biomaterials 26(2005)23, pp. 4817-4827.

[181] Fedorovich, N. E., Oudshoorn, M. H., van Geemen, D., Hennink, W. E., Alblas, J., Dhert, W. J. A. The effect of photopolymerization on stem cells embedded in hydrogels. Biomaterials 30(2009)3, pp. 344-353.

[182] Fairbanks, B. D., Schwartz, M. P., Bowman, C. N., Anseth, K. S. Photoinitiated polymerization of PEG-diacrylate with lithium phenyl-2,4,6-trimethylbenzoylphosphinate: polymerization rate and cytocompatibility. Biomaterials 30(2009)35, pp. 6702-6707.

[183] Williams, H. E., Freppon, D. J., Kuebler, S. M., Rumpf, R. C., Melino, M. A. Fabrication of three-dimensional micro-photonic structures on the tip of optical fibers using SU-8. Optics Express 19(2011)23, pp. 22910-22922.

[184] Sun, H., Matsuo, S., Misawa, H. Three-dimensional photonic crystal structures achieved with two-photon-absorption photopolymerization of resin. Applied Physics Letters 74(1999)6, pp. 786-788.

[185] Miwa, M., Juodkazis, S., Kawakami, T., Matsuo, S., Misawa, H. Femtosecond two-photon stereo-lithography. Applied Physics A: Materials Science & Processing 73(2001)5, pp. 561-566.

[186] Staude, I., Thiel, M., Essig, S., Wolff, C., Busch, K., von Freymann, G., Wegener, M. Fabrication and characterization of silicon woodpile photonic crystals with a complete bandgap at telecom wavelengths. Optics Letters 35(2010)7, pp. 1094-1096.

[187] Claeyssens, F., Hasan, E. A., Gaidukeviciute, A., Achilleos, D. S., Ranella, A., Reinhardt, C., Ovsianikov, A., Shizhou, X., Fotakis, C., Vamvakaki, M., Chichkov, B. N., Farsari, M. Three-Dimensional Biodegradable Structures Fabricated by Two-Photon Polymerization. Langmuir 25(2009)5, pp. 3219-3223.

[188] Koskela, J. E., Turunen, S., Ylä-Outinen, L., Narkilahti, S., Kellomäki, M. Two-photon microfabrication of poly(ethylene glycol) diacrylate and a novel biodegradable photopolymer-

comparison of processability for biomedical applications. Polymers for Advanced Technologies 23(2012)6, pp. 992-1001.

[189] Haas, K., Wolter, H. Synthesis, properties and applications of inorganic–organic copolymers (ORMOCER®s). Current Opinion in Solid State and Materials Science, 4(1999)6, pp. 571-580.

[190] Haas, K.-H. Hybrid Inorganic-Organic Polymers Based on Organically Modified Si-Alkoxides. Advanced Engineering Materials 2(2000)9, pp. 571-582.

[191] Haas, K.-H., Rose, K. Hybrid Inorganic/Organic Polymers with Nanoscale Building Blocks: Precursors, Processing, Properties and Applications. Reviews on Advanced Materials Science 5(2003)1, pp. 47-52.

[192] Schottner, G. Hybrid Sol-Gel-Derived Polymers: Applications of Multifunctional Materials. Chemistry of Materials 13(2001)10, pp. 3422-3435.

[193] Farsari, M., Ovsianikov, A., Vamvakaki, M., Sakellari, I., Gray, D., Chichkov, B., Fotakis, C. Fabrication of three-dimensional photonic crystal structures containing an active nonlinear optical chromophore. Applied Physics A: Materials Science & Processing 93(2008)1, pp. 11-15.

[194] Woggon, T., Kleiner, T., Punke, M., Lemmer, U. Nanostructuring of organic-inorganic hybrid materials for distributed feedback laser resonators by two-photon polymerization. Optics Express 17(2009)4, pp. 2500-2507.

[195] Klein, F., Richter, B., Striebel, T., Franz, C. M., Freymann, G. v., Wegener, M., Bastmeyer, M. Two-Component Polymer Scaffolds for Controlled Three-Dimensional Cell Culture. Advanced Materials 23(2011)11, pp. 1341-1345.

[196] Ovsianikov, A., Schlie, S., Ngezahayo, A., Haverich, A., Chichkov, B. N. Two-photon polymerization technique for microfabrication of CAD-designed 3D scaffolds from commercially available photosensitive materials. Journal of Tissue Engineering and Regenerative Medicine 1(2007)6, pp. 443-449.

[197] Ovsianikov, A., Gaidukeviciute, A., Chichkov, B. N., Oubaha, M., MacCraith, B. D., Sakellari, I., Giakoumaki, A., Gray, D., Vamvaki, M., Farsari, M., Fotakis, C. Two-Photon Polymerization of Hybrid Sol-Gel Materials for Photonics Applications. Laser Chemistry (2008).

[198] Sakellari, I., Gaidukeviciute, A., Giakoumaki, A., Gray, D., Fotakis, C., Farsari, M., Vamvakaki, M., Reinhardt, C., Ovsianikov, A., Chichkov, B. Two-photon polymerization of titanium-containing sol–gel composites for three-dimensional structure fabrication. Applied Physics A: Materials Science & Processing 100(2010)2, pp. 359-364.

[199] Oubaha, M., Copperwhite, R., Gorin, A., Purlys, V., Boothman, C., O'Sullivan, M., Gadonas, R., McDonagh, C., MacCraith, B. D. Novel tantalum based photocurable hybrid sol–gel material employed in the fabrication of channel optical waveguides and three-dimensional structures. Applied Surface Science 257(2011)7, pp. 2995-2999.

[200] Haberko, J., Scheffold, F. Fabrication of mesoscale polymeric templates for three-dimensional disordered photonic materials. Optics Express 21(2013)1, pp. 1057-1065.

[201] Peppas, N. A., Bures, P., Leobandung, W., Ichikawa, H. Hydrogels in pharmaceutical formulations. European Journal of Pharmaceutics and Biopharmaceutics 50(2000)1, pp. 27-46.

[202] Hoffman, A. S. Hydrogels for biomedical applications. Advanced Drug Delivery Reviews 54(2002)1, pp. 3-12.

[203] Okay, O. General properties of hydrogels. In: Gerlach, Gerald and Arndt, Karl-Friedrich. 2010, Springer Berlin Heidelberg. pp. 1-14.

[204] Slaughter, B. V., Khurshid, S. S., Fisher, O. Z., Khademhosseini, A., Peppas, N. A. Hydrogels in Regenerative Medicine. Advanced Materials 21(2009)32-33, pp. 3307-3329.

[205] Nguyen, K. T., West, J. L. Photopolymerizable hydrogels for tissue engineering applications. Biomaterials, 23(2002)22, pp. 4307-4314.

[206] Pitts, J. D., Campagnola, P. J., Epling, G. A., Goodman, S. L. Submicron Multiphoton Free-Form Fabrication of Proteins and Polymers: Studies of Reaction Efficiencies and Applications in Sustained Release. Macromolecules 33(2000)5, pp. 1514-1523.

[207] Pitts, J. D., Howell, A. R., Taboada, R., Banerjee, I., Wang, J., Goodman, S. L., Campagnola, P. J. New Photoactivators for Multiphoton Excited Three-dimensional Submicron Cross-linking of Proteins: Bovine Serum Albumin and Type 1 Collagen. Photochemistry and photobiology 76(2002)2, pp. 135-144.

[208] Pins, G. D., Bush, K. A., Cunningham, L. P., Campagnola, P. J. Multiphoton excited fabricated nano and micro patterned extracellular matrix proteins direct cellular morphology. Journal of Biomedical Materials Research Part A 78A(2006)1, pp. 194-204.

[209] Chen, X., Su, Y., Ajeti, V., Chen, S., Campagnola, P. J. Cell Adhesion on Micro-Structured Fibronectin Gradients Fabricated by Multiphoton Excited Photochemistry. Cellular and Molecular Bioengineering 5(2012)3, pp. 307-319.

[210] Su, P., Tran, Q. A., Fong, J. J., Eliceiri, K. W., Ogle, B. M., Campagnola, P. J. Mesenchymal Stem Cell Interactions with 3D ECM Modules Fabricated via Multiphoton Excited Photochemistry. Biomacromolecules 13(2012)9, pp. 2917-2925.

[211] Basu, S., Rodionov, V., Terasaki, M., Campagnola, P. J. Multiphoton-excited microfabrication in live cells via Rose Bengalcross-linking of cytoplasmic proteins. Optics Letters 30(2005)2, pp. 159-161.

[212] Kaehr, B., Allen, R., Javier, D. J., Currie, J., Shear, J. B. Guiding neuronal development with *in situ* microfabrication. Proceeding of the National Academy of Sciences of the United Stated of America 101(2004)46, pp. 16104-16108.

[213] Kaehr, B., Shear, J. B. Multiphoton fabrication of chemically responsive protein hydrogels for microactuation. Proceeding of the National Academy of Sciences of the United Stated of America 105(2008)26, pp. 8850-8854.

[214] Spivey, E. C., Ritschdorff, E. T., Connell, J. L., McLennon, C. A., Schmidt, C. E., Shear, J. B. Multiphoton Lithography of Unconstrained Three-Dimensional Protein Microstructures. Advanced Functional Materials 23(2013)3, pp. 333-339.

[215] Zhu, J. Bioactive modification of poly(ethylene glycol) hydrogels for tissue engineering. Biomaterials 31(2010)17, pp. 4639-4656.

[216] Qin, X., Torgersen, J., Saf, R., Mühleder, S., Pucher, N., Ligon, S. C., Holnthoner, W., Redl, H., Ovsianikov, A., Stampfl, J., Liska, R. Three-dimensional microfabrication of protein hydrogels via two-photon-excited thiol-vinyl ester photopolymerization. Journal of Polymer Science Part A: Polymer Chemistry 51(2013)22, pp. 4799-4810.

[217] Ovsianikov, A., Mühleder, S., Torgersen, J., Li, Z., Qin, X., Van Vlierberghe, S., Dubruel, P., Holnthoner, W., Redl, H., Liska, R., Stampfl, J. Laser Photofabrication of Cell-Containing Hydrogel Constructs. Langmuir (2013).

[218] Berg, A., Wyrwa, R., Weisser, J., Weiss, T., Schade, R., Hildebrand, G., Liefeith, K., Schneider, B., Ellinger, R., Schnabelrauch, M. Synthesis of Photopolymerizable Hydrophilic Macromers and Evaluation of Their Applicability as Reactive Resin Components for the Fabrication of Three-Dimensionally Structured Hydrogel Matrices by 2-Photon-Polymerization. Advanced Engineering Materials 13(2011)9, pp. B274-B284.

[219] Kufelt, O., El-Tamer, A., Sehring, C., Schlie-Wolter, S., Chichkov, B. N. Hyaluronic Acid Based Materials for Scaffolding via Two-Photon Polymerization. Biomacromolecules 15(2014)2, pp. 650-659.

[220] Engelhardt, S., Hu, Y., Seiler, N., Riester, D., Meyer, W., Krüger, H., Wehner, M., Bremus-Köbberling, E., Gillner, A. 3D-Microfabrication of Polymer-Protein Hybrid Structures with a Q-Switched Microlaser. Journal of Laser Micro/Nanoengineering 6(2011)1, pp. 54-58.

[221] Lee, K. Y., Mooney, D. J. Hydrogels for Tissue Engineering. Chemical Reviews 101(2001)7, pp. 1869-1880.

[222] Ovsianikov, A., Ostendorf, A., Chichkov, B. N. Three-dimensional photofabrication with femtosecond lasers for applications in photonics and biomedicine. Applied Surface Science 253(2007)15, pp. 6599-6602.

[223] Ovsianikov, A., Gruene, M., Pflaum, M., Koch, L., Maiorana, F., Wilhelmi, M., Haverich, A., Chichkov, B. Laser printing of cells into 3D scaffolds. Biofabrication 2(2010)1, pp. 014104.

[224] Torgersen, J., Ovsianikov, A., Mironov, V., Pucher, N., Qin, X., Li, Z., Cicha, K., Machacek, T., Liska, R., Jantsch, V., Stampfl, J. Photo-sensitive hydrogels for three-dimensional laser microfabrication in the presence of whole organisms. Journal of Biomedical Optics 17(2012)10, pp. 105008-105008.

[225] Kim, Y., Park, J., Prausnitz, M. R. Microneedles for drug and vaccine delivery. Advanced Drug Delivery Reviews 64(2012)14, pp. 1547-1568.

[226] Ovsianikov, A., Chichkov, B., Mente, P., Monteiro-Riviere, N. A., Doraiswamy, A., Narayan, R. J. Two Photon Polymerization of Polymer–Ceramic Hybrid Materials for Transdermal Drug Delivery. International Journal of Applied Ceramic Technology 4(2007)1, pp. 22-29.

[227] Gittard, S. D., Miller, P. R., Boehm, R. D., Ovsianikov, A., Chichkov, B. N., Heiser, J., Gordon, J., Monteiro-Riviere, N., Narayan, R. J. Multiphoton microscopy of transdermal quantum dot delivery using two photon polymerization-fabricated polymer microneedles. Faraday Discussions 149(2011)0, pp. 171-185.

[228] Marino, A., Ciofani, G., Filippeschi, C., Pellegrino, M., Pellegrini, M., Orsini, P., Pasqualetti, M., Mattoli, V., Mazzolai, B. Two-Photon Polymerization of Sub-micrometric Patterned Surfaces: Investigation of Cell-Substrate Interactions and Improved Differentiation of Neuron-like Cells. ACS Applied Materials & Interfaces 5(2013)24, pp. 13012-13021.

[229] Turunen, S., Käpylä, E., Lähteenmäki, M., Ylä-Outinen, L., Narkilahti, S., Kellomäki, M. Direct laser writing of microstructures for the growth guidance of human pluripotent stem cell derived neuronal cells. Optics and Lasers in Engineering 55(2014)0, pp. 197-204.

[230] Basu, S., Cunningham, L. P., Pins, G. D., Bush, K. A., Taboada, R., Howell, A. R., Wang, J., Campagnola, P. J. Multiphoton Excited Fabrication of Collagen Matrixes Cross-Linked by a Modified Benzophenone Dimer: Bioactivity and Enzymatic Degradation. Biomacromolecules 6(2005)3, pp. 1465-1474.

[231] Schoen, F. J., Mitchell, R. N. Tissues, the extracellular matrix, and cell-biomaterial interactions. In: Ratner, Buddy D., Hoffman, Allan S., Schoen, Frederick J. and Lemons, Jack E. Biomaterials Science - An Introduction to Materials in Medicine (3rd Edition). 2013, Elsevier. pp. 452-474.

[232] Psycharakis, S., Tosca, A., Melissinaki, V., Giakoumaki, A., Ranella, A. Tailor-made three-dimensional hybrid scaffolds for cell cultures. Biomedical Materials 6(2011)4, pp. 045008.

[233] Terzaki, K., Kissamitaki, M., Skarmoutsou, A., Fotakis, C., Charitidis, C. A., Farsari, M., Vamvakaki, M., Chatzinikolaidou, M. Pre-osteoblastic cell response on three-dimensional, organic-inorganic hybrid material scaffolds for bone tissue engineering. Journal of Biomedical Materials Research Part A 101A(2013)8, pp. 2283-2294.

[234] Terzaki, K., Kalloudi, E., Mossou, E., Mitchell, E. P., Forsyth, V. T., Rosseeva, E., Simon, P., Vamvakaki, M., Chatzinikolaidou, M., Mitraki, A., Farsari, M. Mineralized self-assembled peptides on 3D laser-made scaffolds: a new route toward ´scaffold on scaffold´ hard tissue engineering. Biofabrication 5(2013)4, pp. 045002.

[235] Hidai, H., Jeon, H., Hwang, D. J., Grigoropoulos, C. P. Self-standing aligned fiber scaffold fabrication by two photon photopolymerization. Biomedical Microdevices 11(2009)3, pp. 634-652.

[236] Schlie, S., Ngezahayo, A., Ovsianikov, A., Fabian, T., Kolb, H., Haferkamp, H., Chichkov, B. N. Three-Dimensional Cell Growth on Structures Fabricated from ORMOCER(R) by Two-Photon Polymerization Technique. Journal of Biomaterials Applications 22(2007)3, pp. 275-287.

[237] Weiß, T., Hildebrand, G., Schade, R., Liefeith, K. Two-Photon polymerization for microfabrication of three-dimensional scaffolds for tissue engineering application. Engineering in Life Sciences 9(2009)5, pp. 384-390.

[238] Klein, F., Striebel, T., Fischer, J., Jiang, Z., Franz, C. M., Freymann, G. v., Wegener, M., Bastmeyer, M. Elastic 3D Scaffolds: Elastic Fully Three-dimensional Microstructure Scaffolds for Cell Force Measurements. Advanced Materials 22(2010)8, pp. 868-871.

[239] Greiner, A. M., Jäckel, M., Scheiwe, A. C., Stamow, D. R., Autenrieth, T. J., Lahann, J., Franz, C. M., Bastmeyer, M. Multifunctional polymer scaffolds with adjustable pore size and chemoattractant gradients for studying cell matrix invasion. Biomaterials 35(2014)2, pp. 611-619.

[240] Tayalia, P., Mazur, E., Mooney, D. J. Controlled architectural and chemotactic studies of 3D cell migration. Biomaterials 32(2011)10, pp. 2634-2641.

[241] Ovsianikov, A., Deiwick, A., Van Vlierberghe, S., Pflaum, M., Wilhelmi, M., Dubruel, P., Chichkov, B. Laser Fabrication of 3D Gelatin Scaffolds for the Generation of Bioartificial Tissues. Materials 4(2011)1, pp. 288-299.

[242] Raimondi, M. T., Eaton, S. M., Laganà, M., Aprile, V., Nava, M. M., Cerullo, G., Osellame, R. Three-dimensional structural niches engineered via two-photon laser polymerization promote stem cell homing. Acta Biomaterialia 9(2013)1, pp. 4579-4584.

[243] Cunningham, L. P., Veilleux, M. P., Campagnola, P. J. Freeform multiphoton excited microfabrication for biological applications using a rapid prototyping CAD-based approach. Optics Express 14(2006)19, pp. 8613-8621.

[244] Tayalia, P., Mendonca, C. R., Baldacchini, T., Mooney, D. J., Mazur, E. 3D Cell-Migration Studies using Two-Photon Engineered Polymer Scaffolds. Advanced Materials 20(2008)23, pp. 4494-4498.

[245] Hsieh, T. M., Benjamin Ng, C. W., Narayanan, K., Wan, A. C. A., Ying, J. Y. Three-dimensional microstructured tissue scaffolds fabricated by two-photon laser scanning photolithography. Biomaterials 31(2010)30, pp. 7648-7652.

[246] Kim, S., Qiu, F., Kim, S., Ghanbari, A., Moon, C., Zhang, L., Nelson, B. J., Choi, H. Fabrication and Characterization of Magnetic Microrobots for Three-Dimensional Cell Culture and Targeted Transportation. Advanced Materials 25(2013)41, pp. 5863-5868.

[247] Tottori, S., Zhang, L., Qiu, F., Krawczyk, K. K., Franco-Obregón, A., Nelson, B. J. Magnetic Helical Micromachines: Fabrication, Controlled Swimming, and Cargo Transport. Advanced Materials 24(2012)6, pp. 811-816.

[248] Wittig, R., Waller, E., von Freymann, G., Steiner, R. Direct laser writing-mediated generation of standardized topographies for dental implant surface optimization. Journal of Laser Applications 24(2012)4.

[249] Skarda, V., Rypácek, F., Ilavský, M. Biodegradable Hydrogel for Controlled Release of Biologically Active Macromolecules. Journal of Bioactive and Compatible Polymers 8(1993)1, pp. 24-40.

[250] Serbin, J., Egbert, A., Ostendorf, A., Chichkov, B. N., Houbertz, R., Domann, G., Schulz, J., Cronauer, C., Fröhlich, L., Popall, M. Femtosecond laser-induced two-photon polymerization of organic-inorganic hybrid materials for applications in photonics. Optics Letters 28(2003)5, pp. 301-303.

[251] Lappalainen, R. S., Salomäki, M., Ylä-Outinen, L., Heikkilä, T.,J., Hyttinen, J. A. K., Pihlajamäki, H., Suuronen, R., Skottman, H., Narkilahti, S. Similarly derived and cultured hESC lines show variation in their developmental potential towards neuronal cells in long-term culture. Regenerative Medicine 5(2010)5, pp. 749-762.

[252] Gimble, J., Guilak, F. Adipose-derived adult stem cells: isolation, characterization, and differentiation potential. Cytotherapy 5(2003)5, pp. 362-369.

[253] Zuk, P. A., Zhu, M., Mizuno, H., Huang, J., Futrell, J. W., Katz, A. J., Benhaim, P., Lorenz, H. P., Hedrick, M. H. Multilineage Cells from Human Adipose Tissue: Implications for Cell-Based Therapies. Tissue Engineering 7(2001)2, pp. 211-228.

[254] Sedlačík, Tomáš, Studenovská, Hana, Rypáček, František. Enzymatic degradation of the hydrogels based on synthetic poly(α-amino acid)s. Journal of Materials Science: Materials in Medicine 22(2011)4, pp. 781-788.

[255] Jockusch, S., Landis, M. S., Freiermuth, B., Turro, N. J. Photochemistry and Photophysics of alpha-Hydroxy Ketones. Macromolecules 34(2001)6, pp. 1619-1626.

[256] Lemercier, G., Mulatier, J., Martineau, C., Anémian, R., Andraud, C., Wang, I., Stéphan, O., Amari, N., Baldeck, P. Two-photon absorption: from optical power limiting to 3D microfabrication. Comptes Rendus Chimie 8(2005)8, pp. 1308-1316.

[257] Iosin, M., Stephan, O., Astilean, S., Dupperay, A., Baldeck, P. L. Microstructuration of protein matrices by laser-induced photochemistry. Journal of Optoelectronics and Advanced Materials 9(2007)3, pp. 716-720.

[258] Farsari, M., Filippidis, G., Fotakis, C. Fabrication of three-dimensional structures by three-photon polymerization. Optics Letters 30(2005)23, pp. 3180-3182.

[259] Drakakis, T. S., Papadakis, G., Sambani, K., Filippidis, G., Georgiou, S., Gizeli, E., Fotakis, C., Farsari, M. Construction of three-dimensional biomolecule structures employing femtosecond lasers. Applied Physics Letters 89(2006)14, pp. 144108.

[260] Farsari, M., Filippidis, G., Drakakis, T. S., Sambani, K., Georgiou, S., Papadakis, G., Gizeli, E., Fotakis, C. Three-dimensional biomolecule patterning. Applied Surface Science 253(2007)19, pp. 8115-8118.

[261] Jariwala, S., Tan, B., Venkatakrishnan, K. Micro-fluidic channel fabrication via two-photon absorption (TPA) polymerization assisted ablation. Journal of Micromechanics and Microengineering 19(2009), pp. 115023.

[262] Sivamani, R. K., Stoeber, B., Wu, G. C., Zhai, H., Liepmann, D., Maibach, H. Clinical microneedle injection of methyl nicotinate: stratum corneum penetration. Skin Research and Technology 11(2005)2, pp. 152-156.

[263] Liska, R., Schuster, M., Inführ, R., Turecek, C., Fritscher, C., Seidl, B., Schmidt, V., Kuna, L., Haase, A., Varga, F., Lichtenegger, H., Stampfl, J. Photopolymers for rapid prototyping. Journal of Coatings Technology and Research 4(2007)4, pp. 505-510.

[264] Danilevičius, P., Rekštytė, S., Balčiūnas, E., Kraniauskas, A., Širmenis, R., Baltriukienė, D., Malinauskas, M., Bukelskienė, V., Gadonas, R., Sirvydis, V., Piskarskas, A. Direct Laser Fabrication of Polymeric Implants for Cardiovascular Surgery. Materials Science (Medžiagotyra) 18(2012)2, pp. 145-149.

[265] Lindroos, B., Suuronen, R., Miettinen, S. The Potential of Adipose Stem Cells in Regenerative Medicine. Stem Cell Reviews and Reports 7(2011)2, pp. 269-291.

[266] Pytela, J., Saudek, V., Drobník, J., Rypáček, F. Poly(N5-hydroxyalkylglutamines). IV. Enzymatic degradation of n5-(2-hydroxyethyl)-L-glutamine homopolymers and copolymers. Journal of Controlled Release 10(1989)1, pp. 17-25.

[267] Chiu, H., Kopečková, P., Deshmane, S. S., Kopeček, J. Lysosomal degradability of poly(α-amino acids). Journal of Biomedical Materials Research 34(1997)3, pp. 381-392.

[268] Studenovská, H., Vodička, P., Proks, V., Hlučilová, J., Motlík, J., Rypáček, F. Synthetic poly(amino acid) hydrogels with incorporated cell-adhesion peptides for tissue engineering. Journal of Tissue Engineering and Regenerative Medicine 4(2010)6, pp. 454-463.

[269] Watanabe, W., Arakawa, N., Matsunaga, S., Higashi, T., Fukui, K., Isobe, K., Itoh, K. Femtosecond laser disruption of subcellular organelles in a living cell. Optics Express 12(2004)18, pp. 4203-4213.

[270] De Marco, C., Gaidukeviciute, A., Kiyan, R., Eaton, S. M., Levi, M., Osellame, R., Chichkov, B. N., Turri, S. A New Perfluoropolyether-Based Hydrophobic and Chemically Resistant Photoresist Structured by Two-Photon Polymerization. Langmuir 29(2013)1, pp. 426-431.

[271] Uppal, N., Shiakolas, P. S. Modeling of temperature-dependent diffusion and polymerization kinetics and their effects on two-photon polymerization dynamics. Journal of Micro/Nanolithography, MEMS, and MOEMS 7(2008)4, pp. 043002-043002.

[272] Williams, H. E., Luo, Z., Kuebler, S. M. Effect of refractive index mismatch on multi-photon direct laser writing. Optics Express 20(2012)22, pp. 25030-25040.

[273] Egner, A., Hell, S. W. Aberrations in confocal and multi-photon fluorescence microscopy induced by refractive index mismatch. In: Pawley, James B. 2006, Springer US. pp. 404-413.

[274] Lowman, A. M., Peppas, N. A. Hydrogels. In: Mathiowitz, Edith. Encyclopedia of Controlled Drug Delivery. New York 1999, John Wiley & Sons. pp. 397-418.

[275] Chan, V., Zorlutuna, P., Jeong, J. H., Kong, H., Bashir, R. Three-dimensional photopatterning of hydrogels using stereolithography for long-term cell encapsulation. Lab on a Chip 10(2010)16, pp. 2062-2070.

[276] Maxwell, I., Chung, S., Mazur, E. Nanoprocessing of subcellular targets using femtosecond laser pulses. Medical Laser Application 20(2005)3, pp. 193-200.

ORIGINAL PUBLICATIONS

Publication I

E. Käpylä, S. Turunen, M. Kellomäki

Two-Photon Polymerization of a Polymer-Ceramic Hybrid Material with a Low-Cost Nd:YAG Laser: Preliminary Resolution Study and 3D Fabrication

Micro and Nanosystems 2(2010)2, pp. 87-99.

Publication II

E. Käpylä, S. Turunen, J. Pelto, J. Viitanen, M. Kellomäki

Investigation of the optimal processing parameters for picosecond laser-induced microfabrication of a polymer-ceramic hybrid material

Journal of Micromechanics and Microengineering 21(2011)6, p. 065033

IOP Publishing Journal of Micromechanics and Microengineering

J. Micromech. Microeng. **21** (2011) 065033 (10pp) doi:10.1088/0960-1317/21/6/065033

Investigation of the optimal processing parameters for picosecond laser-induced microfabrication of a polymer–ceramic hybrid material

E Käpylä[1], S Turunen[1], J Pelto[1,2], J Viitanen[2] and M Kellomäki[1]

[1] Department of Biomedical Engineering, Tampere University of Technology, PO Box 692, 33101 Tampere, Finland

[2] VTT Research Centre of Finland, PO Box 1300, 33101 Tampere, Finland

E-mail: elli.kapyla@tut.fi

Received 4 March 2011, in final form 6 April 2011
Published 18 May 2011
Online at stacks.iop.org/JMM/21/065033

Abstract

This paper reports the effect of different process parameters on the resolution of direct laser writing by two-photon polymerization (2PP) with a low-cost Nd:YAG picosecond laser. Microstructures were fabricated from the hybrid polymer–ceramic material Ormocomp® and the impact of varying the laser beam focus position, average laser power and scanning speed were investigated in detail with scanning electron microscopy and atomic force microscopy imaging. With the appropriate laser beam focus settings, suspended structures could be fabricated. The laser intensity range of the so-called polymerization window and damage zone are reported along with the scanning speed range for producing uniform polymer lines. It is shown that very high resolution is achievable with this affordable picosecond laser 2PP system with feature sizes comparable to those previously reported for costly femtosecond laser systems. The discovered relationships between the process parameters and structure dimensions enable the design and fabrication of both 3D microstructures and nanometer scale surface features.

(Some figures in this article are in colour only in the electronic version)

1. Introduction

Photopolymerization by direct laser writing (DLW) is one of the most advanced techniques to produce two- (2D) and three-dimensional (3D) microstructures. Although 3D microfabrication by single-photon absorption has also been demonstrated [1], it is most commonly based on the nonlinear optical phenomenon of two-photon absorption (2PA). The microfabrication method is thus often referred to as two-photon polymerization (2PP). Unlike photolithography, 2PP is a maskless rapid prototyping microfabrication technique that can be used to create structures with a resolution of less than 100 nm [2–5], well beyond the diffraction limit of light. This can be realized by using a tightly focused laser beam to excite a photoinitiator molecule to a higher quantum state by the simultaneous absorption of two photons. The transition results in the formation of radicals which initiate the polymerization chain reaction inside a photoresist. Since 2PA requires very high photon intensity, the polymerization is only initiated at the laser focal point, making 2PP an inherently 3D fabrication method. Arbitrary 3D structures can be created simply by moving the laser focus inside a negative-tone photoresist, after which the non-irradiated resin is dissolved in a development liquid [6, 7]. To date, DLW and 2PP have found numerous applications in fields such as optics, microelectronics and biomedicine. Within these fields, 2PP has been used to create components such as photonic crystals [8–10], wave guides [11, 12], microlenses [13, 14], conductive wires [15] and mechanical oscillators [16] as well as microneedles [17, 18] and patterns for cell growth guidance

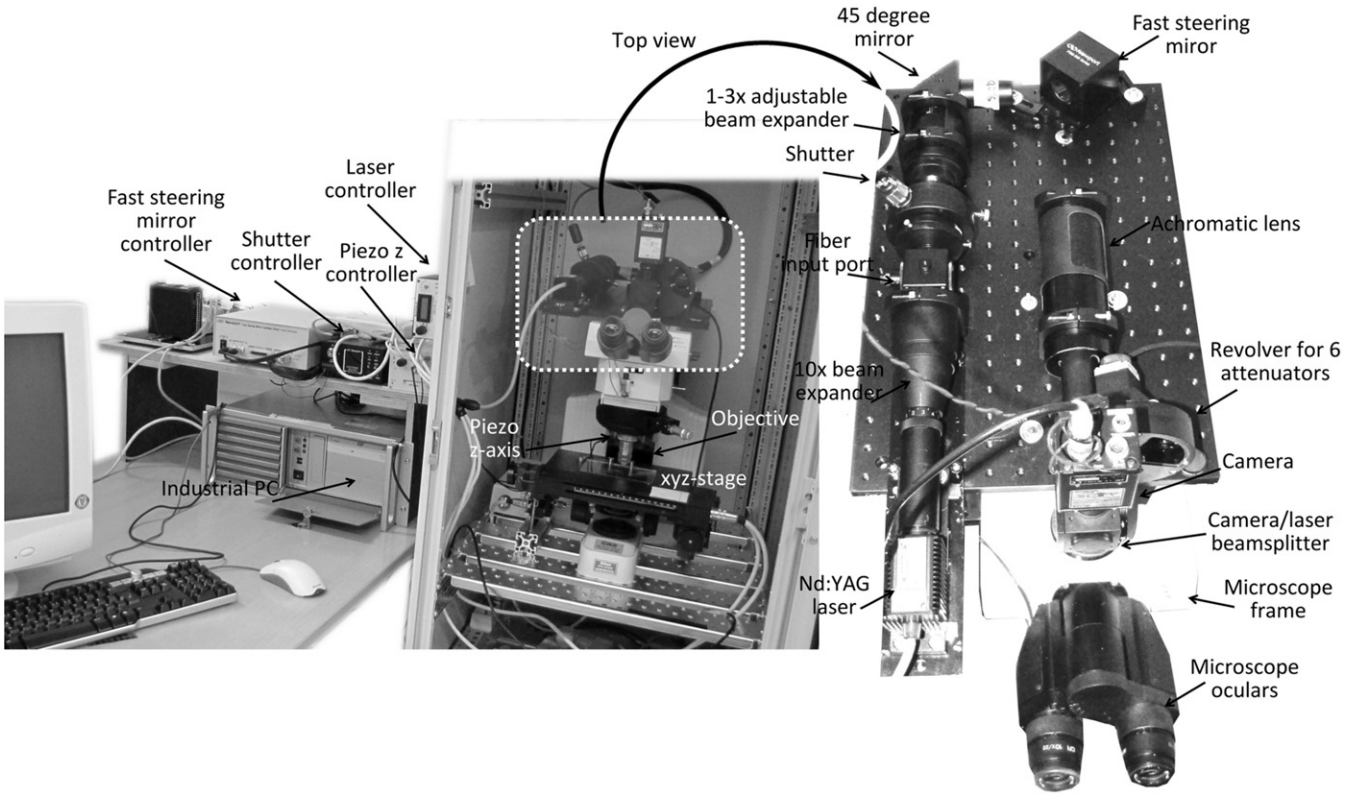

Figure 1. A view of the laser fabrication set-up used for 2PP.

and tissue engineering [19–23]. Although two- or multiphoton absorption is recognized as the mechanism for initiating polymerization, the mechanisms of the polymerization chain reaction are currently under discussion. For processing with tightly focused femtosecond laser pulses with sufficiently high intensity ($\sim$1 TW cm^{-2}), avalanche ionization and thermal polymerization have recently been proposed as the dominating processes for photoresists such as SU-8 and the hybrid sol–gel SZ2080. [24, 25].

The majority of 2PP studies published to date have been conducted with titanium:sapphire femtosecond lasers operating at MHz repetition rates and very high peak powers at infrared wavelengths, typically 780 nm. This type of laser, although effective in 2PP, is very expensive and thus limits the utilization of 2PP. Recently, continuous-wave and picosecond lasers have also been shown applicable for high resolution 3D microfabrication by 2PP [26–32]. Compared to femtosecond lasers, picosecond lasers are generally much more compact and affordable. Thus, the development of 2PP processing with picosecond lasers could enable the use of the technique in more widespread applications, not only in research but also in industry.

The achievable resolution of the 2PP process is highly dependent on the laser system, the material used and the optimization of processing parameters, such as laser power, intensity and scanning speed. Although widely used today in 2PP fabrication, resolution data for the hybrid polymer–ceramic material Ormocomp® have previously been published only in a handful of studies [19, 33, 34], including our previous study [30]. This paper reports the optimization of processing parameters for Ormocomp® with a 2PP system based on a low-cost Nd:YAG picosecond laser operating at 532 nm, combined with a fast steering mirror, a piezo focusing unit and a fast shutter. With this system, the impact of the laser beam focus position, exposure time, average polymerization power (intensity) and scanning speed on the resolution of Ormocomp® structures was studied in detail. Structure dimensions were characterized with both scanning electron microscopy (SEM) and atomic force microscopy (AFM). AFM measurements were also used to confirm the accuracy of the SEM image-based measurements.

2. Materials and methods

2.1. Laser fabrication set-up

The 2PP set-up (figure 1) was based on a frequency-doubled Nd:YAG pulsed laser (PULSELAS-P-1064-300-FC, Alphalas GmbH, Germany) operating at 532 nm with a pulse duration of 800 ps, maximum repetition rate of 15 kHz and output power of 100 mW. A fast steering mirror (FSM-300, Newport Corporation, USA) was used to direct the laser beam in the *xy*-direction whereas the displacement in the *z*-direction was implemented with a piezoelectric objective-lens positioning system (Mipos 250 SGEX, Piezosystem Jena GmbH, Germany). The sample exposure was controlled with a fast electronic shutter (Oriel 76992, Newport Corporation, USA). A mechanical stepper motor-based *xyz*-stage (SCAN 130 $\times$ 85, Märzhäuser Wetzlar GmbH & Co. KG, Germany) was used for the initial

positioning of the sample. The set-up was built over an upright microscope frame (Nikon ECLIPSE ME 600, Nikon, Japan) and the laser was focused into the photosensitive sample through a 50× oil immersion lens (NA = 0.90, Meiji Techno, Japan). In order to overfill the back aperture of the objective lens, the laser beam was expanded 30× with beam expanders. A video camera (CV-M10RS, JAI Corporation, USA) integrated behind a dichroic mirror enabled the online monitoring of the 2PP process. The motion control of the six axes, the shutter control and the camera were computer-controlled via custom-designed operating software.

The average laser output power was attenuated to a suitable polymerization power with optical absorptive filters mounted on a revolver. The attenuated power was further fine-tuned via altering the pump diode current. This also linearly affected the pulse frequency, which had the minimum and maximum values of 5 kHz and 15 kHz, respectively. The average laser power values were measured just before the objective with a power measuring instrument (LaserCheck, Coherent Inc., USA). The laser intensity (I_0) was estimated using [25, 35]:

$$I_0 = \frac{2(E_p/t_p)}{\pi w^2}. \quad (1)$$

Here, E_p is laser pulse energy calculated using the measured average laser power and the corresponding laser pulse frequency, t_p is the pulse duration (800 ps in our case) and w is the laser beam spot radius. The spot radius was estimated as a radius of an Airy disk at 1 e^{-2} level, multiplied by the laser beam quality factor M^2 factor

$$w = M^2 \frac{0.61\lambda}{\mathrm{NA}}, \quad (2)$$

where λ is the laser wavelength and NA is the numerical aperture of the objective lens. For M^2, the value of 1.2 was used, which is typical for the laser type used in this study. With the laser wavelength of 532 nm, NA of 0.90, the spot radius was thus estimated to be 433 nm.

The accessible scanning range of the fast steering mirror with the 50× objective was 310 μm in the x-direction and 220 μm in y-direction. The maximum motion of the piezoelectric objective lens positioning system was 250 μm. However in practice, the scanning range in the z-direction was limited by the height of the 150 μm thick spacer utilized for confining the liquid material on a microscope slide.

2.2. Materials and polymerization procedure

A polymer–ceramic hybrid material Ormocer® US-S4, also known by its trade name Ormocomp® (Micro Resist Technology GmbH, Germany), was used as a photopolymerizable resin. The liquid Ormocomp® precursor contained 1% of a photoinitiator DAROCUR® TPO (Ciba Specialty Chemicals, Switzerland). However, in order to achieve better sensitivity at the 2PA window of 266 nm, 2 wt% of the photoinitiator IRGACURE® 127 (Ciba Specialty Chemicals, Switzerland) was also added into the monomer solution. The Ormocomp® samples were prepared by simple drop casting without any pre- or post-baking steps. The resin was sandwiched between a microscope slide and a coverslip with a 150 μm thick spacer. Surfaces of the microscope slides were modified with 3-(trimethoxysilyl) propyl methacrylate (Sigma-Aldrich Finland Oy, Finland) to promote adhesion of the photoresist via surface-tethered methacrylate groups.

For the resolution study purposes, the desired voxel and line arrays were fabricated by programming the laser focus movement either with a commercial Rhinoceros® CAD program (Robert McNeel & Associates, USA) or with a custom-designed program. After polymerization, the uncured resin was removed by immersing the sample in the Ormodev® developer (Micro Resist Technology GmbH, Germany) for 2–5 min. Finally, the sample was thoroughly rinsed with 2-propanol.

2.3. SEM and AFM imaging

In order to determine the dimensions of the polymerized structures, samples were imaged with a scanning electron microscope (JEOL JSM—6360 LV, JEOL Ltd, Japan or Philips XL-30, Philips Electron Optics, The Netherlands). The pieces of the microscope slides containing the structures were sputter coated with gold in argon atmosphere (SCD 050 Sputter Coater, BAL-TEC AG, Liechtenstein or S 150 Sputter Coater, Edwards Ltd, UK). The sputtering time was set to either 120 s or 190 s, corresponding to a coating thickness of approximately 75 nm or 80 nm, respectively.

Arrays of voxels and lines were also studied by non-contact mode AFM (XE-100, Park Systems Inc., USA). Silicon probes (ACTa-905M, Applied NanoStructures Inc., USA) with a nominal resonance frequency of 300 kHz, spring constant of 4 N m^{-1}, a pyramidal-shaped tip (radius <10 nm) and an aluminum reflective coating were used. Images were acquired with a scan speed of 0.14, 0.15 or 0.20 Hz.

2.4. Resolution studies: effect of process parameters on structure dimensions

For the evaluation of the resolution of the 2PP process, simple voxels and lines were fabricated by varying the different process parameters, namely, laser beam focus position, exposure time, average laser power and scanning speed. In order to study the effect of the laser beam focus position on structure dimensions, so-called ascending scans were performed where the laser beam focus position relative to the glass slide surface was raised stepwise between each structure (z-rise). This simple yet effective method was originally reported by Sun *et al* [36]. In the case of voxels, the effect of the laser exposure time and the beam focus position were studied. Arrays of voxels were produced by raising the laser beam focus position relative to the glass slide surface until complete, yet still surface-bound voxels were created. The laser power was kept constant at 0.54 mW, corresponding to the intensity of 33 GW cm^{-2}.

With ascending line arrays, 11 lines were first polymerized with the z-rise of 1 μm between each line. Following this, six more lines with a z-rise of 5 μm between each line were polymerized. The process is further illustrated in figure 2. The visible reduction of the line height toward the other end

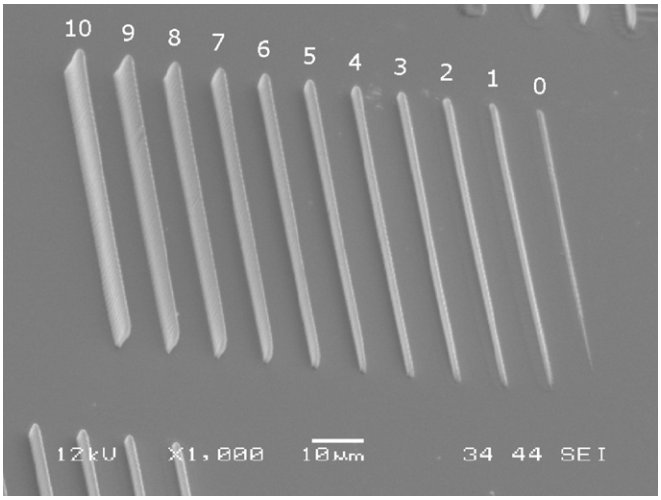

Figure 2. Lines polymerized with the ascending scan method with the average laser power of 1.40 mW and initial z-position of -4. The numbers above the lines signify the laser beam focus positions.

was likely caused by a slight inclination of the microscope glass surface. This was compensated by measuring the line dimensions from five points along the line. A total of three arrays were fabricated with a constant laser power of 1.40 mW (44 GW cm^{-2}) and different initial z-positions (0, -2 μm and -4 μm). The scanning speed was kept constant at 50 μm s^{-1}.

Based on the results obtained from the ascending scans, it was hypothesized that the minimum support height of 10 μm would be needed to produce suspended structures. To confirm this, specially designed overhanging structures were fabricated with the same parameters as the ascending scan lines (1.40 mW laser power, 50 μm s^{-1} scanning speed). Suspended horizontal lines were polymerized on top of supporting walls in order to define which laser beam focus position could produce open structures.

The effect of the average laser power was more extensively studied by polymerizing lines with a constant scanning speed of 50 μm s^{-1}. The power was varied from 0.36 mW to 2.66 mW, corresponding to the intensity range of 26 GW cm^{-2} to 107 GW cm^{-2}, respectively. The effect of scanning speed was then studied by polymerizing lines with the laser powers of 1.00 mW (63 GW cm^{-2}) and 1.20 mW (158 GW cm^{-2}) and varying scanning speed between 10 μm s^{-1} and 1000 μm s^{-1}.

The dimensions of voxels and lines were measured from SEM images with the help of free image processing software (GIMP 2.6), as described previously [30]. Voxels were measured from top-view SEM images. Line widths were measured from the top-view SEM images and line heights generally from SEM images taken from a 45° tilt. However, the heights of fallen lines were estimated from the top-view SEM images. Widths were only measured from upright lines. SEM-based line height was estimated using two different approaches. The heights of the smallest lines with an almost round tilt profile were measured from an angle perpendicular to their longitudinal axis. However, if the line was tall enough for the measurement of the tilt angle from the end of the line, this angle was used as a reference when measuring the height of the individual lines. The accuracy of the resolution data measured from SEM images was verified by AFM imaging.

3. Results

3.1. Ascending scans and the fabrication of suspended structures

The dimensions evaluated from the SEM images of the ascending line arrays are shown in figures 3(*a*) and (*b*) as functions of the laser beam focus position relative to the glass slide surface. It can be seen from figure 3(*b*) that the line width varied only slightly from 1.0 to 2.1 μm with the rising laser beam focus position. It should be noted that especially the taller lines were slightly tilted relative to the z-axis which made them appear wider in the top-view SEM images. Thus, the measured values represent the maximum for the line width. The line height, on the other hand, changed approximately linearly with the z-rise, as expected. However, on average, the calculated actual line height increase was only approximately 0.61 μm $\pm$ 0.28 μm instead of 1 μm, which was the change in the laser beam focus position. The minimum and maximum line heights were found to be approximately 1.0 μm and 8.5 μm, respectively, as seen from figure 3(*a*). The differences in the maximum line heights between the different arrays can be explained by the different initial laser beam focus positions.

It was observed that only the lines with a z-position $\leqslant$10 μm remained attached to the surface and survived the development procedure. This implied that the minimum required laser beam focus position for producing suspended structures with this material and the current 2PP system would be approximately 9 μm. This hypothesis was confirmed by the polymerization tests, as shown by the structures with suspended lines presented in figures 4(*b*)–(*d*).

It can be seen that the suspended lines partly adhered to the adjacent lines. This occurred during the development step and was caused by the surface tension of the rinsing solvent [37–39]. The measured heights of the supporting walls differed from the model dimensions presented in figure 4(*a*), especially as the wall height increased. This could be explained by measurement error caused by the tilting of the structures, material shrinkage or the combination of these effects. Overall, it was discovered that with the focus position of 10 μm and higher (figures 4(*c*) and (*d*)), the lines were no longer surface bound and had the constant height of approximately 5.4 μm.

3.2. Effect of varying the average laser power

Both the width and height of the polymer lines were found to increase with the increasing average laser power, as can be seen from figure 5. Line height, however, was affected much more than line width, which is characteristic of the 2PP phenomenon due to the ellipsoidal shape of the merged voxels that the lines are formed of [36, 40, 41]. By increasing only the laser power, line width was increased from 850 nm to 3.4 μm and line height from 3.3 to 13.6 μm. It can be

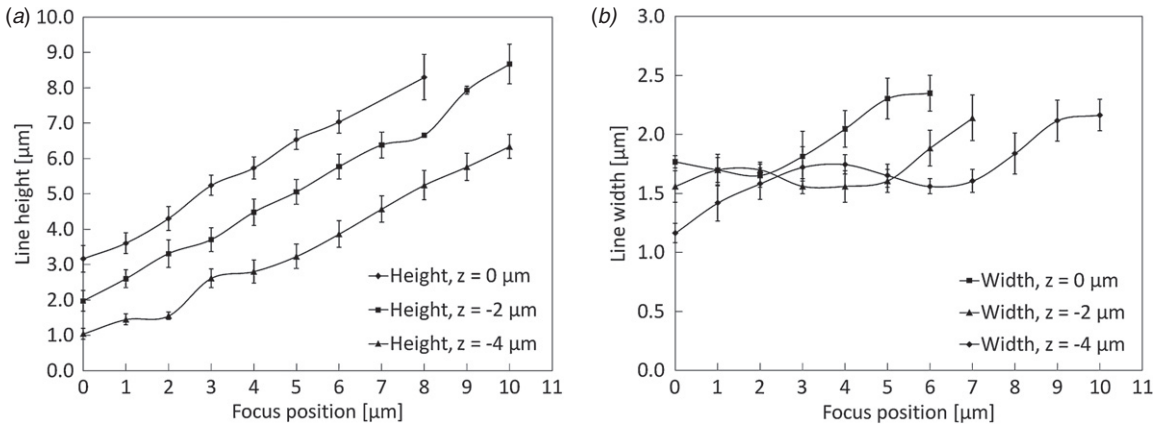

Figure 3. (*a*) Line height and (*b*) width as functions of the laser beam focus position. The dimensions were measured from three arrays fabricated with different initial z-positions, with the negative sign indicating a position closer to the glass slide surface. The data points represent the mean of five measurements ± standard deviation.

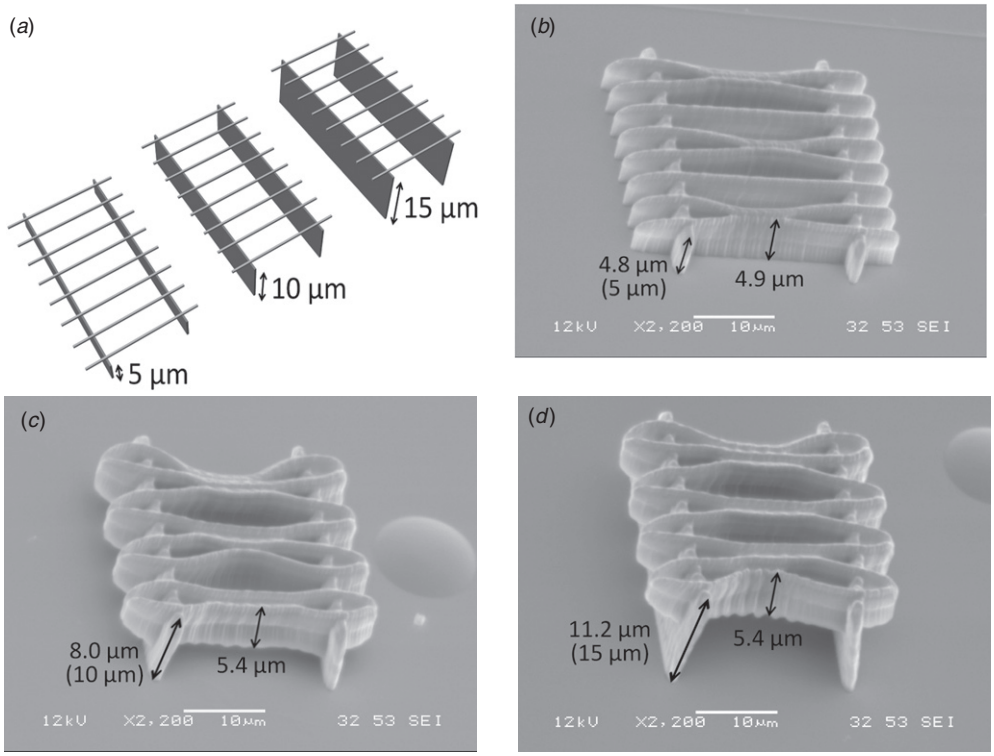

Figure 4. (*a*) The designs of the suspended structures. The distance between each horizontal line was 5 μm. Suspended lines polymerized on top of supporting walls of different measured heights: (*b*) 5.0 μm, (*c*) 8.8 μm and (*d*) 11.5 μm. The corresponding wall heights of the models are in parentheses.

seen from figure 5 that the line height values do not form a continuous graph. This was most likely caused by a slight difference in the initial laser beam focus position between the fabricated line arrays, especially since this discrepancy was only present in the line height graph. Judging by the structure quality, the power range could be divided into the so-called processing window, 0.36–1.61 mW (26–46 GW cm^{-2}), and damage zone. The onset of the damage zone was observed at the average laser power of 1.67 mW (91 GW cm^{-2}) indicated by the increased microbubble formation and distortion of the polymer lines.

3.3. Effect of varying the scanning speed

Figure 6 shows an example of the line arrays polymerized with a constant laser power and an increasing scanning speed. The line width and height measured from the SEM images of the fabricated arrays are depicted in figure 7.

As shown in figure 7, the line dimensions first decreased rapidly with the increasing scanning speed until the scanning speed of 200 μm s^{-1} and then remained nearly constant at higher speeds. However, the uniformity of the lines started to decrease substantially after the scanning speed of 150 μm s^{-1}, as depicted in figure 6. Between the

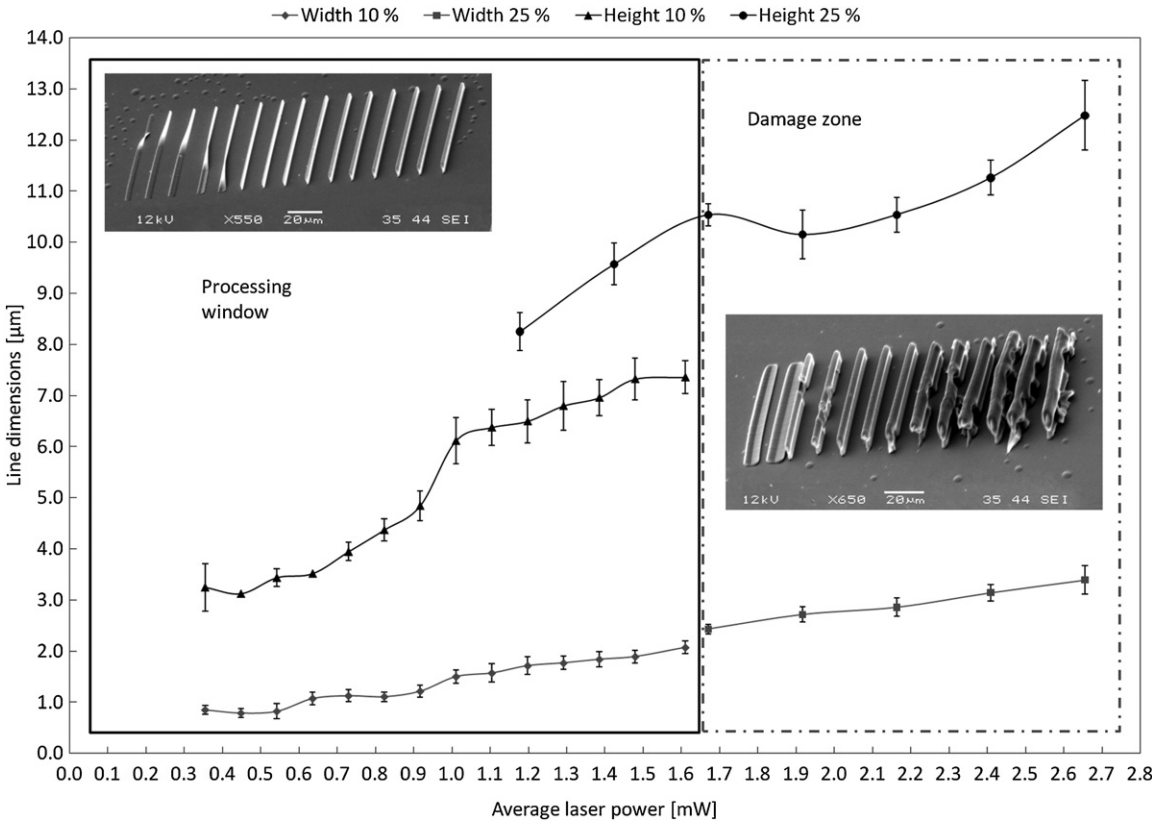

Figure 5. Line dimensions as functions of the average laser power (measured before the objective). Data points represent the mean of five measurements ± standard deviation. SEM images show the quality of the structures inside the processing window (solid line) and the damage zone (dashed line).

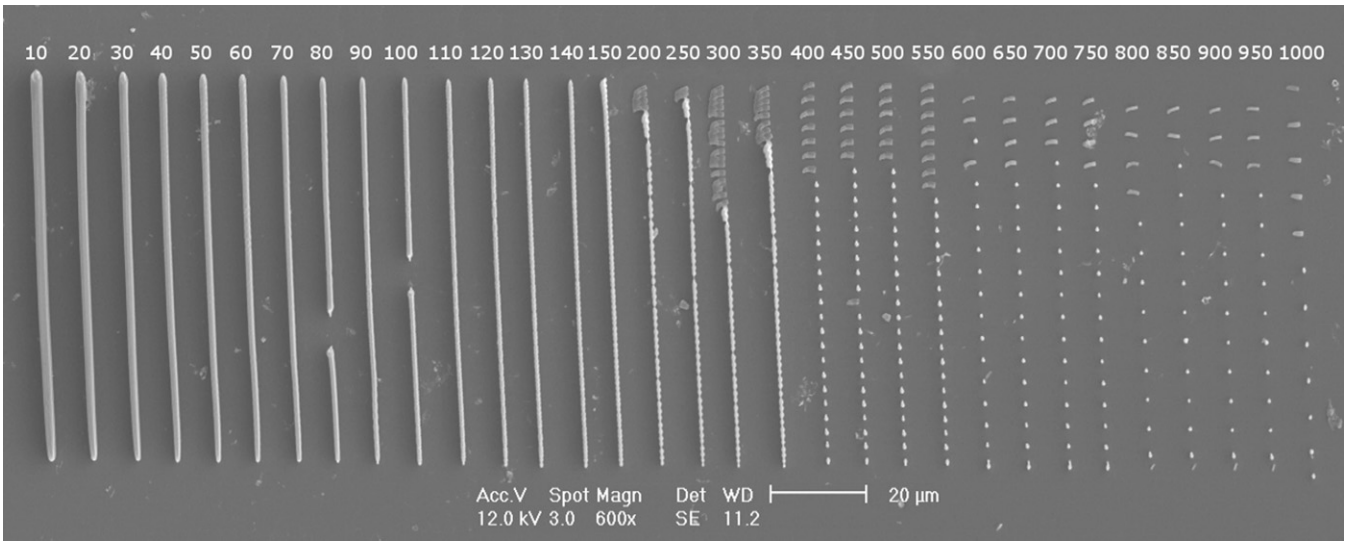

Figure 6. Lines polymerized with the constant laser power of 1.00 mW (63 GW cm^{-2}) and increasing scanning speeds, 10–1000 μm s^{-1} (indicated in white above the lines), in the left-to-right direction. The gaps in the lines fabricated with the scanning speeds of 80 μm s^{-1} and 100 μm s^{-1} were caused by microbubbles.

speeds 200 and 350 μm s^{-1}, the surface roughness of the line increased and some gaps started to form between the individual voxels, which finally led to the formation of completely discontinuous lines at the scanning speed of 400 μm s^{-1} and higher with both of the polymerization powers used. In order to assess the cause of this phenomenon, the so-called spot overlap was calculated from

$$\text{spot overlap } \% = \left(1 - \frac{v}{f \times s}\right) \times 100, \tag{3}$$

where v is the scanning speed, f is the laser pulse frequency and $s = 2w$ is the laser beam spot diameter. In our case,

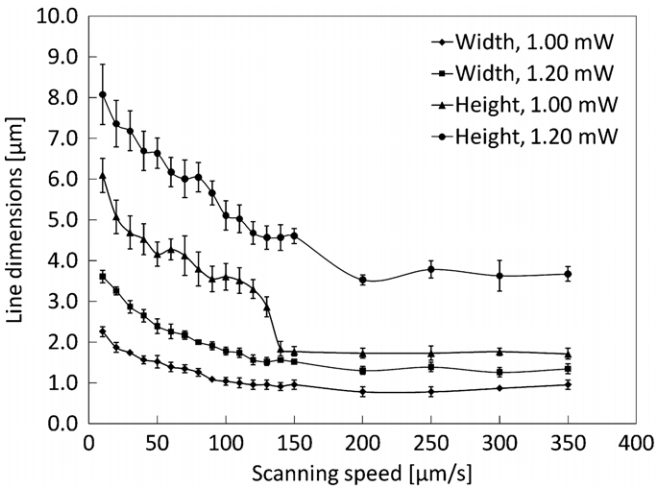

Figure 7. Line dimensions as a function of the scanning speed for the laser powers of 1.00 mW (63 GW cm^{-2}) and 1.20 mW (158 GW cm^{-2}). Data points represent the mean of five measurements ± standard deviation.

the spot diameter was 865 nm. For the used laser powers of 1.00 mW and 1.20 mW, the laser pulse frequency was 6.6 kHz and 3.2 kHz, respectively. Thus, for the scanning speed of 400 μm s^{-1}, the spot overlaps were calculated to be still as high as 93% and 86%. As can be seen from figure 6, the gaps between the voxels further increased at the scanning speeds of 600 and 800 μm s^{-1}. It was found that the length of these gaps, i.e. the inter-voxel distance, was approximately 3, 4 and 6 μm for the scanning speeds of 400, 600 and 800 μm s^{-1}, respectively, and these values were independent of the processing parameters used. Rather than affecting the inter-voxel distance, increasing the polymerization power and lowering the pulse frequency resulted in larger voxels. When analyzed further, it was found that the number of laser pulses occurring during the measured inter-voxel distances was the same for all the distances of 3, 4 and 6 μm within an array fabricated with certain parameters. That is, with the power of 1.00 mW and the pulse frequency of 6.6 kHz, the number of pulses needed to produce one voxel was 49, whereas with 1.20 mW and 3.2 kHz, only 19 pulses were needed. This difference can be explained by the fact that the intensity of the latter pulses was over two times higher, that is 158 GW cm^{-2} compared to 63 GW cm^{-2}.

3.4. Comparison of the AFM and SEM data

In order to measure the dimensions of the structures more precisely and to verify the accuracy of the SEM image-based measurements, voxel and line arrays were imaged with AFM. Figure 8 shows an array of voxels imaged with SEM (*a*) and an example image of the corresponding AFM images (*b*). The measured heights and widths of the complete, fallen voxels are presented in figures 9(*a*) and (*b*), respectively.

The minimum obtained width and height of voxels were found to be 210 nm and 1.95 μm, respectively. Figure 10 shows a SEM image and one example of the corresponding AFM images of an ascending array of lines polymerized with a constant laser power of 1.40 mW (44 GW cm^{-2}) and scanning speed of 50 μm s^{-1}. The line dimensions measured from these images are presented in figure 11. The last fallen line has been omitted.

The previously observed difference between the *z*-rise of the laser beam focus and the increase in line height was confirmed by AFM imaging. Based on the data presented in figure 11(*a*), the average line height increase was only approximately 0.53 μm ± 0.13 μm instead of the 1 μm predicted by the *z*-rise. The cause of this phenomenon is yet to be determined. It can be seen from figures 9 and 11 that measuring from SEM images gives very accurate results. With voxel dimensions, the average difference between the SEM and AFM measurements was approximately 300 nm for voxel width and only 230 nm for voxel height. The slight differences were most likely caused by the challenge of accurately estimating the voxel boundaries from the SEM images. Line height could also be measured very accurately from tilted SEM images, with the average variation of only 500 nm between the two analysis techniques. It was clear, however, that line width could not be reliably measured by AFM due to the very steep profile of the lines. This made it impossible for the tip to accurately reproduce the width profile of the lines, especially with the increasing line height as shown in figure 11(*b*). Based on these results, it can be concluded that the described SEM-based measurement technique is very accurate and appropriate for determining the dimensions of 2PP structures.

4. Discussion

The technique of DLW combined with 2PP is utilized increasingly in various microfabrication applications due to the flexibility to fabricate both 2D and 3D structures with ultra-high resolution. Thus far, most of the research in this field has concentrated on the utilization of costly femtosecond lasers to induce polymerization. The use of more affordable laser types, such as picosecond and continuous-wave lasers, has been very limited. In this work, we have demonstrated 2PP-based microfabrication using an affordable Nd:YAG laser with 800 ps pulses working at the wavelength of 532 nm. With the hybrid polymer–ceramic material Ormocomp®, the effect of different processing parameters on the achievable resolution was studied in detail. By utilizing the so-called ascending scan technique, we successfully demonstrated the fabrication of suspended structures. This result enables the future modeling and fabrication of open structures, such as microchannels and porous scaffolds for tissue engineering.

By varying the average laser power used for polymerization, we defined the so-called processing window and damage zone for the Ormocomp® material. To the best of our knowledge, this is the first time that the polymerization and damage zones have been reported for Ormocomp®. The onset of the damage zone was indicated by increased microbubble formation resulting from the high laser power and intensity, which severely distorted the polymer lines. However, as the intensity at the damage threshold was in the order of 0.1 TW cm^{-2}, an order of magnitude smaller than the

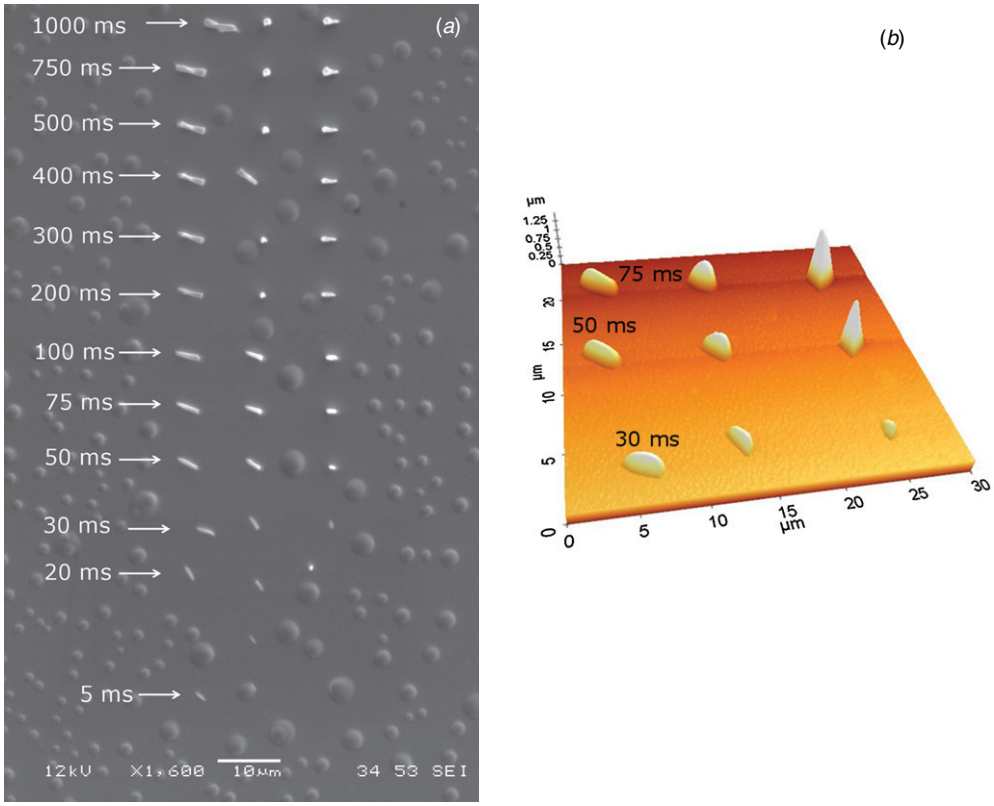

Figure 8. An array of voxels imaged with (*a*) SEM (exposure time for individual voxels indicated in white) and (*b*) an example of a corresponding AFM image. Voxels were fabricated with the ascending scan method with a constant laser power of 0.54 mW (33 GW cm^{-2}) and laser exposure time of 5–1000 ms.

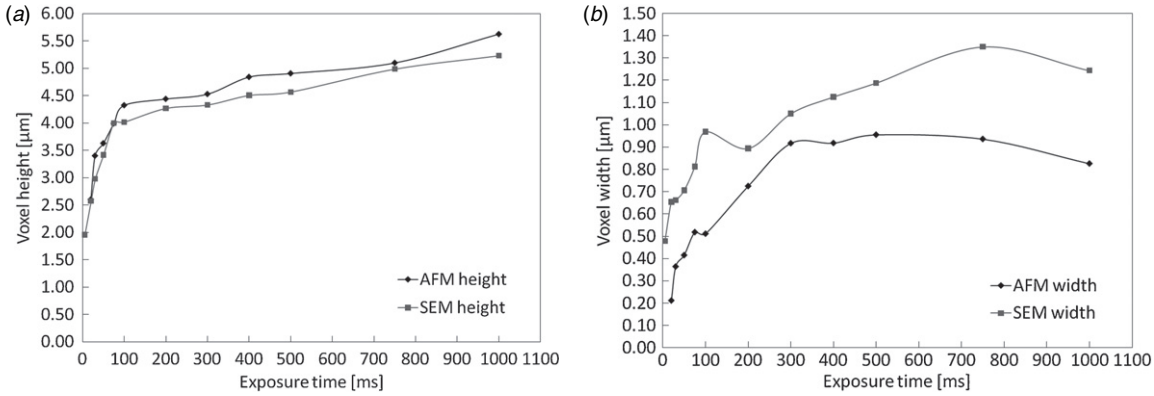

Figure 9. (*a*) Heights and (*b*) widths of the complete, fallen voxels measured from the SEM and AFM images in figure 8.

recently reported breakdown threshold for a polymer–ceramic material [25], it is unlikely that dielectric breakdown was contributing to the material damage. To ensure the integrity of the polymerized structures, fabrication should be carried out within the power and intensity range of the processing window. As demonstrated in figure 5, inside the processing window, the dimensions and the mechanical strength of the structures can be tuned by varying the employed laser power.

When studying the effect of the laser scanning speed on the structure dimensions, it was found that uniform polymer lines could be produced with scanning speeds between 10 and 150 μm s^{-1}. At higher speeds, gaps started to form between the individual voxels, leading to the formation of completely discontinuous lines at the scanning speed of 400 μm s^{-1} and higher. This threshold scanning speed value was found to be independent of the laser polymerization power, suggesting that at high speeds, the scanning speed is the more dominant parameter affecting the structure quality. With the scanning speed of 400 μm s^{-1}, the calculated spot overlap was still 93% and 86% for the two different laser powers and frequencies used. Thus, the complete voxel separation cannot be explained by a lack of spot overlap with this scanning speed. Rather, it can be explained by threshold behavior, which is characteristic of the 2PP phenomenon. The polymerization threshold is not overcome with each laser pulse, but rather with the accumulated fluence of a number of pulses. Thus,

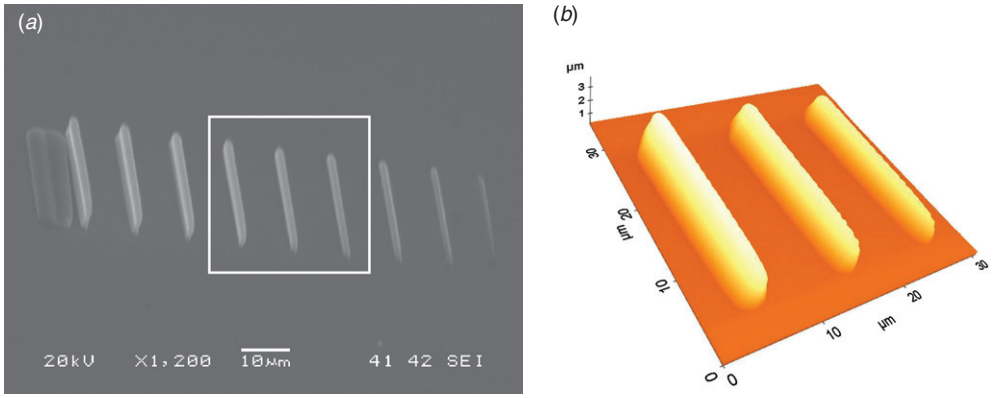

Figure 10. (*a*) SEM image of an ascending array of lines polymerized with the laser power of 1.40 mW (44 GW cm^{-2}) and scanning speed of 50 μm s^{-1}. The last fallen line has been omitted. (*b*) Corresponding AFM image of the fourth, fifth and sixth line from the right, indicated by the white box in the SEM image.

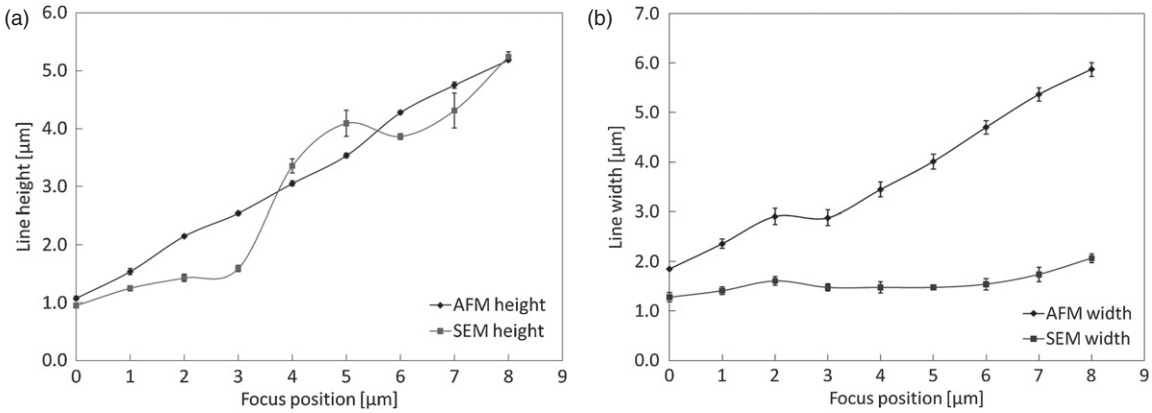

Figure 11. Line (*a*) height and (*b*) width measured from SEM and AFM images as functions of the laser beam focus position. Data points represent the mean of five measurements ± standard deviation.

discontinuous lines were formed even though the spot overlap remained very high. By increasing the polymerization power, however, the size of the voxels could be increased. Below the scanning speed of 400 μm s^{-1}, laser power could thus be used to tune the line size. The optimal scanning speed and polymerization power are case specific. With sufficiently small inter-layer distance, uniform 3D structures could still likely be formed even with scanning speeds as high as 350 μm s^{-1}, given that sufficiently high powers and intensities are used. However, polymerized structures could thus suffer from rough surface and poor mechanical stability. Therefore, the optimal scanning speed is a compromise between decreasing the polymerization time and achieving smooth surfaces and good mechanical integrity. When the smallest achievable feature size is desired, fabrication close to the polymerization threshold is required. However, when aiming for 3D structures with good mechanical stability, moving to a higher power range within the polymerization window can be beneficial as higher scanning speeds can then be used to produce uniform layers with a reduced fabrication time.

The minimum obtained width and height of voxels were found to be 210 nm and 1.95 μm, respectively. This shows a tremendous improvement of 90% and 70% in the voxel-based lateral and longitudinal resolution compared to our previously reported results [30]. The demonstrated capability to fabricate nanometer scale voxels could in the future be utilized for creating additional surface topography on micro scale 3D structures, for example. The aspect ratio of the voxels fabricated with this type of a 2PP set-up remained high, namely between 4 and 12. This can most likely be attributed to the choice of numerical aperture of the objective lens, which in our case was 0.90. It has been shown previously that with a higher numerical aperture, such as 1.40, better resolution in the form of more spherical voxels with an aspect ratio closer to 1 can be obtained. The use of a numerical aperture smaller than 1 generally results in taller and slimmer voxels and thus to high aspect ratio [4, 41, 42]. Resolution data for Ormocomp® has previously been reported only for femtosecond 2PP systems. The best resolution has been reported by Serbin *et al*, who have achieved a minimum voxel width and height of 140 nm and 600 nm, respectively [34]. With a similar fabrication set-up, Woggon *et al* have reported somewhat larger values of 490 nm and 2.3 μm [33]. Thus, the voxel dimensions reported here are comparable to the minimum dimensions reported for Ormocomp® with a femtosecond laser system combined with higher numerical aperture optics. Instead of voxels, Jeon *et al* have studied the fabrication of Ormocomp® lines with a

femtosecond laser with lower numerical aperture optics (NA = 0.55) and reported the minimum line width and height of 800 nm. We achieved a similar minimum line width and height of 1.0 μm with our picosecond laser system. These results prove that very high resolution and even nanometer scale structures are achievable with a low-cost picosecond laser system.

5. Conclusions

We studied the effect of different process parameters on the resolution of 2PP utilizing a low-cost picosecond laser system. The impact of the laser beam focus position, average laser power and scanning speed were investigated with Ormocomp® microstructures. AFM imaging confirmed the presented SEM image-based measurements to be highly accurate. The discovered relationships between the different process parameters and structure dimensions enable the fabrication of both 3D microstructures and nanometer scale surface features. The work shows that very high resolution is achievable with a low-cost picosecond laser system, with feature sizes comparable to those previously reported only for costly femtosecond laser systems. This can in the future enable the use of 2PP in more wide-spread research and industrial applications.

Acknowledgments

The work was funded by the Finnish Cultural Foundation and the Finnish Foundation for Technology Promotion. The authors gratefully acknowledge MSc (Eng) Niina Ahola for AFM imaging and MSc (Eng) Vuokko Heino for SEM imaging.

References

[1] Maruo S and Ikuta K 2000 *Appl. Phys. Lett.* **76** 2656–8
[2] Tan D, Li Y, Qi F, Yang H, Gong Q, Dong X and Duan X 2007 *Appl. Phys. Lett.* **90** 071106–3
[3] Haske W, Chen V W, Hales J M, Dong W, Barlow S, Marder S R and Perry J W 2007 *Opt. Express* **15** 3426–36
[4] Dong X, Zhao Z and Duan X 2008 *Appl. Phys. Lett.* **92** 091113
[5] Juodkazis S, Mizeikis V, Seet K K, Masafumi M and Misawa H 2005 *Nanotechnology* **16** 846
[6] Park S-H, Yang D-Y and Lee K-S 2009 *Laser Photon. Rev.* **3** 1–11
[7] Lee K, Yang D, Park S H and Kim R H 2006 *Polym. Adv. Technol.* **17** 72–82
[8] Seet K K, Mizeikis V, Juodkazis S and Misawa H 2006 *Appl. Phys. Lett.* **88** 221101
[9] Ovsianikov A *et al* 2008 *Laser Chem.* **2008** 493059
[10] Staude I, Thiel M, Essig S, Wolff C, Busch K, von Freymann G and Wegener M 2010 *Opt. Lett.* **35** 1094–6
[11] Klein S, Barsella A, Taupier G, Stortz V, Fort A and Dorkenoo K D 2006 *Appl. Surf. Sci.* **252** 4919–22
[12] Reinhardt C, Seidel A, Evlyukhin A, Cheng W, Kiyan R and Chichkov B 2010 *Appl. Phys.* A **100** 347–52
[13] Cojoc G, Liberale C, Candeloro P, Gentile F, Das G, De Angelis F and Di Fabrizio E 2010 *Microelectron. Eng.* **87** 876–9
[14] Wu D, Wu S, Niu L, Chen Q, Wang R, Song J, Fang H and Sun H 2010 *Appl. Phys. Lett.* **97** 031109–3
[15] LaFratta C N, Lim D, O'Malley K, Baldacchini T and Fourkas J T 2006 *Chem. Mater.* **18** 2038–42
[16] Knoll A, Dürig U, Züger O and Güntherodt H-J 2006 *Microelectron. Eng.* **83** 1261–4
[17] Ovsianikov A, Chichkov B, Mente P, Monteiro-Riviere N A, Doraiswamy A and Narayan R J 2007 *Int. J. Appl. Ceram. Technol.* **4** 22–9
[18] Gittard S D, Ovsianikov A, Monteiro-Riviere N A, Lusk J, Morel P, Minghetti P, Lenardi C, Chichkov B N and Narayan R J 2009 *J. Diabetes Sci. Technol.* **3** 304–11
[19] Jeon H, Hidai H, Hwang D J and Grigoropoulos C P 2010 *J. Biomed. Mater. Res.* A **93** 56–66
[20] Jeon H, Hidai H, Hwang D J, Healy K E and Grigoropoulos C P 2010 *Biomaterials* **31** 4286–95
[21] Klein F, Striebel T, Fischer J, Jiang Z, Franz C M, von Freymann G, Wegener M and Bastmeyer M 2010 *Adv. Mater.* **22** 868–71
[22] Seidlits S K, Schmidt C E and Shear J B 2009 *Adv. Funct. Mater.* **19** 3543–51
[23] Doraiswamy A, Jin C, Narayan R J, Mageswaran P, Mente P, Modi R, Auyeung R, Chrisey D B, Ovsianikov A and Chichkov B 2006 *Acta Biomater.* **2** 267–75
[24] Seet K K, Juodkazis S, Jarutis V and Misawa H 2006 *Appl. Phys. Lett.* **89** 024106–3
[25] Malinauskas M, Zukauskas A, Bickauskaite G, Gadonas R and Juodkazis S 2010 *Opt. Express* **18** 10209–21
[26] Thiel M, Fischer J, von Freymann G and Wegener M 2010 *Appl. Phys. Lett.* **97** 221102–3
[27] Wang I, Bouriau M, Baldeck P L, Martineau C and Andraud C 2002 *Opt. Lett.* **27** 1348–50
[28] Kaehr B, Ertas N, Nielson R, Allen R, Hill R T, Plenert M and Shear J B 2006 *Anal. Chem.* **78** 3198–202
[29] Jariwala S, Venkatakrishnan K and Tan B 2010 *Opt. Express* **18** 1630–6
[30] Käpylä E, Turunen S and Kellomäki M 2010 *Micro Nanosyst.* **2** 87–99
[31] Ritschdorff E T and Shear J B 2010 *Anal. Chem.* **82** 8733–7
[32] Malinauskas M, Danilevičius P and Juodkazis S 2011 *Opt. Express* **19** 5602–10
[33] Woggon T, Kleiner T, Punke M and Lemmer U 2009 *Opt. Express* **17** 2500–7
[34] Serbin J, Egbert A, Ostendorf A, Chichkov B N, Houbertz R, Domann G, Schulz J, Cronauer C, Fröhlich L and Popall M 2003 *Opt. Lett.* **28** 301–3
[35] Liu Y, Nolte D D and Pyrak-Nolte L J 2010 *Appl. Phys.* A **100** 181–91
[36] Sun H-B, Tanaka T and Kawata S 2002 *Appl. Phys. Lett.* **80** 3673–5
[37] Kondo T, Juodkazis S and Misawa H 2005 *Appl. Phys.* A **81** 1583–6
[38] Park S-H, Kim K H, Lim T W, Yang D-Y and Lee K-S 2008 *Microelectron. Eng.* **85** 432–9
[39] Sun M-Z, Li Y, Cui H-B, Yang H and Gong Q-H 2010 *Appl. Phys.* A **100** 177–80
[40] Sun H-B, Takada K, Kim M, Lee K and Kawata S 2003 *Appl. Phys. Lett.* **83** 1104–6
[41] Sun H-B, Maeda M, Takada K, Chon J W M, Gu M and Kawata S 2003 *Appl. Phys. Lett.* **83** 819–21
[42] Fitilis I, Fakis M, Polyzos I, Giannetas V and Persephonis P 2010 *J. Photochem. Photobiol.* A **215** 25–30

Publication III

E. Käpylä, D. B. Aydogan, S. Virjula, S. Vanhatupa, S. Miettinen, J. Hyttinen, M. Kellomäki

Direct laser writing and geometrical analysis of scaffolds with designed pore architecture for three-dimensional cell culturing

Journal of Micromechanics and Microengineering 22(2012)11, p. 115016

J. Micromech. Microeng. **22** (2012) 115016 (13pp) doi:10.1088/0960-1317/22/11/115016

Direct laser writing and geometrical analysis of scaffolds with designed pore architecture for three-dimensional cell culturing

Elli Käpylä[1,2], Dogu Baran Aydogan[1,2], Sanni Virjula[1,2,3,4], Sari Vanhatupa[2,3,4], Susanna Miettinen[2,3,4], Jari Hyttinen[1,2] and Minna Kellomäki[1,2]

[1] Department of Biomedical Engineering, Tampere University of Technology, PO Box 692, FI-33101 Tampere, Finland
[2] BioMediTech, Biokatu 10, FI-33520 Tampere, Finland
[3] Institute of Biomedical Technology, Adult Stem Cell Group, University of Tampere, FI-33014 Tampere, Finland
[4] Science Centre, Pirkanmaa Hospital District, PO Box 2000, FI-33521 Tampere, Finland

E-mail: elli.kapyla@tut.fi

Received 3 July 2012, in final form 28 August 2012
Published 26 September 2012
Online at stacks.iop.org/JMM/22/115016

Abstract
Traditional scaffold fabrication methods used in tissue engineering enable only limited control over essential parameters such as porosity, pore size and pore interconnectivity. In this study, we designed and fabricated five different types of three-dimensionally interconnected, highly porous scaffolds with precise control over the scaffold characteristics. We used two-photon polymerization (2PP) with a commercial polymer–ceramic material (Ormocomp®) for scaffold fabrication. Also for the first time, we analyzed the 2PP fabrication accuracy with respect to scaffold design parameters. Our results showed that the porosity values decreased up to 13% compared to the design specifications due to the fabrication process and the shrinkage of the material. Finally, we showed that our scaffolds supported human adipose stem cell adhesion and proliferation in a six day culture. By precise tuning of scaffold parameters, our design and fabrication method provides a novel approach for studying the effect of scaffold architecture on cell behavior *in vitro*.

S Online supplementary data available from stacks.iop.org/JMM/22/115016/mmedia

(Some figures may appear in colour only in the online journal)

1. Introduction

Cells in the body are typically supported by a complex three-dimensional (3D) extracellular matrix, which varies from tissue to tissue. This environment cannot be accurately represented by traditional two-dimensional (2D) cell culture surfaces, such as well plates. For this reason, cells are often combined with porous scaffold structures that have been fabricated by methods like solvent casting, porogen leaching, freeze drying and gas foaming. However, these types of scaffolds suffer from an inhomogeneous structure, poor reproducibility and lack of precise control over essential scaffold parameters such as pore size, porosity and pore interconnectivity [1]. In order to systematically study cell behavior in a 3D environment, more advanced fabrication methods are needed to produce scaffolds with accurately defined micro- and nanoscale features [1].

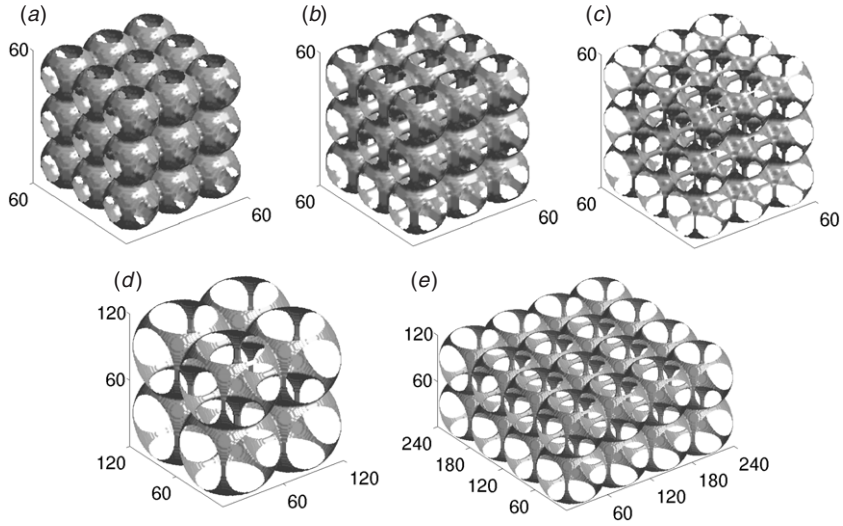

Figure 1. The designed scaffold models: (*a*) type I, (*b*) type II, (*c*) type III, (*d*) type IV and (*e*) type V. The dimensions are given in micrometers.

One potential fabrication approach is a rapid prototyping method of two-photon polymerization (2PP). 2PP is a direct laser writing technique based on the phenomenon of two-photon absorption (2PA). In 2PA, photoinitiator molecules are transformed into radicals by the simultaneous absorption of two photons and these radicals initiate the polymerization chain reaction inside a photosensitive material. Due to the nonlinear nature of the 2PA phenomenon, the polymerization is restricted to the vicinity of the focal spot of the laser beam, which makes 2PP an inherently 3D fabrication method [2, 3]. The smallest elements and the basic building blocks of two-photon polymerized structures are ellipsoidal voxels (volume elements) [4]. The resolution of 2PP can be tuned by the choice of the focusing optics and laser irradiation parameters, and feature sizes below 100 nm can be achieved with optimal conditions [5–8]. Scaffolds with length scales ranging from nanometers to millimeters can be reproducibly created from CAD designs in a single fabrication step.

The precise and flexible micro- and nanofabrication capability has made 2PP an increasingly popular approach for 3D fabrication in optics, microelectronics and biomedicine. In the field of biomedicine, 2PP has been used to create 2D line patterns to study cell adhesion and migration [9–11]. This type of work has also recently been expanded to 3D using hydrogels [12] and structures such as pillar arrays [13, 14] and woodpiles [15, 16]. Another type of approach is to use the unique 3D fabrication capability of 2PP to create scaffolds for cell culturing. It has been shown that hepatocytes cultured on two-photon polymerized scaffolds with interconnected square shaped pores maintained superior liver-specific functions compared to 2D culture [17]. However, the 3D scaffolds fabricated by 2PP thus far have generally had simple cubic [17–19], cylindrical [20, 21] or woodpile designs [22]. Although shown to support adhesion and growth of various cell types, the reported scaffold designs lack tuning of key parameters, such as porosity and pore interconnectivity. Precise control of these parameters is vital because they directly influence oxygen and nutrient delivery and waste removal within scaffolds [23]. The aim of this study was to fabricate scaffolds with precisely defined pore architecture using 2PP and to evaluate the achieved fabrication accuracy. As a proof-of-concept, we also assessed the capability of the scaffolds to support the adhesion and proliferation of human adipose stem cells (hASC) in a six day culture.

2. Materials and methods

2.1. Scaffold design

The design principle was to have full control over scaffold geometry. The scaffolds consisted of repeating unit cells of hollow spheres. This type of unit cell structure was chosen because it enabled the generation of highly porous scaffolds and the straightforward tuning of porosity and interconnectivity values. A MATLAB® routine was coded to create the structures based on initial design parameters such as pore size and pore interconnectivity. The scaffold models were generated as 3D matrices. A total of five different types of scaffolds (types I–V) were designed, as shown in figure 1.

The type I, II and III scaffold models consisted of 20 μm wide unit cells and had the overall size of $3 \times 3 \times 3$ unit cells. The model-based porosities of the type I, II and III scaffolds were calculated as 87.8%, 89.3% and 93.5%, respectively. The type IV and type V scaffolds consisted of a total of $2 \times 2 \times 2$ and $4 \times 4 \times 2$ of 60 μm wide unit cells and had the model-based porosity of 97.8%. The porosities of the scaffold models were calculated using a MATLAB® code in three steps. In the first step, the total volume of each unit cell was calculated. In the second step, the volume of material in each unit cell was calculated. Finally, the total porosity was calculated using the results of the two previous steps. The details of the computation are provided in the appendix. The scaffold models were also designed to have different degrees of interconnectivity. The degree of interconnectivity was assessed by using the diameter of the circular opening connecting the unit cells and the unit cell size. If c represents the circular opening connecting the

Table 1. Design parameters of the scaffold models.

Scaffold model type	I	II	III	IV	V
Number of unit cells	3 × 3 × 3	3 × 3 × 3	3 × 3 × 3	2 × 2 × 2	4 × 4 × 2
Overall size (μm×μm×μm)	60 × 60 × 60	60 × 60 × 60	60 × 60 × 60	120 × 120 × 120	240 × 240 × 120
Wall thickness (μm)	1.0	1.0	1.0	1.0	1.0
Porosity (%)	87.8	89.3	93.5	97.8	97.8
Unit cell dimension (a) (μm)	20	20	20	60	60
Opening diameter (c) (μm)	12	14	18	54	54
Interconnectivity parameter (c/a)	0.60	0.70	0.90	0.90	0.90

unit cells and a is the unit cell size, then c/a is assigned as the interconnectivity parameter. Based on this parameter, the type I scaffold had the lowest interconnectivity and the type III, IV and V scaffolds had the highest interconnectivity. The design parameters of the different scaffold models are summarized in table 1.

2.2. Scaffold fabrication by two-photon polymerization

The scaffolds were fabricated with a custom-built 2PP set-up that has been described previously in [24]. Briefly, the system was based on an Nd:YAG picosecond laser (PULSELAS-P-1064-300-FC, Alphalas GmbH, Germany) emitting at 532 nm with a pulse duration of 800 ps, maximum frequency of 13 kHz and an average output power of 100 mW. The movement of the laser beam in the xy- and z-directions was controlled with a fast steering mirror scanner (FSM-300, Newport Corporation, USA) and a piezo focusing unit (Mipos 250 SGEX, Piezosystem Jena GmbH, Germany), respectively. The laser output power was attenuated to a suitable average polymerization power of approximately 1 mW measured at the back aperture of the objective. The beam was directed through an upright microscope frame (ECLIPSE ME 600, Nikon, Japan) to the microscope objective of choice.

For 2PP, the scaffold models were exported to Rhinoceros® 4.0 CAD program (Robert McNeel & Associates, USA) in .stl file format and sliced to contours in the z-direction. The contour spacing was set to 0.5 μm, which is the minimum value allowed by our current system. A commercial polymer–ceramic hybrid material Ormocomp® (Micro Resist Technology GmbH, Germany) was used as the scaffold material in combination with 2 wt% of the photoinitiator Irgacure®127 (Ciba Specialty Chemicals, Switzerland). For the polymerization, a drop of Ormocomp® was sandwiched between a microscope slide and a coverslip separated by 250 μm thick stainless steel spacer. After the polymerization, the non-illuminated monomer solution was removed by immersing the samples in the Ormodev® solvent (Micro Resist Technology) for approximately 5 min and by rinsing with Ormodev® and hexamethyldisilazane.

The quality of structures fabricated by 2PP is affected by the choice of the microscope objective and the processing parameters, such as average laser power and laser beam scanning speed. In this study, we used 50 × (NA = 0.90) and 20 × (NA = 0.75) oil immersion objectives for polymerization. These objectives focused the laser beam to spot radii of approximately 430 and 520 nm, respectively. The spot radii were estimated as radii of Airy disks, multiplied by the laser beam quality factor M^2 as described in [24]. It has been previously reported that decreasing the numerical aperture of the objective lens can lead to the formation of larger voxels, especially in the z-direction [25, 26]. It was therefore hypothesized that the use of the 20× objective would increase voxel size and enable faster scanning. The type I, II and III scaffolds were produced using the 50× objective, average laser power of 1.1 mW and scanning speed of 120 μm s^{-1}. The type IV scaffold model was used to optimize the processing parameters and minimize fabrication times for the fabrication of the larger type V scaffolds. For this purpose, scanning speeds of 80, 100 and 120 μm s^{-1} were tested with the 50× objective and scanning speeds of 150, 200, 240 and 300 μm s^{-1} with the 20× objective. The average laser power of approximately 1 mW was used with both objectives.

For the cell culturing experiments, type V scaffolds were fabricated on round glass coverslips with the diameter of 9 mm. Two scaffolds were fabricated on each coverslip using the 20× objective, scanning speed of 200 μm s^{-1} and the average laser power of 1.2–1.7 mW. The samples were disinfected by immersion in 70% (v/v) and 99.5% (v/v) ethanol for 15 min each. The ethanol was allowed to fully evaporate before the samples were placed in sterile 24-well plates for culturing.

2.3. Isolation and culturing of adipose stem cells

The study was conducted in accordance with the Ethics Committee of the Pirkanmaa Hospital District (Tampere, Finland, R03058). The hASCs were isolated from an adipose tissue sample collected from one female donor (age 42 yrs) undergoing elective plastic surgery at Tampere University Hospital (Tampere, Finland). The isolation was carried out using mechanical and enzymatic isolation procedures that have been described previously in [27, 28]. In brief, the adipose tissue sample was minced manually and digested with type I collagenase (1.5 mg mL^{-1}, Invitrogen, UK) in a water bath at 37 °C under shaking conditions. After sequential centrifugation and filtration steps, the isolated cells were maintained and expanded in T-75 cm^2 polystyrene flasks in the basal medium (BM) containing Dulbeccos modified Eagle medium/Hams nutrient mixture F-12 (DMEM/F-12 1:1, Invitrogen), 10% human serum (PAA Laboratories GmbH, Austria), 1% L-glutamine (GlutaMAX, Invitrogen) and 1% antibiotics (10 U mL^{-1} penicillin, 10 mg mL^{-1} streptomycin, Lonza, Belgium). The hASCs cultured in BM were detached using TrypLe Select (Invitrogen) and cryo-preserved in liquid nitrogen in a freezing solution containing human serum and 10% dimethyl sulfoxide (Hybri-Max, Sigma-Aldrich, MO,

USA). The thawed hASCs were expanded in BM and seeded at passages 2–5 onto pre-incubated type V scaffolds in a 24-well plate. The scaffolds in each well were first embedded in 500 μl of BM and then seeded with 2×10^4 hASCs in approximately 200 μl of BM. No additional protein coating was used to enhance cell adhesion. A total of four samples were cultured per time point (4 h, 2 d and 6 d). The culture medium was changed twice a week.

For identification and characterization of hASCs, flow cytometric surface marker expression analysis was performed after primary culture at passage 1 by a fluorescence-activated cell sorter (FACSAria, BD Biosciences, Belgium) as described earlier by Lindroos *et al* [29]. Monoclonal antibodies against CD14-phycoerythrin-cyanine (PE-Cy7), CD19-PE-Cy7, CD45R0-allophycocyanin (APC), CD54-fluorecein isothiocyanate (FITC), CD73-PE, CD90-APC (BD Biosciences, CA, USA), CD11a-APC, CD80-PE, CD86-PE, CD105-PE (R&D Systems Inc, MN, USA), CD34-APC and HLA-DR-PE (Immunotools GmbH, Germany) were used. Analysis was performed on 10^4 cells per sample and unstained cell samples were used to compensate for the background autofluorescence levels.

The attachment and viability of hASCs in type V scaffolds were studied using live/dead staining of duplicate samples at each time point. Briefly, the samples were incubated for 35 min at room temperature with a mixture of 0.8 μm ethidium homodimer-1 and 1.0 μm calcein acetoxymethyl ester (Molecular Probes/Invitrogen, OR, USA). The viable cells (green fluorescence) and necrotic cells (red fluorescence) were analyzed by fluorescence imaging (Olympus IX51, Olympus Corporation, Japan).

2.4. Assessment of cells by light microscopy and confocal imaging

In order to evaluate cell migration and proliferation, hASC-seeded samples were studied by a light microscope (Nikon Eclipse TE2000-S, Nikon, Japan) in bright field mode with a 10× air objective at each time point. One sample was also studied using a time-lapse microscopy system (Cell-IQ® v.2, Chip-Man Technologies Ltd, Finland) in phase contrast mode with a 10× air objective for an imaging period of six days. The two- and three-dimensional cell orientations were further studied at each time point from duplicate samples with a confocal microscope (LSM 700, Carl Zeiss Microimaging GmbH, Germany) with a 20× air objective. For the confocal imaging, the actin cytoskeleton and the cell nucleus were stained. In brief, the cells were first fixed and permeabilized with 4% paraformaldehyde containing 0.2% Triton x-100 (Sigma-Aldrich) for 10 min at room temperature and then blocked with 1% bovine serum albumin (Sigma-Aldrich) for 40 min at 4 °C. The primary antibody (goat anti-human vimentin, Millipore Chemicon) was diluted 1:100 with the blocking solution and then incubated with the cells overnight at 4 °C. The next day, Alexa Fluor® 488 conjugated anti-goat secondary antibody (1:500, Invitrogen) together with DAPI (1:1000, Molecular Probes) was diluted in the blocking solution and incubated with the cells for 35 min at room temperature. During the imaging, the samples were covered with distilled water without any additional mounting medium.

2.5. Assessment of scaffolds and cells by SEM imaging

The dimensions of the fabricated scaffolds were measured from SEM images (Philips XL-30, Philips Electron Optics, the Netherlands). For the imaging, samples were sputter coated with gold for 180 s in an argon atmosphere (S 150 Sputter Coater, Edwards Ltd, UK), which corresponded to a coating thickness of approximately 113 nm. The SEM images were analyzed with free software (GIMP 2.6).

The live/dead stained samples were also SEM imaged with the Philips XL-30 microscope. The samples were first fixed with 5% glutaraldehyde (Sigma-Aldrich) in phosphate buffer (pH 7.4) at room temperature for at least 48 h and then dehydrated by a graded ethanol series. The samples were immersed in ion-exchanged water for 15 min and in 10%, 20%, 40%, 60%, 80% (all v/v) ethanol solutions for 10 min each. Lastly, the samples were immersed in 99.5% (v/v) ethanol for 15 min and allowed to fully air dry before storing under vacuum. Prior to SEM imaging, the samples were sputter coated with gold for 120 s in an argon atmosphere (S 150 Sputter Coater, Edwards Ltd, UK), which corresponded to a coating thickness of approximately 75 nm.

3. Results

3.1. Scaffold fabrication

Type I, II and III scaffolds were successfully fabricated with the 50× objective, as shown by the SEM images in figure 2. With scanning speed of 120 μm s^{-1}, a type I scaffold was polymerized in approximately 18 min and type II and III scaffolds in approximately 15 min. Next, a series of type IV scaffolds were fabricated with the 50× and 20× objectives in order to find the optimal processing parameters for the fabrication of type V scaffolds. Figure 3 shows SEM images of the scaffolds fabricated with the 50× objective. Increasing the scanning speed from 80 μm s^{-1} to 120 μm s^{-1} reduced the scaffold IV fabrication time from 60 to 40 min. However, increasing the scanning speed also resulted in structural distortion of the scaffolds, which can be seen highlighted by the arrows in figures 3(*b*) and (*c*).

The difference in voxel size between the 50× and 20× objectives was evaluated from the interphase of the two unit cell layers as demonstrated in figure 4. We found that the scaffold wall height at the interphase increased from approximately 4.1 to 7.9 μm when switching from the 50× objective to the 20× objective. Due to increased voxel size, doubled and tripled scanning speeds could be used for scaffold fabrication with the 20× objective, as demonstrated in figure 5. With the highest scanning speed of 300 μm s^{-1}, the polymerization time of a type IV scaffold reduced to 14 min. It can be seen from figures 5(*e*)–(*h*) that increasing the scanning speed also increased the surface roughness of the scaffolds. Although the scaffolds fabricated with the two highest scanning speeds of 240 and 300 μm s^{-1} retained their shape, they suffered from more random distortions than

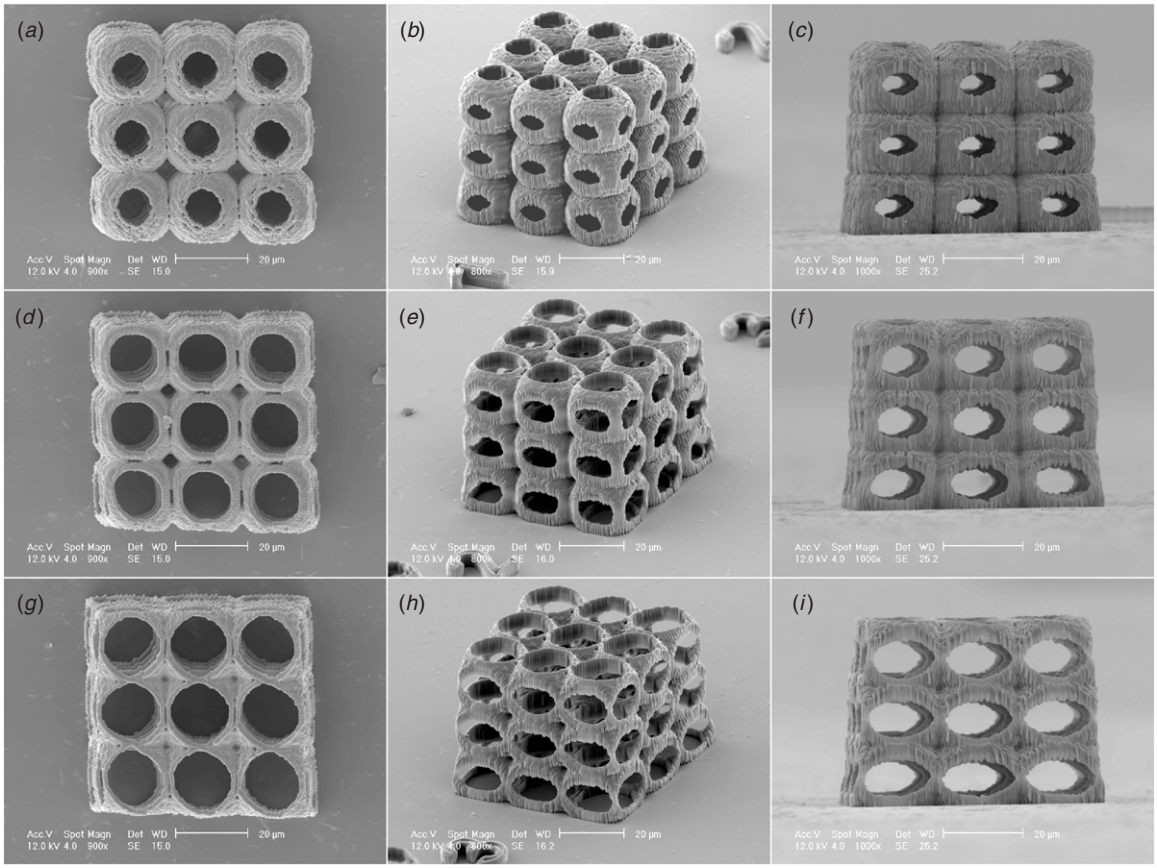

Figure 2. SEM images of scaffolds fabricated with the 50× objective: (*a*)–(*c*) type I, (*d*)–(*f*) type II and (*g*)–(*i*) type III. The images show the scaffolds from the tilt angles of 0° (first column), 60° (second column) and 90° (third column). Scale bars represent 20 μm.

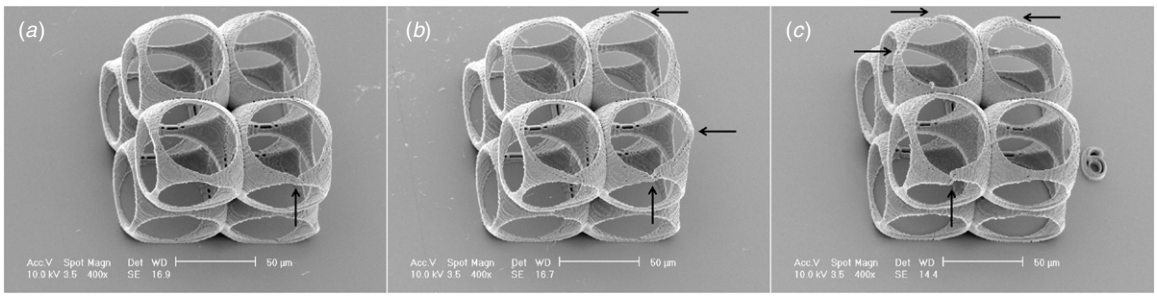

Figure 3. SEM images of type IV scaffolds fabricated with the 50× objective with scanning speeds of (*a*) 80 μm s^{-1}, (*b*) 100 μm s^{-1} and (*c*) 120 μm s^{-1}. The distortions of the scaffolds have been highlighted by arrows. All images have been taken from a 30° tilt. Scale bars represent 50 μm.

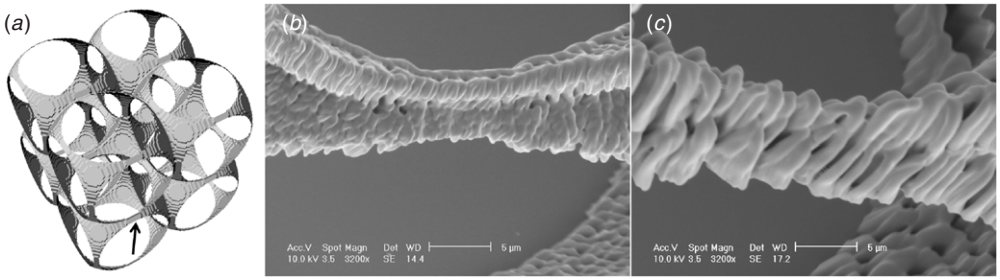

Figure 4. (*a*) The interphase of the two unit cell layers in the type IV scaffold model (indicated by the arrow). SEM images of the interphase polymerized with (*b*) the 50× objective at the scanning speed of 120 μm s^{-1} and (*c*) with the 20× objective at the scanning speed of 300 μm s^{-1}. The SEM images were taken from a 30° tilt. Scale bars represent 5 μm.

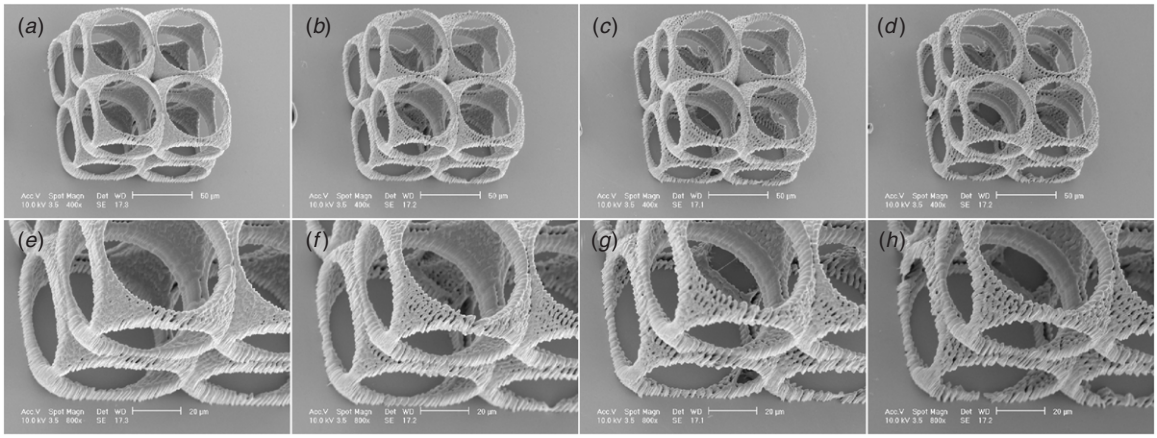

Figure 5. SEM images of type IV scaffolds fabricated with the 20× objective with scanning speeds of 150 μm s^{-1} (*a*) and (*e*), 200 μm s^{-1} (*b*) and (*f*), 240 μm s^{-1} (*c*) and (*g*) and 300 μm s^{-1} (*d*) and (*h*). All images have been taken from a 30° tilt. Scale bars represent 50 μm in (*a*)–(*d*) and 20 μm for (*e*)–(*h*).

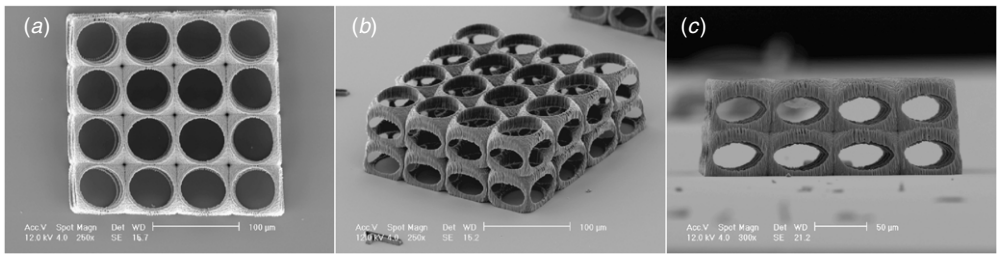

Figure 6. SEM images of a type V scaffold fabricated with the 20× objective with the average laser power of 1.2 mW and the scanning speed of 200 μm s^{-1}. The images show the scaffold from the tilt angles of (*a*) 0°, (*b*) 60° and (*c*) 90°. Scale bars represent 100 μm in (*a*) and (*b*) and 50 μm in (*c*).

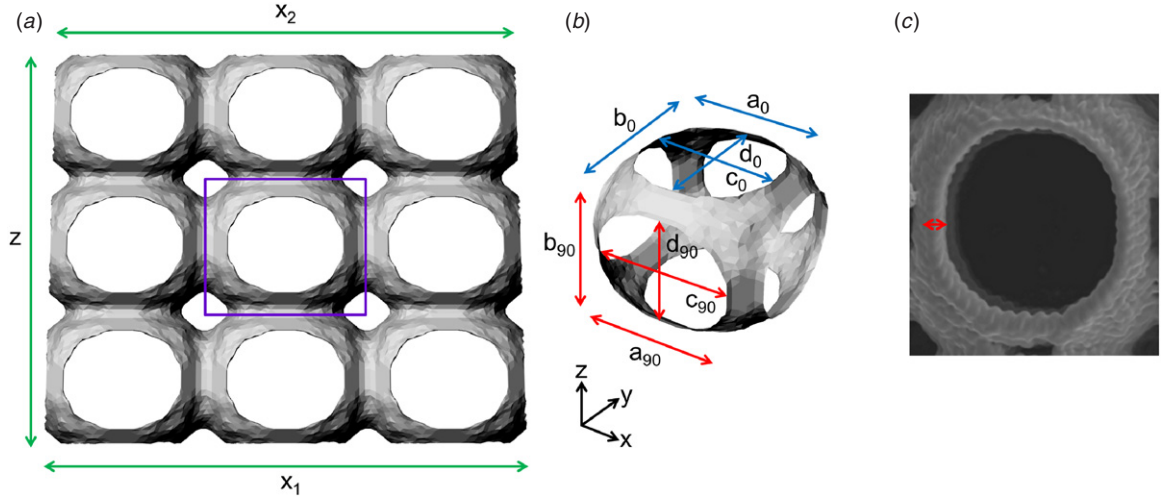

Figure 7. Schematic diagrams of the measured dimensions used to evaluate the two-photon polymerization fabrication accuracy. (*a*) Scaffold dimensions. (*b*) Unit cell dimensions (magnification of the area indicated by the purple box). (*c*) Wall thickness.

scaffolds fabricated with the scanning speeds of 150 and 200 μm s^{-1}. In order to achieve a working compromise between fabrication speed and adequate mechanical stability, the 20× objective and the scanning speed of 200 μm s^{-1} were chosen for the fabrication of type V scaffolds for hASC culturing (figure 6). The polymerization of one type V scaffold took approximately 78 min.

3.2. Geometrical analysis of fabrication accuracy

The accuracy of scaffold fabrication by 2PP was evaluated by measuring the dimensions of type I, II, III and V scaffolds from the SEM images as illustrated in figure 7. Judging by the side-view SEM images (90° tilt), it was evident that all the scaffolds had shrunk during the fabrication process in both *xy*- and *z*-

Table 2. Parameters of different scaffold types fabricated by two-photon polymerization. The scaffold dimensions were measured from the top-view (0° tilt) and side-view (90° tilt) SEM images. Data represent mean ± standard deviation.

	Scaffold type			
	I	II	III	V
a_0 (μm)	19.1 ± 0.2	18.9 ± 0.3	18.7 ± 0.4	58.6 ± 0.9
b_0 (μm)	19.1 ± 0.3	19.0 ± 0.3	19.0 ± 0.6	56.8 ± 0.8
a_{90} (μm)	19.5 ± 0.6	19.3 ± 0.8	19.5 ± 0.7	58.8 ± 2.1
b_{90} (μm)	15.5 ± 0.9	15.4 ± 1.1	15.2 ± 0.6	45.7 ± 1.5
c_0 (μm)	9.9 ± 0.2	12.9 ± 0.2	15.5 ± 0.4	50.3 ± 1.5
d_0 (μm)	10.1 ± 0.2	13.2 ± 0.3	16.0 ± 0.4	47.9 ± 1.3
c_{90} (μm)	9.4 ± 0.5	12.6 ± 0.8	16.5 ± 0.9	49.6 ± 2.0
d_{90} (μm)	5.5 ± 0.2	7.8 ± 0.4	8.9 ± 0.5	27.2 ± 0.5
xy-interconnectivity (c_0/a_0)	0.52 ± 0.01	0.68 ± 0.01	0.83 ± 0.01	0.86 ± 0.02
xz-interconnectivity (d_{90}/b_{90})	0.35 ± 0.02	0.51 ± 0.03	0.59 ± 0.03	0.60 ± 0.02
Wall thickness (μm)	1.0 ± 0.1	1.4 ± 0.1	1.3 ± 0.2	3.1 ± 0.3
x_1 (μm)	61.5	61.0	62.6	243.9
x_2 (μm)	56.8	55.3	55.7	228.5
x-shrinkage (%)	7.6	9.4	11.1	6.3
z (μm)	47.8 ± 0.2	47.1 ± 0.2	46.7 ± 0.1	91.4 ± 0.3
z-shrinkage (%)	20.3 ± 0.3	21.4 ± 0.3	22.1 ± 0.2	23.8 ± 0.3
Porosity (%)	84.7	80.3	81.6	85.0

directions. As depicted in figure 7(*a*), the lateral shrinkage was calculated from the side-view SEM images by comparing the side width at the top of the scaffold (x_2) to the side width at the bottom of the scaffold (x_1). The vertical shrinkage was evaluated by comparing the height of the fabricated scaffolds (z) to the height of the models. The dimensions of the unit cells and the openings were measured from the top-view (0° tilt) and side-view (90° tilt) SEM images as depicted in figure 7(*b*). The scaffold wall thicknesses were estimated by measuring the layer thickness from top-view SEM images as demonstrated in figure 7(*c*). Based on the measured parameters, the porosities of the fabricated scaffolds were calculated using the same three-step method that was used for the scaffold models. The results of the measurements and calculations are shown in table 2.

3.3. Culturing with adipose stem cells

For cell tests, samples with type V scaffolds were seeded with hASCs. Prior to the seeding, the hASCs were characterized by flow cytometric analysis to verify the mesenchymal origin of the cells. The analysis revealed positive expressions of the surface markers characteristic for mesenchymal stem cells (CD73, CD90 and CD105) [30] and lack of the expressions of the markers typically absent in adipose stem cells (CD11a, CD14, CD19, CD45, CD54, CD80, CD86, and HLA-DR). Furthermore, the analysis showed moderate expression of the hematopoietic progenitor and the endothelial cell marker CD34, as shown in figure 8.

The hASC-seeded scaffolds were studied with light microscopy, fluorescence imaging and SEM imaging in order to qualitatively evaluate cell attachment, viability and orientation inside the scaffolds. Figure 9 shows bright field microscopy images of the same scaffold at different time points. We found that most cells were outside the scaffolds right after seeding. However, the cells tended to migrate inside the scaffolds during the six day culture period. Due to this migration as well as cell proliferation, the scaffolds were almost full after day 6. This progression was also seen during the time-lapse imaging period of six days (see supplementary video (available from http://stacks.iop.org/JMM/22/115016/mmedia)).

Live/dead stained samples are shown in figure 10 at different time points. We found that the vast majority of the cells remained viable inside the scaffolds during the culture period. Only a few individual dead cells were seen in samples after two days and six days of culture and the number of dead cells did not increase between these two time points. It should be noted that the red color of the scaffolds was due to nonspecific binding of the red dye. Stained cells could, however, be clearly distinguished despite this background fluorescence. As shown in figure 10(*a*), the cell morphology after 4 h was still round and the cells had not yet fully attached to the glass surface or the scaffolds. After two days (figure 10(*b*)), the cells exhibited a spread out morphology and were well attached to both the scaffold and the surrounding glass surface. By day 6 (figure 10(*c*)), the number of cells inside the scaffolds had increased and the cells had extended processes inside the scaffold structure.

The live/dead stained samples were also SEM imaged and examples of the results are shown in figure 11. By day 6, the cells were seen to reside three dimensionally inside the scaffolds with connections to both the glass surface and the different scaffold layers (figure 11 (*a*)). The cells had extended processes not only along the scaffold walls but also through the open pore space (figure 11 (*b*)) and processes extending even two to four pores were seen.

The 3D orientation of the cells inside the scaffolds was further studied by confocal imaging, as shown in figure 12. It can be seen that the autofluorescence signal of the

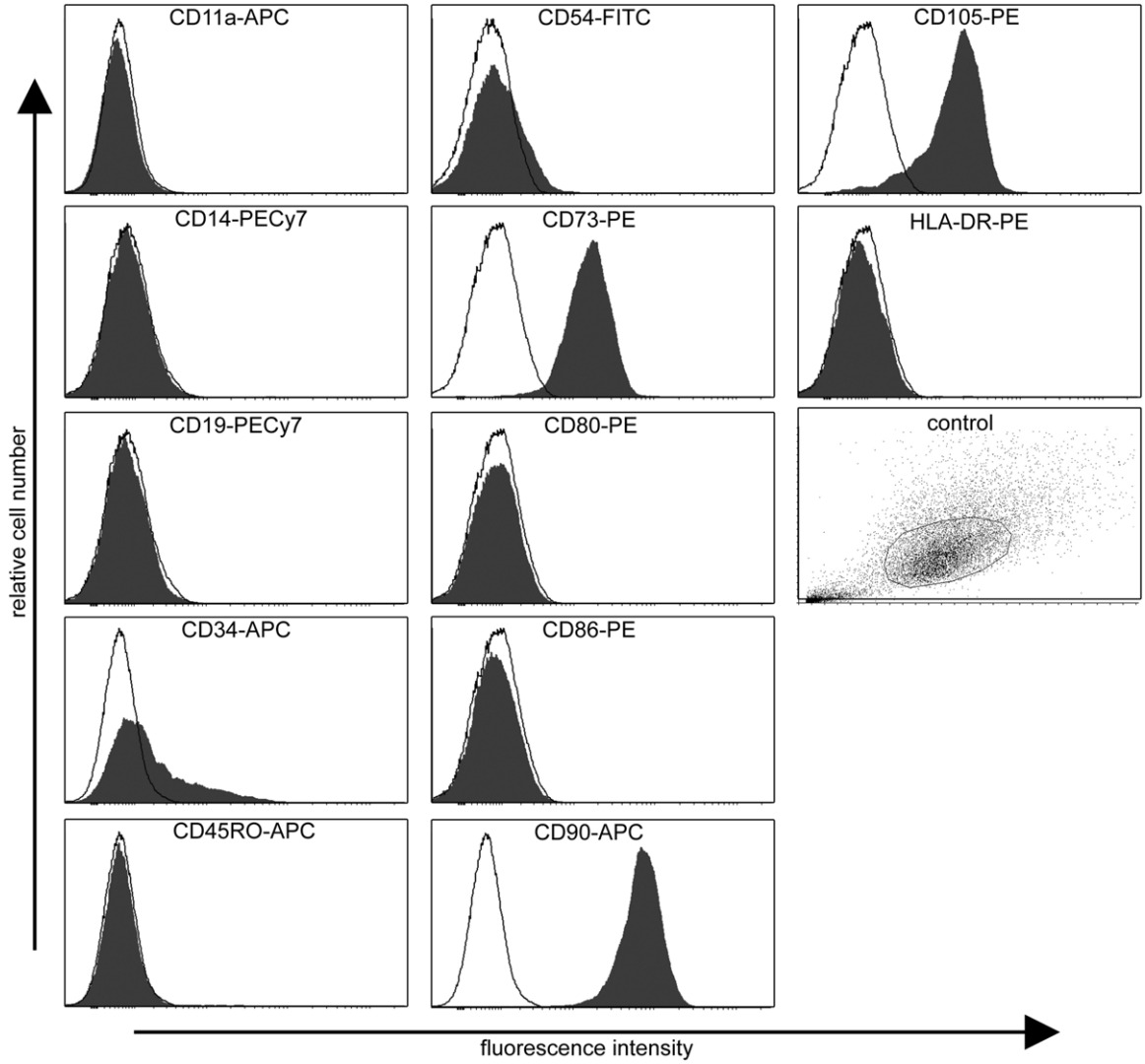

Figure 8. Cell surface marker expression of undifferentiated hASC analyzed by flow cytometry. Histograms show the relative cell number (*y*-axis) and fluorescence intensity (*x*-axis). Empty histograms represent control cells whereas filled histograms represent cells stained with antibody. Unstained control sample dot plot shows particle size and granularity (side scatter versus forward scatter).

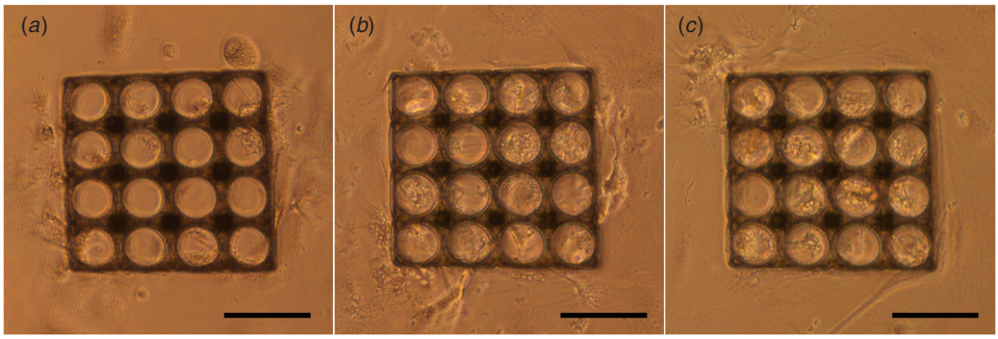

Figure 9. Bright field micrographs of a type V scaffold after (*a*) 4 h, (*b*) 2 d and (*c*) 6 d of culture with adipose stem cells. Scale bars represent 100 μm.

scaffold material overlapped with the blue fluorescence signal of the stained cell nuclei. However, the cell nuclei could be distinguished despite this background fluorescence. The confocal images showed that the cells could form complicated networks through the interconnected pores. Indications of cell divisions were also seen (data not shown). Based on the 3D reconstructions in figure 12, the cells were mostly planar after 4 h. At this stage the cells were attached to the glass surface or only to the first unit cell layer ($z = 40$–$60\,\mu m$). After two days, the cells had made connections also to the second unit

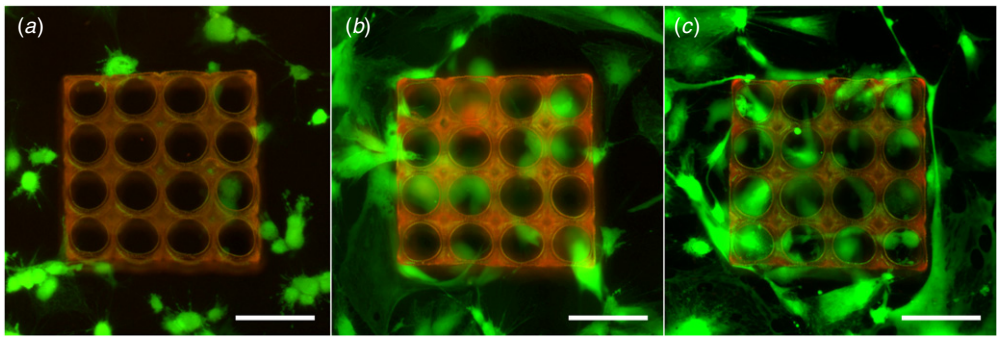

Figure 10. Fluorescence micrographs of type V scaffolds after (*a*) 4 h, (*b*) 2 d and (*c*) 6 d of culture with adipose stem cells. Live cells are stained green and dead cells red. The scaffold fluorescence is due to nonspecific binding of the red dye. Scale bars represent 100 μm.

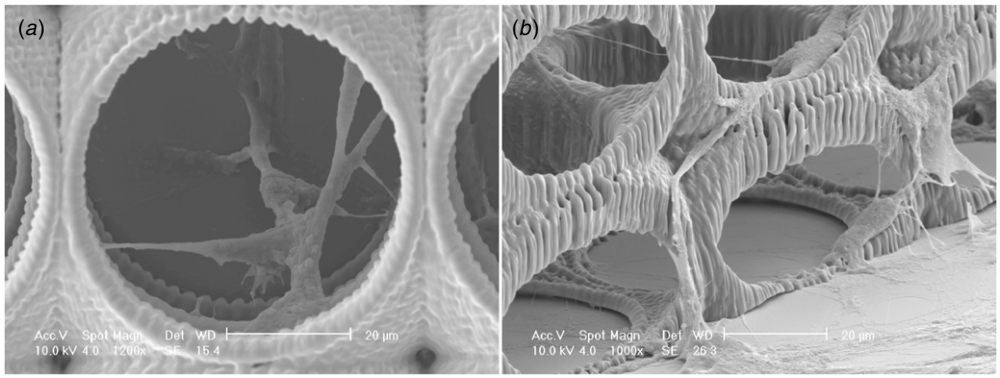

Figure 11. SEM images of type V scaffolds with adipose stem cells after a six day culture. (*a*) Top-view image (0° tilt) of a single cell extending from the glass surface to the upper layers of the scaffold. (*b*) A side-view image (70° tilt) showing multiple cells that have attached to the scaffold walls and formed 3D connections through the pores. Scale bars represent 20 μm.

cell layer ($z = 60$–$90\,\mu$m) mainly by growing upward along the outer walls of the scaffolds. Finally after six days, the scaffolds were nearly full of cells extending through the full height of the scaffolds ($z = 80$–$90\,\mu$m).

4. Discussion

2PP has recently emerged as a promising scaffold fabrication technique for 3D cell culturing and tissue engineering. The main drawback of 2PP is the low writing speed, which also limits the maximum scaffold size. In this study, we used a picosecond laser source which enabled the maximum scanning speed of 120 μm s^{-1} for the Ormocomp® material with the 50× objective. This scanning speed was suitable for fabricating small scaffolds (types I, II and III) with varying degree of porosity and interconnectivity. In order to fabricate larger scaffolds (type V) for hASC culturing, we switched to a 20× objective with a lower numerical aperture which enabled scanning speeds up to 300 μm s^{-1}. Another approach for achieving higher writing speeds would be to use a 2PP system based on a high-frequency femtosecond laser. It has been shown that scanning speeds of several millimeters per second can be reached with such systems [18]. Although using femtosecond lasers can significantly reduce fabrication times, picosecond lasers are more affordable and still suitable for the fabrication of small scale sample series for proof-of-concept testing.

In addition to the laser source and the focusing optics, the fabrication throughput 2PP can be influenced by the choice of the monomers and photoinitiators. In this study, we used the commercial polymer–ceramic material Ormocomp® as the scaffold material. Although Ormocomp® has been originally designed for single-photon polymerization, it has good 2PP processing properties and has also been reported to be non-cytotoxic [31, 32]. To the best of our knowledge, the cytotoxicity of the Irgacure®127 photoinitiator used in this work has not been systematically studied. However, our previously published results [41, 42] as well as the results presented in this paper do not indicate any cytotoxic effects. In the future, our approach could be tested also with custom-synthesized materials and high throughput photoinitiators that have been specifically designed for 2PP [33, 34]. The use of optimized materials is expected to enable the faster fabrication of even larger scaffold structures.

The 2PP technique also allows for the tuning of surface topography due to the voxel structure generated by the laser exposure. This was demonstrated in our study as we found that the surface roughness of the type IV scaffolds increased notably with increasing scanning speed. This resulting increase in the specific surface area of the scaffolds could promote cell attachment [35]. However, it should also be noted that scaffolds

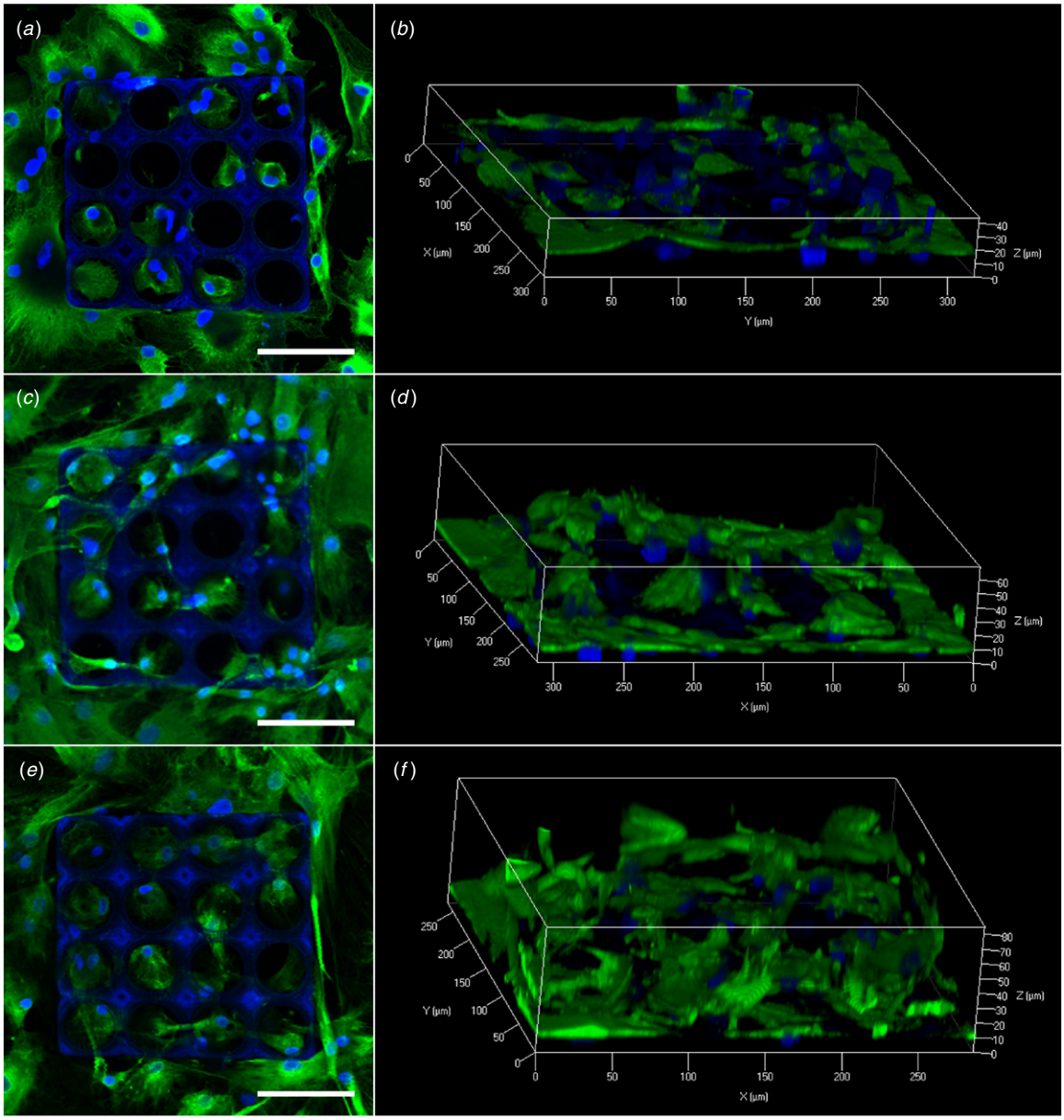

Figure 12. Top views (left column) and 3D reconstructions (right column) of confocal image stacks of type V scaffolds after (*a*) and (*b*) 4 h, (*c*) and (*d*) 2 d and (*e*) and (*f*) 6 d culture with adipose stem cells. The actin cytoskeleton has been stained green and the cell nuclei blue. The scaffolds also appeared blue due to autofluorescence as shown by the left column. Scale bars represent 100 μm.

with a highly porous surface suffered from more random shape distortions. Thus, it is essential to balance the surface quality and the structural integrity of 3D cell culture scaffolds. Based on recently published work, Young's modulus of UV polymerized bulk Ormocomp is approximately 1 GPA [43], whereas the value of 800 MPa has been reported for 2PP beams studied by atomic force microscopy [44]. Similar findings of smaller modulus values of 2PP structures compared to bulk material have also been published for a commercial acrylate resin [45]. The lower modulus values of 2PP structures have been attributed to a lower degree of crosslinking compared to UV polymerized samples. Indeed, Khripin *et al* showed that the elastic modulus of 2PP protein structures can be tuned by changing the scanning speed and thus the degree of crosslinking [46]. Although quantitative mechanical testing was beyond the scope of this paper, it is likely that the modulus of the Ormocomp scaffolds could be tuned between the values of a few hundred MPa to approximately 1 GPa by the choice of the 2PP processing parameters.

To the best of our knowledge, scaffold fabrication accuracy with respect to design parameters has not been previously studied for 2PP. Ovsianikov *et al* recently reported two-photon polymerized scaffolds with approximately 90% porosity but the calculation method was not specified [36]. In our study, the scaffold fabrication accuracy was assessed by comparing the dimensions of the fabricated scaffolds (table 2) to those of the models (table 1). In the *xy*-direction, the unit cell and opening sizes of all four scaffold types were found to correspond well to the models. However, in the *xz*-direction, the fabricated scaffolds clearly

deviated from the original designs. The decrease in scaffold height seemed to be independent from the scaffold design. Therefore, it was most likely caused by the shrinkage of the Ormocomp® material during the development process. The shrinkage behavior associated with 2PP of polymer–ceramic materials similar to Ormocomp® has been reported previously in [37]. The shrinkage is thought to be caused by incomplete polymerization of the materials during 2PP processing and subsequent molecular level collapse during the development [37]. We found that all the scaffolds had shrunk by approximately 6–11% in the *x*-direction. These results are in accordance with the previously reported shrinkage behavior of Ormocomp®, which showed that Ormocomp® can shrink laterally up to 20% depending on the laser power used for 2PP [38]. In the *z*-direction, the scaffolds had shrunk by approximately 20–24%. This decrease in the overall scaffold heights translated to an approximately 45–54% average decrease in the vertical opening height (d_{90}) when compared to the original designs. It should be noted that despite the change in the vertical opening sizes, the interconnectivity ranking of the scaffolds did not change. The fabricated type III and type V scaffolds were still the most interconnected in both *xy*- and *xz*-directions.

The porosities of the fabricated type I, II, III and V scaffolds were calculated as approximately 85%, 80%, 82% and 85%, respectively. The achieved porosities thus differed from the original values by 4–13%. Both the increase in wall thickness and the material shrinkage contributed to the deviation from the original designs. From the fabricated small-scale scaffolds, the least porous and interconnected type I scaffolds corresponded best to the model. The more porous and open architectures of the type II, III and V scaffolds most likely made the structures more susceptible to shrinkage. As wall thickness cannot be significantly decreased without compromising structural integrity, the scaffold fabrication process could be improved by compensating for the lateral and vertical shrinkage. Based on the measured shrinkage reported here, this could be realized by introducing a compensation factor to the scaffold models. This approach has previously been successfully used for the fabrication of photonic crystals [39, 38]. By introducing shrinkage correction, we predict that Ormocomp® scaffolds with porosities of over 90% could be fabricated by 2PP using spherical unit cell designs.

In order to demonstrate the feasibility of our scaffolds as 3D culturing platforms for stem cells, we cultured the largest type V scaffolds with hASCs for a period of up to six days. Human ASCs are an attractive and abundant cell source for tissue engineering applications. They can be easily retrieved in high numbers from either liposuction aspirates or subcutaneous adipose tissue fragments and can be readily expanded *in vitro*. These multipotent cells can also undergo at least adipogenic, osteogenic and chondrogenic differentiation *in vitro* [40]. The culturing of hASCs with two-photon polymerized scaffolds has previously been reported by Ovsianikov *et al* [19]. They showed that methacrylamide-modified gelatin scaffolds with interconnected square-shaped pores could support hASC adhesion, proliferation and differentiation into the adipogenic lineage. However, the achieved porosity and interconnectivity of these scaffolds was not quantified. Also, the 3D orientation of the cells with respect to the scaffold struts and pores was not studied. To the best of our knowledge, this study is the first in which the culturing of hASCs has been tested with Ormocomp® scaffolds of precisely defined geometrical shape. Due to the manual static cell seeding, there was some random variation in the initial number of cells in and around the scaffolds in different samples. However, by day 6 this initial variation was no longer visible and all the scaffolds were nearly full of cells as a result of both cell migration and proliferation. The majority of the cells were viable at each time point during the six day culture. The cells formed connections both along the scaffold walls and through the open pore space. This suggests that the three-dimensionally interconnected pore structure of the scaffolds promoted hASC attachment and growth. Due to the observed vertical shrinkage, the pore interconnectivity of the type V scaffolds was 30% more restricted from the *xz*-direction than from the *xy*-direction. However, this did not seem to impair either the migration of cells into the scaffolds or the proliferation of the cells inside the scaffolds. This implies that despite the deviation from the original scaffold design, the pores were sufficiently open and connected to ensure adequate diffusion of oxygen and nutrients to the cells.

5. Conclusions

In this study, we designed three-dimensionally interconnected porous scaffolds based on spherical unit cells. Our approach enabled the straightforward tuning of scaffold geometry. For the first time, we also assessed the 2PP fabrication accuracy with respect to scaffold designs. We showed that porosity values of the fabricated scaffolds decreased up to 13% compared to our design specifications. This decrease was mainly caused by shrinkage of the polymer–ceramic material. The fabricated scaffolds were shown as a suitable environment for the culturing of human adipose stem cells. In the future, the scaffolds produced by our method could be used to systematically study the effect of scaffold architecture on the adhesion, proliferation and differentiation of various cell types.

Acknowledgments

The financial support of the Finnish Cultural Foundation, Jenny and Antti Wihuri Foundation, the Finnish Funding Agency for Technology and Innovation and the Competitive Research Funding of Pirkanmaa Hospital District is gratefully acknowledged. The authors would like to acknowledge Professor Jouko Viitanen for laser system expertise, Dr Bettina Mannerström for FACS expertise and Ms Anna-Maija Honkala, Ms Miia Juntunen and Ms Sari Kalliokoski for the excellent technical assistance.

Appendix. Porosity calculation

For each sample, porosity was calculated using three steps.

Step 1. Calculate the total volume for each unit cell *i*, (V^i_{cell})

Step 2. Calculate volume of material in each unit cell i, (V^i_{mat})

Step 3. Calculate total porosity of the sample, (P).

Step 1

V^i_{cell} can be calculated for each unit cell i as

$$V^i_{\text{cell}} \approx a^i_0 \cdot b^i_0 \cdot b^i_{90}. \tag{A.1}$$

In order to take into account the structural deformations along x- and y-axes in our calculation, we divided type I, II and III into three layers (l_1, l_2, l_3) and type V into two layers (l_1, l_2) along z-axis. We assumed that no deformation occurs within individual layers, thus $(\forall i \in l, a^i_0 \approx a^i_{90})$. We linearly interpolated the missing data for a^i_0 and b^i_0 needed for the middle layers using the measurements from the top and the bottom of the samples. We also assumed that b^i_{90} values do not change along the rows for the same layer. Furthermore, we assumed that the deformations along the x- and y-axes were the same; thus as the final expression, we used the following instead of equation (A.1):

$$V^i_{\text{cell}} \approx \left(\frac{a^i_0 + b^i_0}{2}\right)^2 \cdot b^i_{90}. \tag{A.2}$$

Step 2

V^i_{mat} can be calculated for each unit cell i as

$$V^i_{\text{mat}} \approx S^i_{\text{mat}} \cdot t \tag{A.3}$$

In equation (A.3), t is the scaffold thickness and S^i_{mat} is the surface area of the material in a unit cell i. For each scaffold, the mean value given in table 2 was used as a constant thickness value for all unit cells.

Note that scaffold models were generated using MATLAB® by subtracting a sphere from a cube for each unit cell. When deformation is taken into account, the spheres within unit cells can be approximated as ellipsoids. Thus S^i_{mat} is the surface area of an ellipsoid bounded by the unit cell. Based on these observations, S^i_{mat} were calculated as follows.

Let $E(x, y, z)$ be an ellipsoid in Cartesian coordinates, located at the origin with semi-axis lengths s_1, s_2 and s_3 along x-, y- and z-axes, respectively. Note that $E(x, y, z)$ is defined in the domain $R_D = \left\{-\frac{s_1}{2} \leqslant x \leqslant \frac{s_1}{2}, -\frac{s_2}{2} \leqslant y \leqslant \frac{s_2}{2}, -\frac{s_3}{2} \leqslant z \leqslant \frac{s_3}{2}\right\}$. If $S_{E_{R_{\text{mat}}}}$ is the surface area of $E(x, y, z)$ patch in region R_{mat}, then

$$\begin{aligned} S^i_{\text{mat}} &= S_{E_{R_{\text{mat}}}} | R_{\text{mat}} \\ &= \left\{-\frac{c_{90}}{2} \leqslant x \leqslant \frac{c_{90}}{2}, -\frac{d_0}{2} \leqslant y \leqslant \frac{d_0}{2}, -\frac{d_{90}}{2} \leqslant z \leqslant \frac{d_{90}}{2}\right\}. \end{aligned} \tag{A.4}$$

$S_{E_{R_{\text{mat}}}}$ can be calculated using the symmetry of the patches as

$$S_{E_{R_{\text{mat}}}} = S_{E_{R_D}} - 8S_{E_{R_1}} - 8S_{E_{R_2}} - 8S_{E_{R_3}}, \tag{A.5}$$

where R_1, R_2 and R_3 are the following regions:

$$\begin{aligned} R_1 &= \left\{\frac{c_{90}}{2} < x \leqslant \frac{s_1}{2}, y \geqslant 0, z \geqslant 0\right\} \\ R_2 &= \left\{x \geqslant 0, \frac{d_0}{2} < y \leqslant \frac{s_2}{2}, z \geqslant 0\right\} \\ R_3 &= \left\{x \geqslant 0, y \geqslant 0, \frac{d_{90}}{2} < z \leqslant \frac{s_3}{2}\right\}. \end{aligned} \tag{A.6}$$

The computation of the surface patches given in equation (A.5) is significantly easier when $E(x, y, z)$ is parametrized as

$$\begin{aligned} x &= s_1 \cos\phi \sin\theta \\ y &= s_2 \sin\phi \sin\theta \\ z &= s_3 \cos\theta; \end{aligned} \tag{A.7}$$

here $\phi \in [0, 2\pi)$ and $\theta \in [0, \pi)$.

Then the surface area for an arbitrary patch $R = \phi_1 \leqslant \phi \leqslant \phi_2, \theta_1 \leqslant \theta \leqslant \theta_2$ can be calculated as

$$\begin{aligned} S_{E_R} = &\int_{\theta_1}^{\theta_2} \sin\phi \int_{\phi_1}^{\phi_2} \\ &\times \sqrt{s_1^2 s_2^2 \cos\phi + s_3^2\left(s_3^2 \cos^2\theta + s_1^2 \sin^2\theta\right)\sin^2\phi}\, \mathrm{d}\theta\, \mathrm{d}\phi. \end{aligned} \tag{A.8}$$

The values for s_1, s_2, s_3, ϕ_1, ϕ_2, θ_1 and θ_2 can easily be obtained via basic trigonometric identities using the measured parameters given in table 2. The integral given in equation (A.8) was calculated numerically using MATLAB®.

Step 3

As the final step, the porosity for a scaffold was calculated as a percentage as follows:

$$P = \left(1 - \frac{\sum_i V^i_{\text{mat}}}{\sum_i V^i_{\text{cell}}}\right) \cdot 100. \tag{A.9}$$

References

[1] Lee J, Cuddihy M J and Kotov N A 2008 *Tissue Eng.* B **14** 61–86
[2] Lee K, Yang D, Park S H and Kim R H 2006 *Polym. Adv. Technol.* **17** 72–82
[3] Sun H and Kawata S 2003 *J. Light. Technol.* **21** 624
[4] Zhang Y, Chen Q, Xia H and Sun H 2010 *Nano Today* **5** 435–48
[5] Juodkazis S, Mizeikis V, Seet K K, Masafumi M and Misawa H 2005 *Nanotechnology* **16** 846
[6] Haske W, Chen V W, Hales J M, Dong W, Barlow S, Marder S R and Perry J W 2007 *Opt. Express* **15** 3426–36
[7] Tan D, Li Y, Qi F, Yang H, Gong Q, Dong X and Duan X 2007 *Appl. Phys. Lett.* **90** 071106
[8] Dong X, Zhao Z and Duan X 2008 *Appl. Phys. Lett.* **92** 091113
[9] Hidai H, Jeon H, Hwang D J and Grigoropoulos C P 2009 *Biomed. Microdevices* **11** 634–52
[10] Jeon H, Hidai H, Hwang D J, Healy K E and Grigoropoulos C P 2010 *Biomaterials* **31** 4286–95
[11] Engelhardt S, Hoch E, Borchers K, Meyer W, Krüger H, Tovar G E M and Gillner A 2011 *Biofabrication* **3** 025003
[12] Lee S, Moon J J and West J L 2008 *Biomaterials* **29** 2962–8

[13] Klein F, Striebel T, Fischer J, Jiang Z, Franz C M, Freymann G V, Wegener M and Bastmeyer M 2010 *Adv. Mater.* **22** 868–71
[14] Klein F, Richter B, Striebel T, Franz C M, Freymann G V, Wegener M and Bastmeyer M 2011 *Adv. Mater.* **23** 1341–5
[15] Tayalia P, Mendonca C R, Baldacchini T, Mooney D J and Mazur E 2008 *Adv. Mater.* **20** 4494–8
[16] Tayalia P, Mazur E and Mooney D J 2011 *Biomaterials* **32** 2634–41
[17] Hsieh T M, Benjamin Ng C W, Narayanan K, Wan A C A and Ying J Y 2010 *Biomaterials* **31** 7648–52
[18] Ovsianikov A, Deiwick A, Van Vlierberghe S, Dubruel P, Müller L, Dräger G and Chichkov B 2011 *Biomacromolecules* **12** 851–8
[19] Ovsianikov A, Deiwick A, Van Vlierberghe S, Pflaum M, Wilhelmi M, Dubruel P and Chichkov B 2011 *Materials* **4** 288–99
[20] Koroleva A, Schlie S, Fadeeva E, Gittard S D, Miller P, Ovsianikov A, Koch J, Narayan R J and Chichkov B N 2010 *J. Opt.* **12** 124009
[21] Koroleva A, Gittard S, Schlie S, Deiwick A, Jockenhoevel S and Chichkov B 2012 *Biofabrication* **4** 015001
[22] Melissinaki V, Gill A A, Ortega I, Vamvakaki M, Ranella A, Haycock J W, Fotakis C, Farsari M and Claeyssens F 2011 *Biofabrication* **3** 045005
[23] Liu C, Xia Z and Czernuszka J T 2007 *Chem. Eng. Res. Des.* **85** 1051–64
[24] Käpylä E, Turunen S, Pelto J and Kellomäki M 2011 *J. Micromech. Microeng.* **21** 065033
[25] Sun H, Maeda M, Takada K, Chon J W M, Gu M and Kawata S 2003 *Appl. Phys. Lett.* **83** 819–21
[26] Fitilis I, Fakis M, Polyzos I, Giannetas V and Persephonis P 2010 *J. Photochem. Photobiol.* A **215** 25–30
[27] Gimble J and Guilak F 2003 *Cytotherapy* **5** 362–9
[28] Zuk P A, Zhu M, Mizuno H, Huang J, Futrell J W, Katz A J, Benhaim P, Lorenz H P and Hedrick M H 2001 *Tissue Eng.* **7** 211–28
[29] Lindroos B, Boucher S, Chase L, Kuokkanen H, Huhtala H, Haataja R, Vemuri M, Suuronen R and Miettinen S 2009 *Cytotherapy* **11** 958–72
[30] Dominici M, Le Blanc K, Mueller I, Slaper-Cortenbach I, Marini F C, Krause D S, Deans R J, Keating A, Prockop D J and Horwitz E M 2006 *Cytotherapy* **8** 315–7
[31] Doraiswamy A, Jin C, Narayan R J, Mageswaran P, Mente P, Modi R, Auyeung R, Chrisey D B, Ovsianikov A and Chichkov B 2006 *Acta Biomater.* **2** 267–75
[32] Ovsianikov A, Schlie S, Ngezahayo A, Haverich A and Chichkov B N 2007 *J. Tissue Eng. Regen. Med.* **1** 443–9
[33] Liska R *et al* 2007 *J. Coating. Tech. Res.* **4** 505–10
[34] Li Z *et al* 2011 *J. Polym. Sci.* A **49** 3688–99
[35] O'Brien F J, Harley B A, Yannas I V and Gibson L J 2005 *Biomaterials* **26** 433–41
[36] Ovsianikov A, Gruene M, Pflaum M, Koch L, Maiorana F, Wilhelmi M, Haverich A and Chichkov B 2010 *Biofabrication* **2** 014104
[37] Ovsianikov A, Shizhou X, Farsari M, Vamvakaki M, Costas F and Chichkov B N 2009 *Opt. Express* **17** 2143–8
[38] Ovsianikov A, Passinger S, Houbertz R and Chichkov B N 2007 Three dimensional material processing with femtosecond lasers *Laser Ablation and its Applications* vol 129 ed C R Phipps (Berlin: Springer) pp 121–157
[39] Sun H, Suwa T, Takada K, Zaccaria R P, Kim M, Lee K and Kawata S 2004 *Appl. Phys. Lett.* **85** 3708–10
[40] Lindroos B, Suuronen R and Miettinen S 2011 *Stem Cell Rev. Rep.* **7** 269–91
[41] Käpylä E, Turunen S and Kellomäki M 2010 *Micro Nanosyst.* **2** 87–99
[42] Koskela J E, Turunen S, Ylä-Outinen L, Narkilahti S and Kellomäki M 2012 *Polym. Adv. Technol.* **23** 992–1001
[43] Schizas C and Karalekas D 2011 *J. Mech. Behav. Biomed. Mater.* **4** 99–106
[44] Klein F, Striebel T, Fischer J, Jiang Z, Franz C M, von Freymann G, Wegener M and Bastmeyer M 2010 *Adv. Mater.* **22** 868–71
[45] Bayindir Z, Sun Y, Naughton M J, LaFratta C N, Baldacchini T, Fourkas J T, Stewart J, Saleh B E A and Teich M C 2005 *Appl. Phys. Lett.* **86** 064105
[46] Khripin C Y, Brinker C J and Kaehr B 2010 *Soft Matter* **6** 2842–8

Publication IV

E. Käpylä, T. Sedlačík, D. B. Aydogan, J. Viitanen, F. Rypáček, M. Kellomäki

Direct laser writing of synthetic poly(amino acid) hydrogels and poly(ethylene glycol) diacrylates by two-photon polymerization

Materials Science and Engineering C: Materials for Biological Applications 43(2014), pp. 280-289

Direct laser writing of synthetic poly(amino acid) hydrogels and poly(ethylene glycol) diacrylates by two-photon polymerization

Elli Käpylä[a,d,*], Tomáš Sedlačík[b], Dogu Baran Aydogan[a,d], Jouko Viitanen[c], František Rypáček[b], Minna Kellomäki[a,d]

[a] Department of Electronics and Communications Engineering, Tampere University of Technology, P.O. Box 692, 33101 Tampere, Finland

[b] Institute of Macromolecular Chemistry of the Academy of Sciences of the Czech Republic, Heyrovského nám. 2, 162 06 Praha 6 – Břevnov, Prague, Czech Republic

[c] VTT Technical Research Centre of Finland, P.O. Box 1300, 33101 Tampere, Finland

[d] BioMediTech, Biokatu 10, 33520 Tampere, Finland

* Corresponding author
Phone: +358401981952. Email: elli.kapyla@tut.fi

Abstract

The additive manufacturing technique of direct laser writing by two-photon polymerization (2PP-DLW) enables the fabrication of three-dimensional microstructures with superior accuracy and flexibility. When combined with biomimetic hydrogel materials, 2PP-DLW can be used to recreate the microarchitectures of the extracellular matrix. However, there are currently only a limited number of hydrogels applicable for 2PP-DLW. In order to widen the selection of synthetic biodegradable hydrogels, in this work we studied the 2PP-DLW of methacryloylated and acryloylated poly(α-amino acid)s (poly(AA)s). The performance of these materials was compared to widely used poly(ethylene glycol) diacrylates (PEGda) in terms of polymerization and damage thresholds, voxel size, line width, post-polymerization swelling and deformation. We found that both methacryloylated and acryloylated poly(AA) hydrogels are suitable to 2PP-DLW with a wider processing window than PEGdas. The poly(AA) with the highest degree of acryloylation showed the greatest potential for 3D microfabrication.

Keywords: Direct laser writing, two-photon polymerization, microfabrication, hydrogel, polyamino acid, poly(ethylene glycol) diacrylate

1. Introduction

Hydrogels are promising matrix candidates for tissue engineering due to their biocompatibility, high water content and tunable biomimetic properties [1]. Combining hydrogels with advanced microfabrication approaches holds great potential for recreating complex extracellular microarchitectures [2]. Among these approaches, direct laser writing by two-photon polymerization (2PP-DLW) offers 3D microfabrication with superior accuracy compared to the widely used methods of UV laser stereolithography and 3D printing [3]. 2PP-DLW is based on the nonlinear optical phenomenon of two-photon absorption (2PA) and the fabricated microstructures are formed by overlapping ellipsoidal voxels (volumetric pixels). Voxel size can be varied by adjusting the processing parameters, such as laser power, exposure time and numerical aperture of the objective lens [4]. With optimal processing conditions, 2PP-DLW enables feature sizes of less than 100 nm and beyond the diffraction limit of light [5]. Furthermore, structures with multiple length scales ranging from sub-micron to millimetre can be fabricated. [6,7]

2PP-DLW can be used for the processing of a variety of materials ranging from traditional photoresists to biopolymers [8]. The 2PP-DLW of hydrogels was first demonstrated with proteins when Pitts et al. reported the crosslinking of bovine serum albumin (BSA) and type I collagen [9,10]. Since then, the processing of various other protein hydrogels, such as fibronectin [11], fibrinogen [12] and BSA combined with laminin [13] has been demonstrated. However, despite their beneficial properties, such as biodegradability, natural hydrogels often suffer from batch-to-batch variation and relatively poor mechanical properties, which limits their use as tissue engineering scaffolds [14]. In order to tune the mechanical properties and photoreactivity, chemically modified natural hydrogels, such as methacrylamide-modified gelatin [15-18], vinyl ester-modified gelatin [17], methacrylate-modified dextran and hyaluronan (HA) [19] have been

recently studied. However, these materials are still biological in origin, which makes them prone to batch-to-batch variability.

Synthetic hydrogels are attractive alternatives to naturally derived materials due to their adjustable properties and customizable chemistry [14]. Polyethylene glycol diacrylate (PEGda), which is the acrylated form of poly(ethylene glycol) (PEG), is one of the most widely used synthetic hydrogels and has been approved by the FDA for several medical applications due to its low toxicity and biocompatilibity [2,20]. PEGda has also been shown well suitable for scaffold fabrication by 2PP-DLW [21,22]. However, a drawback of PEGda is that it is not inherently biodegradable [1,2].

In order to realize the full potential of creating biomimetic microstructures for cell culturing, it is essential to expand the selection of synthetic, degradable hydrogels applicable for 2PP-DLW. The aim of this work was to study the 2PP-DLW of synthetic poly(α-amino acid) hydrogels (poly(AA)s) for the first time. Due to their polypeptide backbone, poly(AA) hydrogels are cleavable in a biological environment by enzyme-catalysed hydrolysis and the rate and enzyme specificity of the degradation can be controlled through copolymerization [23-25]. Hydrogels based on synthetic poly(AA)s have been previously shown suitable for the culturing of porcine mesenchymal stem cells [26]. In this study, we prepared poly(AA)s based on methacryloylated and acryloylated poly[N^5-(2-hydroxyethyl) L-glutamine]s (PHEGs) and compared their 2PP-DLW performance to commercial PEGda hydrogels. The 2PP-DLW of four different PHEG poly(AA) hydrogels and three PEGdas was studied in terms of the fundamental parameters of hydrogel 2PP-DLW, namely the polymerization and damage threshold values, voxel size, line width and post-development swelling and deformation.

2. Materials and methods

2.1. Preparation of macromers

The synthesis of macromers for 2PP-DLW, methacryloylated and acryloylated poly[N^5-(2-hydroxyethyl) L-glutamine]s (PHEGs), is illustrated in Fig. 1 (a) and consists of monomer synthesis, polymerization and two-step modification of the resulting polymers (aminolysis and methacryloylation).

2.1.1. Materials

Tetrahydrofuran, 1,4-dioxane, chloroform, hexane (all from Lach-Ner, Czech Republic), 2-aminoethanol and dimethylacetamide (both from Sigma-Aldrich) were dried with appropriate drying agents, distilled and stored over molecular sieves. Sodium hydrogen carbonate (Fluka), pyridine (Lachema, Czech Republic) and acetic acid (Lach-Ner) were of an analytical grade and were used as obtained. Triphosgene (Chemos, Czech Republic or TCI Europe), methacryloyl chloride and acryloyl chloride (Fluka) were used as obtained [25]. γ-Benzyl L-glutamate (Emmenar Group, India) was recrystallized from distilled water. Poly(ethylene oxide) standards (PEO) were purchased from Polymer Standard Service GmbH (Germany).

2.1.2. Monomer synthesis and polymerization

The synthesis of the monomer, N-carboxyanhydride of γ-benzyl L-glutamate (Figure 1 (a), NCA-BLG) was carried out by the reaction of γ-benzyl L-glutamate (BLG) with triphosgene, basically according to [27], and has been described in detail in [23]. Crude NCA-BLG was crystallized from tetrahydrofuran with the addition of chloroform, recrystallized from chloroform if necessary and stored under nitrogen in a freezer. NCA-BLG was polymerized in dry 1,4-dioxane (0.2 mol/l) with sodium methanolate as an initiator with the initiator-to-monomer ratio 1/200 [28]. The polymer, hydrophobic poly(γ-benzyl L-glutamate) (PBLG, Fig. 1 (a), I.), was precipitated in ethanol and dried under vacuum at 40 °C.

2.1.3. Aminolysis of PBLG

PBLG was aminolyzed in heterogeneous phase with 50-mole excess of 2-aminoethanol at 60 °C for two days [24]. The resulting water-soluble polymer, poly[N^5-(2-hydroxyethyl) L-glutamine] (PHEG, Fig. 1 (a), II.) was precipitated in absolute ethanol, isolated by filtration and dissolved in water. The aqueous polymer solution was neutralized with acetic acid and dialyzed against water (Spectra/Por® 1 with cut off 6000-8000). The dialysed polymer solution was filtered (Whatman 0.2 μm nylon membrane), frozen and freeze-dried.

2.1.4. Methacryloylation and acryloylation of PHEG

Polymerizable methacryloyl or acryloyl groups were introduced in PHEGs by the reaction of the hydroxyethyl side chains of PHEG with methacryloyl chloride (MA-Cl) or acryloyl chloride, respectively. The reaction with MA-Cl was carried out in dry dimethylacetamide (DMA, 2.5 % w/w) by modifying the procedure described in [29]. First, the amount of MA-Cl required to obtain a desired degree of methacryloylation was estimated from the dependence shown in Figure 1 (b), which was based on preliminary model experiments. Second, lithium chloride (5 % w/w to PHEG) was added to prevent physical association of polymer chains. Third, the reaction was cooled by ice to prevent spontaneous crosslinking through radical polymerization. An equimolar amount of pyridine with respect to the chloride reagent was added to capture hydrochloride released by the reaction and to shift the equilibrium in favour of the products. The reaction was stopped after two hours by adding sodium carbonate solution in excess. The reaction mixture was filtered from salts and the filtrate was dialyzed against water, then filtered (Whatman 0.2 μm nylon membrane), frozen and lyophilized. The product (Fig. 1 (a), III.) was stored under nitrogen in a freezer. Practically the same procedure was successfully used for acryloylation.

The molecular weight averages of the methacryloylated and acryloylated PHEGs were determined by size exclusion chromatography (SEC) analysis on a PolySep-GFC-P Linear column (Phenomenex®) with a gradient Knauer system with diode array detection (DAD) and Alltech 3300 evaporative light scattering detection (ELSD). PEO standards were used for calibration and an

isocratic system of 0.05 M ammonium acetate buffer in acetonitrile/water (20:80) as a mobile phase. The flow rate was 0.3 ml/min and the temperature 27 °C. Clarity chromatography software (DataApex Ltd., Czech Rebublic) was used for data analysis.

The degrees of modification of PHEGs were obtained from ^{1}H-NMR spectra (see Supplementary information) in D_2O from the peak area ratio of the methylenes of the side chain acryloyl/methacryloyl groups to the γ-methylenes of the poly(L-glutamine) units: δ(methylenes of methacryloylated PHEGs) = 5.7 and 6.1 ppm, δ(methylenes of acryloylated PHEGs) = 6.0 and 6.4 ppm, δ(γ-methylenes of poly(L-glutamine) unit of polymer) = 2.2-2.5 ppm. The error of these measurements is below 1% of MA units in polymer [29].

2.2. Two-Photon Polymerization Experiments

In this study we used a custom-built 2PP-DLW setup, which was a modified version of the system described previously in [30]. Briefly, the system was based on a frequency doubled femtosecond fibre laser (FP-532-0.2-FS-01, Fianium Ltd., United Kingdom) operating at 532 nm with a pulse duration of 200 fs, repetition rate of 40 MHz, pulse energy of 5.6 nJ and average output power of 200 mW. The beam quality factor M^2 = 1.0 in both the x- and y-directions according to the suppliers specifications. The displacement of the laser beam in the xy- and z-directions was controlled with a fast steering mirror scanner (FSM-300, Newport Corporation, USA) and a piezo focusing unit (Mipos 250 SGEX, Piezosystem Jena GmbH, Germany) respectively. From the mirror scanner, the beam was directed through an upright microscope frame (ECLIPSE ME 600, Nikon, Japan) to a 50x oil immersion microscope objective with NA = 0.90 (Meiji Techno, Japan) with a measured average transmittance of 48%. In order to fill the back aperture and to utilize the full nominal NA of the objective, one 10x and a second adjustable 1 – 3x beam expander were used in the optical path. The laser power was controlled with a motorized attenuator system (UAB Altechna, Lithuania). The laser powers were measured before the objective with the accuracy 200 μW (Power meter Thorlabs PM100 Series with S 310 C sensor).

We tested the 2PP-DLW of two methacryloylated poly(AA)s (PHEG-MA21 and PHEG-MA11) and two acryloylated poly(AA)s (PHEG-A13 and PHEG-A9). We also tested commercial PEGdas with M_n = 575 g/mol (PEGda-575) or 10000 g/mol (PEGda-10000) (Sigma-Aldrich Finland Oy, Finland). Solutions of the PHEGs and PEGda-10000 were prepared by dissolving 20 wt% (w/w) of each of the materials in ion-exchanged water containing 0.6 wt% (w/w) of the photoinitiator Irgacure® 2959 (I2959, Courtesy of BTC Nordic). The liquid PEGda-575 was used either as a 100 wt% solution with 0.6 wt% (w/w) of I2959 (PEGda-575) or as a 20 wt% (w/w) solution in ion-exchanged water containing 0.6 wt% (w/w) of I2959 (PEGda-575-20). For 2PP-DLW, a droplet of the PHEG or PEGda solutions were sandwiched between a glass slide and coverslip separated by a 150 μm thick stainless steel spacer. The slides were pretreated with 3-(trimethoxysilyl) propyl methacrylate (MAPTMS, Sigma-Aldrich Finland Oy, Finland) to enhance the adhesion of the microstructures to the glass surface. For MAPTMS treatment, the slides were first cleaned by a strong soap solution, rinsed with water and 99.5% ethanol and allowed to air dry. The slides were then immersed in a MAPTMS solution (1:200 of MAPTMS in 99.5% ethanol with 3:100 of dilute acetic acid (1:10 glacial acetic acid: water)) for approximately 3 min, rinsed with 99.5% ethanol and allowed to air dry. After 2PP-DLW, the nonilluminated solutions were washed off by immersion in ion-exchanged water for 5-15 min and rinsing with 99.5% ethanol.

2.3. Determination of polymerization and damage thresholds

In order to perform a systematic comparison of the different materials, we determined the polymerization threshold (P_{th}) and the damage threshold (P_D) values for the PHEGs and PEGdas with respect to laser power and scanning speed. Square patterns were polymerized with scanning speeds ranging from 1 μm/s to 175 μm/s and the laser power was tuned to a value where the polymerized line became barely visible and to a value where bubbling of the solution started to occur. The threshold values were determined from three separate samples for all the materials. From the average threshold values, we calculated the dynamic power range, defined as P_D/P_{th}, and the polymerization window (P_w) for each material. The polymerization window was calculated as the

power range between the polymerization and the damage thresholds. In order to process different materials in a wide range of comparable laser powers, we used power values corresponding to approximately 10-90% of the polymerization window for each material according to the formula P = P_w*x + P_{th}, where P_w is the polymerization window, P_{th} is the polymerization threshold and x = 0.10, 0.25, 0.50, 0.75 or 0.90 is the power factor. These values are denoted as 10%, 25%, 50%, 75% and 90% powers for each material. All powers are given as the transmitted values after the objective.

2.4. Polymerization of voxels

Voxel arrays were fabricated using a custom software and the ascending scan method introduced in [31]. Starting with the laser focus positioned close to the glass surface, series of voxels were polymerized by point exposure while the laser focus position was increased by 1 μm between each voxel in order to obtain complete yet surface bound voxels. Three different laser power values, namely 10%, 50% and 90% powers, and exposure times 5-1000 ms were used for voxel fabrication for each material and three identical arrays were fabricated with each laser power. We compared the measured voxel width and height with estimates calculated using an analytical model developed by Serbin et al [32], in which the voxel width (d) and the voxel height (l) are given by

$$d(N_0, t) = r_0\sqrt{\ln\left(\frac{\sigma_2 N_0^2 n\tau}{C}\right)} \quad (1)$$

$$l(N_0, t) = 2z_R\sqrt{\sqrt{\frac{\sigma_2 N_0^2 n\tau}{C}} - 1} \quad (2)$$

$$C = \ln\left(\frac{\rho_0}{\rho_0 - \rho_{th}}\right) \quad (3)$$

$$N_0 = \frac{2}{\pi r_0^2 \tau}\frac{PT}{\upsilon\hbar\omega} \quad (4)$$

where r_0 is the radial distance from the optical axis at the $1/e^2$ level, N_0 is the photon flux on the optical axis, n = νt is the number of pulses, in which ν is the laser repetition rate and t is the exposure time, τ is the laser pulse duration, σ_2 is the effective 2PA cross-section of the photoinitiator, which is a product of 2PA cross-section and quantum efficiency, z_R is the Rayleigh

length, ρ_0 is the initial photoinitiator concentration (0.6 in our case), ρ_{th} is the threshold photoinitiator concentration, P is the average laser power measured before the objective and T is the transmittance of the objective. By using a custom-written Matlab® code, we estimated the unknown model parameters, ρ_{th}, σ_2, r_0 and z_R, by solving the optimization problem which minimized the sum of mean square error between the measurements and the model fit.

2.5. Fabrication of microstructures

We fabricated two types of 3D microstructures, namely rectangular grids and walls, that were designed using Rhinoceros® 4.0 CAD (Robert McNeel & Associates, USA). The grids were used for line width measurements and comprised lines written on rectangular support structures. The grids were fabricated using the scanning speeds of 1-125 μm/s and the approximately 25% (25%-26%), 50% (50%-51.0%), 75% (72%-76%) and 90% (84%-91%) powers corresponding to each scanning speeds for each material. Rectangular walls of different dimensions were fabricated to study the post-development swelling and deformation. The walls were fabricated with the constant scanning speed of 100 μm/s and approximately 90% power for each material (PHEG-A13 96%, PHEG-A9 89%, PHEG-MA21 92%, PHEG-MA11 82% and PEGda-575 90%). The walls were produced using the multipath scanning method described in [33] with a combination of four different wall thicknesses (1, 4, 6 or 8 contours separated by 1 μm) and three different heights (5, 8 or 11 contours separated by 1.5 μm).

2.6. Characterization of microstructures by SEM and confocal imaging

The fabricated microstructures were studied by SEM imaging with either Philips XL-30 (Philips Electron Optics, the Netherlands) or Zeiss ULTRAplus (Carl Zeiss Microimaging GmbH, Germany). Prior to imaging, the samples were vacuum dried for a minimum of 20 h and then sputter coated with gold in an argon atmosphere to a nominal thickness of 75 nm (150 Sputter Coater, Edwards Ltd, UK). Structure dimensions were measured from top view (0° tilt) and side view (90° tilt) SEM images with a free software GIMP 2.6. The dimensions of the rectangular walls

were measured both in the swollen and dry state. For the swollen state measurements, the samples were imaged with a confocal microscope (LSM 700, Carl Zeiss Microimaging GmbH, Germany) with a 20x air objective with NA = 0.55. Prior to imaging, the samples were soaked in ion-exchanged water for approximately 20 h and treated with a fluorescein isothiocyanate (FITC, Sigma-Aldrich Finland Oy, Finland) solution (1 mg/ml FITC in dimethyl sulfoxide) washed off by ion-exchanged water. The samples were imaged inside a droplet of ion-exchanged water with the xy-resolution of 100 nm-1.19 μm and a z-resolution of 1 μm. The width, height, thickness and volume the swollen walls were measured from thresholded confocal image stacks with the free image analysis software FIJI. The dry volumes were calculated from top view and side view SEM images based on the overall walled area, opening area and wall height measured with GIMP 2.6. The volumetric swelling ratios were assumed to be independent of the wall dimensions and were calculated as

$$Volumetric\ swelling\ ratio = \frac{swollen\ volume}{dry\ volume} \qquad (5)$$

The widths of the walls in the dry state were measured from side view SEM images and the dimensional change caused by the swollen-to-dry transition, referred to as xy-deformation %, was calculated as

$$xy - deformation\ \% = \frac{width_{swollen} - width_{dry}}{width_{swollen}}\ x\ 100 \qquad (6)$$

2.7. Statistical analysis

The dynamic power range data and the volumetric swelling ratio data were analysed with the Kruskal-Wallis test followed by post-hoc comparison by the Wilcoxon rank-sum test with Bonferroni correction. A p-value of less than 0.05 was considered significant.

3. Results and discussion

3.1. Material synthesis

The determined degrees of modification, molecular weight averages and dispersities of the PHEGs used in this work are summarized in **Table 1**.

Table 1 The properties of the prepared methacryloylated and acryloylated PHEGs.

Sample Code	Degree of modification [mol %] (A – acryloylation, MA – methacryloylation)	Molecular Weight $\overline{M}_w$ [a)]	Dispersity Đ	Total yield to PHEG[b)]	Yield of modification
PHEG-A13	12.9 (A)	92000	7.16	45%	63%
PHEG-A9	9.4 (A)	92000	6.12	45%	73%
PHEG-MA21	20.7 (MA)	20900	1.61	45%	71%
PHEG-MA11	11.2 (MA)	21500	3.00	45%	77%

[a)] Based on PEO calibration standards

[b)] Yield from γ-benzyl-L-glutamate to PHEG

The PHEG macromonomers are soluble linear polymers. During the 2PP-DLW processing, these linear polymers become covalently crosslinked into a 3D network through radical polymerization of the methacryloyl or acryloyl groups in the side chains. The structure and physical characteristics of the insoluble gel networks are expected to be analogous to that described previously in [23,29]. The only difference in the gels presented here is the use of a photoinitiator to enable the 2PP-DLW process.

3.2. Threshold values and dynamic power ranges

The polymerization threshold (P_{th}) and the damage threshold (P_D) power values and the calculated dynamic power ranges of the PHEGs and PEGdas are shown in Fig 2. Both the P_{th} and P_D increased with increasing scanning speed, as shown by Fig. 2 (a-d). All the PHEGs had very similar thresholds values but the PEGdas had different threshold values depending on the composition of the photopolymer solution. The pure PEGda-575 solution had the lowest P_{th} and P_D that were also the least sensitive to the increase in scanning speed. The water-based PEGda-575-20 and PEGda-10000 solutions had approximately 7 times higher P_{th} than the pure PEGda-575 and 4-6 times higher thresholds than the PHEGs. The P_D of PEGda-575-20, PEGda-10000 and the PHEGs were similar and approximately three times higher than the values of pure PEGda-575. Compared to the pure PEGda-575, the PHEGs had approximately 1.5 times higher P_{th} values, which implies that the PEGda-575-I2959 combination had a slightly better two-photon photosensitivity than the PHEG-I2959 combinations.

As shown by Fig. 2 (e), all the PHEGs had similar dynamic power range values of 7.8-9.4 with no statistically significant differences ($p > 0.05$). The PEGdas, on the other hand, had significantly narrower dynamic power ranges than the PHEGs ($p < 0.01$). Due to the higher P_D, the PHEGs had approximately twice wider dynamic power ranges than pure PEGda-575. A larger dynamic power range is known to be beneficial for 3D microfabrication as it allows for the tuning of the microstructure size in a wider range.[34] Among the PEGdas, PEGda-575 had a significantly wider dynamic power range of 4.6 than the water-based PEGdas ($p < 0.01$). With the very narrow dynamic power ranges of 1.4 and 1.9, the PEGda-575-20 and PEGda-10000 solutions with equal water content to the PHEGs have only limited 2PP-DLW applicability.

It is common practice to report the threshold values determined for only a few scanning speeds. [35-40]. In contrast, we determined the threshold laser power values over a wide range of scanning speeds, which provides more reliable results. Moreover, instead of choosing arbitrary laser powers, we used the 10-90% power values within the polymerization window to fabricate the

PHEG and PEGda microstructures. This approach enabled reliable comparison of 2PP-DLW performance despite the differences in the absolute threshold values.

3.3. Voxel fabrication

Fig. 3 shows the measured width and height of PHEG and PEGda-575 voxels as functions of exposure time and the curves based on Equation (1)-(4). The values of the estimated model parameters are shown in Table 2.

Table 2 The estimated values of the parameters ρ_{th}, σ_2, r_0 and z_R according to the Equation (1)-(4) for the width and height of PHEG and PEGda-575 voxels.

Estimated parameters	PHEG-A13	PHEG-A9	PHEG-MA21	PHEG-MA11	PEGda-575
ρ_{th}	0.26	0.22	0.22	0.23	0.21
σ_2 (cm^4s/photon)	8.8×10^{-52}	2.1×10^{-51}	3.4×10^{-52}	3.7×10^{-52}	3.7×10^{-52}
r_0 (nm)	917	801	704	612	504
z_R (nm)	1684	1298	1305	1435	781

Voxel fabrication with the high water content PEGda-575-20 and PEGda-10000 solutions was also tested but only a few and often distorted voxels could be produced, which were not sufficient for further analysis (data not shown). The PHEG and PEGda-575 voxels fabricated with long exposure times and high powers had elongated and occasionally fragmented shapes, which deviated from the ideal ellipsoidal shape of 2PP-DLW voxels described earlier in [31]. These fringed voxel shapes could be explained by the simultaneous recording of zeroth- and higher-order diffraction patterns, as described by Sun et al [41]. Nevertheless, close to ellipsoidal voxels were achieved with all the materials with short exposure times and 10% laser powers (data not shown).

The minimum achieved voxel sizes (width/height) were 430 nm/2.3 μm for PHEG-A13, 390 nm/2.9 μm for PHEG-A9, 510 nm/2.1 μm for PHEG-MA21, 540 nm/2.6 μm for PHEG-MA11 and 330 nm/2.2 μm for PEGda-575. The minimum voxel sizes for all the materials were approximately 1.5-2 times smaller than the diffraction-limited laser spot, which is a strong indication that the polymerization is indeed based on 2PA. The lateral and axial radii of a diffraction-limited laser spot are given by $r = 0.61\lambda/NA = 360$ nm and $z = 2\lambda n_{oil}/NA^2 = 2.0$ μm respectively (n_{oil} = refractive index of the immersion oil = 1.516) [32,42]. The size of the diffraction-limited spot in our case can thus be estimated as $2r = 720$ nm and $2z = 4.0$ μm.

The measured voxel width and height were in agreement with the analytical model, especially with 10% laser power and short exposure times of 5-250 ms. However, the estimated values for r_0 were approximately 1.7-2.5 times higher for the PHEGs and 1.4 times higher for PEGda-575 than the calculated lateral radius of the diffraction-limited laser spot (r = 360 nm). This disagreement with the theoretical model could be explained by effects of spherical aberration caused by a refractive index mismatch between the immersion oil and the water-based hydrogel materials. Spherical aberration due to refractive index mismatch has been shown affect the size and shape of 2PP-DLW microstructures due to the distortion the laser intensity point spread function [43]. In our set-up, the laser beam is focused through the entire width of the sample (≈ 150 μm), which further increases the effect of spherical aberration. In addition to spherical aberration, this simplified model does not include the effects of radical diffusion, temperature or kinetics of the polymerization process studied by Uppal et al. [44]. This could also attribute to the observed disagreements between the measured voxels dimensions and the model.

The photoinitiator I2959 is widely used in the photopolymerization of hydrogels. It is moderately soluble in water and has been reported cytocompatible with many cell types [45]. I2959 also has an absorption peak close to the half of the wavelength of our laser source, which is required by 2PA [4]. However, the 2PA cross-section (σ_{2PA}) of I2959 has not been previously reported. The estimated values for the effective 2PA cross-section, $\sigma_{2,}$ for the PHEGs and PEGda-575 were in the

order of 10^{-52}-10^{-51} cm^4s/photon. By assuming a quantum efficiency of 0.3 [46], the σ_{2PA} of I2959 is estimated to be in the order of 10^{-53}-10^{-52} cm^4s/photon, in other words 0.001-0.01 GM units (1 GM = 10^{-50} cm^4s/photon). This value is in agreement with the low two-photon absorption cross-section values that have been previously reported for other commercial photoresins [47] and photoinitiators [32].

3.4. Fabrication of grid structures

Stable support structures could not be fabricated using the high water content PEGda-575-20 and PEGda-10000 (data not shown). Similar results have been recently reported by Torgersen et al. who found that although microstructures with 80% water content could be produced of PEGda with a custom photoinitiator, the structures were prone to deformation due to insufficient crosslinking [22]. Fig. 4 shows examples of the SEM images of PHEG and PEGda lines fabricated on rectangular support structures. The PHEG-As polymerized into substantially thicker and more rigid lines than the PHEG-MAs and PEGda-575. The lines fabricated using the PHEG-MAs were easily distorted during the development process. The PHEG-MA11 with the lowest degree of methacyloylation performed the worst and the widths these lines could not be measured due to severe distortion. Although the PEGda-575 lines were stable with most parameter combinations, with the low scanning speeds of 1-5 μm/s they were severely distorted with all the laser powers tested. This drawback is likely due to the low viscosity of the PEGda-575 solution and the motion of the liquid disturbing the polymerization process.

Fig. 5 shows the measured widths of the PHEG-A, PHEG-MA21 and PEGda-575 lines. Nearly constant line widths were achieved with the PHEG-As and PEGda-575 with scanning speeds higher than 25 μm/s by simultaneously controlling the laser power and scanning speed. This approach could in the future be used for fabricating microstructures with variable crosslinking density and yet identical dimensions. As shown by Fig. 5 (a-c), the PHEG-As and PEGda-575 polymerized into measurable lines even with the highest tested scanning speed of 125 μm/s. In contrast, only barely measurable lines were produced of PHEG-MA21 with all the power sets with

the maximum tested scanning speed of 75 μm/s. Based on the number of parameter combinations that could produce measurable lines, the PHEG-As and PEGda-575 had a much wider processing range than PHEG-MA21. This indicates that the 2PP-DLW of the PHEG-As and PEGda-575 is more efficient than the PHEG-MAs and the materials are crosslinked to higher degree. This is consistent with previously published findings of the higher 2PP-DLW reactivity of acrylated macromers compared to methacryloylated analogues [48].

A drawback of our current 2PP-DLW set-up with the PHEGs and PEGda is the relatively low maximum writing speed of 125 μm/s. However, by switching to a lower numerical aperture objective, the writing speed could be improved due to increased voxel size. This approach has been demonstrated previously by Danilevicius et al. [7]. The writing speed is also limited by the low 2PA cross-section of the I2959 initiator and could be further improved by the use of a more efficient photoinitiator system. It has been recently shown that with highly efficient water-soluble photoinitators, writing speeds of even 100 mm/s are achievable [49].

3.5. Swelling and deformation

Fig. 6 shows examples of confocal and SEM images of the rectangular walls and the calculated volumetric swelling ratios. As shown by the oblique view confocal images in Fig. 6 (a), the walls fabricated using the PHEGs strongly absorbed the FITC dye and were uniformly fluorescent. However with PEGda-575, the dye was bound only to the surface of the microstructures and was not absorbed by the bulk material. As shown by Fig. 6 (b), PHEG-MA11 had a significantly higher swelling ratio than PHEG-MA21 ($p < 0.001$), PHEG-A13 ($p < 0.001$), PHEG-A9 ($p < 0.05$) and PEGda-575 ($p < 0.001$). Also, PHEG-A13 had a significantly higher swelling ratio than PHEG-MA21 and PEGda-575 ($p < 0.001$). Volumetric swelling ratio is known to be directly related to the mesh size of hydrogel networks, which governs the diffusive properties and relates to crosslinking density and mechanical properties [50,51]. The low swelling ratio of the small molecular weight PEGda-575 indicates that highly crosslinked structures are formed by 2PP-DLW. The PEGda-575 walls also did not absorb the FITC dye, which is consistent with highly crosslinked networks of

small mesh size. Among the PHEGs, PHEG-MA21 with the highest degree of modification had the lowest swelling ratio and PHEG-MA11 the highest. This is consistent with the observed distortion of PHEG-MA11 microstructures, which was likely caused by limited crosslinking density due to the low degree of methacryloylation. In addition to the degree of modification, the higher swelling ratios of the PHEG-As compared to the PHEG-MA21 could be explained by the over three times higher molecular weights as swelling is known to correlate inversely with molecular weight [52]. It should be noted that as the swelling values were based on samples produced with the 90% laser powers, they represent close to minimal swelling. With lower laser powers, it is likely that swelling ratios would be higher due to a lower degree of crosslinking.

In addition to swelling, we studied the deformation of the hydrogel walls caused by the development process. The open geometry of the rectangular walls was designed to mimic porosity, which is an essential requirement for tissue engineering scaffolds. However, porous structures are especially prone to deformation, which is known to be dominated by the capillary force induced by the surface tension of the evaporating developer [53]. Fig. 7 shows the measured xy-deformation of the PHEG and PEGda-575 walls as functions of the average swollen wall width and height. The PEGda-575 walls exhibited the lowest overall deformation of approximately 6-11%. Among the PHEGs, the PHEG-A13 performed the best with the deformation of approximately 12-18%. Although the water-based PHEGs deformed more than the pure PEGda-575, the high water content is beneficial as it facilitates the incorporation of cells into the 2PP-DLW processing [18]. The pulse energies corresponding to the 90% laser powers used for the fabrication of PHEG walls were 0.3 nJ, which is well below the reported the 1-2 nJ threshold for inducing intracellular ablation [54]. In the future, the PHEGs could thus be tested for the fabrication of cell-laden microstructures. To improve the reliability of the fabrication process, the deformation of PHEG microstructures could be reduced by numerical compensation of the CAD models or by introducing additional crosslinking agents, such as pentaerythritol tetraacrylate (PETA) used by Klein et al. [55].

The magnitude of the deforming force is also known to be influenced by microstructure dimensions [56]. Park et al. have previously shown that increasing height increases the deformation of hollow rectangular columns of identical cross sections [53]. We observed that the deformation of the PHEG microstructures increased notably with both increasing wall width and height, as shown by Fig. 7 (a-d). Contrary to the PHEGs, the deformation of PEGda-575 walls was seemingly not influenced by the dimensional changes. This was most likely due to the small degree of deformation of the highly crosslinked structures.

The fabrication of the grids structures and wall arrays also enabled evaluation of the adhesion between the microstructures and the glass surface. The adhesion of the PEGda-575 structures was found inferior compared to the PHEGs. Of all the PEGda-575 grid patterns and walls, 13% were detached partly or completely during the development process despite the adhesion promoting MAPTMS-treatment on the glass surface. In contrast, none of the PHEG microstructures were detached during fabrication.

4. Conclusions

We studied the 2PP-DLW of PHEG poly(AA) hydrogels for the first time and compared the performance of these novel materials to commercial PEGda hydrogels. With the PHEGs and PEGda-575, we demonstrated microstructure dimensions beyond the diffraction limit of light. We showed that both the acryloylated and methacryloylated PHEGs are applicable to 2PP-DLW over a relatively wide range of processing parameters and that stable 3D structures with 80% water content can be fabricated. Of the PEGdas tested, only the pure PEGda-575 with no added water was well suited for 2PP-DLW processing with I2959. However, the adhesion of PEGda-575 microstructures to glass substrates was poor compared to the PHEGs and the narrower polymerization window limits the tuning of microstructure dimensions. The acryloylated PHEGs performed better than the methacryloylated analogs and produced microstructures that were less prone to deformation. PHEG-A13 with the highest degree of acryloylation showed the greatest overall potential for 3D

fabrication by 2PP-DLW. The findings of this contribution could in the future be used to construct biomimetic microstructures for soft tissue engineering applications.

Acknowledgements

E.K. was financially supported by the Finnish Cultural Foundation and the Doctoral Program of Tampere University of Technology's President. E.K. and M.K. were also supported by the TEKES (the Finnish Funding Agency for Technology and Innovation) Human Spare Parts project. T.S. and F.R. were supported by Czech Science Foundation (Grant No.: P108/11/1857). The authors gratefully acknowledge M.Sc. (Eng.) Taru Karhula for SEM imaging.

References

[1] B.V. Slaughter, S.S. Khurshid, O.Z. Fisher, A. Khademhosseini, N.A. Peppas, Hydrogels in Regenerative Medicine, Adv. Mater. 21 (2009) 3307-3329.

[2] P. Zorlutuna, N. Annabi, G. Camci-Unal, M. Nikkhah, J.M. Cha, J.W. Nichol, A. Manbachi, H. Bae, S. Chen, A. Khademhosseini, Microfabricated Biomaterials for Engineering 3D Tissues, Adv. Mater. 24 (2012) 1782-1804.

[3] T. Billiet, M. Vandenhaute, J. Schelfhout, S. Van Vlierberghe, P. Dubruel, A review of trends and limitations in hydrogel-rapid prototyping for tissue engineering, Biomaterials. 33 (2012) 6020-6041.

[4] K. Lee, D. Yang, S.H. Park, R.H. Kim, Recent developments in the use of two-photon polymerization in precise 2D and 3D microfabrications, Polym. Adv. Technol. 17 (2006) 72-82.

[5] W. Haske, V.W. Chen, J.M. Hales, W. Dong, S. Barlow, S.R. Marder, J.W. Perry, 65 nm feature sizes using visible wavelength 3-D multiphoton lithography, Opt. Express. 15 (2007) 3426-3436.

[6] A. Ovsianikov, V. Mironov, J. Stampfl, R. Liska, Engineering 3D cell-culture matrices: multiphoton processing technologies for biological and tissue engineering applications, Expert Rev. Med. Devices. 9 (2012) 613-633.

[7] P. Danilevicius, S. Rekstyte, E. Balciunas, A. Kraniauskas, R. Jarasiene, R. Sirmenis, D. Baltriukiene, V. Bukelskiene, R. Gadonas, M. Malinauskas, Micro-structured polymer scaffolds fabricated by direct laser writing for tissue engineering, J. Biomed. Opt. 17 (2012) 081405-1.

[8] C.N. LaFratta, J.T. Fourkas, T. Baldacchini, R.A. Farrer, Multiphoton Fabrication, Angew. Chem. Int. Ed. 46 (2007) 6238-6258.

[9] J.D. Pitts, P.J. Campagnola, G.A. Epling, S.L. Goodman, Submicron Multiphoton Free-Form Fabrication of Proteins and Polymers: Studies of Reaction Efficiencies and Applications in Sustained Release, Macromolecules. 33 (2000) 1514-1523.

[10] J.D. Pitts, A.R. Howell, R. Taboada, I. Banerjee, J. Wang, S.L. Goodman, P.J. Campagnola, New Photoactivators for Multiphoton Excited Three-dimensional Submicron Cross-linking of Proteins: Bovine Serum Albumin and Type 1 Collagen, Photochem. Photobiol. 76 (2002) 135-144.

[11] X. Chen, Y. Su, V. Ajeti, S. Chen, P.J. Campagnola, Cell Adhesion on Micro-Structured Fibronectin Gradients Fabricated by Multiphoton Excited Photochemistry, Cell. Mol. Bioeng. 5 (2012) 307-319.

[12] M. Gebinoga, J. Katzmann, U. Fernekorn, J. Hampl, F. Weise, M. Klett, A. Läffert, T.A. Klar, A. Schober, Multi-photon structuring of native polymers: A case study for structuring natural proteins, Eng. Life Sci. 13 (2013) 368-375.

[13] P. Su, Q.A. Tran, J.J. Fong, K.W. Eliceiri, B.M. Ogle, P.J. Campagnola, Mesenchymal Stem Cell Interactions with 3D ECM Modules Fabricated via Multiphoton Excited Photochemistry, Biomacromolecules. 13 (2012) 2917-2925.

[14] J. Zhu, Bioactive modification of poly(ethylene glycol) hydrogels for tissue engineering, Biomaterials. 31 (2010) 4639-4656.

[15] A. Ovsianikov, A. Deiwick, S. Van Vlierberghe, P. Dubruel, L. Möller, G. Dräger, B. Chichkov, Laser Fabrication of Three-Dimensional CAD Scaffolds from Photosensitive Gelatin for Applications in Tissue Engineering, Biomacromolecules. 12 (2011) 851-858.

[16] S. Engelhardt, E. Hoch, K. Borchers, W. Meyer, H. Krüger, G.E.M. Tovar, A. Gillner, Fabrication of 2D protein microstructures and 3D polymer–protein hybrid microstructures by two-photon polymerization, Biofabrication. 3 (2011) 025003.

[17] X. Qin, J. Torgersen, R. Saf, S. Mühleder, N. Pucher, S.C. Ligon, W. Holnthoner, H. Redl, A. Ovsianikov, J. Stampfl, R. Liska, Three-dimensional microfabrication of protein hydrogels via two-photon-excited thiol-vinyl ester photopolymerization, J. Polym. Sci. , Part A: Polym. Chem. 51 (2013) 4799-4810.

[18] A. Ovsianikov, S. Mühleder, J. Torgersen, Z. Li, X. Qin, S. Van Vlierberghe, P. Dubruel, W. Holnthoner, H. Redl, R. Liska, J. Stampfl, Laser Photofabrication of Cell-Containing Hydrogel Constructs, Langmuir. (2013).

[19] A. Berg, R. Wyrwa, J. Weisser, T. Weiss, R. Schade, G. Hildebrand, K. Liefeith, B. Schneider, R. Ellinger, M. Schnabelrauch, Synthesis of Photopolymerizable Hydrophilic Macromers and Evaluation of Their Applicability as Reactive Resin Components for the Fabrication of Three-Dimensionally Structured Hydrogel Matrices by 2-Photon-Polymerization, Adv. Eng. Mater. 13 (2011) B274-B284.

[20] K.Y. Lee, D.J. Mooney, Hydrogels for Tissue Engineering, Chem. Rev. 101 (2001) 1869-1880.

[21] A. Ovsianikov, M. Gruene, M. Pflaum, L. Koch, F. Maiorana, M. Wilhelmi, A. Haverich, B. Chichkov, Laser printing of cells into 3D scaffolds, Biofabrication. 2 (2010) 014104.

[22] J. Torgersen, A. Ovsianikov, V. Mironov, N. Pucher, X. Qin, Z. Li, K. Cicha, T. Machacek, R. Liska, V. Jantsch, J. Stampfl, Photo-sensitive hydrogels for three-dimensional laser microfabrication in the presence of whole organisms, J. Biomed. Opt. 17 (2012) 105008-105008.

[23] T. Sedlačík, H. Studenovská, F. Rypáček, Enzymatic degradation of the hydrogels based on synthetic poly(α-amino acid)s, J. Mater. Sci.: Mater. Med. 22 (2011) 781-788.

[24] J. Pytela, V. Saudek, J. Drobník, F. Rypáček, Poly(N^5-hydroxyalkylglutamines). IV. Enzymatic degradation of n^5-(2-hydroxyethyl)-L-glutamine homopolymers and copolymers, J. Controlled Release. 10 (1989) 17-25.

[25] H. Chiu, P. Kopečková, S.S. Deshmane, J. Kopeček, Lysosomal degradability of poly(α-amino acids), J. Biomed. Mater. Res. 34 (1997) 381-392.

[26] H. Studenovská, P. Vodička, V. Proks, J. Hlučilová, J. Motlík, F. Rypáček, Synthetic poly(amino acid) hydrogels with incorporated cell-adhesion peptides for tissue engineering, J. Tissue. Eng. Regen. Med. 4 (2010) 454-463.

[27] R. Hirschmann, H. Schwam, R.G. Strachan, E.F. Schoenewaldt, H. Barkemeyer, S.M. Miller, J.B. Conn, V. Garsky, D.F. Veber, R.G. Denkewalter, Controlled synthesis of peptides in aqueous medium. VIII. Preparation and use of novel .alpha.-amino acid N-carboxyanhydrides, J. Am. Chem. Soc. 93 (1971) 2746-2754.

[28] E.R. Blout, R.H. Karlson, Polypeptides. III. The Synthesis of High Molecular Weight Poly-γ-benzyl-L-glutamates, J. Am. Chem. Soc. 78 (1956) 941-946.

[29] V. Skarda, F. Rypácek, M. Ilavský, Biodegradable Hydrogel for Controlled Release of Biologically Active Macromolecules, J. Bioact. Compat. Polym. 8 (1993) 24-40.

[30] E. Käpylä, S. Turunen, J. Pelto, M. Kellomäki, Investigation of the optimal processing parameters for picosecond laser-induced microfabrication of a polymer-ceramic hybrid material, J. Micromech. Microeng. 21 (2011) 065033.

[31] H. Sun, T. Tanaka, S. Kawata, Three-dimensional focal spots related to two-photon excitation, Appl. Phys. Lett. 80 (2002) 3673-3675.

[32] J. Serbin, A. Egbert, A. Ostendorf, B.N. Chichkov, R. Houbertz, G. Domann, J. Schulz, C. Cronauer, L. Fröhlich, M. Popall, Femtosecond laser-induced two-photon polymerization of organic-inorganic hybrid materials for applications in photonics, Opt. Lett. 28 (2003) 301-303.

[33] D. Yang, S.H. Park, T.W. Lim, H. Kong, S.W. Yi, H.K. Yang, K. Lee, Ultraprecise microreproduction of a three-dimensional artistic sculpture by multipath scanning method in two-photon photopolymerization, Appl. Phys. Lett. 90 (2007) 079903-3.

[34] C. Martineau, R. Anémian, C. Andraud, I. Wang, M. Bouriau, P.L. Baldeck, Efficient initiators for two-photon induced polymerization in the visible range, Chem. Phys. Lett. 362 (2002) 291-295.

[35] B.H. Cumpston, S.P. Ananthavel, S. Barlow, D.L. Dyer, J.E. Ehrlich, L.L. Erskine, A.A. Heikal, S.M. Kuebler, I.-.S. Lee, D. McCord-Maughon, J. Qin, H. Rockel, M. Rumi, X. Wu, S.R. Marder, J.W. Perry, Two-photon polymerization initiators for three-dimensional optical data storage and microfabrication, Nature. 398 (1999) 51-54.

[36] T. Watanabe, M. Akiyama, K. Totani, S.M. Kuebler, F. Stellacci, W. Wenseleers, K. Braun, S.R. Marder, J.W. Perry, Photoresponsive Hydrogel Microstructure Fabricated by Two-Photon Initiated Polymerization, Adv. Funct. Mater. 12 (2002) 611-614.

[37] T. Baldacchini, C.N. LaFratta, R.A. Farrer, M.C. Teich, B.E.A. Saleh, M.J. Naughton, J.T. Fourkas, Acrylic-based resin with favorable properties for three-dimensional two-photon polymerization, J. Appl. Phys. 95 (2004) 6072-6076.

[38] S.J. Jhaveri, J.D. McMullen, R. Sijbesma, L. Tan, W. Zipfel, C.K. Ober, Direct Three-Dimensional Microfabrication of Hycrogels via Two-Photon Lithography in Aqueous Solution, Chem. Mater. 21 (2009).

[39] S. Engelhardt, Y. Hu, N. Seiler, D. Riester, W. Meyer, H. Krüger, M. Wehner, E. Bremus-Köbberling, A. Gillner, 3D-Microfabrication of Polymer-Protein Hybrid Structures with a Q-Switched Microlaser, J. Laser Micro/Nanoeng. 6 (2011) 54-58.

[40] C. De Marco, A. Gaidukeviciute, R. Kiyan, S.M. Eaton, M. Levi, R. Osellame, B.N. Chichkov, S. Turri, A New Perfluoropolyether-Based Hydrophobic and Chemically Resistant Photoresist Structured by Two-Photon Polymerization, Langmuir. 29 (2013) 426-431.

[41] H. Sun, M. Maeda, K. Takada, J.W.M. Chon, M. Gu, S. Kawata, Experimental investigation of single voxels for laser nanofabrication via two-photon photopolymerization, Appl. Phys. Lett. 83 (2003) 819-821.

[42] S. Inoué, Foundations of Confocal Scanned Imaging in Light Microscopy, in: J.B. Pawley (Ed.), Handbook of Biological Confocal Microscopy, Springer US, New York, 1995, pp. 1-14.

[43] H.E. Williams, Z. Luo, S.M. Kuebler, Effect of refractive index mismatch on multi-photon direct laser writing, Opt. Express. 20 (2012) 25030-25040.

[44] N. Uppal, P.S. Shiakolas, Modeling of temperature-dependent diffusion and polymerization kinetics and their effects on two-photon polymerization dynamics, J. Micro/Nanolithogr. , MEMS, MOEMS. 7 (2008) 043002-043002.

[45] C.G. Williams, A.N. Malik, T.K. Kim, P.N. Manson, J.H. Elisseeff, Variable cytocompatibility of six cell lines with photoinitiators used for polymerizing hydrogels and cell encapsulation, Biomaterials. 26 (2005) 1211-1218.

[46] S. Jockusch, M.S. Landis, B. Freiermuth, N.J. Turro, Photochemistry and Photophysics of alpha-Hydroxy Ketones, Macromolecules. 34 (2001) 1619-1626.

[47] M. Miwa, S. Juodkazis, T. Kawakami, S. Matsuo, H. Misawa, Femtosecond two-photon stereo-lithography, Appl. Phys. A: Mater. Sci. Process. 73 (2001) 561-566.

[48] T. Weiß, R. Schade, T. Laube, A. Berg, G. Hildebrand, R. Wyrwa, M. Schnabelrauch, K. Liefeith, Two-Photon Polymerization of Biocompatible Photopolymers for Microstructured 3D Biointerfaces, Adv. Eng. Mater. 13 (2011) B264-B273.

[49] Z. Li, J. Torgersen, A. Ajami, S. Muhleder, X. Qin, W. Husinsky, W. Holnthoner, A. Ovsianikov, J. Stampfl, R. Liska, Initiation efficiency and cytotoxicity of novel water-soluble two-photon photoinitiators for direct 3D microfabrication of hydrogels, RSC Adv. 3 (2013) 15939-15946.

[50] A.M. Lowman, N.A. Peppas, Hydrogels, in: E. Mathiowitz (Ed.), Encyclopedia of Controlled Drug Delivery, John Wiley & Sons, New York, 1999, pp. 397-418.

[51] N.A. Peppas, P. Bures, W. Leobandung, H. Ichikawa, Hydrogels in pharmaceutical formulations, Eur. J. Pharm. Biopharm. 50 (2000) 27-46.

[52] V. Chan, P. Zorlutuna, J.H. Jeong, H. Kong, R. Bashir, Three-dimensional photopatterning of hydrogels using stereolithography for long-term cell encapsulation, Lab Chip. 10 (2010) 2062-2070.

[53] S. Park, K.H. Kim, T.W. Lim, D. Yang, K. Lee, Investigation of three-dimensional pattern collapse owing to surface tension using an imperfection finite element model, Microelectron. Eng. 85 (2008) 432-439.

[54] I. Maxwell, S. Chung, E. Mazur, Nanoprocessing of subcellular targets using femtosecond laser pulses, Medical Laser Application. 20 (2005) 193-200.

[55] F. Klein, B. Richter, T. Striebel, C.M. Franz, G.v. Freymann, M. Wegener, M. Bastmeyer, Two-Component Polymer Scaffolds for Controlled Three-Dimensional Cell Culture, Adv. Mater. 23 (2011) 1341-1345.

[56] T. Kondo, S. Juodkazis, H. Misawa, Reduction of capillary force for high-aspect ratio nanofabrication, Appl. Phys. A. 81 (2005) 1583-1586.

Figure Captions

Fig. 1. (a) Scheme of preparation of PHEG macromers. (b) Dependence of the degree of methacryloylation on the amount of methacryloyl chloride (MA-Cl) added to the reaction mixture, expressed as a molar ratio of MA-Cl to HEG units in the polymer chain.

Fig. 2. (a-b) Polymerization (P_{th}) and (c-d) damage threshold (P_D) powers of the different PHEGs and PEGdas as functions of scanning speed. The results for PEGda-575 are presented with both the PHEGs (a and c) and the PEGda (b and d) for easier comparison. The data points represent the mean ± standard deviation (n = 3). The solids lines are guides to the eye. (e) The calculated dynamic power range (P_D/P_{th}). The data points represent mean ± standard deviation (n = 8-10).** ($p < 0.01$) indicates significance.

Fig. 3. (a-e) Width and (f-j) height of PHEG and PEGda-575 voxels as functions of exposure time for approximately 10%, 50% and 90% laser powers. The power values corresponding to the percentages are given in brackets. The data points represent the mean ± standard deviation (n = 3), except for PEGda-575 8%, for which n =1-3. The curves represent the estimated theoretical voxel width and height based on the Equation (1)-(4).

Fig. 4. SEM images of PHEGs and PEGda-575 lines fabricated with 75% laser powers 1-75 μm/s scanning speeds. Scale bars represent 10 μm.

Fig. 5. The measured widths of PHEG-As, PHEG-MA21 and PEGda-575 lines as functions of scanning speed for approximately (a) 90%, (b) 75%, (c) 50% and (d) 25% laser powers. The data points represent the mean ± standard deviation (n = 3). The solids lines are guides to the eye.

Fig. 6. (a) Oblique (top row) and side view (middle row) 3D reconstructions of confocal image stacks and side view SEM images (bottom row) of rectangular walls. The walls consisted of 8 contours in the xy-direction and 11 contours in the z-direction. Scale bars represent 10 μm. (b) Volumetric swelling ratios. The data points represent mean ± standard deviation (n = 36 for PHEG-A13, n = 35 for PHEG-A9, n = 27 for PHEG-MA21 and PHEG-MA11, n = 30 for PEGda-575). *** ($p < 0.001$) indicates significance.

Fig. 7. The calculated xy-deformation % (colourbar) of (a) PHEG-A13, (b) PHEG-A9, (c) PHEG-MA21, (d) PHEG-MA11 and (e) PEGda-575 walls as functions of the average swollen wall width and height. The data points represent mean (n = 2-3)

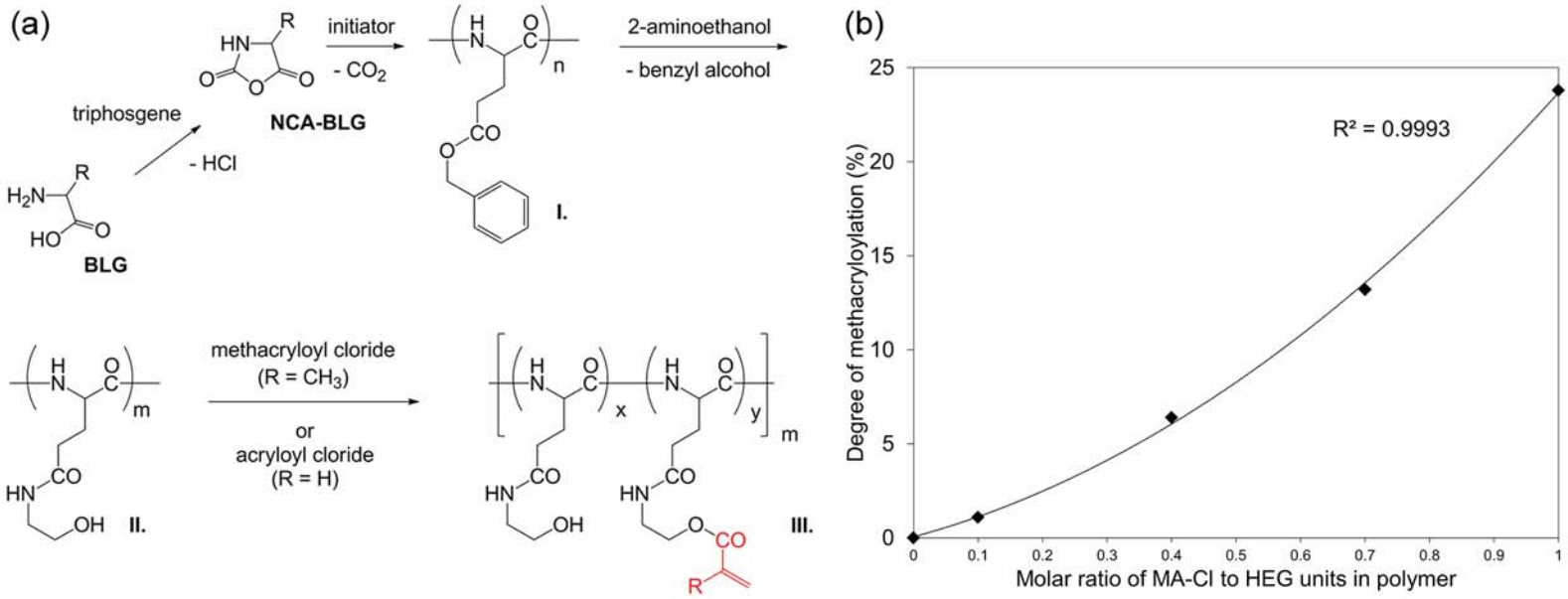
(a)
triphosgene
- HCl
BLG
NCA-BLG
initiator
- CO2
I.
2-aminoethanol
- benzyl alcohol
II.
methacryloyl cloride
(R = CH3)
or
acryloyl cloride
(R = H)
III.
(b)
R² = 0.9993
Degree of methacryloylation (%)
Molar ratio of MA-Cl to HEG units in polymer
0
5
10
15
20
25
0
0.1
0.2
0.3
0.4
0.5
0.6
0.7
0.8
0.9
1

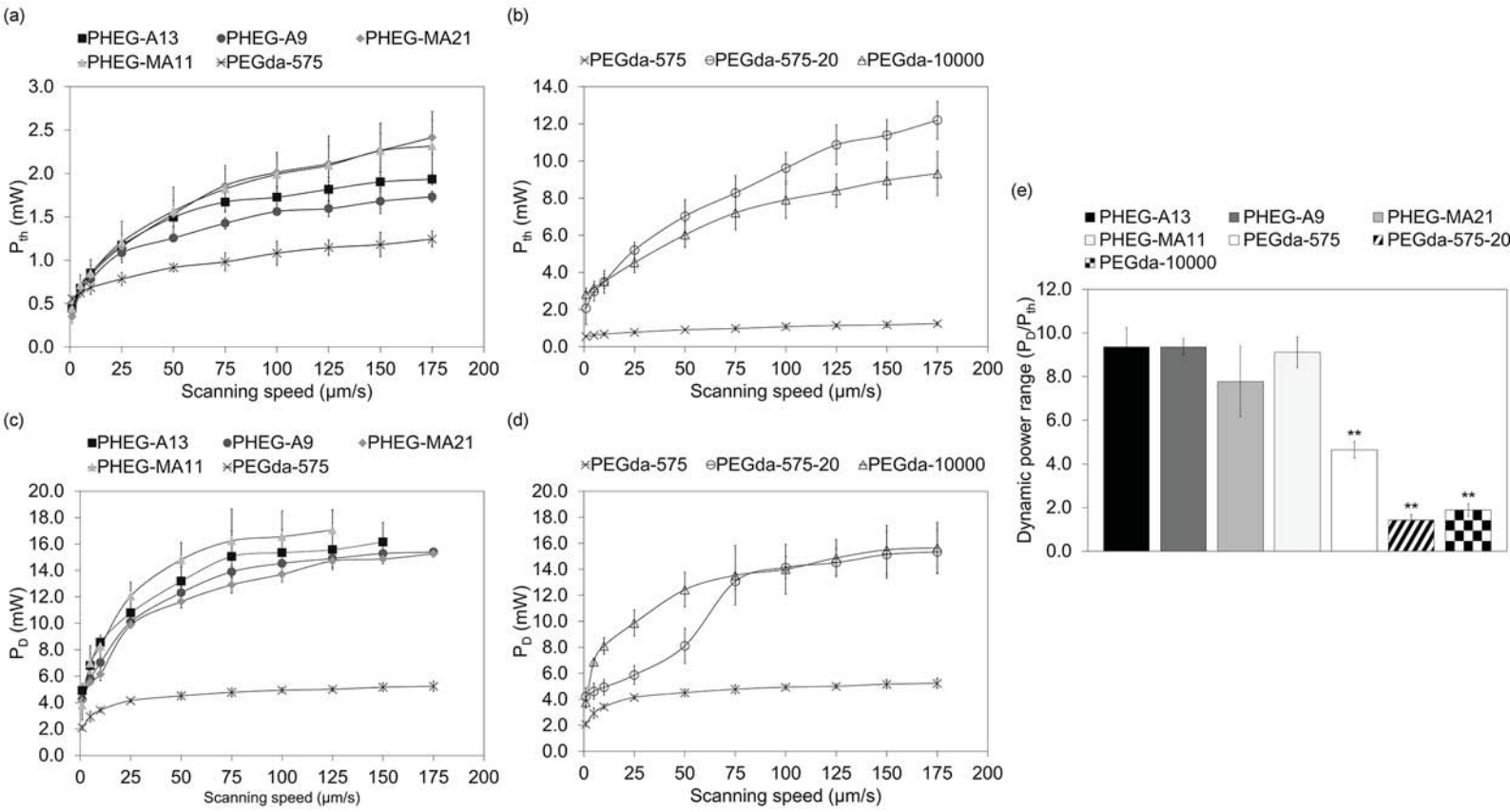
(a)
PHEG-A13
PHEG-A9
PHEG-MA21
PHEG-MA11
PEGda-575
P_{th} (mW)
Scanning speed (μm/s)
(b)
PEGda-575
PEGda-575-20
PEGda-10000
P_{th} (mW)
Scanning speed (μm/s)
(c)
PHEG-A13
PHEG-A9
PHEG-MA21
PHEG-MA11
PEGda-575
P_D (mW)
Scanning speed (μm/s)
(d)
PEGda-575
PEGda-575-20
PEGda-10000
P_D (mW)
Scanning speed (μm/s)
(e)
PHEG-A13
PHEG-A9
PHEG-MA21
PHEG-MA11
PEGda-575
PEGda-575-20
PEGda-10000
Dynamic power range (P_D/P_{th})
**
**
**

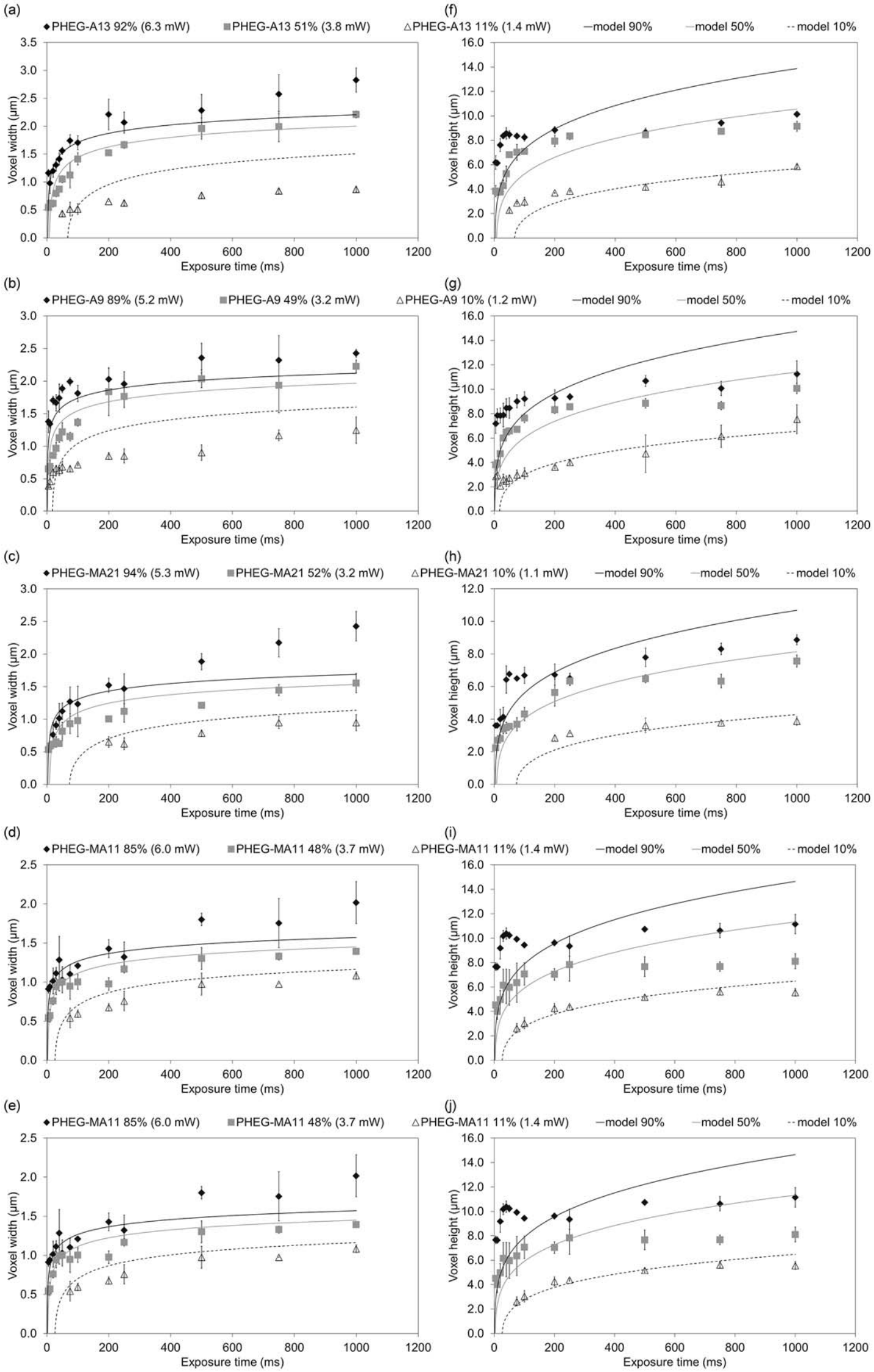
(a)
PHEG-A13 92% (6.3 mW)
PHEG-A13 51% (3.8 mW)
PHEG-A13 11% (1.4 mW)
model 90%
model 50%
model 10%
Voxel width (µm)
Exposure time (ms)
(f)
Voxel height (µm)
Exposure time (ms)
(b)
PHEG-A9 89% (5.2 mW)
PHEG-A9 49% (3.2 mW)
PHEG-A9 10% (1.2 mW)
(g)
(c)
PHEG-MA21 94% (5.3 mW)
PHEG-MA21 52% (3.2 mW)
PHEG-MA21 10% (1.1 mW)
(h)
Voxel hieght (µm)
(d)
PHEG-MA11 85% (6.0 mW)
PHEG-MA11 48% (3.7 mW)
PHEG-MA11 11% (1.4 mW)
(i)
(e)
(j)

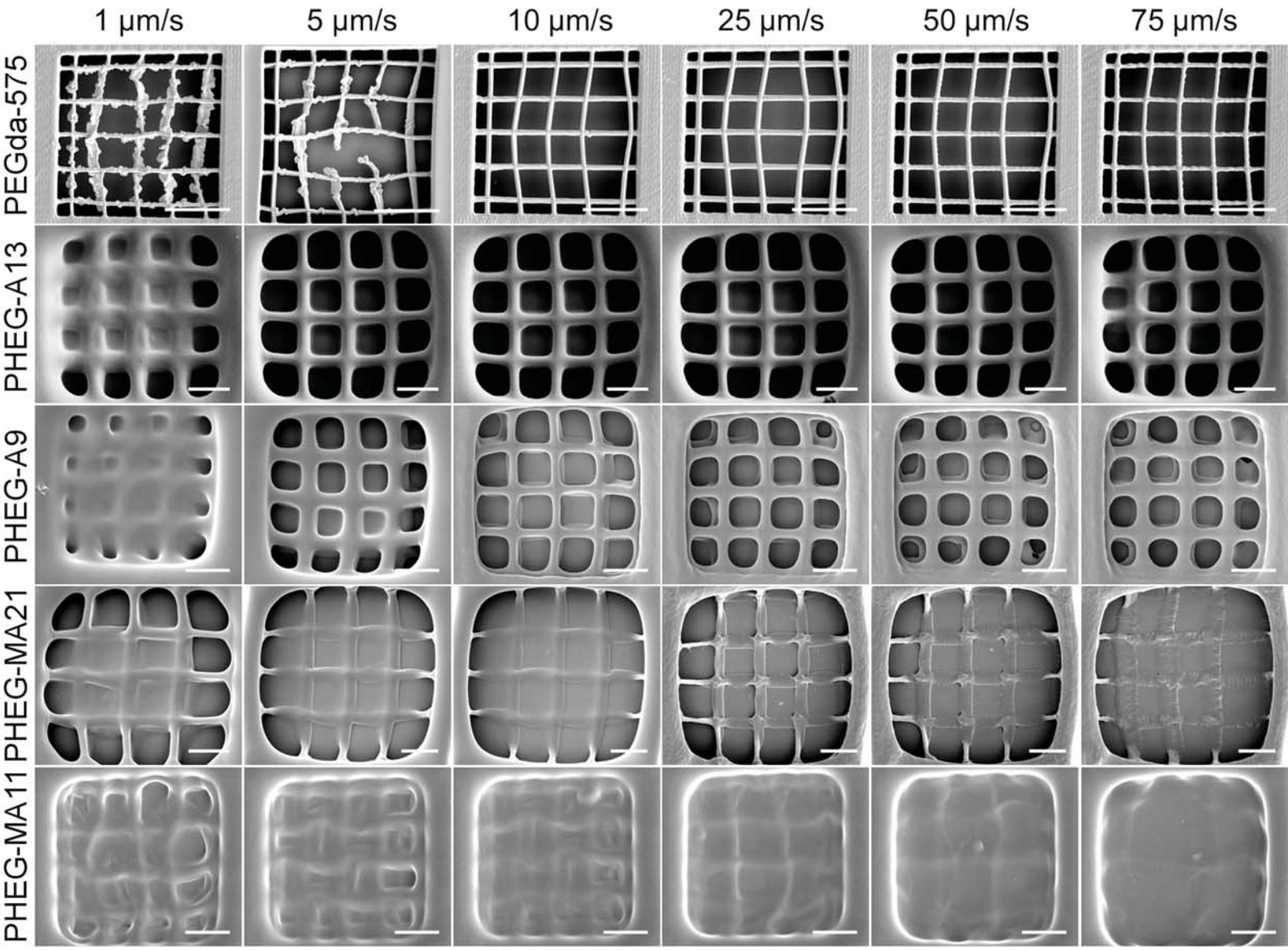
1 µm/s
5 µm/s
10 µm/s
25 µm/s
50 µm/s
75 µm/s
PEGda-575
PHEG-A13
PHEG-A9
PHEG-MA21
PHEG-MA11

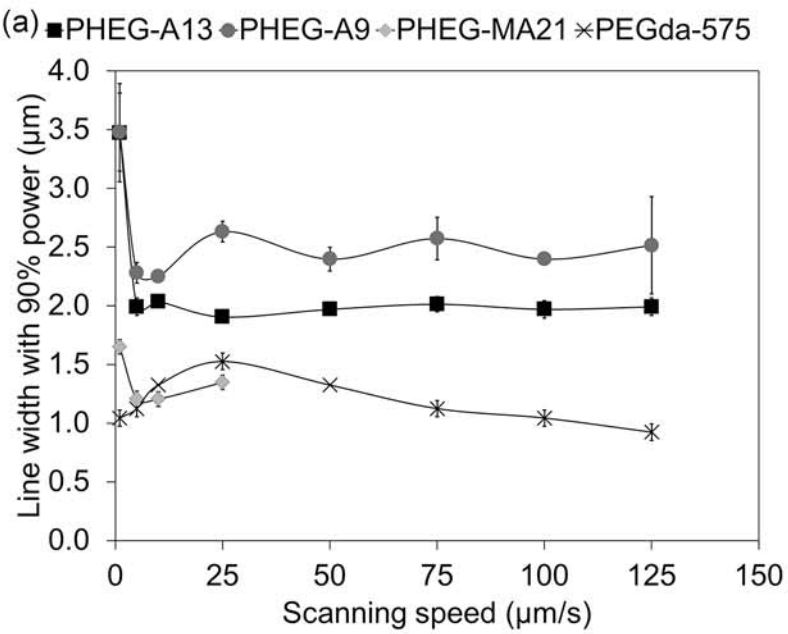
(a)
PHEG-A13
PHEG-A9
PHEG-MA21
PEGda-575
Line width with 90% power (μm)
Scanning speed (μm/s)

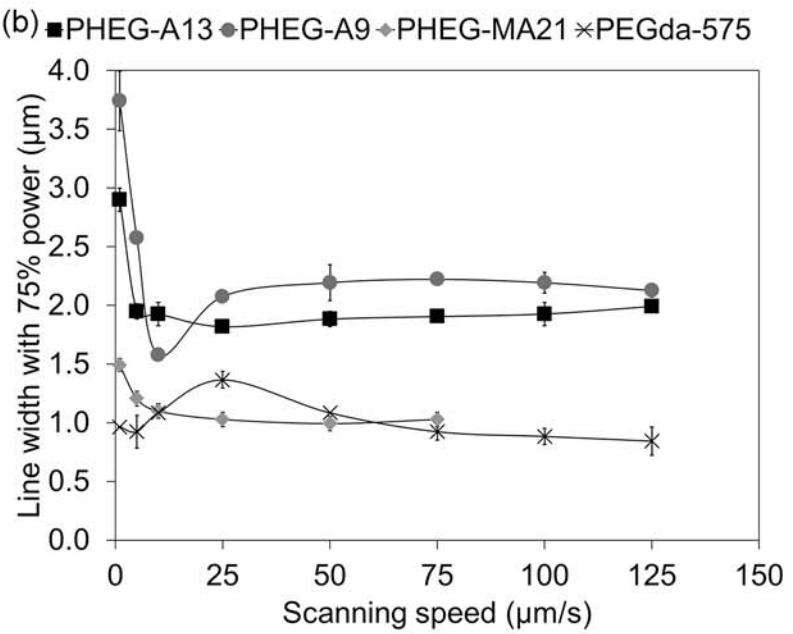
(b)
PHEG-A13
PHEG-A9
PHEG-MA21
PEGda-575
Line width with 75% power (μm)
Scanning speed (μm/s)

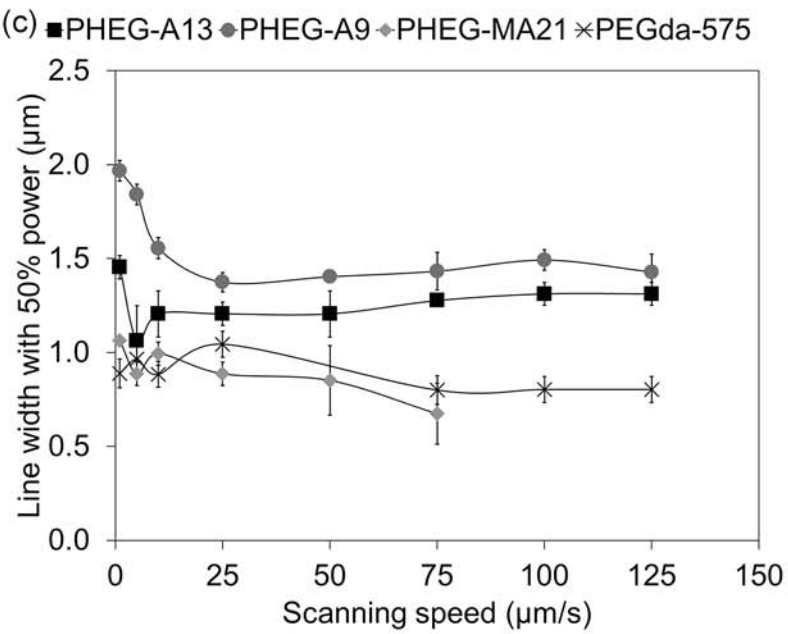
(c)
PHEG-A13
PHEG-A9
PHEG-MA21
PEGda-575
Line width with 50% power (μm)
Scanning speed (μm/s)

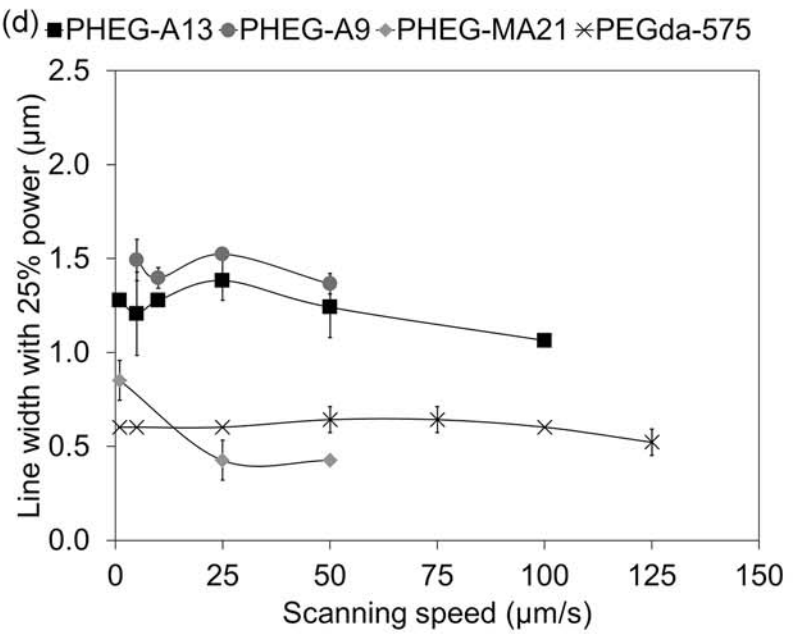
(d)
PHEG-A13
PHEG-A9
PHEG-MA21
PEGda-575
Line width with 25% power (μm)
Scanning speed (μm/s)

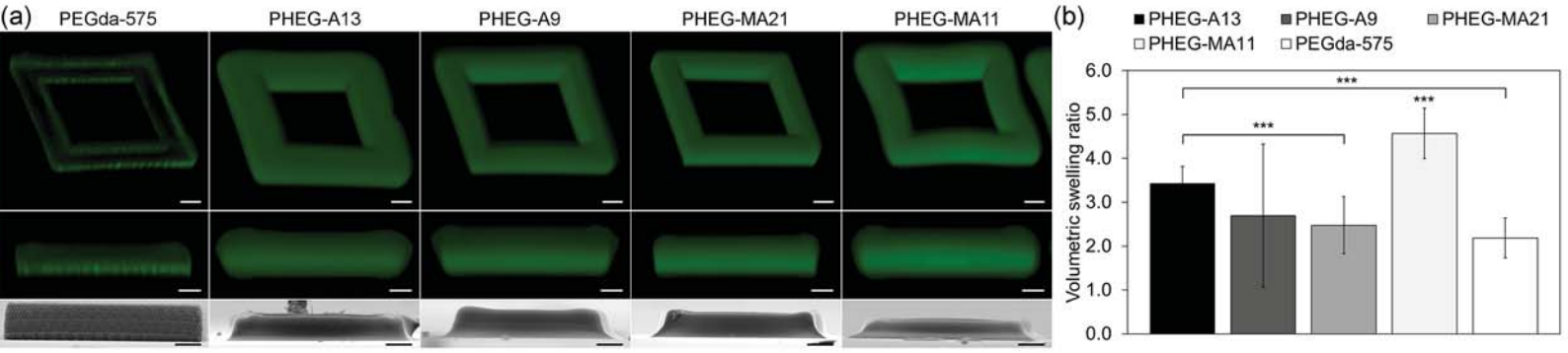
(a)
PEGda-575
PHEG-A13
PHEG-A9
PHEG-MA21
PHEG-MA11
(b)
PHEG-A13
PHEG-A9
PHEG-MA21
PHEG-MA11
PEGda-575
Volumetric swelling ratio
6.0
5.0
4.0
3.0
2.0
1.0
0.0
***
***
***

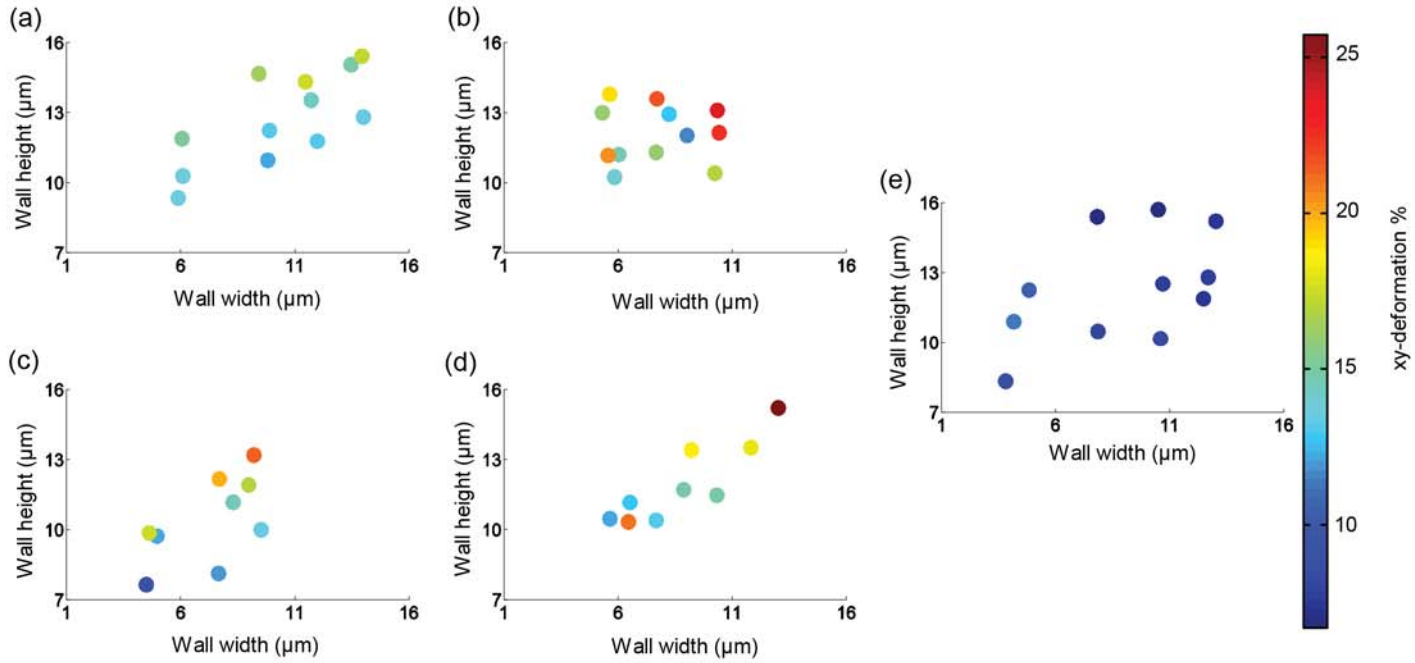
(a)
(b)
(c)
(d)
(e)
Wall height (µm)
Wall width (µm)
16
13
10
7
1
6
11
16
xy-deformation %
25
20
15
10

Tampereen teknillinen yliopisto
PL 527
33101 Tampere

Tampere University of Technology
P.O.B. 527
FI-33101 Tampere, Finland

ISBN 978-952-15-3361-7
ISSN 1459-2045